Fast and Unambiguous Direction Finding for Digital Radar Intercept Receivers

Peter Quoc Cuong Ly

A Thesis Submitted for the Degree of

Doctor of Philosophy

School of Electrical and Electronic Engineering
The University of Adelaide
Adelaide, South Australia

December 2013

For my wife, Joy

The Light of my Life

Contents

List of Figures

List of Tables

Abstract

This thesis considers the problem of angle-of-arrival (AOA) estimation in the context of its application to electronic surveillance systems. Due to the operational requirements of such systems, the AOA estimation algorithm must be computationally fast, accurate and will need to be implemented using sparse, large aperture arrays.

Interferometry is proposed as a suitable algorithm that meets the operational requirements of electronic surveillance systems. However, for sparse array geometries, phase wrapping effects introduce ambiguities to the phase measurements and so unambiguous AOA estimation requires the use of computationally intensive ambiguity resolution algorithms using three or more antennas.

Beamforming and array processing techniques are another class of AOA estimation algorithms that can unambiguously estimate the AOA using sparse, large aperture arrays. While these techniques generally offer better AOA estimation performance than interferometric techniques, they are also comparatively more computationally intensive algorithms. Furthermore, by virtue of using very sparse arrays, high sidelobes in the array beampattern may cause incorrect AOA estimation.

This thesis will introduce the concept of using second-order difference array (SODA) geometries which allow unambiguous AOA estimation to be performed in a computationally efficient manner. In the context of interferometry, the so-called "SODA interferometer" will be shown to synthesise the equivalent output of a smaller virtual aperture to allow unambiguous AOA estimation to be performed at the expense of a coarser estimation performance compared to the physical aperture of the array. It will also be shown that the coarse SODA AOA estimate can be used to cue the conventional ambiguity resolution algorithms to provide higher accuracy in a computationally efficient manner. This thesis will also show that the creation of virtual arrays from SODA geometries can be generalised to a larger number of antennas to allow conventional array processing techniques to perform unambiguous AOA estimation in a computationally fast manner.

The AOA estimation performance of each algorithm is compared through simulations and also verified using experimental data. This thesis will show that the SODA interferometer, SODA-cued ambiguity resolution algorithms and so-called "second-order array processors" can be used to obtain high accuracy AOA estimates in a more computationally efficient manner than the conventional algorithms.

Declaration

I certify that this work contains no material which has been accepted for the award of any other degree or diploma in my name, in any university or other tertiary institution and, to the best of my knowledge and belief, contains no material previously published or written by another person, except where due reference has been made in the text. In addition, I certify that no part of this work will, in the future, be used in a submission in my name, for any other degree or diploma in any university or other tertiary institution without the prior approval of the University of Adelaide and where applicable, any partner institution responsible for the joint-award of this degree.

I give consent to this copy of my thesis, when deposited in the University Library, being made available for loan and photocopying, subject to the provisions of the Copyright Act 1968.

I also give permission for the digital version of my thesis to be made available on the web, via the University's digital research repository, the Library Search and also through web search engines, unless permission has been granted by the University to restrict access for a period of time.

.....

Peter Quoc Cuong Ly

3 December 2013

Acknowledgements

I would like to thank my university supervisor, Professor Doug Gray, for encouraging me to enter the field of signal processing. It was under your mentorship during my final years as a undergraduate student that sparked my interest in a career in signal processing research. Thank you for all of your time, effort and patience over the last ten years. Without your support and encouragement, the completion of this thesis would not have been possible.

I would also like to thank my DSTO supervisor, Dr Stephen Elton, for bringing this PhD to fruition. This thesis would not have been possible without your tireless efforts in negotiating the agreement between the university and DSTO. Your friendship and unwavering support both academically and personally during this candidacy has been an invaluable source of encouragement.

I would also like to thank my co-supervisor, Professor Bevan Bates, for helping me navigate through the necessary administration at the university and DSTO and also for allowing me to join in on a number of experiments to collect experimental data to support this PhD research.

I am grateful for the support of my DSTO superiors, Dr Len Sciacca, Dr Jackie Craig, Dr Warren Marwood, Dr Peter Gerhardy and Brian Reid, for providing me with the opportunity to undertake this PhD research as part of my DSTO working arrangements. I am also grateful for the support from my DSTO colleagues, including but not limited to Simon Herfurth, John Quin, Phil Wandel, Jarrad Shiosaki, Andrew Evans and Songsri Sirianunpiboon for their assistance with the hardware development and experimental trials.

I would like to express my gratitude to my family for their unconditional love and support. I would like to thank my parents for instilling in me the appreciation of academic excellence and the value of persistence. I would also like to thank my sister for grounding me in reality.

Finally, I thank my wife, Joy, for being my rock during the last seven years. Not only do you deserve credit for helping me academically, but your unwavering support, patience and faith in me helped me get through some of my darkest times. You are my light.

Publications

Some parts of this thesis have been published for presentation at conferences. The following list is the bibliographic information pertaining to these preliminary presentations.

- Ly, P. Q. C., Elton, S. D., Li, J. & Gray, D. A., "Computationally Fast AOA Estimation Using Sparse Large Aperture Arrays for Electronic Surveillance," in *Proceedings of the IEEE International Conference on Radar (RADAR 2013)*, 2013. Accepted.
- Ly, P. Q. C., Elton, S. D., Gray, D. A., & Li, J., "Unambiguous AOA Estimation Using SODA Interferometry for Electronic Surveillance," in *Proceedings of the IEEE Sensor Array and Multichannel Signal Processing Workshop (SAM 2012)*, pp. 277–280, 2012.
- Ly, P. Q. C., Gray, D. A., Elton, S. D., & Bates, B. D., "A Digital Interferometric Testbed for ES/ELINT Research," in *Proceedings of the Seventh Direction Finding and Geolocation Symposium*, 2008.

Acronyms

Acronym	Description
ADC	Analogue to Digital Converter
AOA	Angle of Arrival
CAS	Common Angle Search
CBF	Conventional Phaseshift Beamforming
COS	Correlative Interferometry using the Cosine Cost Function
CRLB	Cramér-Rao Lower Bound
CW	Continuous Wave
DOA	Direction of Arrival
DF	Direction Finding
DFT	Discrete Fourier Transform
DSTO	Defence Science and Technology Organisation
ELINT	Electronic Intelligence
ES	Electronic Support
ESM	Electronic Support Measures
EW	Electronic Warfare
FFT	Fast Fourier Transform
FMCW	Frequency Modulated Continuous Wave
FOV	Field of View
FPGA	Field Programmable Gate Array
GSPS	Giga-Samples Per Second, 1×10^9 Samples Per Second
LPI	Low Probability of Intercept
LS	Correlative Interferometry using the Least Squares Cost Function
MSPS	Mega-Samples Per Second, 1×10^6 Samples Per Second
MLE	Maximum Likelihood Estimator
MSE	Mean Square Error
MUSIC	Multiple Signal Classification
POI	Probability of Intercept
PRI	Pulse Repetition Interval
RMS	Root Mean Square
RMSE	Root Mean Square Error
RWR	Radar Warning Receiver
SBI	SODA-Based Inference
SNR	Signal to Noise Ratio
SODA	Second Order Difference Array
TDC	Time to Digital Converter
TDOA	Time Difference of Arrival
TOA	Time of Arrival
TOB	Time of Burst

Notation

Symbols

The following symbols will be used throughout this thesis:

Symbol	Description
η	Signal to Noise Ratio
A	Peak Amplitude of the Signal
f	Carrier Frequency of the Signal
λ	Wavelength of the Signal's Carrier Frequency
φ	Initial Phase of the Signal
θ	Azimuth Component of the Signal's Angle of Arrival
ϕ	Elevation Component of the Signal's Angle of Arrival
t_s	Sample Interval
f_s	Sampling Rate (or Sampling Frequency)
τ	Propagation Time Delay Between Two Antennas
ψ	Propagation Phase Delay Between Two Antennas
d	Distance Between Two Antennas (or Interferometer Baseline)
t	Time Instance
$s(t)$	Continuous Time-Varying Signal Without Noise
$x(t)$	Continuous Time-Varying Signal With Noise
$\epsilon(t)$	Continuous Time Additive Gaussian Noise
$s[n]$	Discrete Time-Varying Signal Without Noise
$x[n]$	Discrete Time-Varying Signal With Noise
$\epsilon[n]$	Discrete Time Additive Gaussian Noise
$\beta(\theta)$	Phase Error due to Channel Imbalance
N	Number of Samples
K	Number of Antennas
M	Number of Interferometer Baselines
D	Set of Interferometer Baselines
Υ	Set of Potential Ambiguity Numbers for a Single Baseline
Ω	Set of Ambiguity Number Combinations from all Baselines
σ	Standard Deviation of Noise
$v(\theta)$	Propagation Delay for a Single Baseline
$\boldsymbol{v}(\theta)$	Propagation Delay Vector for all Baselines
$\Delta\theta$	Azimuth Grid Search Resolution
$\mathrm{BW_{NN}}$	Null-to-Null Beamwidth

Scripts and Accents

Scripts and accents will be used to confer additional meaning to the above symbols.

- A single letter subscript specifies that the associated parameter belongs to a specific hardware channel. For example, A_k and f_k refers to the peak amplitude and carrier frequency of the k-th receiver channel. A single letter subscript can also specify that the parameter belongs to a particular interferometric baseline. For example, ψ_m and d_m refers to the phase delay and baseline of the m-th interferometer baseline. When only a single letter subscript is used, it is generally implied that the specified parameter refers to an arbitrary interferometer baseline.
- A double letter subscript specifies the parameter of a particular channel with respect to another channel. For example, ψ_{kl} and d_{kl} refers to the phase delay and interferometer baseline of the k-th antenna relative to the l-th antenna. When a double letter subscript is used, it is generally implied that the specified parameter refers to a specific interferometer baseline.
- The subscript $_s$ specifies a steered parameter that is under the control of the radar intercept receiver. For example, θ_s refers to the steered AOA of a grid search algorithm for AOA estimation.
- The superscript ^{u} specifies an uncalibrated parameter that is subject to channel imbalances.
- The superscript ^{c} specifies a calibrated parameter free of channel imbalances.
- The tilde accent $\tilde{}$ specifies a measured parameter. In particular, when specifying the phase delay measurement, ψ refers to the unwrapped, unambiguous phase delay, however, $\tilde{\psi}$ refers to the measured, ambiguous phase delay that is constrained to the interval $[-\pi, \pi]$.
- The hat accent $\hat{}$ specifies an estimated parameter.
- Plain typeface symbols, e.g. $v(\theta)$, are used to denote scalar variables.
- Bold typeface symbols in lower case characters, e.g. $\boldsymbol{v}(\theta)$, are used to denote vector variables.
- Bold typeface symbols in upper case characters, e.g. $\boldsymbol{R}$, are used to denote matrix variables.

Mathematical Operators

Operator	Description
round $[a]$	Rounds the scalar a to the nearest integer.
$\lceil a \rceil$	Rounds the scalar a upwards to the next integer.
$\lfloor a \rfloor$	Rounds the scalar a downwards to the next integer.
$\odot$	Cartesian product.
$\boldsymbol{a}^T$ or $\boldsymbol{A}^T$	Transpose of the vector, $\boldsymbol{a}$, or matrix, $\boldsymbol{A}$.
$\boldsymbol{a}^H$ or $\boldsymbol{A}^H$	Hermitian (complex conjugate) transpose of the vector, $\boldsymbol{a}$, or matrix, $\boldsymbol{A}$.

Units

All parameters are assumed to adhere to the International System of Units (or SI units).

The units of phase-related values, such as the phase delay and angle-of-arrival, are assumed to be expressed in radians for all mathematical expressions. However, for readability, the phase-related values will often be expressed in degrees in the text and figures.

Chapter 1

Introduction

1.1 Introduction

This thesis aims to investigate computationally fast and highly accurate angle-of-arrival (AOA) estimation algorithms that can be implemented in digital microwave radar intercept receivers for real-time electronic surveillance. While the problem of AOA estimation, or direction finding (DF), has been studied extensively in many different fields, such as radar [1], sonar [2], astronomy [2], meteorology [3] and communications [2, 4], the specific application of AOA estimation to the electronic support (or electronic surveillance) environment warrants some additional attention due to the unique and demanding operational requirements of radar intercept systems.

The AOA of a radar signal is an important parameter to be estimated by the radar intercept receiver as it can be exploited in a number of strategic and operationally useful ways. However, due to the trade-off that generally exists between the accuracy and computation time of an algorithm, the choice of the AOA estimation algorithm must strike the right balance between accuracy and computational speed. This thesis aims to investigate high accuracy, but possibly sub-optimal, AOA estimation algorithms that are computationally fast and are suited for real-time operation in radar intercept receivers.

1.2 Electronic Support

The interception and exploitation of radar signals has been an important objective of military reconnaissance since the development of the radar [5–7]. In a field known as *electronic support* (ES), information gathered from so-called radar intercept receivers is used by military platforms to enhance situational awareness of the operating environment, provide self-protection and contribute to *electronic intelligence* (ELINT) databases [1, 5, 6].

Radar intercept receivers classify and identify radars by analysing their signal waveforms. This is achieved by using hardware that can reliably detect and measure the characteristics of all radar signals in the environment. The characteristics of the intercepted radar signal that are generally estimated include the signal's

- amplitude,

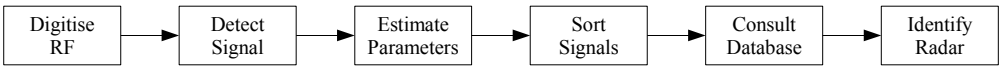

Figure 1.1: Block diagram of the typical functions performed by a radar intercept receiver.

- frequency,
- duration,
- time-of-arrival (TOA),
- angle-of-arrival (AOA),
- intra-pulse modulation characteristics (e.g. modulation type and characteristics), and
- inter-pulse characteristics (e.g. pulse repetition interval (PRI) and PRI stagger patterns) [5, 8].

Once the characteristics of all radar signals have been estimated, radar intercept receivers use the estimated parameters to sort the collection of intercepted signals to identify all of the intercepts that belong to a single radar emitter. An ELINT database of known radar emitters is then consulted to find the radar emitter that exhibits parameters that best match the estimated characteristics of the observed intercepts [1, 5].

Traditionally, there have been two types of radar intercept receivers, namely ELINT systems and tactical ES systems. ELINT systems are designed to gather high fidelity data to generate high quality representations of the radar signals. These signals are then used to contribute to ELINT databases which are used by tactical ES systems to identify the radars observed in the field [5]. For ELINT systems, the accuracy of the estimation algorithms is generally more important than the computation time as the analysis can often be performed offline.

On the other hand, tactical ES systems are designed to provide the operators of military platforms with real-time, early warning of radar emitters that are operating in the vicinity of the platform [9]. For this reason, tactical ES systems are sometimes called *early warning receivers*. Tactical ES systems are traditionally distinguished as either *electronic support measures* (ESM) systems or *radar warning receivers* (RWRs). ESM systems are typically operated by a human operator in an interactive manner while RWRs are typically fully automated systems. In extreme operating environments, a tactical ES system may receive in excess of hundreds of thousands of radar intercepts per second [1, 6]. While the accuracy of the estimation algorithms is important, the data throughput that can be continuously sustained by the system is also an important consideration. As a result, tactical ES systems may need to trade-off some accuracy in the parameter estimation algorithms for the sake of improvements in the data throughput. The development of computationally fast algorithms is a major driver of the research presented in this thesis.

With the advent of high fidelity digital receivers, the traditional roles of ELINT and tactical ES systems have become increasingly blurred. It is not uncommon for modern radar intercept receivers to undertake both roles.

1.3 The Importance of Direction Finding

The AOA of a radar intercept is a particularly important parameter to estimate because it can be exploited in a number of operationally useful ways, including

- enhance situational awareness [5, 6, 9, 10],
- enhance signal sorting (or deinterleaving) algorithms [5],
- cue electronic attack measures (such as jammers) or electronic protection measures (such as chaff) [1, 9, 10],
- improve the signal collection [2], and
- perform the beaming manoeuvre as discussed below.

1.3.1 Situational Awareness

Situational awareness of the operating environment is critically important to help determine the engagement priorities, tactics and the electronic order of battle [6, 9, 10]. Accurate AOA estimates can help to improve the situational awareness by associating lines of bearings to each detected platform. When the AOA from multiple radar intercept receivers are used in conjunction with geolocation algorithms, it is possible to further localise detected platforms to geographical coordinates [4–6, 11].

1.3.2 Signal Deinterleaving

Radar intercept receivers typically receive anywhere from hundreds to hundreds of thousands of radar intercepts per second from multiple emitters [1, 6]. As part of its typical processing, radar intercept receivers must sort through the collected data and associate all of the intercepts to their respective emitters. This process is known as *signal deinterleaving*.

Parameters such as the signal's carrier frequency, pulse duration, modulation characteristics, and pulse train parameters such as the PRI and PRI stagger patterns, are traditionally effective deinterleaving parameters [5, 8]. However, the traditional deinterleaving parameters are not effective against radars with similar transmission characteristics or modern parameter-agile radars that are capable of changing their transmission parameters on a pulse-by-pulse basis [12]. On the other hand, since the AOA of a signal cannot be disguised in a practical manner, high precision AOA estimates can be used to effectively deinterleave the signal from these types of radars, provided that the radars are sufficiently separated in angle [1, 5, 6, 8, 13, 14].

1.3.3 Electronic Attack and Electronic Protection Measures

Knowledge of an adversary's bearing can assist the platform's electronic attack systems (such as jammers) and electronic counter measures systems (such as chaff) by more efficiently directing the platform's resources to deal with a threat from a given bearing [1, 9, 10].

1.3.4 Signal Enhancement

By exploiting the multi-channel output of an antenna array with the signal's AOA, coherent processing can be performed using *beamforming* methods to improve the signal-to-noise ratio (SNR) of the intercepted signal [2]. With a higher quality signal representation, the accuracy of the parameter estimation algorithms will also be improved [15–17].

1.3.5 Beaming Manoeuvre

Accurate AOA information can provide operators of highly manoeuvrable platforms with the ability to temporarily "disappear" from the view of Doppler radars with moving target indicator (MTI) displays. Many contemporary radars exploit the Doppler effect to detect and track moving platforms. The Doppler frequency shift, f_d, of a moving platform is given by

$$f_d = 2\frac{v_r}{c}f, \tag{1.1}$$

where v_r is the *radial* velocity of the platform, c is the speed of light and f is the carrier frequency of the radar signal [1, 18]. Since the Doppler radar specifies the frequency of the signal, these radars are able to estimate the platform's radial velocity by measuring the Doppler frequency of the return signal. Radar targets that are determined to have a non-zero velocity are typically displayed on a MTI display, however, targets with little to no velocity are generally considered as background clutter and so are hidden from the MTI display [1, 18].

From a self-protection perspective, a moving platform can minimise its Doppler returns to the radar by changing its trajectory to be perpendicular to the direction of the radar. In this trajectory, the velocity of the platform (relative to the radar) will be mostly tangential. With little to no radial velocity, the radar will measure a Doppler frequency close to zero, i.e. $f_d \approx 0$ Hz, and so the Doppler returns from the moving platform will likely fall into the background clutter of the radar's processor. As a result, the MTI display will likely disregard the moving platform as a stationary object. This tactical manoeuvre is known as the *beaming manoeuvre*.

The beaming manoeuvre is typically only useful for highly manoeuvrable platforms, such as fast jets, which can rapidly change their trajectory. Very fast and very accurate AOA estimates are required to successfully perform the beaming manoeuvre. In practice, it would be difficult for moving platforms to maintain an operationally useful trajectory while perpendicular to the Doppler radar for an extended period of time. However, each time the beaming manoeuvre is performed, the Doppler radar must restart its tracking process. The platform may then exploit this small time interval to either move closer

to, or further away from, the Doppler radar.

Finally, it should be noted that the beaming manoeuvre is only effective against Doppler radars. Radars that do not exploit the Doppler effect will not be affected by this manoeuvre.

1.4 Problem Statement

This thesis is concerned with investigating and experimentally validating computationally fast and highly accurate AOA estimation algorithms for real-time operation with a focus on their implementation in digital microwave radar intercept receivers, and in particular, tactical ES systems. This application imposes additional constraints on the AOA estimation algorithms and will be discussed in more detail below.

1.4.1 Design Constraints of a Radar Intercept Receiver

As a real-time surveillance system, radar intercept receivers are designed to exploit emissions from non-cooperative radars with unknown signal characteristics. Due to the diverse range of radars in operation, radar intercept receivers must be able to detect and measure the parameters of radar signals with unknown bandwidths over a very wide frequency range. Microwave radar intercept receivers are traditionally concerned with radars operating between $2-18$ GHz [8]. Furthermore, since many radars may be operating simultaneously, the hardware and signal processing of the radar intercept receiver must be sufficiently fast to provide near real-time surveillance of the environment and to maintain a high probability of intercept (POI) for all radar emissions. Finally, the monetary cost of the radar intercept receiver must be affordable to allow the deployment of such systems across a large fleet of military platforms.

The operational requirements of a typical microwave radar intercept receiver can be summarised as follows [8]:

- be able to intercept signals between $2-18$ GHz,
- be able to simultaneously monitor a wide frequency range (typically 500 MHz or more),
- be able to intercept narrowband and wideband signals (typically up to 500 MHz or more),
- be able to exploit multiple, simultaneously illuminating signals,
- maintain near real-time operation in a high signal density environment,
- maintain a high POI at all times, and
- be cost effective.

The above requirements impose a number of hardware and signal processing constraints on the radar intercept receiver. Firstly, in order to maintain a high POI at all times, a

multi-antenna, multi-channel digital receiver is required to provide instantaneous coverage of the entire field-of-view.

Secondly, in order to operate over a wide frequency range, the multi-channel digital receiver must be able to receive signals over the entire frequency range, i.e. $2 - 18$ GHz. This requires hardware components, such as antennas, tuners, filters, amplifiers and power dividers, to be capable of operating over the entire frequency range. The cost of these wideband components is generally quite high, particularly for multiple, phase-coherent, wideband microwave tuners. At current prices, the cost of such a system can range from tens to hundreds of thousands of dollars per channel. Hence, contemporary radar intercept receivers often only utilise a small number of channels, typically $4 - 16$ channels, for a single platform.

Furthermore, wideband antennas that are capable of receiving signals between $2 - 18$ GHz are typically physically large devices as they must have an aperture large enough to receive the lowest frequency of interest. Examples of wideband antennas include cavity-backed spirals, bi-conical and horn antennas. The use of physically large antennas in a multi-antenna system imposes a lower limit on the minimum antenna spacings that can be physically achieved.

Thirdly, in order to digitally capture a signal with minimal distortion, the Nyquist criterion requires the sampling rate of the multi-channel digital receiver to be twice the bandwidth of the (real) signal. While many conventional radar signals have relatively low bandwidths (relative to the carrier frequency), i.e. up to about 100 MHz, some modern radar signals have been known to have very high bandwidths, i.e. greater than 1 GHz. Thus, radar intercept receivers must have a high sample rate (and hence high speed digitiser) to correctly receive wideband radar signals. The use of high speed digitisers translates to high data rates and so has implications on the computation time available for the signal processing.

Finally, radar intercept receivers may need to operate in dense signal environments, such as commercial ports and harbours, where hundreds of radars may be operating simultaneously. In these situations, it is not uncommon for the radar intercept receiver to see tens to hundreds of thousands of radar signals per second. The throughput of such a large volume of signals, especially at a high sample rate, has further implications on the computation time available for the signal processing.

1.4.2 One-Way Propagation Advantage

Radar systems suffer a two-way propagation loss as a transmitted signal must travel to a target and then be reflected back in order to be observed by the radar. The radar must therefore transmit its signal with enough power to ensure that sufficient energy is received upon the signal's return. On the other hand, the radar intercept receiver residing on the target can intercept the radar signal as soon as the signal hits the platform. At this point, the radar signal has only suffered a one-way propagation loss [1, 5, 6]. Thus, while radar intercept receivers face rather challenging hardware requirements, one advantage that these systems have is that the intercepted signals generally have high signal-to-noise ratios due to the one-way propagation of the signal.

This is often termed the *range advantage* of the radar intercept receiver.

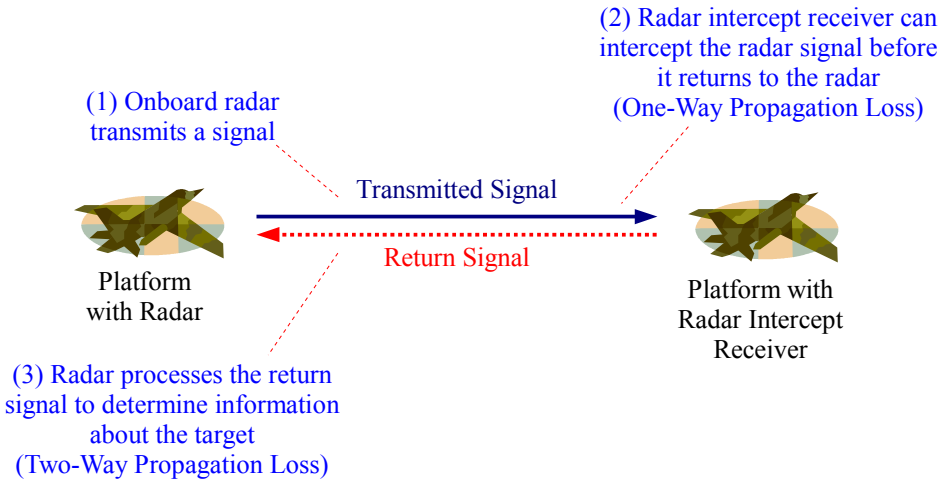

Figure 1.2: Radar intercept receivers have a range advantage over the radar.

1.4.3 Implications for AOA Estimation

In light of the operational objectives of radar intercept receivers and the intended applications for the AOA estimates, the performance requirements of the AOA estimation algorithm can be summarised as follows:

- Estimate the AOA of any signal between $2-18$ GHz,
- Estimate the AOA of narrowband and wideband signals (up to 500 MHz or more),
- Estimate the AOA of pulsed and continuous wave (CW) radar signals, and
- Estimate the AOA of multiple, simultaneously illuminating signals.

Furthermore, given the hardware requirements of radar intercept receivers, implementation of the AOA estimation algorithms are subject to the following constraints:

- The number of independent channels available to perform AOA estimation is small, typically $4-16$ antennas for the entire platform (or $2-4$ antennas per quadrant).
- The AOA estimation algorithm must be sufficiently fast to facilitate near real-time operation.
- There is a lower limit to the minimum spacing that can be achieved for the antenna array due to the use of physically large, wideband antennas.

In the following chapter, this thesis will propose that interferometry is a suitable AOA estimation technique that meets all of the above performance and hardware requirements. However, since interferometry requires a short antenna spacing to perform unambiguous AOA estimation, the use of physically large, wideband antennas will cause the AOA estimation to be highly ambiguous. The primary focus of this thesis will therefore be to obtain unambiguous, high accuracy AOA estimates using sparse large aperture arrays in a computationally efficient manner. A significant part of this thesis is that the results of the theoretical analysis will be verified experimentally.

1.4.4 Assumptions

For the sake of brevity, this thesis will make a few simplifying assumptions about the intercepted radar signal. Unless otherwise stated, it will generally be assumed that

- the signal has been correctly detected and captured,
- the signal has a high SNR (typically about 5 dB to 15 dB),
- the signal is a burst of continuous wave (CW),
- the signal is narrowband (i.e. unmodulated),
- the signal lies in the same plane as the intercept receiver,
- only one signal is received at a time,
- the intercept receiver uses a uniform sampling rate that satisfies the Nyquist criterion, and
- the frequency estimation has negligible error.

This thesis is concerned with the AOA estimation of *post-detected* signals. It is assumed that the radar intercept receiver has appropriate detection logic to determine the presence of a radar signal and appropriate digital recording logic to ensure that the radar signal has been correctly digitised in its entirety.

Due to the one-way propagation advantage, it is generally reasonable to assume that conventional pulsed radar signals are intercepted with a typical SNR of $5 - 15$ dB [5, 6, 12].

Radar signals are traditionally pulses, i.e. short bursts of energy. Unlike CW signals which are continuously transmitted, pulsed signals are only transmitted for short durations (typically nanoseconds to microseconds). As a consequence, the signal waveform has a well defined leading and trailing edge which are characteristic of the start and end of the transmission as illustrated in Figure 1.3. However, during the parameterisation of the radar signal, the leading and trailing edges are usually removed prior to parameter estimation and so the signal may be considered as a short duration CW signal.

While radars have traditionally used narrowband (unmodulated) signals, modern radars have been known to include frequency or phase modulation on the signal waveform to improve the performance of the radar [1, 12]. However, for many modern radars, the bandwidth of the modulated radar signal is below 50 MHz and so can effectively be considered a narrowband signal at the microwave carrier frequencies. Furthermore, a number of so-called *low probability of intercept* (LPI) radars transmit a relatively narrowband signal over a long duration [12, 19, 20], such as the PILOT radar which can transmit a signal with a 55 MHz bandwidth over a 1 millisecond interval [12]. Over a short observation interval, say 1 microsecond, the change in frequency is relatively small and may be considered as effectively constant. Hence, these type of LPI signals can often be considered as a sequence of short narrowband signals and so the assumption that the radar signal is narrowband applies. While truly wideband waveforms, with instantaneous bandwidths of 500 MHz or higher, do exist [12], the consideration of these

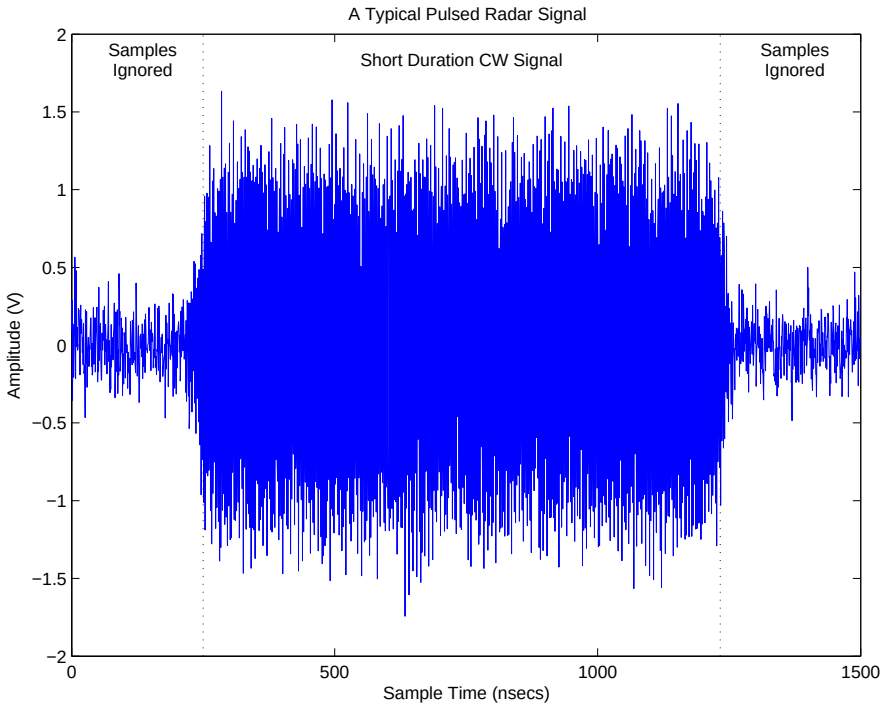

Figure 1.3: A typical pulsed radar signal has a well-defined leading and trailing edge.

waveforms is considered to be beyond the scope of this thesis.

The assumption that the intercepted radar signal lies in the same plane as the radar intercept receiver is made so that the elevation component of the AOA can be ignored for mathematical brevity. Due to their intended use to provide early warning of radar emitters, ES and ELINT systems are typically operated at large distances from the radar and so the co-plane assumption is usually justified. In practice, the elevation of the AOA can be estimated using the same azimuth-only AOA estimation algorithms for an antenna array placed physically orthogonal to the azimuth antenna array [4, 11, 16]. However, it should be noted that independently estimating the azimuth and elevation components of the AOA is subject to coning errors and must be appropriately compensated [6, 11].

In a given operating environment, it is possible for multiple radars to be simultaneously illuminating the radar intercept receiver. Traditionally, the combination of a low number of radars and low duty cycle signals meant that so-called *pulse-on-pulse* or *signal-on-signal* situations, where the radar signals from multiple emitters overlap during a single interception, were extremely rare. However, with the proliferation of radars in military and commercial applications, and with the current trend of using longer duty cycle signals, the modern electronic surveillance signal environment is becoming increasingly crowded. The likelihood of signal-on-signal situations is therefore much more likely to occur. However, for phase-based AOA estimation methods, such as interferometry, the phase of the signal can be accurately measured in the frequency domain. For signal-on-signal scenarios, provided that the signals are sufficiently separated in frequency, the phases of each signal can be independently estimated and so the corresponding AOA

of each signal can also be estimated. Thus, while signal-on-signal scenarios can occur, it is reasonable for phase-based methods to assume that the signal environment only contains one signal provided that the signals have different frequencies. However, note that this assumption is not valid when two or more signals have the same frequency or when the phases are estimated in the time domain.

Conventional digital receiver design theory requires that the sampling rate of a digital receiver to be at least twice the bandwidth of the (real) signal. In recent years, there has been growing interest in a field known as *compressive sensing* which aims to sample so-called "sparse signals" below the Nyquist rate [21–24]. The advantage of compressive sensing techniques is that the the amount of data required to correctly represent the signal can be significantly reduced and therefore can help to alleviate hardware design issues associated with the transfer, storage and processing of data. However, to the knowledge of the author, digital radar intercept receivers which implement compressive sensing techniques are not yet commonly used in practice. This thesis shall therefore assume that contemporary digital radar intercept receivers use conventional sampling techniques, i.e. a uniform sampling rate that satisfies the Nyquist criterion.

Finally, the use of interferometry to estimate the AOA of the signal requires knowledge of the carrier frequency of the signal. For electronic surveillance problems, the carrier frequency of the signal is generally not known and so must also be estimated from the intercepted signal. However, since the frequency estimation problem has been well studied in the literature [15, 25–31], the topic of frequency estimation is considered to be beyond the scope of this thesis. Furthermore, in Section 6.2.1, it will be shown that small frequency errors, of say 1 MHz, have little effect on the AOA estimation at microwave frequencies. Since a number of well-known frequency estimators are able to achieve better than 1 MHz RMS error at the SNRs and signal durations that are of interest in this thesis [15, 25–31], this thesis shall assume that the frequency estimation errors are negligible.

1.5 Organisation of this Thesis

The research undertaken in this thesis is divided into two parts. The first part (Chapter 2 - Chapter 5) is concerned with the theory of contemporary AOA estimation techniques. The second part (Chapter 6 - Chapter 8) is concerned with the practical implementation and experimental verification of the theoretical algorithms.

In Chapter 2, a summary of contemporary direction finding techniques that are suitable for implementation in radar intercept receivers is provided. The general performance of each technique and its advantages and disadvantages are discussed. At the conclusion of this chapter, an argument will be presented which nominates interferometry as the most suitable AOA estimation algorithm for both modern ES and ELINT systems, while array processing methods may be preferred for ELINT systems.

In Chapter 3, the theory of contemporary interferometers is presented. This chapter will show that short baseline interferometers provide unambiguous AOA estimates but have relatively poor AOA estimation accuracy. On the other hand, long baseline in-

terferometers provide high accuracy AOA estimates but are ambiguous. A number of contemporary ambiguity resolution algorithms are presented and the estimation performance and computational complexity of each algorithm is compared in a consistent manner. At the conclusion of this chapter, some practical considerations will be discussed, including how to apply interferometry to estimate the AOA of multiple signals that are simultaneously illuminating the antenna array and how to obtain a 360° field-of-view.

In Chapter 4, an alternative implementation of an interferometer using a second-order difference array (SODA) is presented. It will be shown that the SODA interferometer allows unambiguous AOA estimation to be performed using a sparse array geometry in a computationally efficient manner. This chapter will also show that the SODA interferometer can be used to cue the conventional ambiguity resolution algorithms to reduce the computational time of the conventional algorithms while maintaining high accuracy performance. The SODA interferometer, and SODA-cued algorithms such as the SODA-Based Inference (SBI) interferometer, are considered ideal candidates for implementation in ES and ELINT systems.

In Chapter 5, the concept of second-order processing is extended to traditional (first-order) beamforming and array processing methods. This chapter will show that the second-order processing enabled by the SODA geometry can reduce the number of computations required to unambiguously estimate the AOA compared to the conventional first-order array processors. The second-order array processing methods will also be shown to provide comparable AOA estimation performance to the equivalent first-order methods for very sparse SODA geometries.

In Chapter 6, the necessity for hardware calibration will be discussed. The calibration process is complicated by the fact that the channel imbalances may be dependent on the signal's AOA (which is the parameter to be estimated *after* calibration). The calibration process is further complicated by the phase ambiguity problem introduced by the necessity to use physically large antennas. This chapter will discuss two calibration methods that can be applied to remove the channel imbalances. Finally, this chapter will also show that when channel imbalances are present, some of the theoretically efficient ambiguity resolution algorithms discussed in Chapter 3 can become impractically slow.

In Chapter 7, the Electronic Support (ES) Testbed will be presented. The ES Testbed is a multi-channel digital receiver system developed to experimentally validate ES algorithms, including AOA estimation. In this chapter, the hardware architecture, data encoding and basic data processing is presented.

In Chapter 8, the experiments conducted using the ES Testbed (Chapter 7) to collect real-world data will be discussed. The AOA estimation algorithms (Chapter 3 - Chapter 5) and calibration algorithms (Chapter 6) will be applied to the collected data to experimentally validate their performance.

Finally, this thesis will be concluded in Chapter 9. The key findings of this thesis and the major contributions of this research will be summarised. This chapter will also identify areas that may warrant further research.

1.6 Original Contributions

There are a number of areas which the author believes this thesis makes an original contribution:

1. In Chapter 3, a number of contemporary ambiguity resolution algorithms for long baseline interferometry are collated and described in a consistent notation. The AOA estimation performance of each algorithm is compared against the Cramér-Rao Lower Bound using a consistent set of simulation parameters. To the knowledge of the author, such a comparison has not been published in any other work.

2. A significant portion of this thesis is dedicated to the application of second-order analysis to derive an interpolated virtual array for unambiguous AOA estimation. While the use of second-order array geometries has been considered before, the application of the so-called SODA interferometer in the ES context to resolve phase ambiguities resulting from physically large wideband antennas has not been considered before. Furthermore, in Section 4.5.2, the adaptation of the SODA interferometer to slightly non-linear array geometries, and the extent of non-linearity that can be tolerated, has not yet been studied. This analysis is particularly useful for practical installations where conformal mounting may be required.

3. In Chapter 5, second-order array processing methods are considered. While similar virtual arrays have been previously considered in the array processing literature, to the knowledge of the author, the generation of the virtual array using a SODA geometry and its practical application for radar intercept receivers in a computationally fast manner has not been considered before.

4. In Chapter 6, the application of second-order analysis to derive a simple unambiguous calibration method for SODA interferometry and other SODA-related algorithms is also an original contribution. This contribution is particularly important as it allows the SODA-based algorithms to be implemented in hardware in a practical manner while retaining a computationally fast performance.

5. Finally, in Chapter 8, the results of field experiments are presented to experimentally validate all of the theoretical AOA estimation algorithms and calibration methods discussed in this thesis. In particular, the experimental verification of the SODA interferometer, SBI interferometer and second-order array processors and their comparison against the conventional methods is another original contribution. This contribution consists of conducting the field experiments, analysing the collected data and applying the theoretical algorithms to the experimental data.

Chapter 2

Contemporary Direction Finding Techniques

Direction finding systems have been in development since David Edward Hughes and Heinrich Hertz first conducted tests on radio transmissions in the late 1800s [4, 5]. In this chapter, some of the contemporary direction finding methods that are suitable for implementation in microwave radar intercept receivers are discussed.

2.1 Spinning Antenna

One of the first direction finders is a mechanically spinning antenna system where a highly directional antenna is physically rotated in azimuth (and elevation) to search for radar signals. The AOA of a radar intercept is simply the angle at which the spinning antenna is physically directed when the intercept is detected [5, 6, 9]. Modern spinning antenna systems have been able to achieve AOA estimation accuracies to about one-tenth of the antenna beamwidth [10] (typically of the order of $1° - 5°$ RMS).

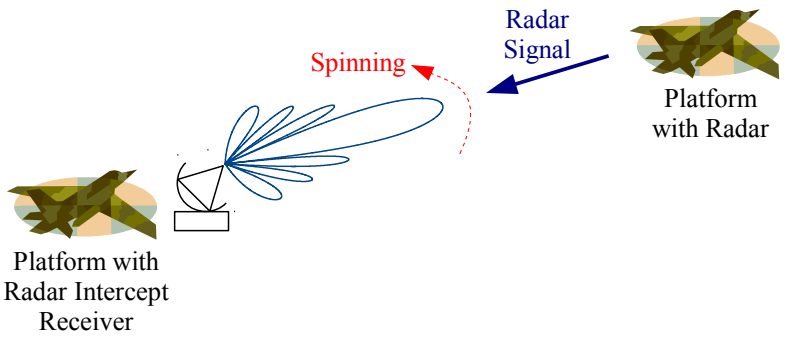

Figure 2.1: A mechanical spinning antenna direction finding system.

Spinning antenna systems are simple to understand, cheap to implement, and remain highly prevalent in modern electronic surveillance systems. Spinning antennas have an advantage in that their directional antennas inherently provide some directional isolation and hence are able to obtain good quality collections of a single signal when multiple radars are simultaneously transmitting from different azimuths. However, this is also

a disadvantage since multiple radar signals from different azimuths cannot be received simultaneously.

In order to successfully intercept a radar signal, the radar intercept receiver's spinning antenna and the radar's transmitting antenna (which may also be spinning) must be directly facing each other as illustrated in Figure 2.1. Since the radar is an uncooperative emitter, this condition may or may not be met. In the jargon of electronic warfare, the probability of this happening is known as the *probability of intercept* (POI). Since the spinning antenna must be physically rotated, some time is required to mechanically steer the antenna. Contemporary spinning antenna systems typically take a few hundred milliseconds to a few seconds to complete a full 360° rotation in azimuth [5]. Since conventional pulsed radars typically have signal durations and pulse repetition intervals in the order of microseconds and milliseconds, the relatively slow scan times of the spinning antenna can severely hinder the surveillance performance of these systems. In other words, there is a high probability that a spinning antenna will not "see" an illuminating radar because it happens to be "looking away" while the radar is transmitting in the direction of the intercept receiver as illustrated in Figure 2.2.

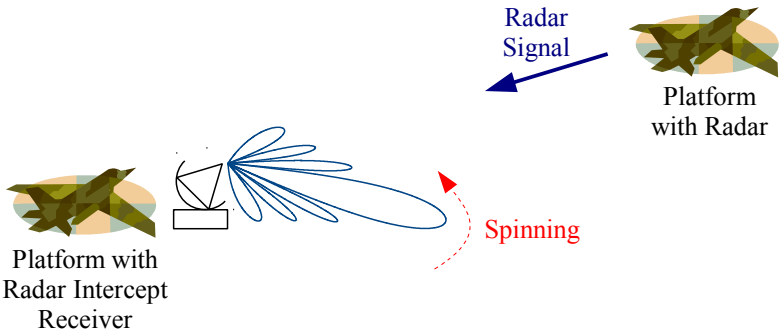

Figure 2.2: The radar intercept receiver may not "see" an illuminating radar signal if it happens to be "looking away" from the radar.

The inherently poor POI performance of this technique is one of the main drawbacks of using spinning antennas for surveillance purposes. Ongoing maintenance associated with the physical wear-and-tear of mechanical parts also make the spinning antenna system unattractive.

2.2 Amplitude Comparison

The need to mechanically scan for radar signals can be eliminated by the use of multi-antenna systems. By simultaneously intercepting the same signal through different antennas, the AOA of the signal can be determined by exploiting the characteristics of the antenna beampattern and antenna array geometry. In *amplitude comparison* systems, directional antenna beampatterns are exploited such that the ratio of the measured power levels of each channel are designed to be unique for each AOA over the entire surveillance range of the system, i.e. the *field of view* (FOV). By eliminating the need to mechanically scan for radar signals, the POI performance of these multi-antenna systems is a significant improvement over spinning antenna systems [1].

2.2.1 Loop Antennas

The earliest amplitude comparison direction finding system used two orthogonal loop antennas to provide overlapping sinusoidal beampatterns. In this arrangement, the ratio of the measured power levels of each channel forms an unique tangential relationship with the AOA which can be used to estimate the AOA of the signal. An independent "sense" antenna is required to resolve the 180° ambiguity that arises due to the symmetry of the beampatterns [4]. These systems are also commonly known as Watson-Watt direction finders and generally have AOA estimation accuracies of a few degrees RMS [4].

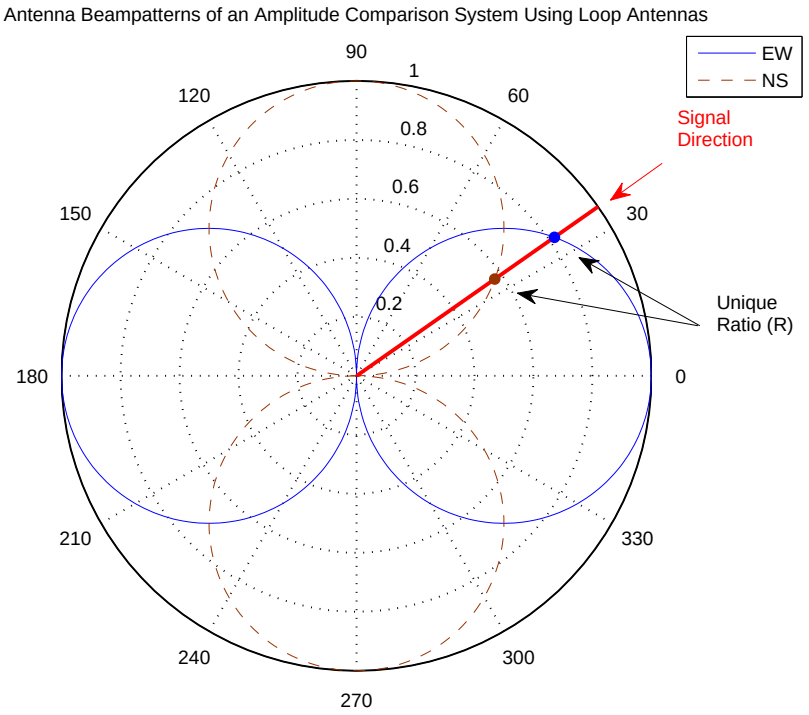

Figure 2.3: Beampattern of two orthogonal loop antennas. The orthogonal sinusoidal beampatterns ensure a unique ratio between the measured power levels of each channel for each AOA.

2.2.2 Adcock Arrays

The early Watson-Watt direction finders were designed to operate in the high frequency (HF) ranges and so were susceptible to interference from horizontally-polarised skywave propagations through the ionosphere. To overcome this problem, Adcock arrays using vertically-polarised, omnidirectional dipole or monopole antennas were later used in place of loop antennas [4, 6, 9, 32]. Adcock arrays approximate two orthogonal sinusoidal beampatterns through a linear combination of the antenna outputs. Furthermore, the output of all antennas can be combined in a manner to resolve the 180° ambiguity without the need for an independent sense antenna [4]. Adcock arrays are typically constructed using 4 or 8 antennas and have been known to achieve AOA estimation accuracies of about 2.5° RMS [10].

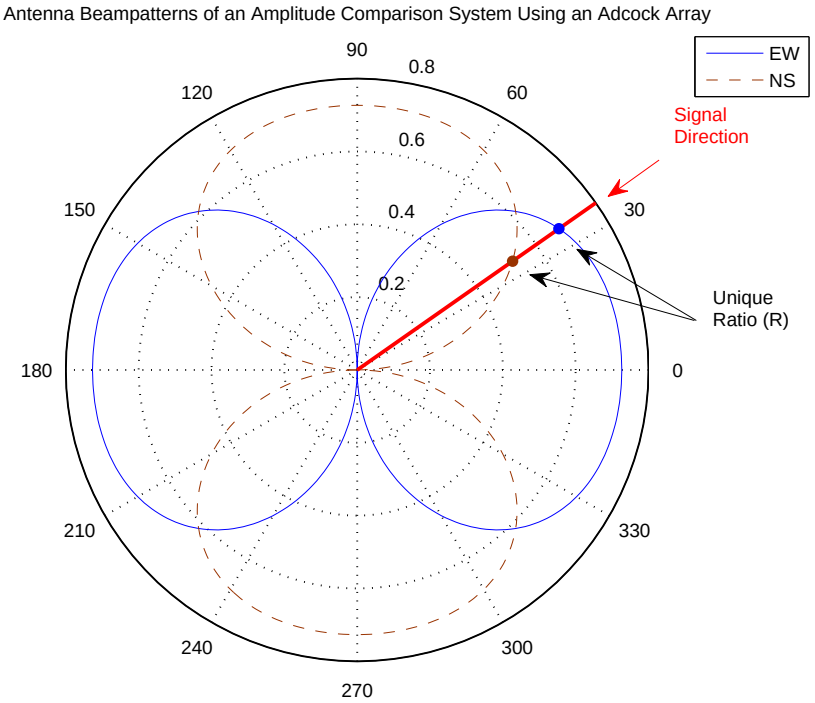

Figure 2.4: Beampattern of an Adcock array comprising of 4 dipole antennas with a radius of $\lambda/5$, where λ is the wavelength of the signal of interest. A linear combination of the omnidirectional beampatterns can produce two orthogonal, near-sinusoidal beampatterns that are comparable to the beampatterns of two loop antennas.

Watson-Watt direction finding systems using loop antennas and Adcock arrays have been in use for nearly a hundred years and are still popular today for fixed frequency applications, such as communications [4]. However, from an electronic surveillance perspective, a significant drawback of these systems is that the loop, dipole and monopole antennas are inherently narrowband devices. Since microwave radar intercept receivers are intended to operate over a wide frequency range, typically $2 - 18$ GHz, a single Adcock array will not be sufficient to cover the entire frequency range. While it is possible to have separate antenna arrays for each frequency, such a solution would not be cost effective. Furthermore, modern radar signals may have bandwidths greater than the frequency range that loop, dipole and monopole antennas are capable of receiving.

While other types of omnidirectional antennas exist with wideband characteristics, such as bi-conical antennas, these antennas tend to be physically large and cannot be mounted in a fashion that will satisfy the antenna spacing requirements of Adcock arrays. Thus, while the Watson-Watt technique remains popular for fixed frequency applications, its use in electronic surveillance is limited.

2.2.3 Cavity-Backed Spiral Antennas

In order to cope with the wide frequency range requirements of radar intercept receivers, wideband, cavity-backed spiral antennas were later used in amplitude comparison systems [5, 6, 9, 14]. These antennas have near-sinusoidal, or Gaussian-like, beampatterns that can be directly exploited in an amplitude comparison system as depicted in Figure

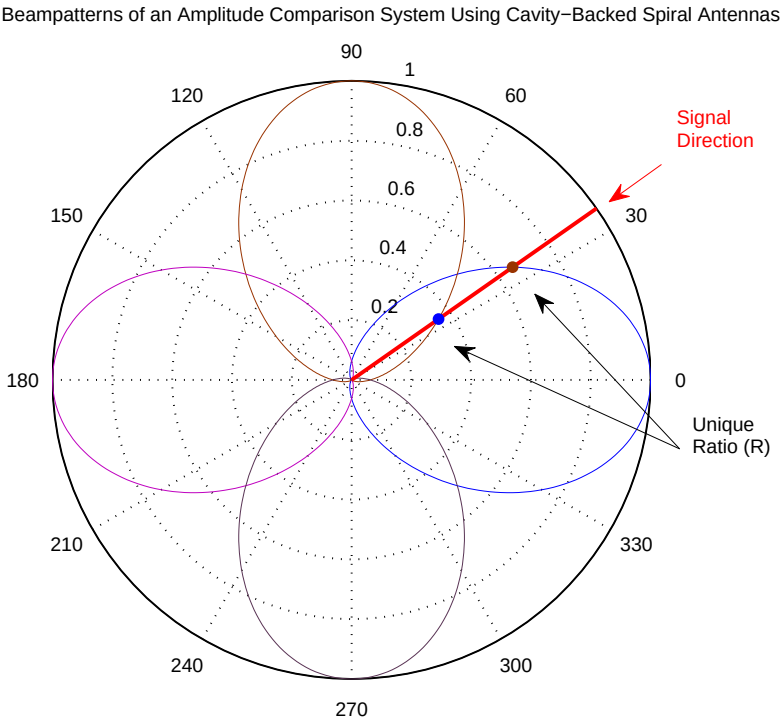

Figure 2.5: Beampatterns of four cavity-backed spiral antennas with a squint angle of 90° between the antennas.

2.5.

Unlike Adcock arrays, where the sinusoidal beampattern is derived from multiple carefully placed omnidirectional antennas, cavity-back spiral antennas inherently exhibit a near sinusoidal, or Gaussian-like, beampattern. As a consequence, these amplitude comparison systems do not impose a specific antenna spacing requirement. In other words, the physical size of the antennas and their exact positions do not affect the AOA estimation performance provided that there is a sufficient physical angular rotation between the antenna boresights (i.e. squint angles). These systems can often tolerate conformal mounting on a platform (such as on the wings of an aircraft or around the mast of a ship) with little impact on the AOA estimation performance. Furthermore, since the Gaussian-like beampatterns are not symmetric about 180°, different pairs of antennas will be used to estimate the AOA at the geometric ambiguities observed in the loop antenna and Adcock array configurations. Thus, these amplitude comparison systems do not require an additional sense antenna.

Since amplitude comparison systems rely on comparing power measurements from multiple antennas, these systems are agnostic to the signal frequency and any phase or frequency modulation in the radar signal's waveform and so the amplitude comparison technique is inherently a wideband direction finding technique. Furthermore, since power measuring circuitry are simple and cheap to implement in analogue hardware, the implementation costs of amplitude comparison systems are relatively low [33, 34]. Due to their effectiveness against both narrowband and wideband signals, low implementation

cost and high POI performance, amplitude comparison systems using cavity-backed spiral antennas have been a popular DF technique for microwave radar intercept receivers for many decades.

Despite their advantages, amplitude comparison systems have two significant disadvantages. Firstly, the power of the intercepted signal is one of the least reliable parameters that can be estimated when the signal is corrupted by receiver noise and so the angular accuracy of these systems is relatively poor. A typical amplitude comparison system can achieve an AOA estimation accuracy of about $5° - 15°$ RMS [8, 10, 35]. In contrast, modern phase-based direction finding techniques, such as interferometry, can typically achieve sub-degree accuracies using the same number of antennas against the same types of signals [5, 8–10, 16, 36].

Furthermore, amplitude comparison techniques typically measure the signal power in the time-domain and so are only effective when one signal is illuminating the antenna array. Traditionally, single-signal scenarios have been a reasonable assumption. However, as the modern electronic surveillance signal environment becomes increasingly crowded, the possibility of signal-on-signal environments also becomes increasingly higher. The effectiveness and reliability of amplitude comparison systems in the modern signal environment is therefore reduced.

2.3 Frequency-Difference-of-Arrival

Frequency-difference-of-arrival (FDOA) techniques exploit the Doppler effect to estimate the AOA of the intercepted signal. In these systems, one antenna is physically rotated around a reference antenna. The circular motion of the moving antenna causes a sinusoidal Doppler shift relative to the frequency measured by the reference antenna. The angle at which the Doppler shift goes from positive to negative is the AOA of the signal. In practical systems, the rotating antenna can be replaced by a circular array of antennas that are sequentially switched into the receiver [4, 6]. FDOA direction finding systems have been known to achieve angular accuracies of about 3° RMS [10].

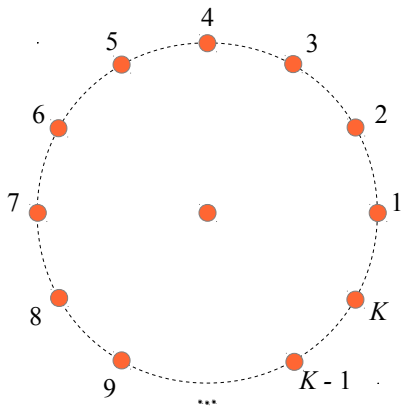

Figure 2.6: A FDOA direction finding array comprising of K antennas.

A significant disadvantage of the FDOA technique is that these systems require the signal

to illuminate the antenna array over a long interval (typically in the order of milliseconds) to allow the Doppler frequency shift to be measured. Since many conventional radars transmit short duration pulses (in the order of microseconds), the FDOA technique will not be effective against these radar signals.

2.4 Time-Difference-of-Arrival

Time-difference-of-arrival (TDOA) techniques exploit the propagation delay between two spatially separated antennas to estimate the AOA of the signal. Since the separation between the antennas is known and the propagation speed of electromagnetic waves is constant, the delay between the times that each channel receives the signal can be used to estimate the AOA of the intercept [4, 5].

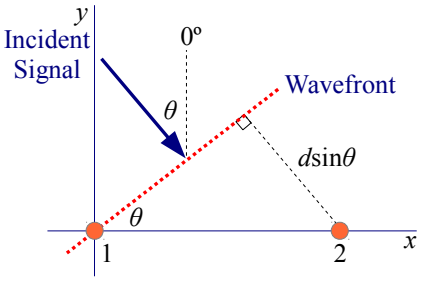

Figure 2.7: A signal incident upon a pair of spatially separated antennas must travel a further distance to reach the second antenna after arriving at the first antenna.

There are two common methods for measuring the propagation delay. The first is to measure the difference between the time-of-arrival (TOA) of the pulses measured by each channel. The TOA measurement may be obtained directly in hardware using time-to-digital converter (TDC) devices [37, 38] or alternatively calculated from digital samples representing the signal using parameter estimation methods. The second method is to correlate the outputs of the two channels in the time-domain [39]. This method generally performs better than the TOA method since it makes use of the entire signal duration as opposed to a single instant in time. However, this performance improvement comes at the expense of increased computation.

The accuracy of TDOA systems generally depends on the accuracy and precision of the propagation delay estimation and the length of the antenna separation. The accuracy of the propagation delay estimation depends on the time delay estimation algorithm and the signal and receiver characteristics, such as the signal duration and signal-to-noise ratio (SNR), while the precision of the propagation delay estimate depends on the timing resolution of the digital samples. In general, for an antenna separation of tens of metres, good AOA accuracy, say less than 1° RMS, will require the accuracy and precision of the propagation delay estimates to be in the order hundreds of picoseconds. Shorter baselines will further reduce the accuracy and precision requirement to tens of picoseconds.

The precision requirement of TDOA systems can be achieved through the use of modern high precision TDCs which can offer timing resolutions below 100 ps [38]. Alternatively,

high sample rate analogue-to-digital converter (ADC) devices capable of digitising 12.5 GSPS or more have also become available [40]. This sample rate corresponds to a timing resolution of 80 ps, which may be further improved with interpolation.

TDOA direction finders are agnostic to the signal waveform and so work effectively on both narrowband and wideband signals. However, these systems are only capable of processing one signal at a time and so are prone to errors when multiple signals are simultaneously illuminating the radar intercept receiver. Furthermore, while TDOA direction finders work well against conventional, pulsed radar signals they do not work effectively against continuous-wave (CW) signals. Since CW signals do not have a well-defined start time, TOA estimation cannot be performed. Furthermore, CW signals are generally periodic and so correlation-based time delay estimation methods may be ambiguous.

2.5 Interferometry

An alternative approach to measuring the propagation time delay between two receivers is to measure the equivalent propagation phase delay between the measured signals of each channel. For narrowband signals, the measured phase delay can be directly translated to the equivalent propagation time delay, which can then be used to estimate the AOA of the signal. This technique is sometimes known as *phase-difference-of-arrival* (PDOA), but is more commonly known as *interferometry* [5, 9].

One advantage of interferometry is that very accurate phase measurements can be obtained with digital hardware at moderate sampling rates and so high accuracy AOA estimates can be obtained with shorter baselines and without the demanding timing constraints required by TDOA systems. Modern digital interferometers can typically achieve sub-degree accuracies [5, 8–10, 16, 36]. Furthermore, with some preprocessing, interferometers are able to accurately estimate the AOA of multiple signals provided that the signals are sufficiently separated in frequency.

The performance of interferometers can be improved by using longer baselines. However, due to the circular nature of phase measurements, the AOA estimation is only unambiguous for antenna separations which are less than one-half of the wavelength of the highest frequency of interest. This ambiguity problem has been extensively studied in the literature and can be overcome by combining interferometers with other independent AOA estimation methods [35, 41, 42] or by using multiple long baselines [5, 6, 8, 9].

Conventional interferometers often assume a narrowband signal and so are generally narrowband techniques. However, it is also possible to estimate the AOA of certain wideband signals using interferometry through some additional processing to reduce the bandwidth of the signal [43, 44].

2.6 Beamforming and Array Processing

Beamforming and array processing techniques coherently exploit the propagation delays between the elements of an antenna array to estimate the AOA of the signal. Since the

propagation delays are a function of the AOA, array processors attempt to estimate the AOA by performing an exhaustive search to find the AOA with corresponding propagation delays that best match the measured propagation delays. In principle, when the propagation delays corresponding to the signal's AOA are used, the receiver outputs can be brought "in phase" with each other so that the signal components will coherently sum (while the uncorrelated noise components cancel) to produce a strong array output. On the other hand, when the propagation delays corresponding to an incorrect AOA is used, the receiver outputs will not coherently sum and so will produce a weaker array output [2, 45].

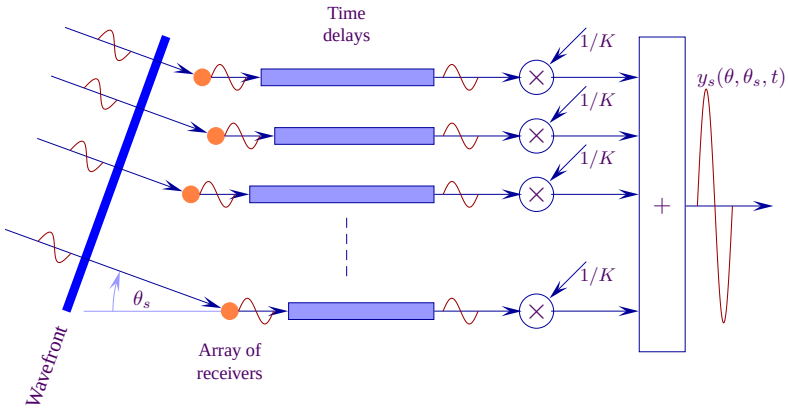

Figure 2.8: Array processors use AOA-dependent propagation time or phase delays to coherently sum the array output.

The process of searching through all of the possible AOAs is the electronic equivalent to a mechanically scanning directional antenna. The electronic scanning capabilities of array processors offer much greater flexibility and higher AOA estimation performance than their mechanical counterparts. Furthermore, while traditional array processors often assume a narrowband signal, array processors can also be developed for wideband signals [43, 45, 46].

Beamforming and array processing techniques have long been considered the epitome of detection and AOA estimation techniques. These algorithms offer significant processing gains including:

- **Array Gain** - The gain of an array processor is achieved by virtue of a coherent summation of multiple antenna outputs. In general, a K-antenna array will have have a gain factor of K. This means that an additional 3 dB of signal-to-noise ratio (SNR) can be obtained each time the number of antennas is doubled.
- **Multiple Signals** - The signal waveform from multiple spatially separated signals simultaneously illuminating the antenna array can be individually localised and characterised. In general, a K-antenna array can estimate the AOA of up to $K-1$ spatially separated signals.
- **Interference Mitigation** - Interferences, such as jammers, own-ship emissions,

or communications signals, can be mitigated to improve the interception of the signals of interest.

- **Flexible Scheduling** - Electronic scanning allows sophisticated search patterns to be implemented that can be dynamically adapted to the operating environment. Electronic scanning allows the search pattern to focus on particular bearings of interest or at bearings that have previously intercepted a signal before. This also allows the intercept receiver to better allocate its resources to perform other tasks.

Despite their many advantages, array processors have a significant disadvantage in that they are computationally intensive algorithms. For each intercept, an array processor must search through all the possible AOA that the array geometry allows. For each AOA, the antenna outputs are weighted and summed to test for the presence of a signal. Depending on the search resolution, this process can amount to a significant number of computations.

Furthermore, in order to enhance the signal waveform through coherent summation, the digital samples from each channel must be made available to a central processor to perform coherent processing. For a large number of channels and/or high data rates, this presents a significant amount of data that needs to be transferred around the system. While distributed processing and data reduction techniques can be applied at intermediate stages to reduce the data rate, in general, the final data rate is still significantly high and the corresponding latency of such data transfers can severely hinder the surveillance performance of the system. However, note that if the system is only required to perform AOA estimation, the data transfer problem can be alleviated by only transferring a single value representing the estimated propagation time delay or phase delay of each channel to the central processor instead of the entire sequence of digital samples.

2.7 Summary

In this chapter, a number of contemporary direction finding techniques that are relevant to microwave radar intercept receivers were discussed. The spinning antenna is the simplest of all direction finding techniques, but has a relatively coarse AOA estimation performance and poor POI performance. However, given their low implementation costs, spinning antennas are still commonly used today, either in their own right as the primary direction finding system or as a secondary backup system.

Amplitude comparison systems using cavity-backed spiral antennas have traditionally been used as a low-cost method to perform reliable, but low accuracy, AOA estimation with a high POI performance. However, in the modern ES environment, there has been a trend for modern low probability of intercept (LPI) radar signals to transmit signals at lower power with longer durations. This trend, combined with a growing number of radar emitters in a typical operating environment, renders amplitude comparison direction finders ineffective in the modern and future ES environment.

FDOA systems are effective against narrowband signals that are present for long durations and are particularly effective against modern LPI radars which exploit long duration signals. However, they are not effective against traditional short duration radar

signals, which are still commonly encountered in the modern ES environment.

TDOA systems can exploit all types of radar signals including narrowband and wideband signals, and short and long duration signals. However, TDOA systems require long antenna baselines and very accurate and precise timing resolutions for good AOA estimation performance. Due to the physical limitations of a platform (e.g. an aircraft or ship), the available space for mounting antennas may be limited. Hardware with good timing resolutions may also be prohibitively expensive. Furthermore, TDOA systems are not able to estimate the AOA of multiple signals simultaneously illuminating the array.

On the other hand, interferometers offer high speed and high accuracy AOA estimation without the drawbacks of TDOA systems. That is, interferometers do not require very long baselines or very accurate timing resolutions. Furthermore, interferometers are able to accurately estimate the AOA of multiple signals simultaneously illuminating the antenna array provided that the signals are at different frequencies. However, a drawback is that conventional interferometry assumes a narrowband signal model and so is not effective against wideband signals. However, as discussed in Section 1.4.4, many of the modern LPI radar signals can be considered as a sequence of narrowband signals. Furthermore, it is possible to construct specific interferometers that can directly exploit wideband signals, such as chirp signals. Since interferometers are able to achieve all of the design objectives of ES and ELINT systems outlined in Section 1.4.3, this thesis proposes that interferometry provides the best balance between the AOA estimation performance and the computation time of the algorithm and so is an ideal candidate for implementation in ES and ELINT systems.

Finally, array processing techniques are considered the epitome of detection and AOA estimation techniques since they can offer a number of significant advantages, including statistically optimal AOA estimation of simultaneous signals and SNR improvement of very weak signals. Due to these advantages, many applications use array processing techniques for the joint detection and AOA estimation of signals. However, array processing techniques are computationally intensive algorithms and their use to enhance the signal waveform through coherent summation requires very high data transfer rates. Since this thesis is only concerned with the AOA estimation of post-detected signals, the signal enhancement and detection aspects of the array processing is not relevant for thesis. Furthermore, since interferometry can also provide statistically optimal AOA estimation, and slightly sub-optimal implementations are many orders of magnitude faster than array processing algorithms, interferometry is arguably a more suitable AOA estimation algorithm for near-real time tactical ES systems. However, array processing methods may still be desired for ELINT systems when the AOA accuracy is more important than the computational speed of the algorithm.

Chapter 3

Interferometry

3.1 Introduction

Interferometry exploits the propagation phase delay between two spatially separated antennas to estimate the AOA of a signal. The principles of interferometry have been well established since the early 1900's. Early interferometers were analogue systems designed to operate at high frequency (HF) bands against signals with relatively small bandwidths. Due to the cost and complexities of implementing phase-coherent, multi-channel analogue receivers at microwave frequencies, analogue interferometers were prohibitively expensive for wide scale implementation in ES systems on military platforms. As a result, analogue interferometers were often limited to specialised high-end applications, such as ELINT systems, where the requirements for high accuracy AOA estimation justified the implementation cost.

In recent decades, the advent of high speed analogue-to-digital converters (ADCs), field programmable gate arrays (FPGAs) and digital computing has led to the development of high fidelity digital receivers. With modern technologies, the implementation of phase-coherent, multi-channel digital receivers has become increasingly more cost effective. Furthermore, the flexibility of digital computing has allowed the implementation of higher performance algorithms compared to the traditional analogue systems. In recent years, there has been a rising interest in digital interferometers to provide fast and accurate AOA estimation for military ES and ELINT systems.

In this chapter, the principles of interferometry and some of the contemporary implementations of digital interferometers will be presented. Contemporary digital techniques to resolve the ambiguities of multiple long baseline interferometers will also be presented.

3.2 Signal Model

In this section, the signal model that will be used to describe the intercepted radar signal from multiple spatially separated antennas will be established. While most of the algorithms presented can be generalised to any array geometry, this thesis shall concentrate on linear arrays.

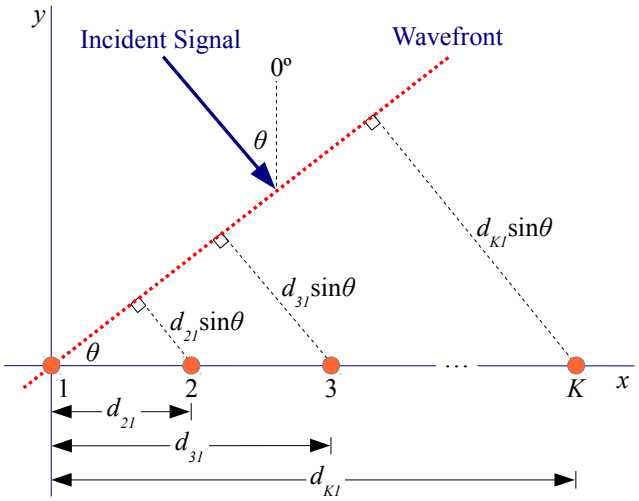

Figure 3.1: Relationship between the antenna separation and propagation delay of the signal arrival for a linear array.

3.2.1 Propagation Delays

Consider a linear array of antennas as depicted in Figure 3.1. In interferometry and array processing, it is conventional to define the antenna positions in Cartesian coordinates. Let the k-th and l-th antennas be located at position vectors, $\mathbf{u}_k$ and $\mathbf{u}_l$, where

$$\mathbf{u}_k = \begin{bmatrix} x_k \\ y_k \\ z_k \end{bmatrix} \quad \text{and} \quad \mathbf{u}_l = \begin{bmatrix} x_l \\ y_l \\ z_l \end{bmatrix} \tag{3.1}$$

are vector coordinates which specify two points in Cartesian space and x, y and z are the scalar values of the antenna position along the x-axis, y-axis and z-axis respectively. The distance vector between these two points can be written as

$$\mathbf{d}_{kl} = \begin{bmatrix} d_{kl,x} \\ d_{kl,y} \\ d_{kl,z} \end{bmatrix} = \begin{bmatrix} x_k - x_l \\ y_k - y_l \\ z_k - z_l \end{bmatrix}. \tag{3.2}$$

Since radar intercept receivers are intended to provide early warning of the presence of radars, the radar intercept receiver is generally operated at large distances from the radar. The radar signal arriving at the radar intercept receiver's antenna array can therefore be reasonably approximated as a uniform plane wave. Due to the spatial separation between the antennas, the signal wavefront arrives at each antenna at slightly different times. These propagation delays are a function of the array geometry and the AOA of the signal.

It is natural to define the AOA of an intercept in terms of geographical coordinates such that the AOA of the signal is defined in terms of an azimuth component, θ, and elevation component, ϕ, as depicted in Figure 3.2. The geographical coordinates can be converted into Cartesian coordinates through the following transformation

$$\mathbf{u}_{\theta,\phi} = \begin{bmatrix} \sin\theta\cos\phi \\ \cos\theta\cos\phi \\ \sin\phi \end{bmatrix}. \tag{3.3}$$

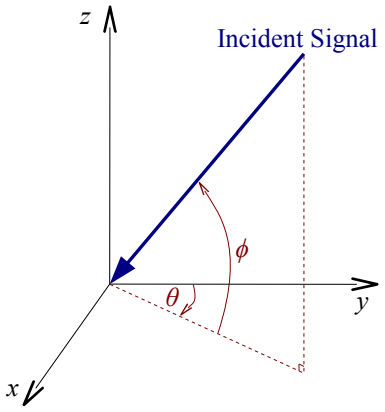

Figure 3.2: The geographical coordinate system.

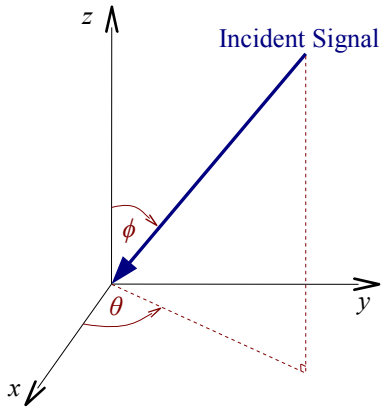

Figure 3.3: The spherical polar coordinate system.

In the geographical coordinate system, the azimuth angles are measured *clockwise* from the y-axis and the elevation angle is measured from the xy-plane towards the z-axis as depicted in Figure 3.2. This is in contrast to the spherical polar coordinates commonly used in mathematics where the azimuth angles are measured *counter-clockwise* from the x-axis of the equivalent Cartesian representation and the elevation angle is measured from the z-axis *towards* the xy-plane as depicted in Figure 3.3.

Using the geographical coordinate system, the additional distance that the signal wavefront must travel from the l-th antenna to the k-th antenna can then be expressed as

$$\bar{d}_{kl} = \mathbf{u}_{\theta,\phi}^T \mathbf{d}_{kl} = d_{kl,x} \sin\theta \cos\phi + d_{kl,y} \cos\theta \cos\phi + d_{kl,z} \sin\phi, \tag{3.4}$$

where the superscript ^{T} denotes the vector transpose operation. The corresponding propagation delay is then given by

$$\tau_{kl} = \frac{\bar{d}_{kl}}{c} = \frac{d_{kl,x}}{c} \sin\theta \cos\phi + \frac{d_{kl,y}}{c} \cos\theta \cos\phi + \frac{d_{kl,z}}{c} \sin\phi, \tag{3.5}$$

where c is the speed of light. For mathematical convenience, it is generally assumed that the origin of the coordinate system coincides with the position of an arbitrarily chosen reference antenna – typically the first antenna. Another common assumption is that the elevation angle of the AOA is often assumed to be zero, i.e. $\phi = 0°$, and so the radar signal and radar intercept receiver both lie entirely in the xy-plane. Furthermore, for a linear array, the Cartesian coordinate system can be arbitrarily arranged so that the antennas all lie on the x-axis, as depicted in Figure 3.1, and so the propagation delay between the k-th and l-th antennas reduces to

$$\tau_{kl} = \frac{d_{kl}}{c} \sin\theta, \tag{3.6}$$

where $d_{kl,y} = 0$, $d_{kl,z} = 0$ and $\phi = 0°$. In the above expression, the subscript x is omitted from $d_{kl,x}$ for notational brevity.

3.2.2 Narrowband Signal Model

Traditional narrowband radar signals can be modelled as a single tone, $s(t)$, as a function of time, t, as follows

$$s(t) = Ae^{j(2\pi ft+\varphi)}, \tag{3.7}$$

where A, f and φ are the signal's peak amplitude, carrier frequency and initial phase respectively. For practical systems, the ideal signal is corrupted by an additive noise component, $\epsilon(t)$. For a multi-channel system with K antennas, the signal of the k-th antenna with respect to the l-th antenna is given by

$$x_{kl}(t) = s(t+\tau_{kl}) + \epsilon_k(t) = Ae^{j(2\pi f(t+\tau_{kl})+\varphi)} + \epsilon_k(t), \tag{3.8}$$

where $k = 1, 2, \ldots, K$ and τ_{kl} is the propagation time for the signal to reach the k-th antenna after arriving at the l-th antenna as defined in (3.6).

The receiver noise in the k-th channel, $\epsilon_k(t) \sim \mathcal{N}(0, \sigma^2_{\epsilon_k})$, is modelled as an independent and identically distributed, complex-valued, zero mean, white Gaussian random variable with variance, $\sigma^2_{\epsilon_k}$. The receiver noise is assumed to be independent for each receiver. The real and imaginary components of $\epsilon_k(t)$ have an equal variance that is given by $\sigma^2_k = \sigma^2_{\epsilon_k}/2$. It is generally reasonable to assume that the receiver noise power in each channel is the same and so the complex receiver noise power can be written more generally as $\sigma^2_\epsilon = \sigma^2_{\epsilon_1} = \sigma^2_{\epsilon_2} = \cdots = \sigma^2_{\epsilon_K}$, and the corresponding real and imaginary noise power can be written as $\sigma^2 = \sigma^2_1 = \sigma^2_2 = \cdots \sigma^2_K$. The signal-to-noise ratio (SNR) of the signal, η, can then be defined as

$$\eta = \frac{A^2}{\sigma^2_\epsilon} = \frac{A^2}{2\sigma^2}. \tag{3.9}$$

For a narrowband signal and a linear array geometry, the propagation time can be readily converted into an equivalent phase as follows,

$$\psi_{kl} = 2\pi f\tau_{kl} = \frac{2\pi f d_{kl}}{c}\sin\theta. \tag{3.10}$$

For a multi-channel digital receiver, the digital sampling of the signal occurs at regular, discrete time intervals, t_s. For a collection of N samples, the n-th digital sample of the narrowband signal model can be re-written as

$$x_{kl}[n] = Ae^{j(2\pi fnt_s+\varphi+\psi_{kl})} + \epsilon_k[n], \tag{3.11}$$

which corresponds to the time instance, $t = nt_s$, and $n = 0, 1, \ldots, N-1$.

It should be noted that the propagation time, τ_{kl}, is actually a time advance for positive θ and a time delay for negative θ. Similarly, the propagation phase, ψ_{kl}, is a phase advance for positive θ and a phase delay for negative θ. However, for notational brevity, this thesis will generally refer to τ_{kl} and ψ_{kl} as the propagation time delay and phase delay respectively.

3.3 Interferometry

By estimating the frequency of the signal and the phase delay between the outputs of two antennas, the AOA of the signal can be estimated by re-arranging (3.10) to give

$$\hat{\theta} = \arcsin\left(\frac{c\hat{\psi}}{2\pi f d}\right), \tag{3.12}$$

where the accent $\hat{}$ denotes an estimated parameter. Since only two antennas are considered, the subscripts for ψ and d have been omitted from (3.12) for notational brevity.

The antenna separation, d, is often referred to as the *baseline* of the interferometer. When discussing the performance of AOA estimation algorithms, it is often convenient to use the term *broadside* to indicate a signal arriving from an AOA of $\theta = 0°$ (i.e. perpendicular to the interferometer baseline) and the term *endfire* to indicate a signal arriving from $\theta = \pm 90°$ (i.e. parallel to the interferometer baseline).

The expression (3.12) allows the AOA of a single signal with a phase delay of ψ and a frequency f to be estimated. However, as will be discussed in Section 3.4.1, the AOA of multiple signals can also be estimated by carefully isolating the phase delay and frequency of each signal in the frequency domain.

In ES applications, the radar intercept receiver usually does not know the frequency of the intercepted signal and so in practice the frequency must be estimated from the intercepted signal. However, the frequency estimation problem is considered beyond the scope of this thesis and so this thesis shall assume that the frequency estimation errors are negligible. Due to the frequency dependence of the interferometer, this thesis shall explicitly write all expressions in terms of the signal frequency, f, rather than the signal wavelength, λ, which is more commonly used in the AOA estimation literature. The signal frequency and wavelength are related by

$$\lambda = \frac{c}{f}. \tag{3.13}$$

3.3.1 Relationship to TDOA

Interferometry is closely related to the time-difference-of-arrival (TDOA) technique. While the TDOA technique directly estimates the propagation delay through correlation or measurements of the time-of-arrival (TOA) of the pulses in each channel, interferometers can be considered to be *indirectly* estimating the propagation delay through the equivalent phase delay as follows [47],

$$\hat{\tau} = \frac{\hat{\psi}}{2\pi f}. \tag{3.14}$$

The AOA of the signal can then be estimated as

$$\hat{\theta} = \arcsin\left(\frac{c\hat{\tau}}{d}\right). \tag{3.15}$$

The advantage of interferometry is that accurate phase delay measurements can be obtained with less demanding hardware than direct TDOA techniques. Furthermore,

while direct TDOA methods can only estimate the AOA of one signal at a time, interferometers can have the ability to estimate the AOA of multiple signals simultaneously provided that they have different frequencies.

3.4 AOA Estimation in the Presence of Receiver Noise

The effect of receiver noise is an important consideration in all practical electronic systems. Unlike systematic errors, which can be mitigated through calibration (Chapter 6), receiver noise errors cannot be eliminated but their effects can be minimised through the careful selection of algorithms.

In interferometry, the receiver noise errors affect the AOA estimation by manifesting as random errors in the frequency and phase delay estimation. However, as stated in Section 1.4.4, this thesis shall assume that the frequency estimation errors are negligible. This section will therefore assume that receiver noise errors manifest entirely as phase delay estimation errors.

3.4.1 Maximum Likelihood Estimate

The maximum likelihood estimate (MLE) of the AOA using two spatially separated antennas, $\hat{\theta}_{\text{MLE}}$, is derived in Appendix A.2.2 and can be shown to be

$$\hat{\theta}_{\text{MLE}} = \arcsin\left(\frac{c\hat{\psi}_{\text{MLE}}}{2\pi f d}\right), \tag{3.16}$$

where $\hat{\psi}_{\text{MLE}}$ is the maximum likelihood estimate of the phase delay between the two antennas and can be estimated as

$$\hat{\psi}_{\text{MLE}} = \angle X_2(f) X_1^*(f), \tag{3.17}$$

and $X_1(f) = \sum_{n=0}^{N-1} x_1[n] e^{-j2\pi f n t_s}$ and $X_2(f) = \sum_{n=0}^{N-1} x_2[n] e^{-j2\pi f n t_s}$ are the Fourier coefficients of each channel at the signal frequency, f.

A common implementation of this method is to perform a Discrete Fourier Transform (DFT) on the output of each channel and then compute the difference between the phases of the Fourier coefficients corresponding to the signal frequency. Since this implementation is based on the DFT algorithm, the performance of the AOA estimation inherits all of the advantages and disadvantages of the DFT algorithm. That is, the maximum likelihood estimator for AOA estimation is expected to perform well at low SNR. Furthermore, since the Fourier transform is essentially a frequency channeliser, the phase delay corresponding to signals from different frequencies can be isolated to the relevant frequency bins. Thus, provided that two or more signals are sufficiently separated in frequency such that their signal energy falls into different frequency bins, the corresponding phase delay for each signal can be independently estimated. This provides the interferometer with the ability to estimate the AOA of multiple narrowband signals that may be simultaneously illuminating the antenna array.

On the other hand, this implementation also inherits the drawbacks of the DFT algorithm. In particular, the DFT implementation is prone to scalloping losses due to

spectral leakage [48]. If the signal frequency does not fall exactly on a single DFT frequency bin, some of the signal energy will leak into the adjacent frequency bins resulting in a reduced signal power in the main frequency bin of interest. In the worst case, the signal frequency will lie exactly halfway between two frequency bins which causes the effective SNR of the signal to be attenuated by 3.92 dB (assuming no windowing function has been applied). The effects of the scalloping loss can be reduced by zero-padding the signal prior to the DFT [49]. If the signal data length is doubled through zero-padding, the scalloping loss can be reduced to 0.91 dB. However, this reduction in the scalloping loss comes at the expense of requiring a DFT length that is twice the signal data length. While windowing functions may offer some improvement, they may not be able to completely eliminate the spectral leakage problem [8, 49, 50]. Furthermore, interpolation methods using multiple DFT bins [51–53] and spectral optimisation algorithms [2, 8] can also reduce, or even eliminate, the effects of scalloping losses. However, this improvement comes at the expense of greater computational complexity. The use of windowing functions, interpolation and spectral optimisation algorithms is considered beyond the intended scope of this discussion. For the purposes of AOA estimation, it is sufficient to say that the DFT implementation can achieve good performance when the signal frequency lies exactly on a single DFT frequency bin but can suffer some performance degradation when the signal frequency lies between two frequency bins. Since the DFT can be efficiently implemented using Fast Fourier Transform (FFT) algorithms, then using "big-Oh" notation [54, 55], the FFT implementation of the maximum likelihood estimator without further optimisation has an algorithm complexity of $O(2N \log_2 N+1)$, where N is the number of digital samples.

Since phase-based frequency estimators do not suffer from scalloping losses, an alternative implementation of the maximum likelihood estimator is to first estimate the frequency of the signal using a phase-based frequency estimator and then directly calculate the Fourier coefficients at the estimated frequency. This implementation is significantly faster with an algorithm complexity of $O(3N + 1)$. However, phase-based frequency estimators can only estimate the frequency of one signal and so this technique is not effective when multiple signals are simultaneously illuminating the antenna array. Furthermore, phase-based frequency estimators only work well for signals with high SNR, typically above 10 dB [15, 25–31]. At lower SNRs, the frequency estimation errors are not negligible and so this implementation will introduce large errors to the phase delay estimation.

3.4.2 Time-Domain Methods

At high SNR (typically above 10 dB), the receiver noise in each channel may be modelled as an additive phase noise [25]. Under this assumption, the narrowband signal model may be written as

$$x_{kl}[n] \approx Ae^{j(2\pi f n t_s + \varphi + \psi_{kl} + z_k[n])}, \tag{3.18}$$

where the additive receiver noise, $\epsilon_k[n]$, has been converted to an equivalent phase noise, $z_k[n]$, which has a variance, $\sigma^2_{z_k}$,

$$\sigma^2_{z_k} = \frac{1}{2\eta}. \tag{3.19}$$

Using this signal model, two time-domain phase delay estimators, denoted TD1 and TD2 respectively, can be defined as follows [15, 26, 27]

$$\hat{\psi}_{\mathrm{TD1}} = \frac{1}{N}\sum_{n=0}^{N-1} \angle x_2[n]x_1^*[n], \tag{3.20}$$

$$\hat{\psi}_{\mathrm{TD2}} = \angle \frac{1}{N}\sum_{n=0}^{N-1} x_2[n]x_1^*[n]. \tag{3.21}$$

The corresponding interferometric AOA estimators are

$$\hat{\theta}_{\mathrm{TD1}} = \arcsin\left(\frac{c\hat{\psi}_{\mathrm{TD1}}}{2\pi f d}\right), \tag{3.22}$$

$$\hat{\theta}_{\mathrm{TD2}} = \arcsin\left(\frac{c\hat{\psi}_{\mathrm{TD2}}}{2\pi f d}\right). \tag{3.23}$$

The first time-domain method, TD1, is an average of the instantaneous phase delay angles measured between the two channels. In contrast, the second time-domain method, TD2, computes a single phase delay angle from the average of the complex phasors. While both methods have an algorithm complexity of $O(N+1)$, the TD2 estimator is generally preferred since it is more robust against phase wrapping errors and is also computationally more efficient since it only requires one arctangent operation. Unlike the FFT-based MLE implementation, these methods will only estimate the correct phase delay when there is one narrowband signal present.

3.4.3 Cramér-Rao Lower Bound for a Two-Antenna Interferometer

The Cramér-Rao Lower Bound (CRLB) specifies the minimum variance that can be obtained for any unbiased estimator and is often used as a benchmark for optimal performance [2, 45, 56]. Estimators that achieve the CRLB are considered to be *optimal* or *statistically efficient*. Estimators that achieve the CRLB at high SNR are said to be *asymptotically efficient*. The performance of the AOA estimators can be evaluated by comparing their mean-square-error (MSE) against the CRLB, or equivalently, by comparing the root-mean-square (RMS) error against the square-root of the CRLB, or root-CRLB.

The CRLB for AOA estimation using a two-antenna array is derived in Appendix A.3.2 as follows

$$\mathrm{CRLB}(\theta) = \mathrm{CRLB}(\psi)\cdot\left(\frac{c}{2\pi f d\cos\theta}\right)^2 = \frac{1}{\eta N}\cdot\left(\frac{c}{2\pi f d\cos\theta}\right)^2, \tag{3.24}$$

where $\mathrm{CRLB}(\psi)$ is the CRLB of the phase delay estimate and is given by

$$\mathrm{CRLB}(\psi) = \frac{1}{\eta N}. \tag{3.25}$$

3.4.4 Performance Comparison

In this section, the AOA estimation performance of the two-antenna interferometers are evaluated as a function of the signal's SNR and AOA respectively. The RMS error performance of each algorithm is compared against the root-CRLB using Monte Carlo simulations with $\mathcal{Q} = 10,000$ receiver noise realisations to compute the RMS error of the angle estimate, $\hat{\theta}_{\text{RMS}}$, as follows,

$$\hat{\theta}_{\text{RMS}} = \sqrt{\frac{1}{\mathcal{Q}} \sum_{q=1}^{\mathcal{Q}} \left(\hat{\theta}_q - \theta\right)^2}, \tag{3.26}$$

where $q = 1, 2, \ldots, \mathcal{Q}$, $\hat{\theta}_q$ represents the AOA estimate of the q-th receiver noise realisation and θ represents the true AOA of the signal. In these simulations, the parameters are assumed to be $\theta = 23.42°$, $f = 18$ GHz, $d = \lambda/2 = 8.3333$ mm, $N = 2048$ samples, and $t_s = 750$ ps. It is assumed that the signal frequency has been estimated with negligible estimation error.

Figure 3.4 shows the RMS error performance of each algorithm as a function of SNR. In this simulation, the FFT-based MLE utilises a 2048-point FFT which ensures that the signal frequency lies exactly on a FFT frequency bin. This simulation shows that all of the interferometer implementations are asymptotically efficient in the sense that their RMS errors achieve the root-CRLB at high SNR. The SNR thresholds for the FFT-based MLE (which uses a FFT-based frequency estimator), phase-based MLE (which uses a phase-based frequency estimator) and the two time-domain estimators are -18 dB, -11 dB, 8 dB and 8 dB respectively.

This simulation verifies the following:

- The FFT-based MLE has the best performance in the sense that it has the lowest RMS errors at low SNR. This performance is attributed to the processing gain of the FFT.
- The phase-based MLE performs worse than the FFT-based MLE at low SNR due to its reliance on a phase-based frequency estimator which in turn requires a high SNR signal.
- The phase-based MLE generally performs better than the two time-domain methods due to the processing gain of the frequency channelisation it performs while estimating the AOA.
- The TD2 estimator generally has a lower RMS error than the TD1 estimator because it is more robust against phase wrapping errors at low SNR.

Figure 3.5 repeats the above simulation with the FFT-based MLE utilising a 2050-point FFT. In this example, the signal frequency lies exactly halfway between two FFT frequency bins and so the FFT-based MLE no longer achieves the root-CRLB. This performance degradation is attributed to the scalloping losses that arise due to spectral leakage and is consistent with the expected performance of a signal whose SNR is attenuated by 3.92 dB. While the use of a larger FFT with zero padding can alleviate the problem, this example highlights the fact that the FFT-based MLE may not be optimal

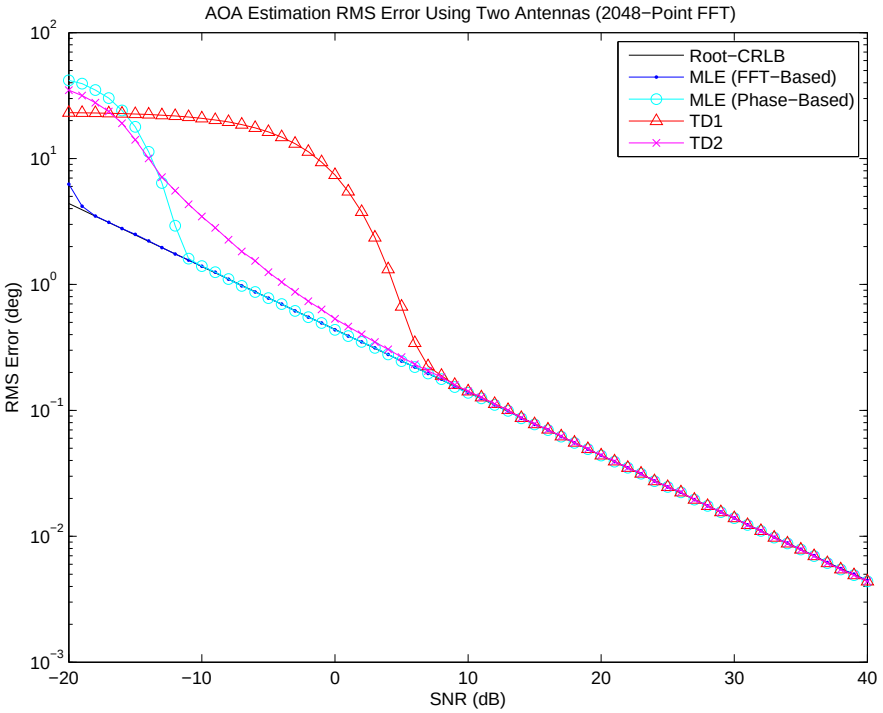

Figure 3.4: Comparison of the RMS errors of an interferometer as a function of SNR. Simulation parameters: $\theta = 23.42°$, $f = 18$ GHz, $d = 8.3333$ mm, $N = 2048$ samples, and $t_s = 750$ ps. A 2048-point FFT was used to calculate the phase delays of the FFT-based MLE.

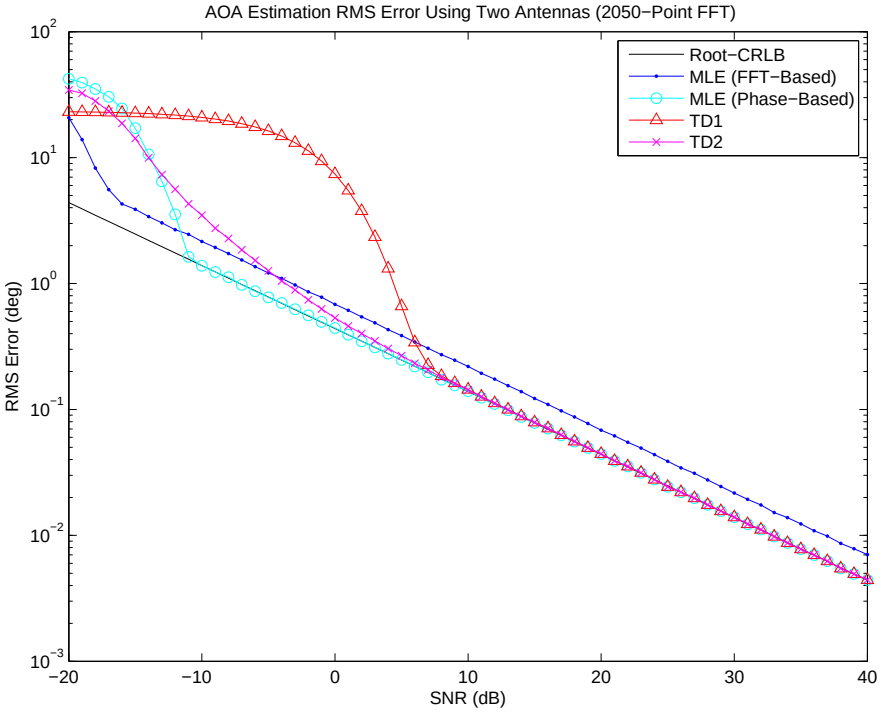

Figure 3.5: Comparison of the RMS errors of an interferometer as a function of SNR. Simulation parameters: $\theta = 23.42°$, $f = 18$ GHz, $d = 8.3333$ mm, $N = 2048$ samples, and $t_s = 750$ ps. A 2050-point FFT was used to calculate the phase delays of the FFT-based MLE.

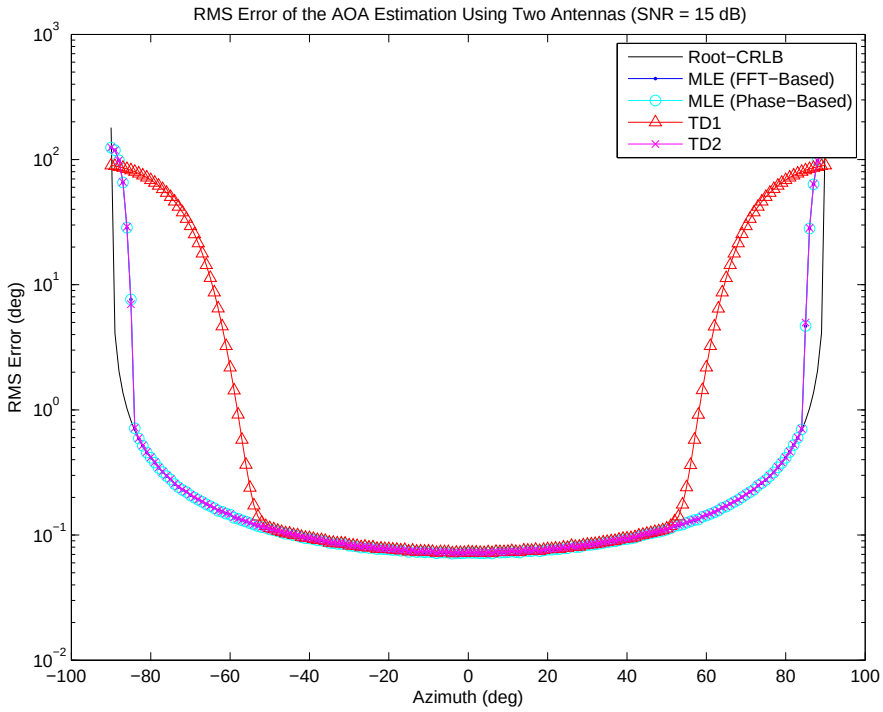

Figure 3.6: Comparison of the RMS errors of an interferometer as a function of AOA. Simulation parameters: $\eta = 15$ dB, $f = 18$ GHz, $d = 8.3333$ mm, $N = 2048$ samples, and $t_s = 750$ ps. A 2048-point FFT was used to calculate the phase delays of the FFT-based MLE.

when spectral leakage occurs. The FFT-based MLE will generally require the use of windowing functions, interpolation methods and/or spectral optimisation methods to minimise the effects of scalloping losses. Furthermore, this example verifies that the RMS error performance of the other estimators are not affected by scalloping losses.

Figure 3.6 shows the RMS error performance of each algorithm as a function of AOA. In this simulation, the SNR is 15 dB and the FFT-based MLE uses a 2048-point to avoid scalloping losses. All other simulation parameters are set to the same values as the previous simulations. This figure shows that at 15 dB SNR all of the estimators generally achieve the root-CRLB but rapidly fail when the magnitude of the AOA exceeds some threshold. The AOA threshold is $\pm 84°$ for the two MLE and TD2 estimators and $\pm 50°$ for the TD1 estimator. This threshold behaviour is characteristic of interferometers and is attributed to the circular nature of the phase measurements. The AOA estimation is more accurate about broadside (i.e. $\theta = 0°$) and becomes increasingly worse as the AOA tends towards endfire (i.e. $\theta = \pm 90°$). This suggests that beyond a certain AOA threshold, phase wrapping errors in the phase delay measurements cause large errors in the AOA estimation. This threshold behaviour limits the practical range of angles that an algorithm can reliably estimate the AOA below a certain error tolerance. The span of this angular range is termed the *field-of-view* (FOV) of the algorithm. In this example, the two MLE and the TD2 estimators can estimate the AOA below an accuracy of $1°$ RMS with a FOV of $169°$. Similarly, the TD1 estimator has a FOV of $117°$.

Finally, Figure 3.4 and Figure 3.6 verify that the TD1 estimator is inferior to the TD2 estimator at low SNR and when the AOA of the signal is close to endfire. Since the TD2 estimator is also faster than the TD1 estimator, the TD2 estimator is generally preferred if a time-domain AOA estimation method is required.

3.4.5 RMS Error of an Interferometer

When discussing the performance of an algorithm, it is often desirable to have an analytical expression to describe the RMS error of that algorithm. Due to the complexity of the mathematical derivation, an exact analytical expression to describe the RMS errors of a specific implementation of a two-antenna interferometer under all conditions has thus far been elusive [57–59]. However, since the RMS errors of all four interferometer implementations have been shown to be asymptotically efficient at high SNR, it is reasonable to approximate the RMS errors of a two-antenna interferometer at high SNR using the expression for the root-CRLB as follows [5],

$$\delta\theta_{\text{RMS}} \approx \frac{1}{\sqrt{\eta N}} \cdot \frac{c}{2\pi f d \cos\theta}. \tag{3.27}$$

Note that by recognising that the RMS errors of the phase delay is given by

$$\delta\psi_{\text{RMS}} = \frac{1}{\sqrt{\eta N}}, \tag{3.28}$$

then first-order differential error analysis techniques can also be applied to (3.12) to derive the same expression for the RMS error of a two-antenna interferometer [5, 36, 41].

3.5 Long Baseline Interferometry

In this section, it will be shown that the accuracy of the AOA estimation can be significantly improved using so-called *long baseline interferometers*. Inspection of (3.27) suggests that an interferometer's AOA estimation accuracy can be improved by one or more of the following:

- increasing the SNR of the signal,
- increasing the signal duration (and hence number of samples),
- increasing the signal frequency,
- operating closer to broadside (i.e. $\theta = 0°$), and/or
- increasing the antenna separation.

Since the parameters of the radar signal are beyond the control of the radar intercept receiver, the first three parameters cannot be changed. Some improvement in the AOA estimation accuracy can be gained by actively rotating the interferometer baseline to operate closer to the broadside region. For moving platforms, this can be achieved by changing the trajectory of the platform, while for stationary platforms, this can be achieved by using multiple, short baseline interferometers with different orientations and appropriately switching between the baselines on an intercept-by-intercept basis. However, these methods will only provide a small improvement in the AOA estimation

performance and may be impractical to achieve. The most practical method to improve the AOA estimation performance is to utilise a longer baseline interferometer.

Figure 3.7 shows the unwrapped, unambiguous phase delays for a short baseline ($d_{\text{short}} = \lambda/2$) and a long baseline ($d_{\text{long}} = 5\lambda$) interferometer. From (3.27), it is expected that the RMS errors of the long baseline interferometer will be 10 times lower than the RMS errors of the short baseline interferometer operating under the same conditions, since

$$\frac{\delta\theta_{\text{RMS,long}}}{\delta\theta_{\text{RMS,short}}} = \frac{1/5\lambda}{1/0.5\lambda} = \frac{1}{10}. \tag{3.29}$$

Figure 3.8 shows the peak errors in the AOA estimation for each baseline corresponding to a peak error of $\pm 5^\circ$ in the phase delay measurement. For the short-baseline interferometer (i.e. the blue area bounded by the solid line), the peak error in the AOA estimation is $\pm 1.59^\circ$. For the long-baseline interferometer (i.e. the red area bounded by the dashed line), the peak error is $\pm 0.159^\circ$. This example verifies that the AOA estimation errors are reduced by a factor of 10 in the long baseline interferometer.

While long baseline interferometers offer improved AOA estimation performance, they also introduce an ambiguity problem because the theoretical phase delays can exceed $\pm\pi$, however, the phase delays can only be measured between $[-\pi, \pi]$ due to the circular nature of phases. Phase delay values that exceed this interval will be aliased back into the same interval and so leads to ambiguities since an ambiguous phase delay measurement cannot be distinguished from its 2π ambiguity. This effect is known as *phase wrapping*.

To further illustrate the relationship between the AOA accuracy and phase ambiguities, Figure 3.9 shows that an unambiguous AOA estimate is obtained for a signal arriving from $\theta = 23.42^\circ$ using a short baseline ($d_{\text{short}} = \lambda/2$) interferometer. In this figure, the AOA estimate is plotted as a triangle with the peak displaying the estimated AOA and the width of the base reflecting the peak error of $\pm 1.59^\circ$ corresponding to a peak error of $\pm 5^\circ$ in the phase delay measurement. On the other hand, Figure 3.10 shows the ambiguous AOA estimates for the same signal using a longer baseline ($d_{\text{long}} = 5\lambda$) interferometer. At the true AOA of $\theta = 23.42^\circ$, the peak error is reduced to $\pm 0.159^\circ$ corresponding to the same phase delay measurement error. While the long baseline interferometer has a significant performance gain, the ambiguities in the AOA estimation needs to be resolved for correct AOA estimation.

The ambiguity problem can be described mathematically as follows. Recall that the phase delay between two antennas is defined as

$$\psi = \frac{2\pi f d}{c} \sin\theta. \tag{3.30}$$

The maximum and minimum values of the phase delay will correspond to $\theta = \pm 90^\circ$, and so the phase delays will be bounded by

$$-\frac{2\pi f d}{c} \leq \psi \leq \frac{2\pi f d}{c}. \tag{3.31}$$

In order to ensure that the unambiguous phase delays and the measured phase delays maintain a unique relationship, the unambiguous phase delays must lie completely within

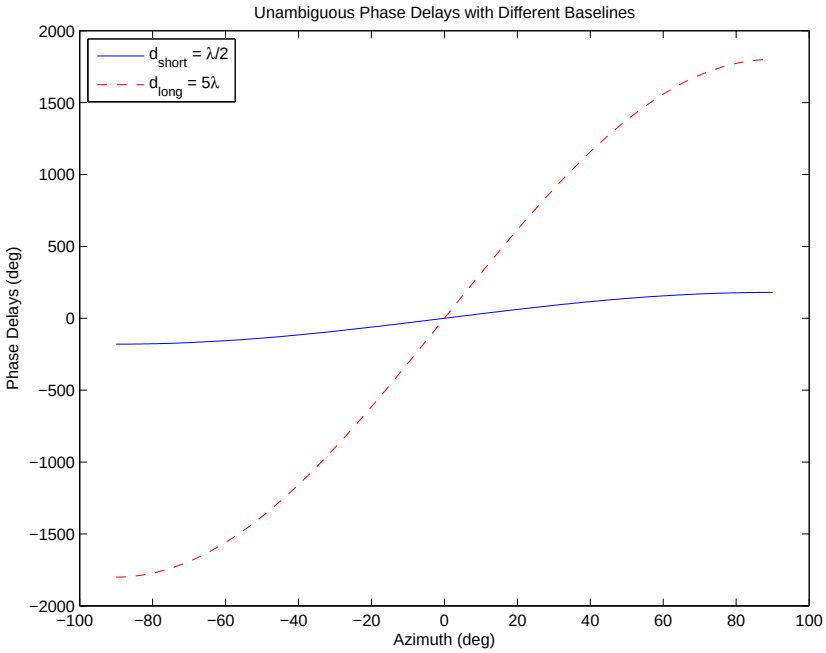

Figure 3.7: Unambiguous phase delays as a function of AOA for a short and long baseline interferometer. Simulation parameters: $f = 18$ GHz, $\lambda = 16.67$ mm, $d_{\text{short}} = \lambda/2$ and $d_{\text{long}} = 5\lambda$.

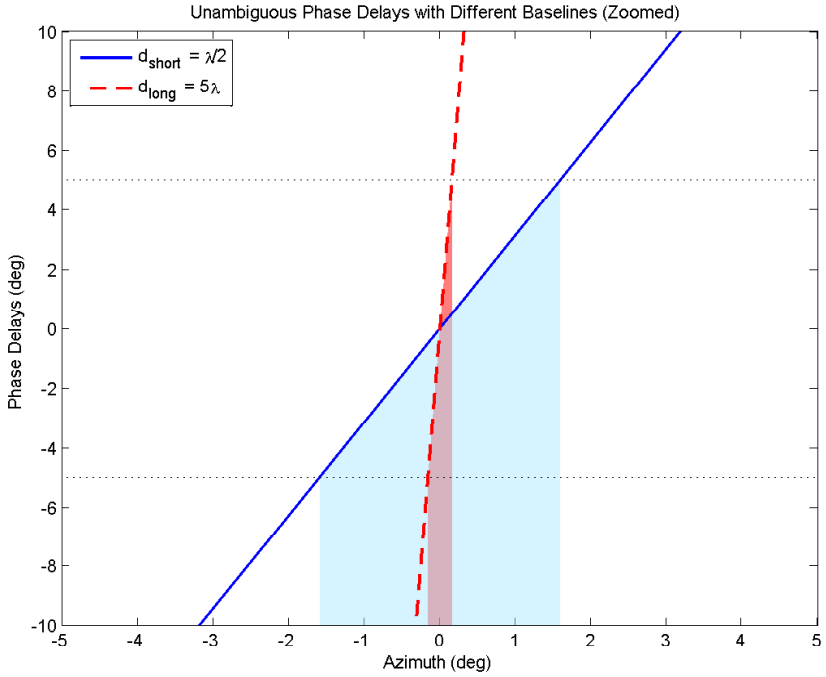

Figure 3.8: Peak error in the AOA estimation for a short and long baseline interferometer due to a peak phase error is $\delta\psi_{\text{peak}} = \pm 5°$. Simulation parameters: $\theta = 0°$, $f = 18$ GHz, $\lambda = 16.67$ mm, $d_{\text{short}} = \lambda/2$ and $d_{\text{long}} = 5\lambda$.

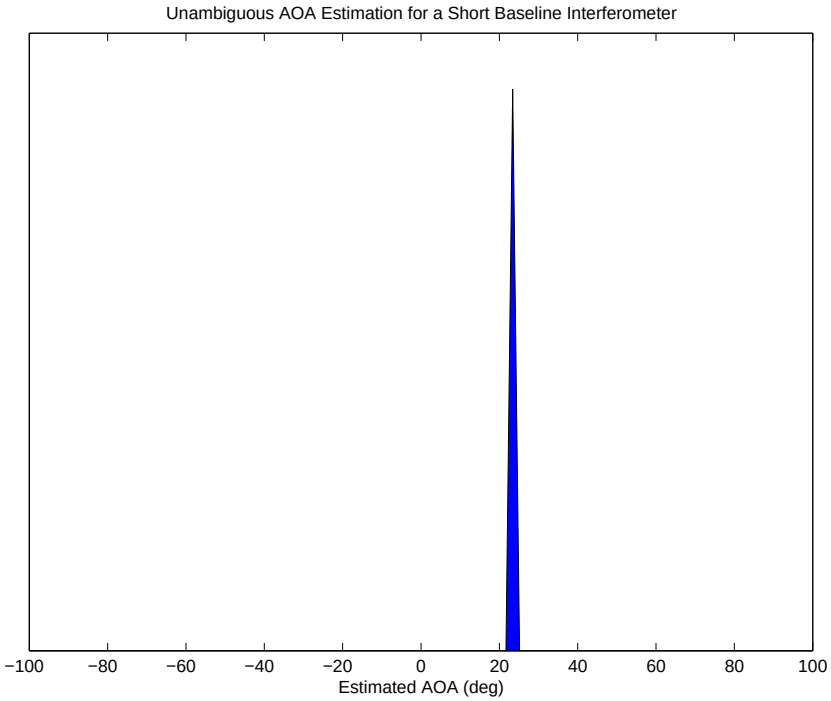

Figure 3.9: This plot shows that a short baseline interferometer obtains unambiguous AOA estimates. However, the estimation errors (as indicated by the widths of the triangles) are also larger. In this plot, $\theta = 23.42°$, $f = 18$ GHz, $d_{\text{short}} = \lambda/2$ and the peak phase error is $\delta\psi_{\text{peak}} = \pm 5°$.

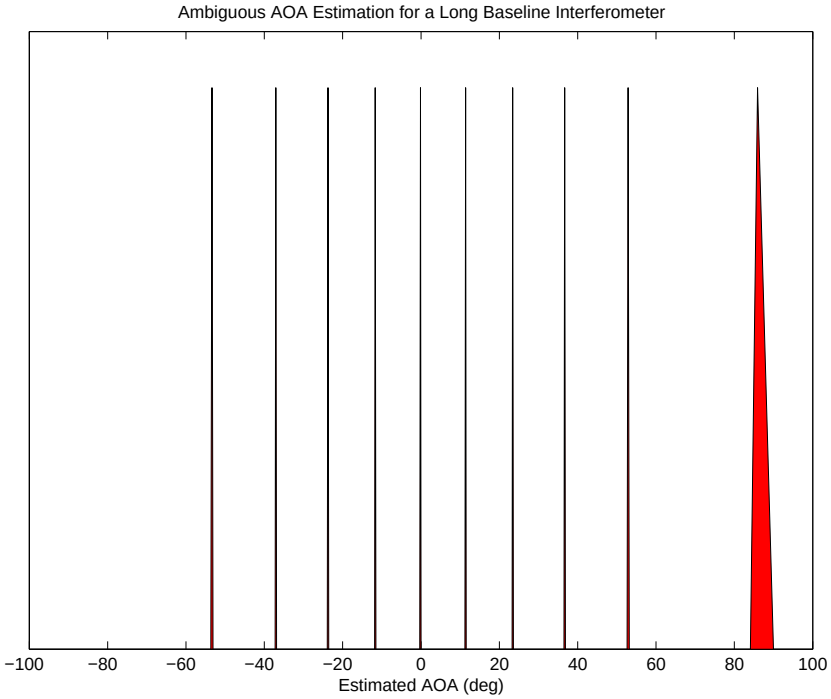

Figure 3.10: This plot shows that a long baseline interferometer has lower estimation errors (as indicated by the widths of the triangles) but are ambiguous. In this plot, $\theta = 23.42°$, $f = 18$ GHz, $d_{\text{long}} = 5\lambda$ and the peak phase error is $\delta\psi_{\text{peak}} = \pm 5°$.

the interval $[-\pi, \pi]$. This is only true when the antenna separation is "short" in the sense that it satisfies the following constraint,

$$d \leq \frac{c}{2f} = \frac{\lambda}{2}. \tag{3.32}$$

For "long" baselines, where $d > \lambda/2$, the unambiguous phase delay, ψ, will exceed the interval $[-\pi, \pi]$ and is given by

$$\psi = \tilde{\psi} + \rho 2\pi, \tag{3.33}$$

where $\tilde{\psi} \in [-\pi, \pi]$ represents the measured, ambiguous phase delay, and ρ is an integer representing the possible ambiguity numbers which correspond to one of the 2π ambiguities of the phase delay measurements and is bounded by

$$\left\lceil -\frac{fd}{c} - \frac{\tilde{\psi}}{2\pi} \right\rceil \leq \rho \leq \left\lfloor \frac{fd}{c} - \frac{\tilde{\psi}}{2\pi} \right\rfloor, \tag{3.34}$$

where $\lfloor \cdot \rfloor$ and $\lceil \cdot \rceil$ represent the floor and ceiling operations respectively. For a given phase delay measurement, $\tilde{\psi}$, the complete set of ambiguity numbers, $\Upsilon(\tilde{\psi})$, is written as

$$\Upsilon(\tilde{\psi}) = \left\{ \left\lceil -\frac{fd}{c} - \frac{\tilde{\psi}}{2\pi} \right\rceil, \ldots, -2, -1, 0, 1, 2, \ldots, \left\lfloor \frac{fd}{c} - \frac{\tilde{\psi}}{2\pi} \right\rfloor \right\}. \tag{3.35}$$

The total number of ambiguities, $N^a_{\Upsilon(\tilde{\psi})}$, i.e. the number of elements in $\Upsilon(\tilde{\psi})$, is given by

$$N^a_{\Upsilon(\tilde{\psi})} = \text{round}\left[\frac{2fd}{c} \right], \tag{3.36}$$

where round$[\cdot]$ represents the rounding operation.

The corresponding ambiguous AOAs of a long baseline interferometer are given by

$$\hat{\theta}(\rho) = \arcsin\left(\frac{c(\tilde{\psi} + \rho 2\pi)}{2\pi f d} \right). \tag{3.37}$$

Ambiguity resolution methods are required to correctly resolve the unambiguous AOA from all of the ambiguous possibilities.

Example 3.1
Consider a long baseline interferometer with a baseline, $d_{\text{long}} = 5\lambda$. The signal frequency is assumed to be $f = 18$ GHz and the corresponding wavelength is $\lambda = 16.67$ mm. For an AOA of $\theta = 23.42°$, (3.30) gives the unambiguous phase delay as

$$\psi = 715.44°. \tag{3.38}$$

Due to phase wrapping, the measured, ambiguous phase delay is

$$\tilde{\psi} = [\psi]_{2\pi} = -4.56°. \tag{3.39}$$

The complete set of ambiguity numbers can then be calculated from (3.35) as follows

$$\Upsilon(\tilde{\psi} = -4.56°) = \{-4, -3, -2, -1, 0, 1, 2, 3, 4, 5\}. \tag{3.40}$$

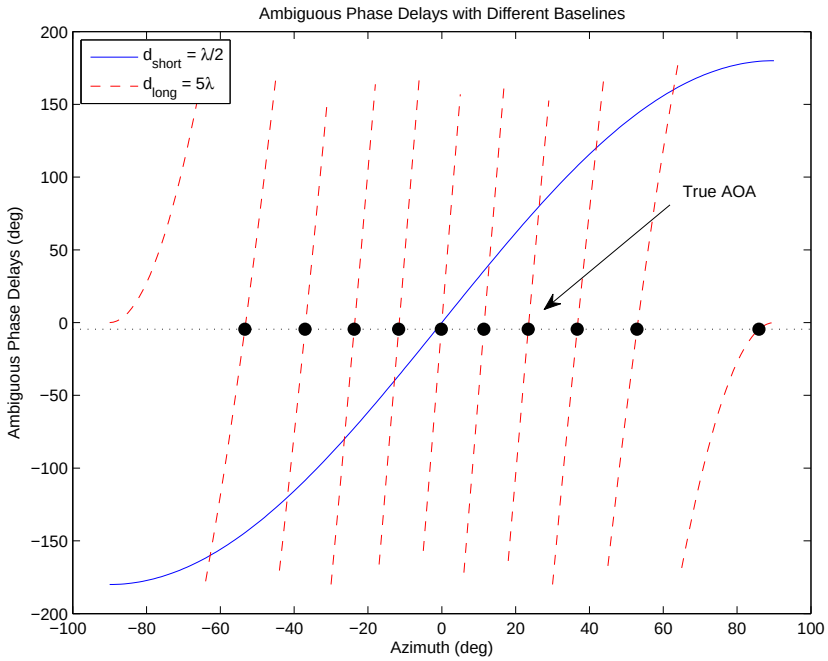

Figure 3.11: Ambiguous phase delays as a function of AOA for a short and long baseline interferometer. Simulation parameters: $f = 18$ GHz, $\lambda = 16.67$ mm, $d_{\text{short}} = \lambda/2$ and $d_{\text{long}} = 5\lambda$. The black dots represent the ambiguous AOAs that correspond to an ambiguous phase delay measurement of $\tilde{\psi} = -4.56°$.

This set contains a total of $N^a_{\Upsilon(\tilde{\psi})} = 10$ possible ambiguities. From (3.37), the corresponding set of ambiguous AOA estimates are

$$\hat{\theta}(\rho \in \Upsilon(\tilde{\psi})) = \{-53.37°, -37.05°, -23.74°, -11.69°, \quad (3.41)$$
$$-0.1451°, 11.39°, 23.42°, 36.69°, 52.89°, 85.92°\} \quad (3.42)$$

Based on a single measured, ambiguous phase delay, $\tilde{\psi} = -4.56°$, the radar intercept receiver cannot determine which of the above ambiguities is the true AOA of the signal. Figure 3.11 plots this example pictorially. ∎

By virtue of the lower RMS error performance, long baseline interferometers also have an increased field-of-view (FOV). For a given RMS error tolerance, $\delta\theta_{\text{tol}}$, the maximum positive and negative AOA that can be estimated by an interferometer, $\pm\theta_{\max}$, can be approximated by re-arranging (3.27) to give

$$\pm\,\theta_{\max} \approx \pm \arccos\left(\frac{1}{\sqrt{\eta N}} \cdot \frac{c}{2\pi f d \delta\theta_{\text{tol}}}\right). \quad (3.43)$$

The FOV of an interferometer can therefore be written as

$$\text{FOV} = \theta_{\max} - \theta_{\min} \approx 2\arccos\left(\frac{1}{\sqrt{\eta N}} \cdot \frac{c}{2\pi f d \delta\theta_{\text{tol}}}\right). \quad (3.44)$$

Figure 3.12 shows the FOV with various RMS error tolerances as a function of the array aperture. This figure shows that as the array aperture is increased, the FOV rapidly approaches 180°.

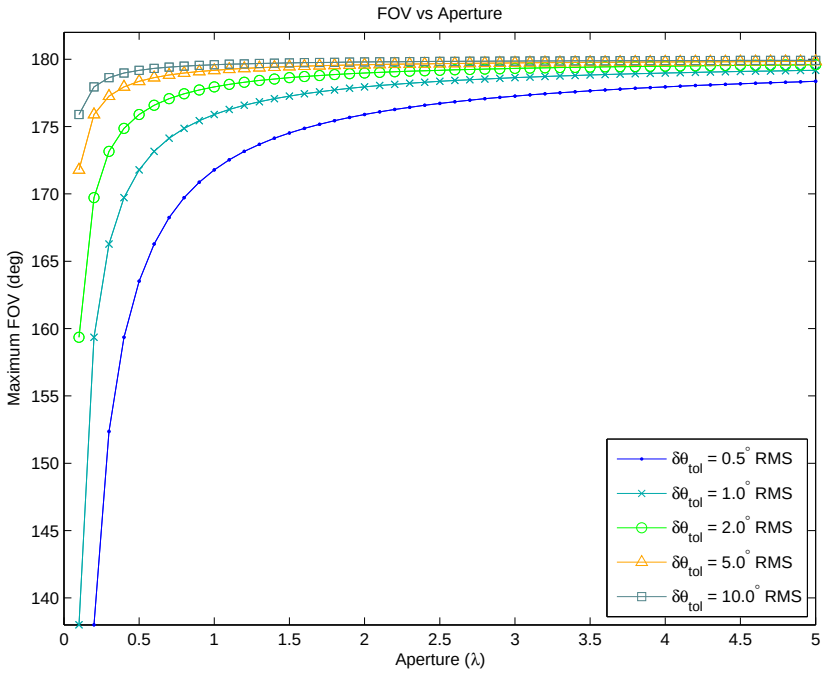

Figure 3.12: This plot shows the improvement in FOV for a given maximum error tolerance as a function of the aperture.

3.6 Ambiguity Resolution Using Independent Methods

The objective of using an independent direction finding method is to obtain an unambiguous AOA estimate that can be used to "select" the correct AOA from the set of ambiguous AOA estimates from a long baseline interferometer [35, 41, 42, 60]. In general, the AOA estimates of the independent method are assumed to have a low, or "coarse", angular accuracy while the long baseline interferometer has a much higher angular accuracy. In order to perform ambiguity resolution, the angular accuracy of the independent method must be accurate enough so that only one of the ambiguous AOA estimates will be associated with the coarse AOA estimate. As a rule of thumb, three times the RMS error of the independent coarse method, $\delta\theta_{\text{RMS,coarse}}$, should be less than or equal to one half of the smallest angular separation between the ambiguities, $\delta\theta_{\text{amb,min}}$. That is,

$$3\delta\theta_{\text{RMS,coarse}} \leq \frac{\delta\theta_{\text{amb,min}}}{2}, \tag{3.45}$$

or

$$\delta\theta_{\text{RMS,coarse}} \leq \frac{\delta\theta_{\text{amb,min}}}{6}. \tag{3.46}$$

Due to the nature of arcsine functions, $\delta\theta_{\text{amb}}(\rho)$ will tend to be smaller about broadside and larger towards endfire and so the smallest angular separation between the ambiguities can be approximated as

$$\delta\theta_{\text{amb,min}} \approx \arcsin\left(\frac{c(\tilde{\psi}+2\pi)}{2\pi f d}\right) - \arcsin\left(\frac{c\tilde{\psi}}{2\pi f d}\right) \approx \frac{c}{fd}. \tag{3.47}$$

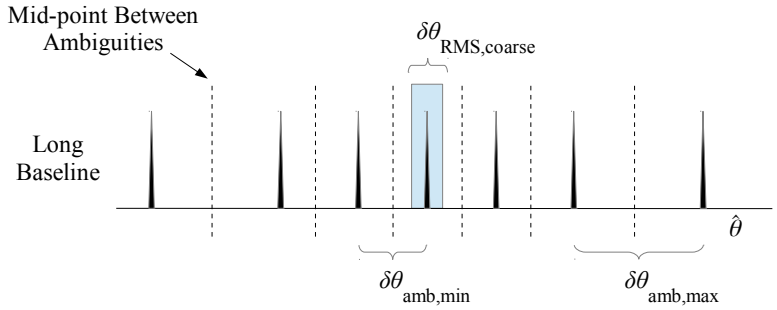

Figure 3.13: Successful ambiguity resolution using an independent method requires that the coarse AOA estimate has a RMS error that satisfies $\delta\theta_{\text{RMS,coarse}} \leq \delta\theta_{\text{amb,min}}/6$.

The required accuracy of the independent AOA estimation method can then be written as

$$\delta\theta_{\text{RMS,coarse}} \leq \frac{\delta\theta_{\text{amb,min}}}{6} \approx \frac{c}{6fd}. \tag{3.48}$$

As a corollary, given the RMS error of a coarse AOA estimation method, the antenna separation of a long baseline interferometer should satisfy

$$d \leq \frac{c}{6f\delta\theta_{\text{RMS,coarse}}}. \tag{3.49}$$

3.6.1 Amplitude Comparison

Amplitude comparison direction finders have been identified as a suitable contender to provide the necessary coarse AOA estimate for ambiguity resolution at low microwave frequencies [35, 41, 42]. In [35], such a system was demonstrated to achieve approximately 0.65° RMS for signals received between $0.5 - 2$ GHz.

However, amplitude comparison systems are less effective at resolving the ambiguities at higher frequencies. For a amplitude comparison system with a RMS error of 10°, (3.49) suggests that the maximum antenna spacing for the corresponding long baseline interferometer is 15.9 mm (or about 0.95λ at 18 GHz). Since physically large antennas that are capable of receiving signals between $2 - 18$ GHz generally exceed 4.5λ (at 18 GHz), long baseline interferometers using these antennas will also exceed 4.5λ. Thus, the amplitude comparison system will not have sufficient accuracy to resolve the ambiguities of long baseline interferometer at higher frequencies.

3.6.2 Short Baseline

Another method to resolve the ambiguities is to use a short baseline interferometer in conjunction with a long baseline interferometer [61]. The short baseline interferometer will provide the unambiguous coarse AOA estimate, while the long baseline interferometer will provide the ambiguous high accuracy AOA estimates. The simplest implementation of such a system will require three antennas with a common reference antenna.

From (3.27) and (3.49), the maximum long baseline interferometer that can be used with the short baseline interferometer can be shown to be

$$d_{\text{long}} \leq d_{\text{short}} \cdot \frac{\pi}{3} \cos\theta_{\max} \sqrt{\eta N}, \tag{3.50}$$

where d_{short} and d_{long} are the antenna separations for the short and long baseline interferometers respectively, η is the SNR, N is the number of samples, and $\theta_{\max}$ refers to the maximum AOA to be estimated by the short baseline interferometer. In general, $\theta_{\max}$ is limited to the desired FOV of the short baseline interferometer.

If an application requires a very high accuracy such that the coarse AOA estimation provided by the short baseline interferometer does not have enough accuracy to directly resolve the ambiguities of the long baseline interferometer then additional auxiliary antennas may be used to provide intermediate baselines to allow successive ambiguity resolution. For M interferometer baselines, the d_m baseline must satisfy

$$d_m \leq d_{m-1} \cdot \frac{\pi}{3} \cos\theta_{\max} \sqrt{\eta N}, \tag{3.51}$$

where $m = 2, 3, \ldots, M$ and $d_1 \equiv d_{\text{short}}$ is the unambiguous short baseline interferometer.

Mathematically, this inference-based ambiguity resolution algorithm can be formulated as described below. Note that since the resolved phase delays and AOA have a unique one-to-one relationship, it is computationally more efficient to resolve the ambiguous phase delays rather than the ambiguous AOA estimates.

Consider a set of M measured ambiguous phase delays, $\Psi = \{\tilde{\psi}_1, \tilde{\psi}_2, \ldots, \tilde{\psi}_M\}$, and their corresponding antenna separations, $D = \{d_1, d_2, \ldots, d_M\}$, where $m = 1, 2, \ldots, M$ and each $\tilde{\psi}_m \in [-\pi, \pi]$. It is assumed that the interferometer baselines are sorted into ascending order and that the first phase delay corresponds to a short baseline interferometer and is unambiguous.

Let Ψ_m and D_m denote the m-th element of Ψ and D respectively. For $m \geq 2$, the expected unambiguous phase delay, $\hat{\Psi}_{m,\text{inferred}}$, of the D_m baseline can be inferred from the previous baseline, D_{m-1}, and the previously resolved phase delay, $\hat{\Psi}_{m-1,\text{resolved}}$, as follows,

$$\hat{\Psi}_{m,\text{inferred}} = \frac{D_m}{D_{m-1}} \hat{\Psi}_{m-1,\text{resolved}}, \tag{3.52}$$

where $\tilde{\Psi}_{1,\text{resolved}} = \tilde{\psi}_1$ is unambiguous. The ambiguity number of the D_m baseline, ρ_m, can then be estimated as

$$\hat{\rho}_m = \text{round}\left[\frac{\hat{\Psi}_{m,\text{inferred}} - \tilde{\psi}_m}{2\pi}\right], \tag{3.53}$$

and so the resolved, unambiguous phase delay of the D_m baseline, $\hat{\Psi}_{m,\text{resolved}}$, is

$$\hat{\Psi}_{m,\text{resolved}} = \tilde{\psi}_m + \hat{\rho}_m 2\pi. \tag{3.54}$$

The final AOA estimate can then be obtained from the resolved phase delay of the longest baseline. This process is illustrated graphically in Figure 3.14.

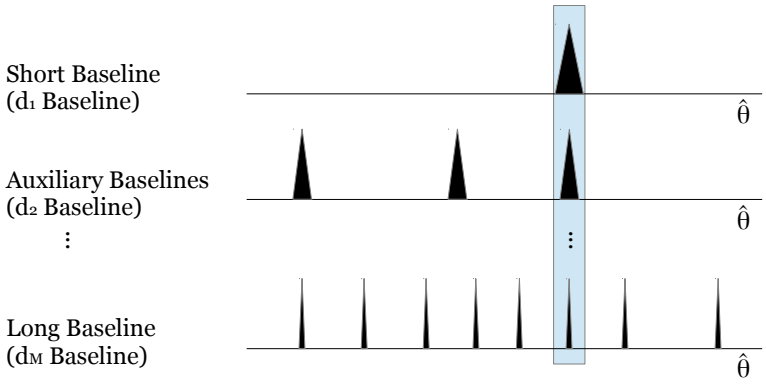

Figure 3.14: A short-baseline interferometer can be used to successively resolve the ambiguities of the longer baselines. In this figure, the width of the triangles indicate the RMS errors associated with the interferometer baselines. The RMS error improves as the coarse AOA estimation method successively resolves the ambiguities of the longer baselines.

3.7 Ambiguity Resolution Using Multiple Baselines

Ambiguity resolution using independent, non-interferometric AOA estimation methods may impose additional constraints on the design of the direction finding systems. For example, amplitude comparison systems require that directional antennas be mounted at physically squinted angles, while TDOA systems may require very long baselines and/or very high sample rate digitisers. Furthermore, the accuracy of these algorithms may not be sufficient to resolve the ambiguities of the long baseline interferometer at higher frequencies. On the other hand, ambiguity resolution using a short-baseline interferometer requires that at least one pair of antennas be spaced no more than one-half a wavelength apart (at the highest frequency of operation). In practice, these design constraints may not be achievable due to the size of the antenna or mounting characteristics of the platform.

In this section, alternative ambiguity resolution methods which make use of multiple long baseline interferometers constructed from the sparse array geometry are presented. These methods are loosely based on the Chinese Remainder Theorem (CRT) and require appropriately chosen interferometer baselines. For large apertures, unambiguous AOA estimates can generally be obtained with fewer intermediate baselines than the "short-baseline" ambiguity resolution method. For simplicity, the methods discussed in this section will be described in terms of a non-uniform linear array, however, the results can be generalised to arbitrary array geometries. All phase delay measurements are assumed to be performed in the frequency domain using the FFT implementation and it is further assumed that no scalloping losses occur.

3.7.1 The Chinese Remainder Theorem

The Chinese Remainder Theorem was developed by the Chinese mathematician, Sun Tzu, in the third century AD to solve a system of simultaneous congruences [8, 62–64]. The theorem provides a common solution that simultaneously satisfies a set of constraints specified by a system of congruences with positive integer variables.

Theorem 3.7.1
Suppose $\gamma_1, \gamma_2, \ldots, \gamma_M$ are positive integers which are pairwise co-prime, i.e. the greatest common denominator of all of the integers is 1. For a sequence of integers, $r_1, r_2, \ldots, r_M$, let there exist an integer Λ that solves the following system of simultaneous congruences.

$$\begin{aligned} [\Lambda]_{\gamma_1} &\equiv r_1, && (3.55)\\ [\Lambda]_{\gamma_2} &\equiv r_2, && (3.56)\\ &\vdots && (3.57)\\ [\Lambda]_{\gamma_M} &\equiv r_M, && (3.58) \end{aligned}$$

where $[\,\cdot\,]_{\gamma_m}$ represents the modulo γ_m operation and $m = 1, 2, \ldots, M$. The solution to Λ (modulo Γ) can be shown to be [8, 62]

$$\Lambda = \left[\sum_{m=1}^{M} r_m b_m \frac{\Gamma}{\gamma_m}\right]_{\Gamma}, \tag{3.59}$$

where

$$\Gamma = \prod_{m=1}^{M} \gamma_m, \tag{3.60}$$

and b_m denotes the modular multiplicative inverse of Γ/γ_m such that

$$\left[b_m \frac{\Gamma}{\gamma_m}\right]_{\gamma_m} = 1. \tag{3.61}$$

In other words, b_m is the smallest positive, real integer that satisfies (3.61). ∎

Example 3.2
Consider the following system of congruences,

$$\begin{aligned} [\Lambda]_7 &= 3, && (3.62)\\ [\Lambda]_3 &= 2. && (3.63) \end{aligned}$$

In this example, $\gamma_1 = 7$, $\gamma_2 = 3$, $r_1 = 3$, $r_2 = 2$ and $M = 2$. The product, Γ, is given by

$$\Gamma = \prod_{m=1}^{M} \gamma_m = 7 \times 3 = 21, \tag{3.64}$$

For $m = 1$,

$$\frac{\Gamma}{\gamma_1} = \frac{21}{7} = 3, \tag{3.65}$$

and so finding the modular multiplicative inverse, b_1, is a search for the smallest positive real integer that satisfies the following expression

$$\left[b_1 \frac{\Gamma}{\gamma_1}\right]_{\gamma_1} = [b_1 \times 3]_7 = 1. \tag{3.66}$$

b_1	$b_1\Gamma/\gamma_1$	$[b_1\Gamma/\gamma_1]_{\gamma_1}$
1	3	3
2	6	6
3	9	2
4	12	5
5	15	1
6	18	4
⋮	⋮	⋮

Table 3.1: Possible candidates for b_1.

Table 3.1 lists some possible candidates for b_1 and the corresponding solution to the expression $[b_1\Gamma/\gamma_1]_{\gamma_1}$. This table shows that the smallest positive, real integer that satisfies (3.66) occurs when $b_1 = 5$.

Similarly, for $m = 2$,

$$\frac{\Gamma}{\gamma_2} = \frac{21}{3} = 7, \tag{3.67}$$

and so finding the modular multiplicative inverse, b_2, is a search for the smallest positive real integer that satisfies the following expression

$$\left[b_2\frac{\Gamma}{\gamma_2}\right]_{\gamma_2} = [b_2 \times 7]_3 = 1. \tag{3.68}$$

Table 3.2 lists some possible candidates for b_2 and the corresponding solution to the expression $[b_2\Gamma/\gamma_2]_{\gamma_2}$. This table shows that the smallest positive integer that satisfies (3.68) is $b_2 = 1$.

b_2	$b_2 \cdot \Gamma/\gamma_2$	$[b_2 \cdot \Gamma/\gamma_2]_{\gamma_2}$
1	7	1
2	14	2
3	21	0
4	28	1
5	35	2
6	42	0
⋮	⋮	⋮

Table 3.2: Possible candidates for b_2.

From (3.59), the solution to the system of congruences is therefore given by

$$\begin{aligned}
\Lambda &= \left[\sum_{m=1}^{M} r_m b_m \frac{\Gamma}{\gamma_m}\right]_{\Gamma} && (3.69)\\
&= [(3 \times 5 \times 3) + (2 \times 1 \times 7)]_{21} && (3.70)\\
&= [59]_{21} && (3.71)\\
&= 17. && (3.72)
\end{aligned}$$

Thus, the solution to the system of congruences is 17 (modulo 21). ∎

Application of the CRT for Ambiguity Resolution

The Chinese Remainder Theorem has been applied to resolve the ambiguities of multiple long baseline interferometers [62–69]. The following formulation is based on the work by Zheng *et al.* [62].

Consider M long baseline interferometers with antenna separations $d_1, d_2, \ldots, d_M$, such that

$$\frac{\lambda_{\min}}{2} < d_1 < d_2 < \ldots < d_M. \tag{3.73}$$

Let d_0 represent a larger distance such that each interferometer baseline can be written as

$$d_m = \frac{d_0}{\gamma_m}, \tag{3.74}$$

where d_m represents the m-th interferometer baseline, γ_m is a positive integer divisor of d_0, and $m = 1, 2, \ldots, M$. It is assumed that the interferometer baselines and d_0 is chosen such that the integers specified by γ_m are co-prime, i.e. the greatest common divisor for $\gamma_1, \gamma_2, \ldots, \gamma_M$ is 1.

Recall that the unambiguous phase delay of the d_m baseline, ψ_m, is given by

$$\psi_m = \frac{2\pi f d_m}{c} \sin\theta = \tilde{\psi}_m + \rho_m 2\pi, \tag{3.75}$$

where $\tilde{\psi}_m \in [-\pi, \pi]$ is the measured, ambiguous phase delay and ρ_m is an integer representing the ambiguity numbers constrained by (3.34). Substituting (3.74) into (3.75) and re-arranging gives

$$\frac{f d_0 \sin\theta}{c} = \gamma_m \frac{\tilde{\psi}_m}{2\pi} + \rho_m \gamma_m. \tag{3.76}$$

Since ρ_m is an integer, (3.76) can be written as

$$[\Lambda]_{\gamma_m} = r_m, \tag{3.77}$$

where Λ is a quantity that is common between all interferometer baselines given by

$$\Lambda = \frac{f d_0}{c} \sin\theta, \tag{3.78}$$

and r_m is the remainder term given by

$$r_m = \gamma_m \frac{\tilde{\psi}_m}{2\pi}. \tag{3.79}$$

Since γ_m is an integer by definition and the normalised measured phase delay, $\tilde{\psi}/2\pi$, lies in the interval $[-0.5, 0.5]$, the remainder term, r_m, can be approximated by an integer. Since the right-hand side of (3.77) is approximately an integer, then Λ is also approximately an integer. Furthermore, since the remainder term is defined using modulo arithmetic, negative values corresponding to negative AOAs can be converted to an equivalent positive integer representation (although this step does not need to be explicitly performed). Thus, (3.77) specifies a system of congruences with approximately

positive integer parameters that can be solved using the CRT algorithm. Given that the solution to Λ is specified by (3.59), the AOA of the signal can then be unambiguously estimated as

$$\hat{\theta} = \arcsin\left(\frac{c\Lambda}{fd_0}\right). \tag{3.80}$$

In practice, two additional modifications will need to be made to the above algorithm. Firstly, since the phase delays are measured as a continuous variable but the CRT algorithm requires that the remainder term be an integer, (3.79) must be replaced with a rounded value, $\tilde{r}_m$, such that

$$\tilde{r}_m = \text{round}\left[r_m\right], \tag{3.81}$$

where round$[\,\cdot\,]$ represents the rounding operation. Secondly, the CRT algorithm only applies to positive integer parameters and so will only estimate positive solutions of Λ (modulo Γ) and hence positive AOAs. However, negative AOAs can be still estimated with an appropriate correction to the estimated value of Λ. For a linear array, the AOA of the signal lies in the interval $\theta \in [-90°, 90°]$, and so from (3.78), the possible values of Λ will be constrained by $\Lambda \in [-B, B]$, where

$$B = \frac{fd_0}{c}. \tag{3.82}$$

The CRT algorithm estimates positive values for Λ (modulo Γ) in the interval $\Lambda \in [0, 2B]$ and so the negative values of Λ, $[-B, 0)$, is mapped to the region $(B, 2B]$. The AOA of the signal can then be unambiguously estimated for both positive and negative angles as follows

$$\hat{\theta} = \begin{cases} \arcsin\left(\dfrac{c\Lambda}{fd_0}\right) & \Lambda \leq B, \\ \arcsin\left(\dfrac{c(\Lambda - \Gamma)}{fd_0}\right) & \Lambda > B. \end{cases} \tag{3.83}$$

Example 3.3
Consider two interferometer baselines where $d_1 = 3\lambda/2$, $d_2 = 7\lambda/2$, $\lambda = 16.67$ mm, the signal frequency is $f = 18$ GHz and the AOA of the signal is $\theta = 23.42°$. This example shall assume an ideal signal without any receiver noise.

The first step in this example is to re-express the AOA estimation problem as a system of congruences. Let d_0 be the lowest common multiple of d_1 and d_2, i.e. $d_0 = 21\lambda/2$. This implies that $\gamma_1 = 7$ and $\gamma_2 = 3$, which satisfies (3.74) as follows,

$$d_1 = \frac{d_0}{\gamma_1} = \frac{21\lambda/2}{7} = 3\lambda/2, \tag{3.84}$$

$$d_2 = \frac{d_0}{\gamma_2} = \frac{21\lambda/2}{3} = 7\lambda/2. \tag{3.85}$$

For $\theta = 23.42°$, the unambiguous phase delays are

$$\psi_1 = \frac{2\pi f d_1}{c}\sin\theta = 214.63°, \tag{3.86}$$

$$\psi_2 = \frac{2\pi f d_2}{c}\sin\theta = 500.81°. \tag{3.87}$$

However, the measured, ambiguous phase delays are

$$\tilde{\psi}_1 = [\psi_1]_{2\pi} = -145.37^\circ, \tag{3.88}$$
$$\tilde{\psi}_2 = [\psi_2]_{2\pi} = 140.81^\circ. \tag{3.89}$$

The rounded remainder terms, $\tilde{r}_m$, are therefore

$$\tilde{r}_1 = \text{round}\left[\gamma_1 \frac{\tilde{\psi}_1}{2\pi}\right] = \text{round}[-2.8266] \approx -3, \tag{3.90}$$

$$\tilde{r}_2 = \text{round}\left[\gamma_2 \frac{\tilde{\psi}_2}{2\pi}\right] = \text{round}[1.1734] \approx 1. \tag{3.91}$$

In this example, the system of congruences that must be solved can be written as

$$[\Lambda]_7 = -3 \tag{3.92}$$
$$[\Lambda]_3 = 1. \tag{3.93}$$

This system of congruences can now be solved in a similar manner to Example 3.2. Consider that Γ is given by

$$\Gamma = \prod_{m=1}^{M} \gamma_m = 7 \times 3 = 21, \tag{3.94}$$

and so,

$$\frac{\Gamma}{\gamma_1} = \frac{21}{7} = 3, \tag{3.95}$$
$$\frac{\Gamma}{\gamma_2} = \frac{21}{3} = 7. \tag{3.96}$$

Since these values are the same as Example 3.2, the corresponding modular multiplicative inverses are $b_1 = 5$ and $b_2 = 1$ as shown in Table 3.1 and Table 3.2 respectively. From (3.59), the solution to this system of congruences is therefore given by

$$[\Lambda]_\Gamma = \left[\sum_{m=1}^{M} r_m b_m \frac{\Gamma}{\gamma_m}\right]_\Gamma \tag{3.97}$$
$$= [(-3 \times 5 \times 3) + (1 \times 1 \times 7)]_{21} \tag{3.98}$$
$$= [-38]_{21}\,. \tag{3.99}$$

While the computed value of Λ is a negative value (modulo 21), it is conventional to re-express Λ in positive terms by taking into account the modulus as follows,

$$[\Lambda]_\Gamma = [-38]_{21} \equiv 4. \tag{3.100}$$

Prior to estimating the AOA, the appropriate expression for the AOA estimation must first be determined from (3.83). In this example, the boundary conditions for Λ is specified by

$$B = \frac{f d_0}{c} = 11. \tag{3.101}$$

Since $\Lambda < B$, the AOA of the signal can be estimated as

$$\hat{\theta} = \arcsin\left(\frac{c\Lambda}{fd_0}\right) = 22.39^\circ. \quad \blacksquare \tag{3.102}$$

Example 3.4
Consider the same example as above but this time the AOA is negative, i.e. $\theta = -23.42^\circ$. In this scenario, the measured, ambiguous phase delays are

$$\tilde{\psi}_1 = [\psi_1]_{2\pi} = 145.37^\circ, \tag{3.103}$$
$$\tilde{\psi}_2 = [\psi_2]_{2\pi} = -140.81^\circ. \tag{3.104}$$

The corresponding rounded remainder terms, $\tilde{r}_m$, are

$$\tilde{r}_1 = \text{round}\left[\gamma_1\frac{\tilde{\psi}_1}{2\pi}\right] = \text{round}[2.8266] \approx 3, \tag{3.105}$$

$$\tilde{r}_2 = \text{round}\left[\gamma_2\frac{\tilde{\psi}_2}{2\pi}\right] = \text{round}[-1.1734] \approx -1, \tag{3.106}$$

and so the system of congruences can be written as

$$[\Lambda]_7 = 3 \tag{3.107}$$
$$[\Lambda]_3 = -1. \tag{3.108}$$

Using the intermediate results from the previous example, it can be shown that the solution to Λ is

$$\Lambda = \left[\sum_{m=1}^{M} r_m b_m \frac{\Gamma}{\gamma_m}\right]_\Gamma \tag{3.109}$$
$$= [(3\times 5\times 3) + (-1\times 1\times 7)]_{21} \tag{3.110}$$
$$= [38]_{21} \tag{3.111}$$
$$\equiv [17]_{21}\,. \tag{3.112}$$

In this example, the solution to Λ is greater than the boundary condition specified by (3.101), i.e. $\Lambda > B$, and so the AOA of the signal can be estimated from (3.83) as follows

$$\hat{\theta} = \arcsin\left(\frac{c(\Lambda-\Gamma)}{fd_0}\right) = -22.39^\circ. \quad \blacksquare \tag{3.113}$$

Due to the rounding operation performed in (3.81), the CRT algorithm suffers from quantisation as the approximation of r_m as an integer quantises the possible values of the AOA estimates and hence introduces an additional bias error to the AOA estimation. This quantisation effect can be observed in Example 3.3 and Example 3.4 where the magnitude of the true AOA is 23.42° but the magnitude of the estimated AOA is 22.39°. The difference is the quantisation error of 1.03°. This quantisation effect is further illustrated in Figure 3.15 which plots the estimated AOA of an ideal (noiseless) signal against the true AOA for two baselines with $d_1 = 3\lambda/2$ and $d_2 = 7\lambda/2$. This example shows that the CRT algorithm will only estimate the AOA as one of 21 possible AOA values for this particular combination of d_1 and d_2. Furthermore, as noted in [62–69], the CRT algorithm is not robust since small errors in the remainder term, r_m, can produce large errors in the AOA estimation, particularly at the quantisation boundaries.

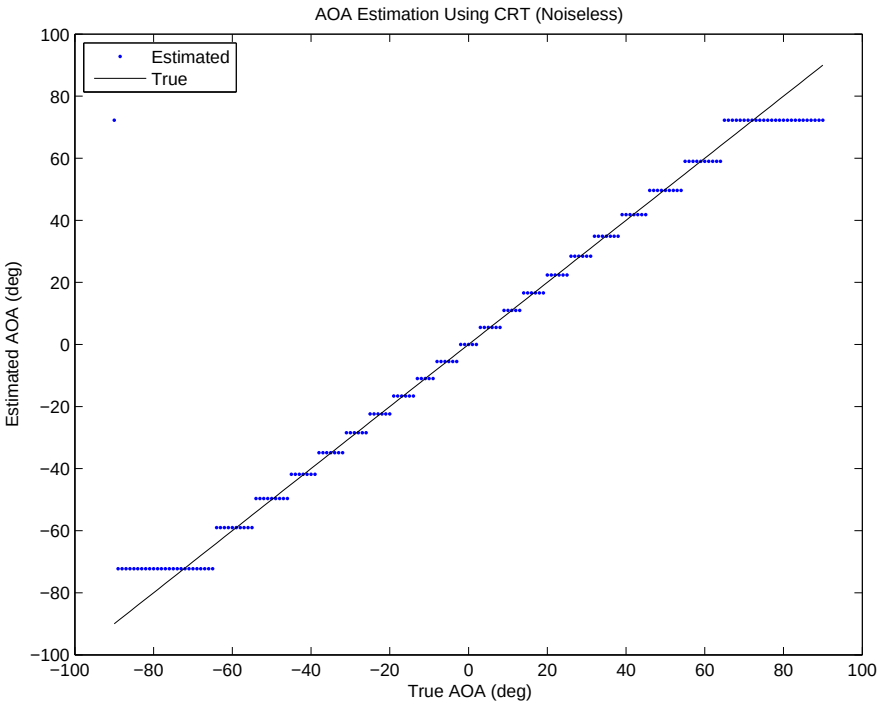

Figure 3.15: AOA estimation using the CRT ambiguity resolution algorithm on a noiseless signal produces quantised estimates. Simulation parameters: $d_1 = 3\lambda/2$, $d_2 = 7\lambda/2$, $f = 18$ GHz, $\lambda = 16.67$ mm.

3.7.2 Non-Uniform Array Geometry

The limitations of the CRT ambiguity resolution algorithm described above can be overcome with an alternative interpretation of the CRT algorithm as described by Tsui [8]. From (3.77), the CRT algorithm suggests that when the interferometer baselines are not integer multiples of each other, a common angle dependent quantity, Λ, will exist that can be uniquely estimated. This further suggests that a unique relationship may exist between the set (or combination) of measured, ambiguous phase delays from each baseline and the signal's AOA. In other words, for sparse non-uniform arrays, there will only be one AOA estimate that is common among all of the ambiguities of the long baseline interferometers. An example of this scenario is illustrated in Figure 3.16.

The requirement for non-uniform baselines can be formulated mathematically by first deriving an expression for the relationship between the measured, ambiguous phase delays of two interferometer baselines and then ensuring that the set of measured, ambiguous phase delays are unique for all AOAs.

Relationship Between the Measured, Ambiguous Phase Delays at θ

Consider the phase delays of two long interferometric baselines, d_k and d_m, when the

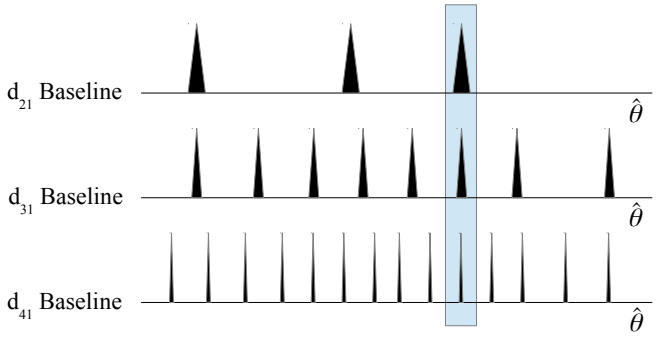

Figure 3.16: For interferometers with non-uniform antenna spacings, there will only be one AOA that is common among the ambiguities of the long baselines.

AOA is θ. The unambiguous phase delays, $\psi_k(\theta)$ and $\psi_m(\theta)$, are

$$\psi_k(\theta) = \frac{2\pi f d_k}{c}\sin\theta = \tilde{\psi}_k(\theta) + \rho_k 2\pi, \tag{3.114}$$

$$\psi_m(\theta) = \frac{2\pi f d_m}{c}\sin\theta = \tilde{\psi}_m(\theta) + \rho_m 2\pi, \tag{3.115}$$

where $\tilde{\psi}_k(\theta), \tilde{\psi}_m(\theta) \in [-\pi, \pi]$ are the measured, ambiguous phase delays and ρ_k, ρ_m are integers representing the ambiguity numbers as constrained by (3.34).

Without loss of generality, it is assumed that $d_k > d_m$. In this section, all phase delay notations have been explicitly written as a function of θ to distinguish between the phase delay measurements from different AOA.

The expressions (3.114) and (3.115) can be re-arranged to give the following equality,

$$\frac{2\pi f}{c}\sin\theta = \frac{\tilde{\psi}_k(\theta) + \rho_k 2\pi}{d_k} = \frac{\tilde{\psi}_m(\theta) + \rho_m 2\pi}{d_m}. \tag{3.116}$$

This can be further arranged to give an expression that describes the relationship between the measured, ambiguous phase delays of each baseline at θ, as follows,

$$\tilde{\psi}_k(\theta) = \frac{d_k}{d_m}\tilde{\psi}_m(\theta) + 2\pi\left(\frac{d_k}{d_m}\rho_m - \rho_k\right). \tag{3.117}$$

Measured, Ambiguous Phase Delays at a Different AOA, θ'

Consider the phase delays of the same interferometer baselines for a different AOA, θ'. The unambiguous phase delays, $\psi_k(\theta')$ and $\psi_m(\theta')$, are

$$\psi_k(\theta') = \frac{2\pi f d_k}{c}\sin\theta' = \tilde{\psi}_k(\theta') + \rho'_k 2\pi, \tag{3.118}$$

$$\psi_m(\theta') = \frac{2\pi f d_m}{c}\sin\theta' = \tilde{\psi}_m(\theta') + \rho'_m 2\pi, \tag{3.119}$$

where $\tilde{\psi}_k(\theta'), \tilde{\psi}_m(\theta') \in [-\pi, \pi]$ are the measured, ambiguous phase delays and ρ'_k, ρ'_m are integers representing the ambiguity numbers as constrained by (3.34). Note that the

parameters $\tilde{\psi}_k(\theta')$, $\tilde{\psi}_m(\theta')$, ρ'_k and ρ'_m for θ' are generally different from the parameters $\tilde{\psi}_k(\theta)$, $\tilde{\psi}_m(\theta)$, ρ_k and ρ_m for θ.

Uniqueness of the Set of Measured, Ambiguous Phase Delays at Different AOAs

Let $\Psi(\theta)$ denote the set of measured, ambiguous phase delays from each interferometer baseline for an AOA, θ, as follows,

$$\Psi(\theta) = \left\{ \tilde{\psi}_k(\theta), \tilde{\psi}_m(\theta) \right\}. \tag{3.120}$$

In order to ensure that the set of ambiguous phase delays from all baselines is unique for each AOA, the set of measured, ambiguous phase delays, $\Psi(\theta)$, for θ must not be the same as the set of measured phase delays, $\Psi(\theta')$, for a different AOA, θ', i.e.

$$\Psi(\theta) \neq \Psi(\theta'). \tag{3.121}$$

This expression requires that the elements of each set to not be simultaneously pairwise equal. In other words, uniqueness requires at least one of the following conditions must be true,

$$\psi_k(\theta) \neq \psi_k(\theta'), \qquad \text{or} \tag{3.122}$$

$$\psi_m(\theta) \neq \psi_m(\theta'). \tag{3.123}$$

While the unambiguous phase delays measured at θ and θ' will be different, it is possible that the measured, ambiguous phase delays of one baseline to be the same due to phase wrapping. As an example, consider that an ambiguity exists in the d_m baseline such that the same ambiguous phase delay is measured at θ and θ'. While the unambiguous phase delays are unique, i.e. $\psi_m(\theta) \neq \psi_m(\theta')$, it is possible that for this particular pair of AOAs, the measured phase delays are ambiguous such that

$$\tilde{\psi}_m(\theta) \equiv \tilde{\psi}_m(\theta'). \tag{3.124}$$

When this occurs, the ambiguity numbers will differ, i.e. $\rho_m \neq \rho'_m$, however these values cannot be directly measured. In this example, (3.123) is not satisfied and so (3.122) must be satisfied in order to ensure that $\Psi(\theta)$ and $\Psi(\theta')$ are unique.

For the d_k baseline, the corresponding measured, ambiguous phase delay due to θ' can be determined by substituting θ', ρ'_k and ρ'_m into (3.117) to give

$$\tilde{\psi}_k(\theta') = \frac{d_k}{d_m}\tilde{\psi}_m(\theta') + 2\pi\left(\frac{d_k}{d_m}\rho'_m - \rho'_k\right). \tag{3.125}$$

Since it is assumed that $\tilde{\psi}_m(\theta) \equiv \tilde{\psi}_m(\theta')$, the above expression can be re-written as

$$\begin{aligned} \tilde{\psi}_k(\theta') &= \frac{d_k}{d_m}\tilde{\psi}_m(\theta) + 2\pi\left(\frac{d_k}{d_m}\rho'_m - \rho'_k\right), \\ &= \tilde{\psi}_k(\theta) + 2\pi\left(\frac{d_k}{d_m}(\rho'_m - \rho_m) - (\rho'_k - \rho_k)\right). \end{aligned} \tag{3.126}$$

Inspection of (3.126) suggests that the ambiguous phase delays, $\tilde{\psi}_k(\theta)$ and $\tilde{\psi}_k(\theta')$, will only be the same if d_k is an integer multiple of d_m, *or* $(\rho'_m - \rho_m)$ is an integer multiple

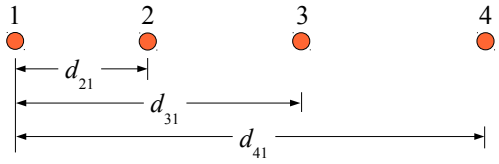

Figure 3.17: A simple set of interferometer baselines comprising of 4 antennas.

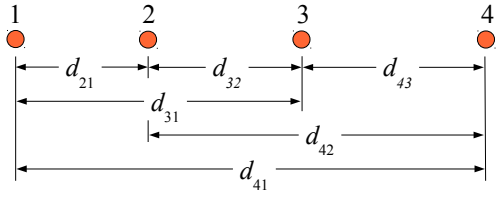

Figure 3.18: An extended set of interferometer baselines comprising of 4 antennas.

of d_m. In practice, d_m can be readily chosen to ensure that $(\rho'_m - \rho_m)$ is not an integer multiple of d_m. Thus, if d_k is chosen such that it is also not an integer multiple of d_m then the right hand side of (3.126) will not be an integer multiple of 2π. This ensures that the ambiguous phase delays measured by the d_k baseline at θ and θ' are unique. In other words, (3.122) can be satisfied with an appropriate choice of the d_k and d_m and so this guarantees that the set of phase delays is unique for each AOA, i.e. $\Psi(\theta) \neq \Psi(\theta')$. This unique relationship can be exploited to unambiguously estimate the AOA of the signal.

This formulation does not assume integer parameters and so there is no quantisation problem due to rounding. Furthermore, the conditions imposed on the interferometer baselines are more relaxed in this formulation compared with the CRT algorithm. Finally, while only two baselines were considered in this discussion, the result generalises to any number of baselines.

3.7.3 Number of Baselines

For an array of antennas, the position of one antenna is usually arbitrarily chosen to be the reference position. All antenna positions and outputs are then defined relative to this reference. By convention, the reference antenna is assumed to be the first antenna.

For a K-antenna interferometer, a simple set of interferometer baselines can be formed by taking the first antenna as the reference and then using the outputs of the subsequent antennas to form $K-1$ independent interferometer baselines as depicted in Figure 3.17. In this case, the set of measured phase delays will be

$$\Psi_{\text{simple}} = \left\{\tilde{\psi}_{21}, \tilde{\psi}_{31}, \ldots, \tilde{\psi}_{K1}\right\}, \tag{3.127}$$

which correspond to the simple set of interferometer baselines, D_{simple}, where

$$D_{\text{simple}} = \{d_{21}, d_{31}, d_{41}, \ldots, d_{K1}\}. \tag{3.128}$$

In [70], it was shown that there is a small, but statistically significant, performance gain by considering an extended set of interferometer baselines that contains all of the unique piecewise combinations of baselines which are formed when each antenna is successively

used as the reference as depicted in Figure 3.18. In this case, $K(K-1)/2$ interferometer baselines can be formed and the extended set of measured phase delays will be

$$\Psi_{\text{extended}} = \left\{ \tilde{\psi}_{21}, \tilde{\psi}_{31}, \tilde{\psi}_{41}, \ldots, \tilde{\psi}_{K1}, \tilde{\psi}_{32}, \tilde{\psi}_{42}, \ldots, \tilde{\psi}_{K2}, \ldots \tilde{\psi}_{K,K-1} \right\}, \tag{3.129}$$

which corresponds to the extended set of interferometer baselines, D_{extended}, where

$$D_{\text{extended}} = \{ d_{21}, d_{31}, d_{41}, \ldots, d_{K1}, d_{32}, d_{42}, \ldots, d_{K2}, \ldots, d_{K,K-1} \}. \tag{3.130}$$

Since the ambiguity resolution methods discussed in the subsequent discussions are equally valid for the simple and extended set of interferometer baselines, the algorithms will be generically discussed in terms of M interferometer baselines which correspond to the antenna separations, $d_1, d_2, \ldots, d_M$. For the simple set of baselines, there are $M = K - 1$ interferometer baselines and the antenna separations are given by D_{simple}. For the extended set of baselines, there are $M = K(K-1)/2$ interferometer baselines and the antenna separations are given by D_{extended}.

3.7.4 Maximum Likelihood Estimator

The maximum likelihood estimator (MLE) for the AOA using a non-uniform linear array is derived in Appendix A.2.1. For a M baseline interferometer, the maximum likelihood estimate of the AOA is given by

$$\hat{\theta} = \overset{\text{argmax}}{\theta_s} J_{\text{MLE}}(\theta_s), \tag{3.131}$$

where

$$J_{\text{MLE}}(\theta_s) = \sum_{m=1}^{M} \cos\left(\tilde{\psi}_m - \psi_m(\theta_s) \right), \tag{3.132}$$

where $\tilde{\psi}_m \in [-\pi, \pi]$ is the measured, ambiguous phase delay and $\psi_m(\theta_s)$ is the unambiguous phase delay corresponding to a search angle, θ_s. The MLE algorithm can be interpreted as a grid search algorithm that looks for the angle, θ_s, whose corresponding set of phase delays best match the measured data. The search angle, θ_s, is a parameter controlled by the AOA estimation algorithm and is not to be confused with the signal's AOA, θ. By using baselines that are not integer multiples of each other, the measured, ambiguous phase delays are guaranteed to be unique for each signal AOA, θ. When $\theta_s = \theta$, the summation produces a large peak that can be used to indicate the AOA of the signal.

In general, the number of search angles, G, can be arbitrarily large or small and is determined by the desired search range and resolution. For example, if the algorithm searches over angles between $[-90°, 90°]$ with an equal resolution of $1°$, then $G = 181$. If a $5°$ resolution is tolerable, then $G = 37$. However if a $0.1°$ resolution is required, then $G = 1801$. Furthermore, there is no requirement that the search angles be equi-spaced, or that they cover the full interval between $[-90°, 90°]$. For example, it may be desirable to monitor the interval $[-10°, 10°]$ with a $0.1°$ resolution and the intervals $[-60°, -10°)$ and $(10°, 60°]$ with a $5°$ resolution, and so in this case scenario $G = 221$.

The MLE algorithm described in this section only considers an interferometric implementation. Maximum likelihood estimators using array processing and subspace approximations will be discussed in Chapter 5.

Optimisation Using Newton's Method

Since the MLE algorithm is a grid search algorithm, the search space is quantised to a discrete set of possibilities and so quantisation errors can occur if the true AOA lies between two grid points. In practice, optimisation methods, such as Newton's Method [2, 71], gradient descent [2], or interpolation methods are often used to reduce, or even eliminate, the quantisation error. In this thesis, Newton's Method, as described in [71], will be used to refine the AOA estimate as follows

$$\hat{\theta}^{(\gamma+1)} = \hat{\theta}^{(\gamma)} - \frac{J'_{\text{MLE}}(\hat{\theta}^{(\gamma)})}{J''_{\text{MLE}}(\hat{\theta}^{(\gamma)})}, \tag{3.133}$$

where $J'_{\text{MLE}}(\hat{\theta}^{(\gamma)})$ and $J''_{\text{MLE}}(\hat{\theta}^{(\gamma)})$ represent the first and second derivatives of the maximum likelihood cost function $J_{\text{MLE}}(\hat{\theta}^{(\gamma)})$ with respect to $\theta^{(\gamma)}$, Γ is the number of iterations, $\gamma = 1, 2, \ldots, \Gamma$, and the initial estimate is set to the grid search estimate that corresponds to the maximum output of the maximum likelihood cost function. The optimisation algorithm is performed until a specified maximum number of iterations has been completed or until the difference between iterative estimates falls below a specified tolerance, i.e. $|\hat{\theta}^{(\gamma+1)} - \hat{\theta}^{(\gamma)}| \leq \delta\theta_{\text{tol}}$, where $\delta\theta_{\text{tol}}$ is the chosen tolerance. For good initial estimates that are close to the true AOA, the actual number of iterations may be significantly less than the maximum number of iterations.

For the maximum likelihood cost function, the first and second derivatives of $J_{\text{MLE}}(\hat{\theta}^{(\gamma)})$ are given by

$$J'_{\text{MLE}}(\hat{\theta}^{(\gamma)}) = \sum_{m=1}^{M} \sin\left(\tilde{\psi}_m - \psi_m(\theta)\right) \psi'_m(\theta), \tag{3.134}$$

$$J''_{\text{MLE}}(\hat{\theta}^{(\gamma)}) = -\sum_{m=1}^{M} \cos\left(\tilde{\psi}_m - \psi_m(\theta)\right) \psi'_m(\theta)^2 + \sin\left(\tilde{\psi}_m - \psi_m(\theta)\right) \psi_m(\theta), \tag{3.135}$$

where $\psi'_m(\theta)$ is the first derivative of $\psi_m(\theta)$ and is given by

$$\psi'_m(\theta) = \frac{2\pi f d_m}{c} \cos\theta. \tag{3.136}$$

It is important to note that the cost function $J_{\text{MLE}}(\hat{\theta}^{(\gamma)})$ may contain many peaks and that Newton's Method only finds the closest local peak. This suggests that if the initial estimate is closer to one of the sidelobes than the main lobe, then the output of Newton's Method may estimate the AOA erroneously. This further suggests that the initial estimate used to initialise Newton's Method (i.e. the grid search estimate) must be accurate enough so that it lies within the main lobe of the cost function.

Algorithm Complexity

A typical execution of the MLE algorithm requires that the phase delays of each interferometer baseline to be estimated. Assuming that a FFT is performed to estimate the phase delays in the frequency domain, as described by (3.17), the algorithm complexity to estimate the phase delays is $O(\Phi + M)$, where $\Phi = KN \log_2 N$ represents the number

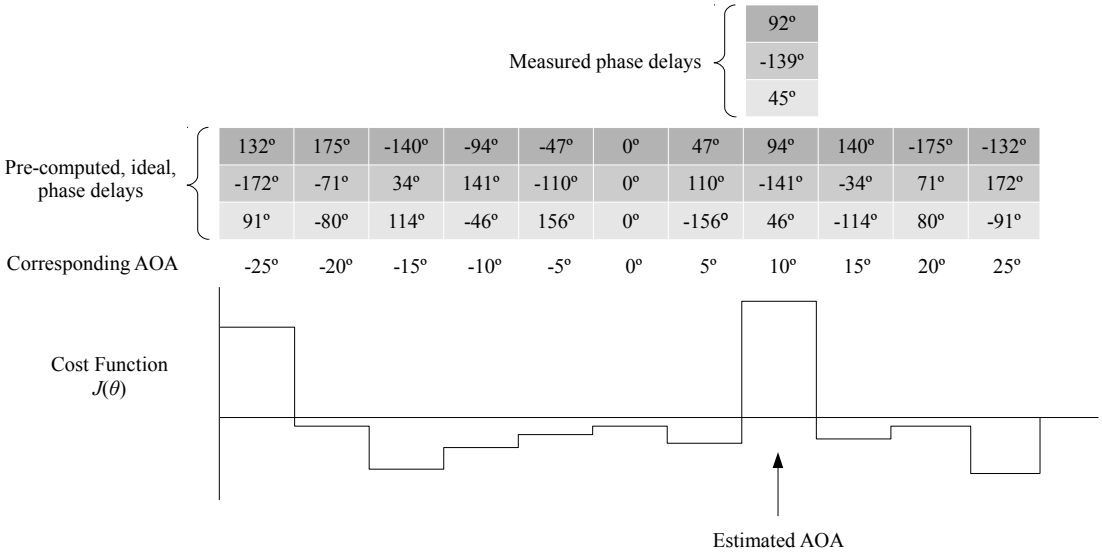

Figure 3.19: The correlative interferometer searches for the set of true phase delays that best match the measured, ambiguous phase delays.

of operations to perform the FFT on each antenna output, K is the number of antennas, N is the number of samples and M is the number of baselines.

The next part of the MLE algorithm involves the grid search. For each search angle, the value of the cost function described by (3.132) is performed. This computation has an approximate algorithm complexity of $O(M)$. For G search angles, the approximate algorithm complexity of the grid search is $O(GM)$.

Finally, Newton's Method is used to refine the grid search estimate. For each iteration, Newton's Method requires calculating the derivatives of the array output from (3.134) and (3.135) which are $O(M)$ operations. For Γ iterations, the approximate algorithm complexity of the optimisation is then $O(2\Gamma M)$.

The total approximate algorithm complexity of the MLE algorithm is therefore $O(\Phi + M(G + 2\Gamma + 1))$. It should be noted that this expression for the algorithm complexity is effectively an approximation of the number of loops performed by the algorithm. It does not represent a detailed analysis for all operations in the algorithm. Furthermore, it does not distinguish between the speed of individual operations, such as addition and multiplication.

3.7.5 Correlative Interferometers

Correlative interferometers resolve the ambiguities by correlating, or "phase-matching", the set of measured, ambiguous phase delays with a set of true, unambiguous phase delays. The search angle that corresponds to the set of true phase delays that best match the data is considered the AOA of the signal. The operation of a correlative interferometer is illustrated graphically in Figure 3.19.

For a M baseline interferometer, the correlative interferometer estimates the AOA by

searching for the maximum of the correlation cost function, $J(\theta)$, as follows,

$$\hat{\theta} = \underset{\theta_s}{\text{argmax}} J(\theta_s). \tag{3.137}$$

Several correlation cost functions have been proposed in the literature [70, 72–75], including:

- The Cosine (COS) Function Criterion

$$J_{\cos}(\theta_s) = \sum_{m=1}^{M} \cos\Big(\tilde{\psi}_m - \psi_m(\theta_s)\Big), \tag{3.138}$$

- Least-Squares (LS) Criterion

$$J_{\text{LS}}(\theta_s) = -\sum_{m=1}^{M} \Big(\Big[\tilde{\psi}_m - \psi_m(\theta_s)\Big]_{2\pi}\Big)^2, \tag{3.139}$$

where $\tilde{\psi}_m \in [-\pi, \pi]$ is the measured, ambiguous phase delay and $\psi_m(\theta_s)$ is the unambiguous phase delay corresponding to the search angle θ_s. Note that (3.132) is identical to (3.138) and so the maximum likelihood estimator discussed in Section 3.7.4 is essentially a specific implementation of a correlative interferometer.

Example 3.5
Consider the same two-baseline interferometer as Example 3.3, where $d_1 = 3\lambda/2$, $d_2 = 7\lambda/2$, $\lambda = 16.67$ mm and $f = 18$ GHz. Figure 3.20 shows the normalised cosine and least-squares cost functions when $\theta = 23.42°$ for a noiseless signal. Given a cost function, $J(\theta_s)$, which has a maximum and minimum value of $J_{\max}$ and $J_{\min}$ respectively, the normalised cost function, $J_{\text{norm}}(\theta_s)$, can be written as

$$J_{\text{norm}}(\theta_s) = \frac{J(\theta_s) - J_{\min}}{J_{\max} - J_{\min}}. \tag{3.140}$$

This example shows that cosine and least-squares cost functions both have a single correlation peak at $\theta = 23.42°$ and exhibit high sidelobes at other angles. High sidelobes can occur with correlative interferometry when a particular array geometry measures similar phase delays at different angles. In this example, while the sidelobes occur at the same angles in both functions, the cosine cost function consistently has lower sidelobes than the least squares cost function. This suggests that while both cost functions can be used to correctly estimate the AOA of the signal, the cosine cost function is expected to be more robust against noise due to its consistently lower sidelobes. ∎

Optimisation Using Newton's Method

Since the correlative interferometer is also a grid search algorithm, Newton's Method, as described by (3.133), can also be used to remove the quantisation errors that arise due to a discrete search resolution. Since the cosine cost function is identical to the

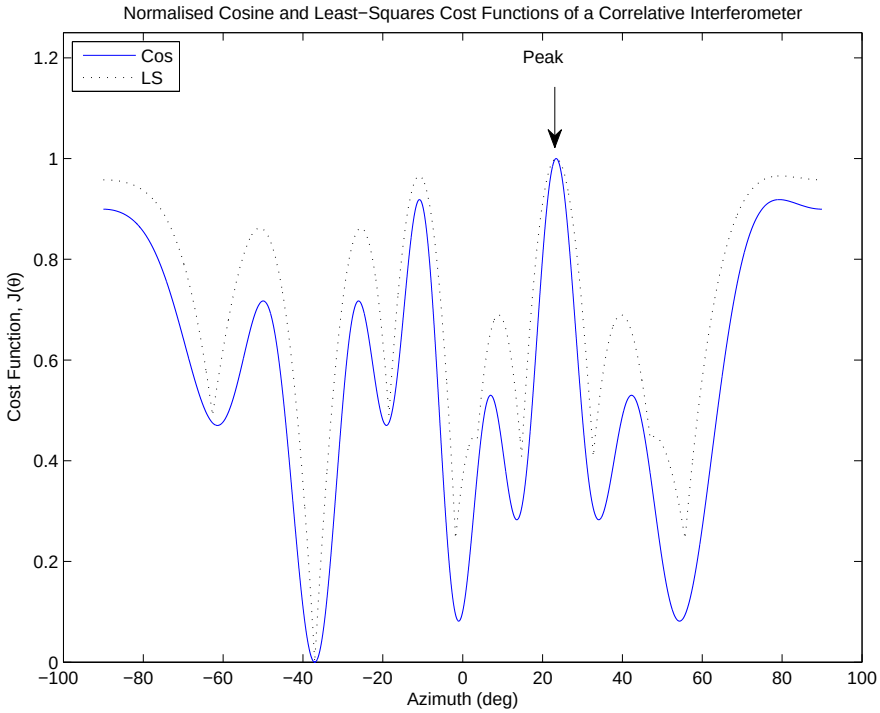

Figure 3.20: Example of the cosine and least squares cost functions for a correlative interferometer. These cost functions have been normalised to the same scale for visual comparison.

maximum likelihood cost function, the first and second derivatives of $J_{\cos}(\hat{\theta}^{(\gamma)})$ are also given by (3.134) and (3.135) respectively.

For the least squares cost function, the first and second derivatives of $J_{\mathrm{LS}}(\hat{\theta}^{(\gamma)})$ can be shown to be

$$J'_{\mathrm{LS}}(\hat{\theta}^{(\gamma)}) = 2\sum_{m=1}^{M}\left[\tilde{\psi}_m - \psi_m(\theta_s)\right]_{2\pi}\psi'_m(\theta), \tag{3.141}$$

$$J''_{\mathrm{LS}}(\hat{\theta}^{(\gamma)}) = -2\sum_{m=1}^{M}\psi'_m(\theta)^2 + \left[\tilde{\psi}_m - \psi_m(\theta_s)\right]_{2\pi}\psi_m(\theta_s). \tag{3.142}$$

Algorithm Complexity

In a similar manner to the maximum likelihood estimator, the correlative interferometer has an approximate algorithm complexity of $O(\Phi + M(G + 2\Gamma + 1))$, where $\Phi = KN\log_2 N$, K is the number of antennas, N is the number of samples, M is the number of baselines, G is the number of search angles, and Γ is the number of iterations used by Newton's Method.

3.7.6 Common Angle Search

Exhaustive Search

An intuitive and straightforward algorithm to resolve the AOA ambiguities is to explicitly search for the unique common AOA among all of the AOA ambiguities from each

baseline. However, due to noise, it will be unlikely that the any of the ambiguous AOAs in each baseline will exactly match, and so the common angle search (CAS) algorithm becomes a search for the closest matching set of ambiguous AOAs.

Since there is a unique relationship between the ambiguous AOAs and the ambiguous phase delays, the CAS algorithm can be formulated as a search for the common "normalised phase delays" (i.e. the ratio of the ambiguous phase delay and the interferometer baseline). This is a slightly more efficient implementation since it avoids the computationally expensive arcsine function.

Generalising (3.116), the phase delay relationship of a system of M interferometer baselines can be written as follows,

$$\frac{2\pi f}{c}\sin\theta = \frac{\tilde{\psi}_1 + \rho_1 2\pi}{d_1} = \frac{\tilde{\psi}_2 + \rho_2 2\pi}{d_2} = \cdots = \frac{\tilde{\psi}_M + \rho_M 2\pi}{d_M}. \tag{3.143}$$

This expression suggests that at a given AOA, there will exist a particular combination of ambiguity numbers that will satisfy the above equality. Since it is assumed that the interferometer baselines are not integer multiples of each other, it is guaranteed that there will only be AOA estimate that is common among the ambiguities of all of the baselines, and hence one unique combination of ambiguity numbers that will satisfy the equality.

Consider that the d_m interferometer baseline has a set of possible ambiguity numbers, $\Upsilon_m(\tilde{\psi}_m)$, that are constrained by (3.34) as follows

$$\Upsilon_m(\tilde{\psi}_m) = \left\{ \left\lceil -\frac{f d_m}{c} - \frac{\tilde{\psi}_m}{2\pi} \right\rceil, \ldots, -2, -1, 0, 1, 2, \ldots, \left\lfloor \frac{f d_m}{c} - \frac{\tilde{\psi}_m}{2\pi} \right\rfloor \right\}, \tag{3.144}$$

where $m = 1, 2, \ldots, M$. The exhaustive set of possible combinations of ambiguity numbers, $\Omega_{\text{exhaustive}}$, can then be written as the Cartesian product of the elements of $\Upsilon_m(\tilde{\psi}_m)$ for each baseline as follows,

$$\Omega_{\text{exhaustive}} = \Upsilon_1(\tilde{\psi}_1) \odot \Upsilon_2(\tilde{\psi}_2) \odot \cdots \odot \Upsilon_M(\tilde{\psi}_M), \tag{3.145}$$

where $\odot$ denotes the Cartesian product operator. Each element in $\Omega_{\text{exhaustive}}$ is a vector, $\boldsymbol{\rho}$, that represents one unique combination of the ambiguity numbers from each interferometer baseline. The total number of elements contained in $\Omega_{\text{exhaustive}}$ is given by

$$Q_{\text{exhaustive}} = \prod_{m=1}^{M} N^a_{\Upsilon_m(\tilde{\psi}_m)}, \tag{3.146}$$

where

$$N^a_{\Upsilon_m(\tilde{\psi}_m)} = \text{round}\left[\frac{2 f d_m}{c}\right] \tag{3.147}$$

represents the number of ambiguities contained in $\Upsilon_m(\tilde{\psi}_m)$ for the d_m baseline as specified by (3.147).

The CAS algorithm can then be described as the minimisation of a cost function, $J_{\text{CAS}}(\boldsymbol{\rho}^q)$, as follows,

$$\hat{\theta} = \underset{\boldsymbol{\rho}^q \in \Omega_{\text{exhaustive}}}{\arg\min} J_{\text{CAS}}(\boldsymbol{\rho}^q), \tag{3.148}$$

where

$$J_{\text{CAS}}(\boldsymbol{\rho}^q) = \sum_{m=1}^{M} \left| \frac{\tilde{\psi}_m + \rho_m^q 2\pi}{d_m} - \frac{\tilde{\psi}_M + \rho_M^q 2\pi}{d_M} \right|, \tag{3.149}$$

$$= \sum_{m=1}^{M} \frac{1}{d_m} \left| \tilde{\psi}_m - \frac{d_m}{d_M}\tilde{\psi}_M - 2\pi \left(\frac{d_m}{d_M}\rho_M^q - \rho_m^q \right) \right|, \tag{3.150}$$

and $\boldsymbol{\rho}^q = \{\rho_1^q, \rho_2^q, \ldots, \rho_M^q\}$ is a vector representing the q-th combination of ambiguity numbers from $\Omega_{\text{exhaustive}}$, ρ_m^q represents the ambiguity number of the d_m baseline for the q-th combination, and $q = 1, 2, \ldots, Q_{\text{exhaustive}}$. Once the set of ambiguity numbers that minimises $J_{\text{CAS}}(\boldsymbol{\rho}^q)$ has been found, the AOA can be estimated using the longest baseline to provide the best AOA estimation performance in noise.

While the CAS algorithm and correlative interferometers are both search-based algorithms, they differ because they search over different parameters. The correlative interferometer searches over all possible AOAs while the CAS algorithm searches over all possible ambiguities of the measured phase delays. The search space of the CAS algorithm is generally smaller than the correlative interferometer.

Example 3.6
Consider the same two-baseline interferometer described in Example 3.3, where $d_1 = 3\lambda/2$, $d_2 = 7\lambda/2$, $\lambda = 16.67$ mm, $f = 18$ GHz, and $\theta = 23.42°$. At this AOA, the measured, ambiguous phase delays are

$$\tilde{\psi}_1 = [\psi_1]_{2\pi} = [214.63°]_{2\pi} = -145.37°, \quad \text{where } \rho_1 = 1, \tag{3.151}$$

$$\tilde{\psi}_2 = [\psi_2]_{2\pi} = [500.81°]_{2\pi} = 140.81°, \quad \text{where } \rho_2 = 1. \tag{3.152}$$

In this example, equations (3.144) and (3.147) suggest that the d_1 and d_2 baselines will have 3 and 7 ambiguities respectively, where

$$\Upsilon_1(\tilde{\psi}_1) = \{-1, 0, 1\}, \tag{3.153}$$

$$\Upsilon_2(\tilde{\psi}_2) = \{-3, -2, -1, 0, 1, 2, 3\}, \tag{3.154}$$

and so a total of $Q_{\text{exhaustive}} = 21$ unique combinations of ρ_1 and ρ_2 can be defined. These combinations are listed in Table 3.3 and the corresponding cost function is illustrated in Figure 3.21. This figure shows that the minimum of the cost function occurs for the 19-th combination of ambiguity numbers which corresponds to $\rho_1 = 1$ and $\rho_2 = 1$. These estimated ambiguity numbers match the true ambiguity numbers in (3.151) and (3.152) and so the ambiguity is successfully resolved in this example. ∎

Subset Search

The performance of the exhaustive phase delay search can be significantly improved by recognising that only a subset of possible combinations of ambiguity numbers will

Combination	$\boldsymbol{\rho}^q$	
q	ρ_1	ρ_2
1	-1	-3
2	-1	-2
3	-1	-1
4	-1	0
5	-1	1
6	-1	2
7	-1	3
8	0	-3
9	0	-2
10	0	-1
11	0	0
12	0	1
13	0	2
14	0	3
15	1	-3
16	1	-2
17	1	-1
18	1	0
19	1	1
20	1	2
21	1	3

Table 3.3: Possible combinations of ρ_1 and ρ_2.

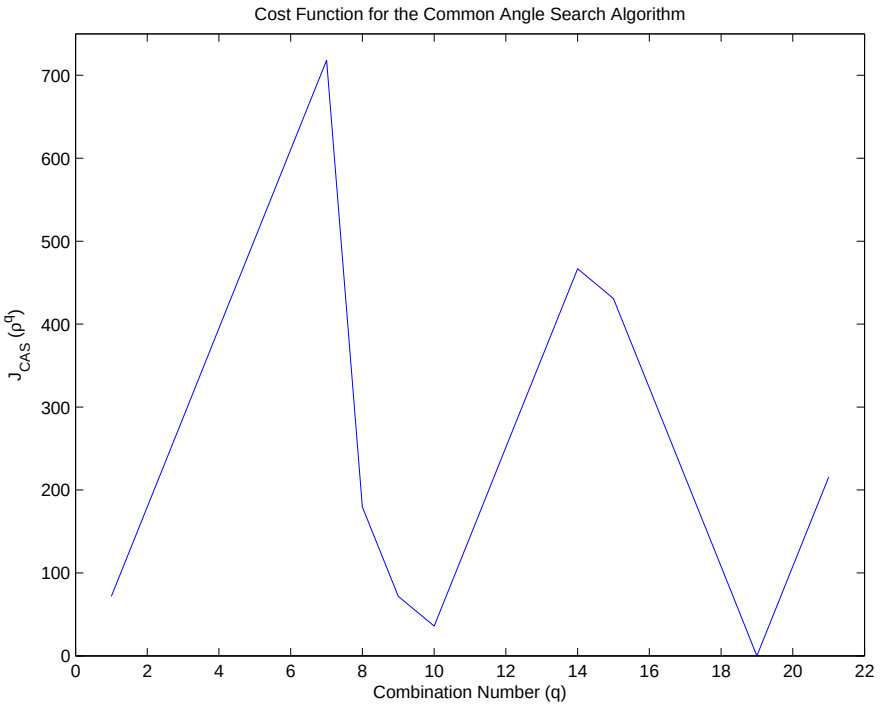

Figure 3.21: Example of the cost function for the exhaustive CAS algorithm.

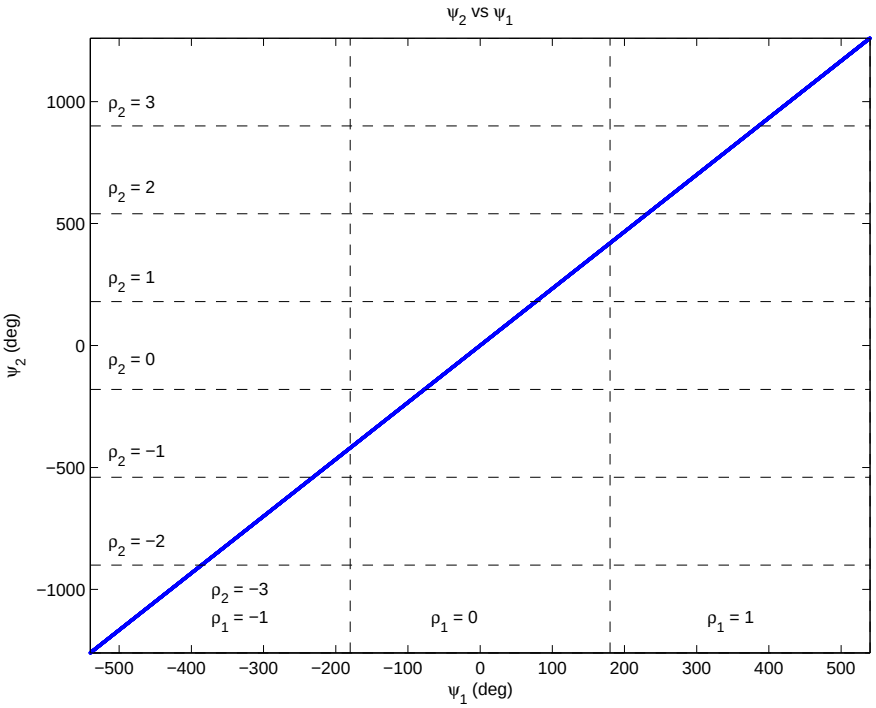

Figure 3.22: Plot of the unambiguous phase delays of the d_2 baseline against the d_1 baseline.

correspond to a valid AOA. Let Ω_{subset} be a subset of $\Omega_{\text{exhaustive}}$ which only contain the combinations of ambiguity numbers that correspond to a valid AOA in the interval $\theta \in [-90°, 90°]$. In general, the number of elements in Ω_{subset} will be smaller than the number of elements in $\Omega_{\text{exhaustive}}$, i.e.

$$Q_{\text{subset}} \leq Q_{\text{exhaustive}}, \tag{3.155}$$

where Q_{subset} is the number of elements in Ω_{subset}.

Example 3.7

Figure 3.22 plots the unambiguous phase delays of the d_2 baseline as a function of the unambiguous phase delays of the d_1 baseline, i.e. ψ_2 vs ψ_1. Each point on this line corresponds to a unique azimuth between $\theta \in [-90°, 90°]$. The corresponding ambiguity numbers, ρ_1 and ρ_2, for each phase delay are also shown. This figure shows that while there are a total of 21 possible combinations of ambiguity numbers, only 9 of these combinations will correspond to a valid AOA estimate. Written as an ordered pair of the form (ρ_1, ρ_2), these combinations are $(-1, -3)$, $(-1, -2)$, $(-1, -1)$, $(0, -1)$, $(0, 0)$, $(0, 1)$, $(1, 1)$, $(1, 2)$ and $(1, 3)$. By only considering the subset of valid combinations, the number of combinations can be reduced by

$$\frac{21 - 9}{21} \times 100\% = 57.1\%. \quad \blacksquare \tag{3.156}$$

Algorithm Complexity

Like the correlative interferometers, a typical execution of the CAS algorithm requires that the phase delays of each interferometer baseline to be estimated. Assuming that a

FFT is performed to estimate the phase delays in the frequency domain, as described by (3.17), the algorithm complexity to estimate the phase delays is $O(\Phi + M)$, where $\Phi = KN \log_2 N$ represents the number of operations to perform the FFT on each antenna output, K is the number of antennas, N is the number of samples and M is the number of baselines.

The next part of the CAS algorithm involves the grid search for the combination of ambiguity numbers, i.e. $\boldsymbol{\rho}^q$, that minimises the cost function $J_{\text{CAS}}(\boldsymbol{\rho}^q)$. For each $\boldsymbol{\rho}^q$, the computation of the cost function has an algorithm complexity of $O(M)$. The approximate algorithm complexity of the entire grid search is $O(MQ_{\text{subset}})$, where Q_{subset} is the number of ambiguity number combinations that correspond to a valid AOA. The total approximate algorithm complexity of the CAS algorithm is therefore $O(\Phi + M(Q_{\text{subset}} + 1))$.

3.7.7 Line Fitting

Recall from (3.117) that the relationship between the measured phase delays for two interferometer baselines can be written as

$$\tilde{\psi}_k = \frac{d_k}{d_m}\tilde{\psi}_m + 2\pi\left(\frac{d_k}{d_m}\rho_m - \rho_k\right). \tag{3.157}$$

This expression is essentially the equation of a line of the form $y = \alpha x + \beta$, where the dependent value is $y = \tilde{\psi}_k$, the independent value is $x = \tilde{\psi}_m$, the slope is $\alpha = d_k/d_m$ and the y-axis intercept is $\beta = 2\pi\left((d_k/d_m)\rho_m - \rho_k\right)$. For each combination of ambiguity numbers, the slope remains the same but the y-axis intercept changes. This suggests that there will be a separate line segment for every combination of ambiguity numbers which correspond to a valid AOA. In the presence of noise, the ambiguity resolution algorithm becomes a search for the line segment that is closest to the point representing the measured phase delays.

Example 3.8
Consider the same two-baseline interferometer as described in Example 3.3, where $d_1 = 3\lambda/2$, $d_2 = 7\lambda/2$, $\lambda = 16.67$ mm, $f = 18$ GHz and $\theta = 23.42°$. Figure 3.23 plots the line segments that are formed by the measured, ambiguous phase delays of the d_2 baselines when plotted as a function of the measured, ambiguous phase delays of the d_1 baseline, i.e. $\tilde{\psi}_2$ vs $\tilde{\psi}_1$. Due to phase wrapping, the phase delay relationship between ψ_2 and ψ_1 now correspond to 9 different line segments. Each point on one of these line segments corresponds to a unique azimuth between $\theta \in [-90°, 90°]$.

Recall that for $\theta = 23.42°$, the measured, ambiguous phase delays are

$$\tilde{\psi}_1 = [\psi_1]_{2\pi} = [214.63°]_{2\pi} = -145.37° \quad \text{where } \rho_1 = 1, \tag{3.158}$$
$$\tilde{\psi}_2 = [\psi_2]_{2\pi} = [500.81°]_{2\pi} = 140.81° \quad \text{where } \rho_2 = 1. \tag{3.159}$$

Plotting the point $(\tilde{\psi}_1, \tilde{\psi}_2) = (-145.37°, 140.81°)$ on Figure 3.23 (as indicated by the red circle) shows that this point falls on the line segment corresponding to $\rho_1 = 1$ and $\rho_2 = 1$. These ambiguity numbers match the true

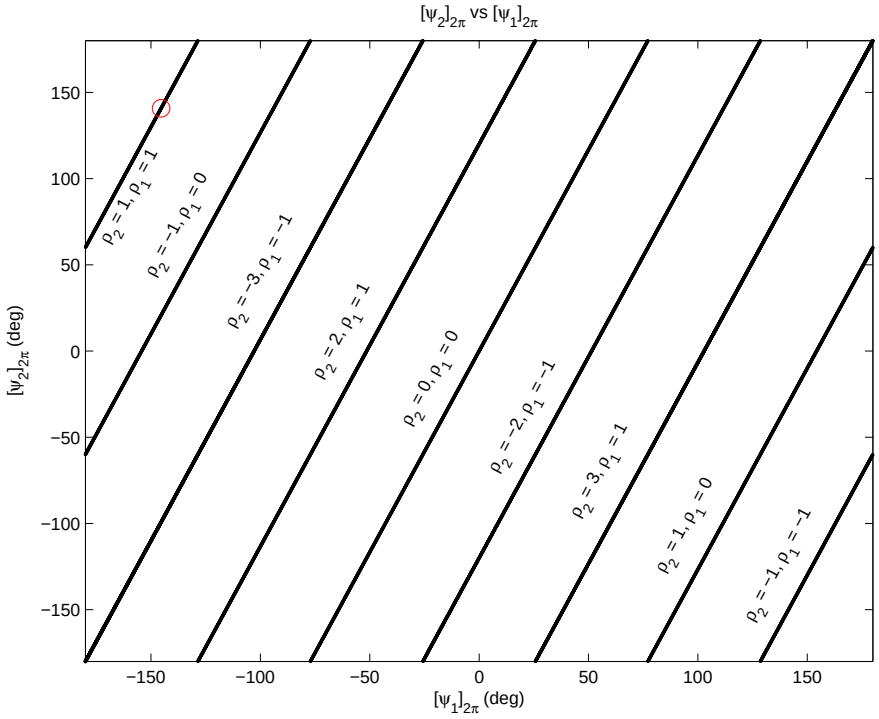

Figure 3.23: Plot of the ambiguous phase delays of the d_2 baseline against the d_1 baseline.

ambiguity numbers in (3.158) and (3.159) and so the ambiguity is successfully resolved in this example. ∎

The key to the line fitting algorithm is to correctly determine the line segment that the point representing the measured phase delays lies on. In practice, noise effects will generally mean that the point will not lie exactly on any line segment. As a result, it is possible that the wrong line segment is chosen, particularly at low SNR. When this occurs, the AOA error is significant because the ambiguity numbers corresponding to adjacent line segments are not incremental.

In order to avoid large AOA estimation errors, the line fitting algorithm works best for relatively short baselines which have few line segments. If more than two baselines are available, the line fitting algorithm can be performed on the shortest baselines and then successively applied to the longer baselines. By omitting any ambiguities resolved from the shorter baselines, the number of ambiguities in the longer baselines can be reduced. Once the estimated ambiguity numbers have been found, the AOA can then be estimated using the longest baseline to provide the best AOA estimation performance in noise.

Mathematical Approach

The search for the most appropriate line segment can be formulated mathematically as a search for the line segment with the shortest Euclidean distance to the measured phase delay point. For a point (x_1, y_1) and a line $y = \alpha x + \beta$, the shortest Euclidean distance,

$J_{\text{Euclidean}}$, between the point and the line is given by

$$J_{\text{Euclidean}} = \frac{|y_1 - \alpha x_1 - \beta|}{\sqrt{\alpha^2 + 1}}. \tag{3.160}$$

Writing the phase delay measurements from the d_m and d_k baseline as an ordered pair, $(x_1, y_1) = (\tilde{\psi}_m, \tilde{\psi}_k)$, the Euclidean distances from this point to each of the line segments specified by (3.157) can be written as

$$J_{\text{line}}(\boldsymbol{\rho}^q) = \frac{d_m}{\sqrt{d_k^2 + d_m^2}} \left| \tilde{\psi}_k - \frac{d_k}{d_m}\tilde{\psi}_m - 2\pi \left(\frac{d_k}{d_m}\rho_m^q - \rho_k^q \right) \right|, \tag{3.161}$$

where $\boldsymbol{\rho}^q = \{\rho_k^q, \rho_m^q\}$ is a vector representing the q-th combination of ambiguity numbers from Ω_{subset}, and ρ_k^q, ρ_m^q represents the ambiguity number of the d_k and d_m baselines for the q-th combination respectively. The mathematical line fitting algorithm can therefore be considered a search for the combination of ambiguity numbers, ρ_k and ρ_m, that minimises the cost function, $J_{\text{line}}(\boldsymbol{\rho}^q)$.

The line fitting ambiguity resolution algorithm can be extended to M interferometer baselines as follows,

$$J_{\text{line}}(\boldsymbol{\rho}^q) = \sum_{m=1}^{M} \frac{d_M}{\sqrt{d_m^2 + d_M^2}} \left| \tilde{\psi}_m - \frac{d_m}{d_M}\tilde{\psi}_M - 2\pi \left(\frac{d_m}{d_M}\rho_M^q - \rho_m^q \right) \right|, \tag{3.162}$$

where $\boldsymbol{\rho}^q = \{\rho_1^q, \rho_2^q, \ldots, \rho_M^q\}$. Comparing (3.162) with (3.150) shows that the cost functions for the line fitting and the CAS algorithms are quite similar. The difference between the two cost functions only lies in the scaling values, $d_M/\sqrt{d_m^2 + d_M^2}$ and $1/d_m$ respectively. Since these scaling values do not affect the relationship between the ambiguity numbers, ρ_m^q and ρ_M^q, the two cost functions are essentially scaled-equivalents.

Look-Up-Table Approach

The line fitting algorithm can be more efficiently implemented using a look-up-table. Figure 3.24 represents the plot in Figure 3.23 as a look-up-table with a 20° resolution to resolve the ambiguities of the d_2 baseline. In this algorithm, the measured phase delays are converted into an address that can be used to "look-up" the corresponding ambiguity numbers from the look-up table [76, 77].

Example 3.9
Consider the same two-baseline interferometer described in Example 3.3, where $d_1 = 3\lambda/2$, $d_2 = 7\lambda/2$, $\lambda = 16.67$ mm, $f = 18$ GHz and $\theta = 23.42°$. Recall that for $\theta = 23.42°$, the measured, ambiguous phase delays are

$$\tilde{\psi}_1 = [\psi_1]_{2\pi} = [214.63°]_{2\pi} = -145.37° \qquad \text{where } \rho_1 = 1, \tag{3.163}$$
$$\tilde{\psi}_2 = [\psi_2]_{2\pi} = [500.81°]_{2\pi} = 140.81° \qquad \text{where } \rho_2 = 1. \tag{3.164}$$

Since the look-up-table in Figure 3.24 represents the phases from −180° to 180° with a 20° resolution, the measured phase delays can be converted into

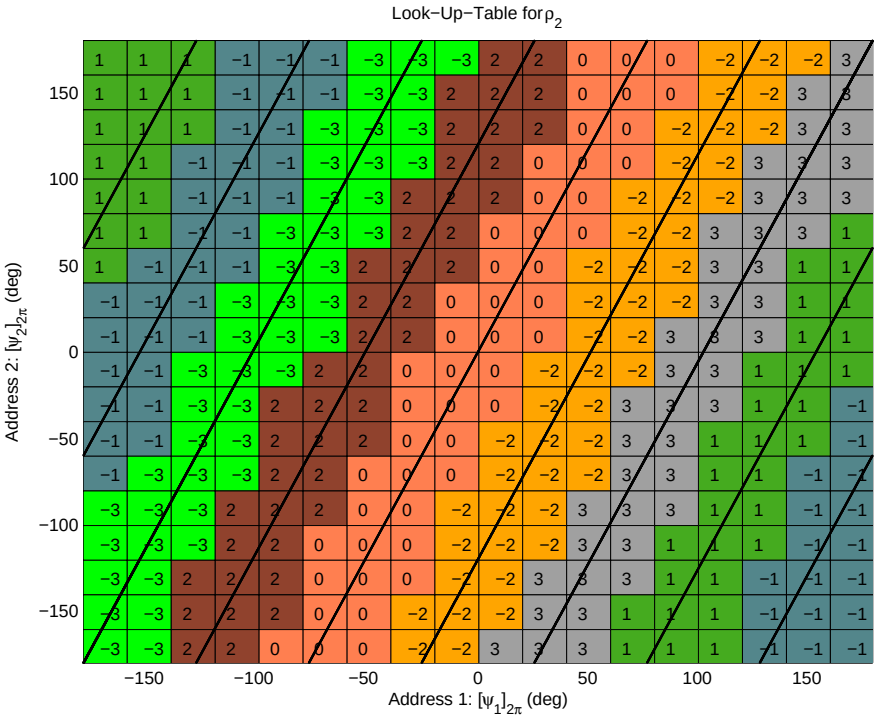

Figure 3.24: Look-up-table representation of Figure 3.23. Each entry in the look-up-table represents the corresponding ambiguity number for ρ_2 for a given combination of ambiguous phase delay measurements, $\tilde{\psi}_1$ and $\tilde{\psi}_2$. Note that the row address is counted upwards and the column address is counted rightwards.

an equivalent address as follows,

$$\tilde{\psi}_1 \implies \lceil(-145.37^\circ + 180^\circ)/20^\circ\rceil \equiv \text{Address 2}, \tag{3.165}$$

$$\tilde{\psi}_2 \implies \lceil(140.81^\circ + 180^\circ)/20^\circ\rceil \equiv \text{Address 17}, \tag{3.166}$$

Hence, by looking up the Column 2 for $\tilde{\psi}_1$ and the Row 17 for $\tilde{\psi}_2$ of the look-up-table, the estimated ambiguity number for the d_2 baseline is $\rho_2 = 1$ and so the ambiguity number is correctly resolved in this example. ∎

The advantage of the look-up table approach is that it can be readily implemented in digital hardware, particularly field-programmable-gate arrays (FPGAs). Since FPGAs are designed to rapidly access look-up-tables, this approach can be performed in a single addressing operation.

A significant drawback of this implementation is that the look-up table quantises the transition boundaries between two line segments. As previously mentioned, if the wrong ambiguity number is selected, the AOA errors are significant because the ambiguity numbers corresponding to adjacent line segments are not incremental. Consequently, the look-up table must be designed with adequate resolution to minimise the quantisation errors at the transition boundaries. This tends to result in very large look-up tables which in turn require large amounts of digital memory.

A separate look-up-table is required for each pair of interferometer baselines and each table will generally need to cover the full range of possible phase delay measurements for the two baselines. For a regular angular resolution, Δq, a $L \times L$ look-up table containing L^2 entries will be required, where

$$L = \left(\frac{2\pi}{\Delta q} + 1 \right)^2. \tag{3.167}$$

A look-up table with a 1° resolution will contain $130,321$ entires, while a look-up table with a 0.1° resolution will contain $12,967,201$ entries. Thus, the speed advantage of the look-up table implementation is offset by the hardware resources required to implement it.

Algorithm Complexity

Like the previous algorithms, the line fitting algorithm requires that the phase delays of each interferometer baseline to be estimated. Assuming that a FFT is performed to estimate the phase delays in the frequency domain, as described by (3.17), the algorithm complexity to estimate the phase delays is $O(\Phi + M)$, where $\Phi = KN \log_2 N$ represents the number of operations to perform the FFT on each antenna output, K is the number of antennas, N is the number of samples and M is the number of baselines.

Since the mathematical implementation of the line fitting algorithm is essentially a scaled equivalent of the CAS algorithm, the algorithm complexity of this approach is also $O(\Phi + M(Q_{\text{subset}} + 1))$, where Q_{subset} is the number of ambiguity number combinations that correspond to a valid AOA.

Furthermore, since the look-up-table implementation of the line fitting algorithm can resolve the ambiguity in a single addressing operation which has an algorithm complexity of $O(1)$, the total algorithm complexity of this approach is $O(\Phi + M + 1)$.

3.8 Performance Comparison

In this section, the RMS error performance of the ambiguity resolution algorithms discussed in Section 3.7 are evaluated using Monte Carlo simulations and compared against the square-root of the Cramér-Rao Lower Bounds (CRLB), or root-CRLB.

3.8.1 Cramér-Rao Lower Bound for a Non-Uniform Linear Array

The CRLB for AOA estimation using a non-uniform linear array is derived in Appendix A.3.1. For a K-antenna non-uniform linear array, the CRLB is given by

$$\text{CRLB}(\theta) = \frac{1}{\eta N} \cdot \left(\frac{c}{2\pi f \cos\theta} \right)^2 \cdot \frac{1}{2\bar{d}^2}, \tag{3.168}$$

where

$$\bar{d}^2 = \sum_{k=2}^{K} d_{k1}^2 - \frac{1}{K} \left(\sum_{k=2}^{K} d_{k1} \right)^2, \tag{3.169}$$

and d_{k1} is the distance of the k-th antenna relative to the first (reference) antenna.

Since some algorithms use all antennas and others only use two antennas in their final AOA estimation, two different CRLBs are defined to reflect the bounds obtained using (a) the widest antenna pair and (b) all available antennas. The square-root of these bounds shall be referred to as the "d_{K1}-root-CRLB" and "K-antenna root-CRLB" respectively.

3.8.2 Array Geometry

A 4-antenna non-uniform linear array will be used in these simulations. The antennas are assumed to be positioned at 0 mm, 106.0 mm, 464.1 mm and 937.5 mm respectively and are specifically chosen to correspond to the antenna positions used in an experiment that will be discussed in Chapter 8. Assuming the intercepted signal is a single-tone with a frequency of $f = 9410$ MHz, the interferometer baselines are effectively $d_{21} = 3.32\lambda$, $d_{31} = 14.56\lambda$ and $d_{41} = 29.41\lambda$. All antenna spacings are chosen to ensure that no baseline is an integer multiple of another baseline to allow the ambiguity resolution algorithms to be applied. This array geometry is depicted in Figure 3.25.

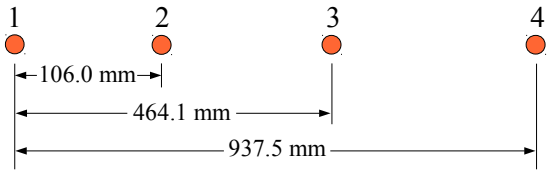

Figure 3.25: Array geometry for the performance comparison.

The performance comparison will initially be performed on a 3-antenna subset comprising of Antennas 1, 3 and 4. A second comparison will then be conducted using all four antennas to show that the performance of the algorithms can be improved at low SNR with additional auxiliary antennas (i.e. Antenna 2).

It should be noted that of all of the ambiguity resolution algorithms discussed in Section 3.7, only the MLE algorithm and correlative interferometers simultaneously exploit the phase delays from all available antennas in their final AOA estimation. The other ambiguity resolution algorithms use all available antennas for ambiguity resolution, but ultimately only use the phase delay from the widest antenna pair in its final AOA estimation.

As discussed in [70], there is a small, but statistically significant, performance improvement when all of the antenna outputs are used to estimate the AOA. This statement can be verified by considering the RMS errors of the interferometer as approximated by the square root of the CRLB at high SNR. For different antenna configurations, the expression for the RMS error is identical with the exception of the $\bar{d}^2$ term in (3.168). When only the widest antenna pair is used to perform the AOA estimation with this array geometry, it can be shown that

$$\bar{d}_{41}^2 = 432.47\lambda^2. \tag{3.170}$$

In comparison, when all four antennas are used to perform the AOA estimation,

$$\bar{d}^2_{\text{4-Ant}} \approx 528.88\lambda^2. \tag{3.171}$$

The RMS errors of the 4-antenna interferometer is therefore expected to be lower than the RMS errors of the 2-antenna interferometer constructed from the widest antenna pair by a factor of $\sqrt{528.88/432.47} \approx 1.223$. Due to this small but statistically significant performance gain, it is generally desirable to use all of the available antennas in the AOA estimation algorithm. In this performance comparison, it will be assumed that the correlative interferometers will construct all of the $M = K(K-1)/2$ possible baselines from a K antenna non-uniform linear array.

In general, it is expected that algorithms that use three antennas to estimate the AOA will also perform better than the d_{41} baseline interferometer. However, it is interesting to note that in this particular example, the $\bar{d}^2$ term for the 3-antenna array geometry is given by

$$\bar{d}^2_{\text{3-Ant}} \approx 432.49\lambda^2, \tag{3.172}$$

and so there will be a small, but barely noticeable, difference between the RMS error performance of the d_{41} baseline interferometer and the 3-antenna interferometer.

3.8.3 Monte Carlo Simulations

Monte Carlo simulations are used to evaluate the AOA estimation performance of each of the algorithms discussed in Section 3.7. These simulations assume that the intercepted signal is a single-tone with a frequency of $f = 9410$ MHz and so the interferometer baselines are effectively $d_{21} = 3.32\lambda$, $d_{31} = 14.56\lambda$ and $d_{41} = 29.41\lambda$.

The signal is assumed to arrive from an AOA of $\theta = 23.42^\circ$ and has an initial phase of $\varphi = 0^\circ$. For each noise realisation, it is assumed that $N = 2048$ digital samples are collected at a sample interval of $t_s = 750$ ps, which corresponds to a signal duration of 1.536 μs. The phase delays are estimated using the FFT maximum likelihood estimator implemented using a 2048-point FFT. It is assumed that no scalloping losses occur in these simulations. The hardware configuration and signal parameters are intentionally chosen to correspond to an experimental trial that will be discussed in Chapter 7 and Chapter 8.

RMS Error Comparison

Figure 3.26 to Figure 3.29 show the RMS error performance of each algorithm evaluated using $\mathcal{Q} = 10,000$ receiver noise realisations. Most of the algorithms discussed in Section 3.7 have been implemented with the exception of the mathematical line fitting algorithm. Consideration of this algorithm is omitted since it is functionally equivalent to the CAS algorithm. In these simulations, the correlative interferometers have been implemented using a look-up-table with a search resolution of 0.1° and the look-up-table line fitting (LF) algorithm is implemented with a 1° angular resolution. Newton's Method optimisation of the correlative interferometer grid search is allowed to perform a maximum of $\Gamma_{\max} = 100$ iterations and the convergence tolerance is set to $\delta\theta_{\text{tol}} = 1^\circ \times 10^{-5}$.

Figure 3.26 and Figure 3.27 show the RMS error performance of each algorithm using the 3-antenna array geometry. This figure verifies that there is no noticeable difference between the expected RMS errors (i.e. root-CRLB) of an AOA estimation algorithm if only the widest antenna pair or all three antennas is used to perform the AOA estimation. This figure also shows that the CAS and LF algorithms perform asymptotically well in the sense that they achieve the d_{41}-root-CRLB at SNRs above 8 dB and 9 dB respectively.

In this example, the performance of the correlative interferometers using the MLE and least-squares (LS) cost functions have an identical performance. Due to the discrete nature of the look-up table, the grid search of both correlative interferometers are unable to estimate the AOA beyond a resolution of 0.1° and hence consistently suffer from a quantisation error of 0.02° at SNRs above 3 dB. In this example, optimisation of the grid search estimates using Newton's Method is able to completely remove the effects of quantisation. While the maximum number of iterations was set to $\Gamma_{\max} = 100$ iterations, convergence of the AOA estimates generally occurred after $\Gamma_{\text{actual}} = 2$ iterations.

Figure 3.28 and Figure 3.29 show that with the inclusion of a fourth auxiliary antenna (i.e. Antenna 2), the SNR thresholds reduce significantly. In this example, the SNR threshold for the MLE and LS correlative interferometers and the CAS algorithm are all reduced to -11 dB. The SNR threshold for the LF algorithm is reduced to 1 dB. As expected, the correlative interferometers are able to achieve the 4-antenna root-CRLB while the other ambiguity resolution algorithms are only able to achieve the d_{41}-root-CRLB.

Relative Execution Time

In addition to computing the AOA accuracy of each algorithm, these Monte Carlo simulations also measured the average execution time of each algorithm. It should be noted that the absolute execution time of each algorithm is a system-dependent metric that is dependent on a number of factors, including

- the computing hardware used to run the simulations,
- the efficiency of the programming language, and
- the efficiency of the program code.

The *absolute* execution times are therefore a meaningless metric since a slow algorithm may simply be the result of slow computing hardware or inefficient programming. However, the *relative* execution time of each algorithm is still a useful indicator of the algorithm's relative computational speed.

Table 3.4 shows the average relative execution time of each algorithm while performing a single AOA estimation using the 4-antenna array geometry described in Section 3.8.2. These values have been normalised to the execution time of a so-called "SODA interferometer" that will be introduced in the next chapter. This normalisation is intentionally performed to allow a direct comparison of the relative execution time with the algorithms that will be introduced in the subsequent chapters. The algorithms are

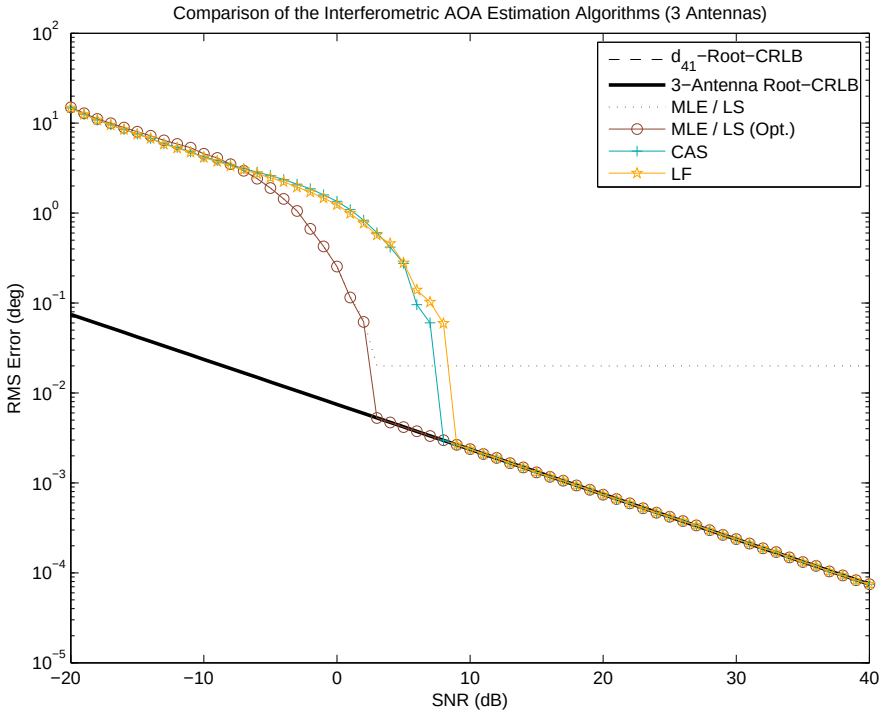

Figure 3.26: RMS error performance of each algorithm as a function of SNR. Simulation parameters: $K = 3$ antennas, $\theta = 23.42°$, $f = 9410$ MHz, $\varphi = 0°$, $N = 2048$ samples, $t_s = 750$ ps and $\mathcal{Q} = 10,000$ realisations. The "Opt." label indicates that Newton's Method optimisation has been performed.

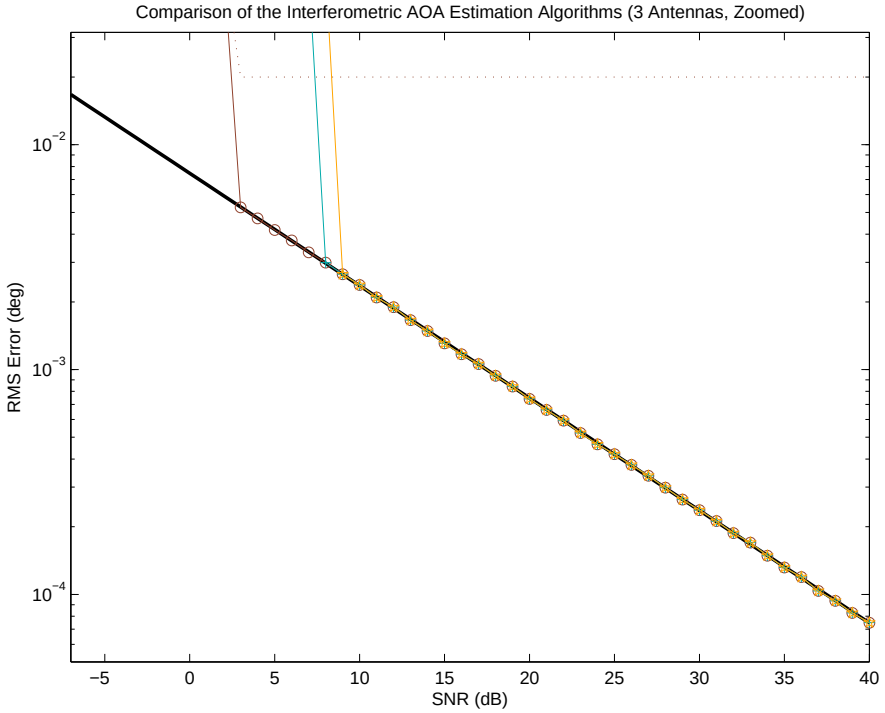

Figure 3.27: RMS error performance of each algorithm as a function of SNR. Simulation parameters: $K = 3$ antennas, $\theta = 23.42°$, $f = 9410$ MHz, $\varphi = 0°$, $N = 2048$ samples, $t_s = 750$ ps and $\mathcal{Q} = 10,000$ realisations.

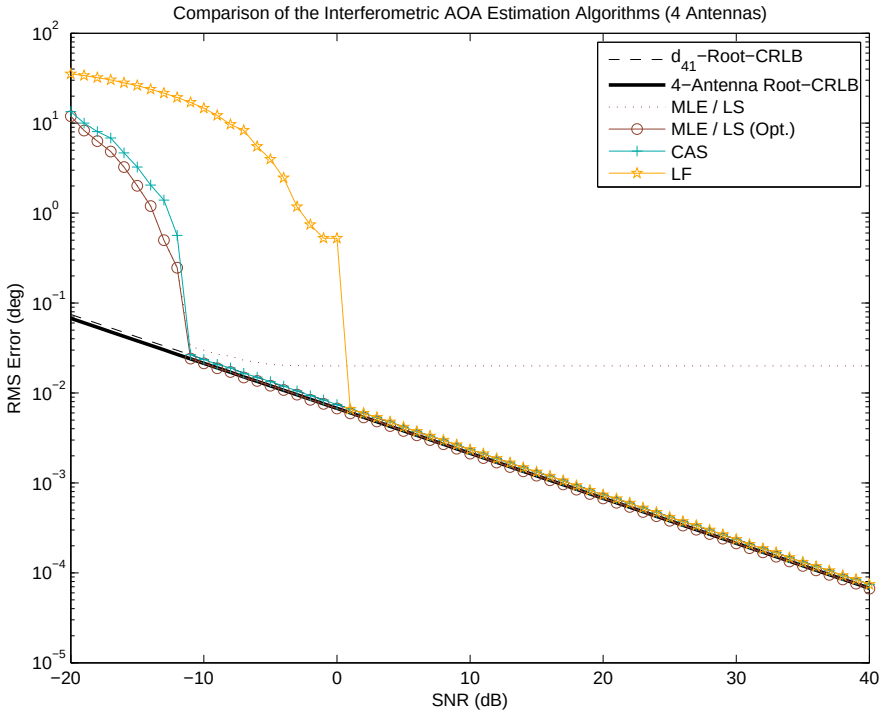

Figure 3.28: RMS error performance of each algorithm as a function of SNR. Simulation parameters: $K = 4$ antennas, $\theta = 23.42°$, $f = 9410$ MHz, $\varphi = 0°$, $N = 2048$ samples, $t_s = 750$ ps and $\mathcal{Q} = 10,000$ realisations. The "Opt." label indicates that Newton's Method optimisation has been performed.

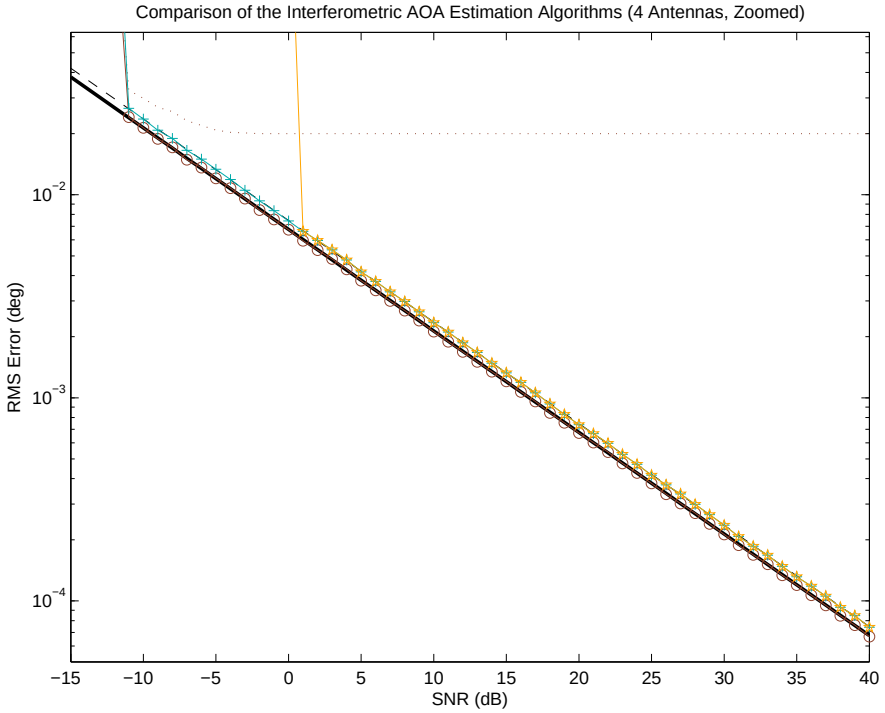

Figure 3.29: RMS error performance of each algorithm as a function of SNR. Simulation parameters: $K = 4$ antennas, $\theta = 23.42°$, $f = 9410$ MHz, $\varphi = 0°$, $N = 2048$ samples, $t_s = 750$ ps and $\mathcal{Q} = 10,000$ realisations.

Algorithm	Algorithm Complexity	Relative Time
LF	$O(\Phi + M + 1)$	1.03
CAS	$O(\Phi + M(Q_{\text{subset}} + 1))$	1.22
MLE / COS	$O(\Phi + M(G + 1))$	12.42
MLE / COS (Opt.)	$O(\Phi + M(G + 2\Gamma + 1))$	12.55
LS	$O(\Phi + M(G + 1))$	136.34
LS (Opt.)	$O(\Phi + M(G + 2\Gamma + 1))$	136.94

Table 3.4: Relative execution times for the conventional ambiguity resolution algorithms. The "Opt." label indicates that Newton's Method optimisation has been performed.

presented in the order of increasing execution time, i.e. from fastest to slowest.

This table verifies that the LF algorithm is the fastest conventional ambiguity resolution algorithm. The CAS algorithm has a comparable performance to the LF algorithm. The correlative interferometers are considerably slower with the MLE algorithm being approximately one order of magnitude slower and the LS algorithm approximately two orders of magnitude slower than the LF algorithm.

3.9 Other Considerations

3.9.1 Multiple Signals

The interferometers described in this chapter all assume that the phase delay between two antennas has the form specified by (3.10). However, this expression is only valid when a single signal is illuminating the antenna array. If two or more signals are simultaneously illuminating the antenna array, the output of each antenna will be a superposition of the signal waveforms and so the phase delay can no longer be represented by (3.10). In order to correctly estimate the AOA of each signal a method of isolating the individual phase delay from each signal is required prior to the AOA estimation.

As discussed in Section 3.4.1, one method of isolating the individual phase delays of each signal is to use a FFT algorithm to transform the phase delay information from the time-domain into the frequency-domain as described by (3.17). The phase delays of multiple signals can then be isolated to the individual frequency bins of the FFT provided that the signals have different frequencies.

Finally, it should be mentioned that beamforming and array processing methods can inherently estimate the AOA of multiple signals. These techniques will be discussed in Chapter 5.

3.9.2 Optimal Linear Array Geometries

The ambiguity resolution algorithms and examples discussed in this chapter have all been presented using arbitrarily chosen linear array geometries. Other than requiring that the interferometer baselines be non-integer multiples of each other, there was no discussion on the optimal number of antennas or the optimal antenna positions for

a given aperture. The number of antennas and their positions have two important implications on the performance of the interferometer, namely

i the aperture of the array, i.e. the length of the widest antenna pair, approximately governs the magnitude of the RMS error of the AOA estimation in the presence of noise, and

ii the sparsity of the array, i.e. how far apart the antennas are spaced, affect the number of ambiguities and how far apart the ambiguities are, i.e. the magnitudes and positions of the sidelobes, which in turn affect the ability of the ambiguity resolution algorithms to correctly resolve the ambiguities.

Due to the inverse relationship between the interferometer baseline and its RMS error performance, the length of the widest antenna pair is generally chosen to be as long as practically tolerable, subject to the mounting and physical constraints of the application and the ability of the ambiguity resolution algorithm to robustly resolve the ambiguities.

The robustness of the ambiguity resolution algorithm significantly depends on the number of antennas and their positions. In general, for a given aperture, the extent of the sparsity of the antenna array determines the robustness of the ambiguity resolution algorithm in the presence of noise. By using more antennas or by reducing the spacing between antennas, the sparsity of the antenna array can be reduced such that the ambiguities of each baseline are spaced further apart and so the ambiguities from multiple baselines are unlikely to correlate at angles other than the signal's AOA. In other words, there will be lower sidelobes in the correlation cost function and so the ambiguity resolution algorithm will more likely resolve the ambiguities correctly. On the other hand, if less antennas are used or the spacing between antennas are increased, the sparsity of the antenna array will increase so that the ambiguities of each baseline are spaced closer together and so ambiguities from multiple baselines are likely to correlate at angles other than the signal's AOA. In other words, there will be higher sidelobes in the correlation cost function and so the ambiguity resolution algorithm will be more susceptible to ambiguity resolution errors.

Hence, the number of antennas and their positions are important design considerations which affect the robustness of the ambiguity resolution algorithms. While there has been extensive research into the problem of optimal non-uniform linear array geometries [78–83], in general there is no single optimal design formula for linear array geometries. For the purposes of this thesis, the problem of optimal array geometries is considered to be beyond the scope of this research. Rather, in Chapter 4, a specific array geometry will be presented which can be exploited in a manner that achieves unambiguous, high accuracy AOA estimates in a more computationally efficient manner than the conventional interferometric methods presented in this chapter. This array geometry will form the basis of all subsequent discussions in this thesis.

3.9.3 Field-of-View

The field-of-view (FOV) of an interferometer is an important design consideration as it specifies the range of angles that the interferometer can estimate the AOA of a signal with reasonable accuracy. There are two aspects to the FOV consideration, namely the

range of angles that can be viewed and the *accuracy* associated with the FOV.

For a linear array, the range of angles that can be estimated by an interferometer is limited by its AOA estimation performance in the endfire region. In these regions, the AOA approaches $\pm 90^\circ$ and so the corresponding phase delay approaches $\pm\pi$. With the addition of noise errors, the measured phase delays can cross the $\pm\pi$ boundary which results in large AOA estimation errors since a signal arriving from 90° may be estimated as arriving from -90° and vice versa. These large AOA estimation errors therefore reduce the practical FOV of the interferometer. From (3.44), the practical FOV of an interferometer with a RMS error tolerance, $\delta\theta_{\text{tol}}$, may be approximated by

$$\text{FOV} \approx 2 \arccos\left(\frac{1}{\sqrt{\eta N}} \cdot \frac{c}{2\pi f d \delta\theta_{\text{tol}}}\right). \tag{3.173}$$

This expression shows that FOV of an interferometer is dependent on the the SNR of the signal, the operating frequency, the signal duration (or number of samples) and the interferometer baseline (or array aperture). Figure 3.30 and Figure 3.31 show the maximum FOV for a number of error tolerances as a function of SNR and frequency respectively. These figures assume that the interferometer baseline is unambiguous (i.e. $d = \lambda/2$) and demonstrate that the FOV increases with SNR and frequency. Similarly, Figure 3.32 shows the maximum FOV for a number of maximum error tolerances as a function of the aperture of the interferometer. This figure assumes that the SNR is 15 dB and the frequency is $f = 18$ GHz. This figure demonstrates that the FOV increases as the array aperture increases.

360° FOV Using Linear Arrays

It is well known in array processing literature that linear antenna arrays are unable to distinguish the phase delays from signals arriving from a cone centred along the array axis due to symmetry. This is a geometric ambiguity and is not to be confused with the phase measurement ambiguities associated with long baseline interferometers. If the elevation component of the AOA is ignored, the cone of geometric ambiguities reduces to a 180° ambiguity problem, where it is not known whether a signal is arriving from the "front" or "back" hemispheres of the array as illustrated in Figure 3.33.

Due to the 180° geometric ambiguity problem, linear array interferometers are often described as having a FOV between $[-90^\circ, 90^\circ]$. For linear arrays, a "sensing" mechanism is required to resolve this ambiguity. This can be achieved by using directional, "sense" antennas to determine whether a signal comes from the front or back hemispheres. Alternatively, directional antennas with beampatterns that inherently reject signals from the rear hemisphere, such as horns or cavity-backed spirals, can be used.

Furthermore, Figure 3.30 to Figure 3.32 show that the FOV of a linear array interferometer is typically less 180°, particularly at low SNR. This reduction in FOV is attributed to the fact that random errors in the phase delay measurements can cause large AOA estimation errors when the phase delay measurements straddle the $\tilde{\psi} = \pm\pi$ boundary.

As a result of the above, three or more independent linear arrays with different rotation angles, or "looking" angles, are required to obtain a reliable 360° field-of-view as

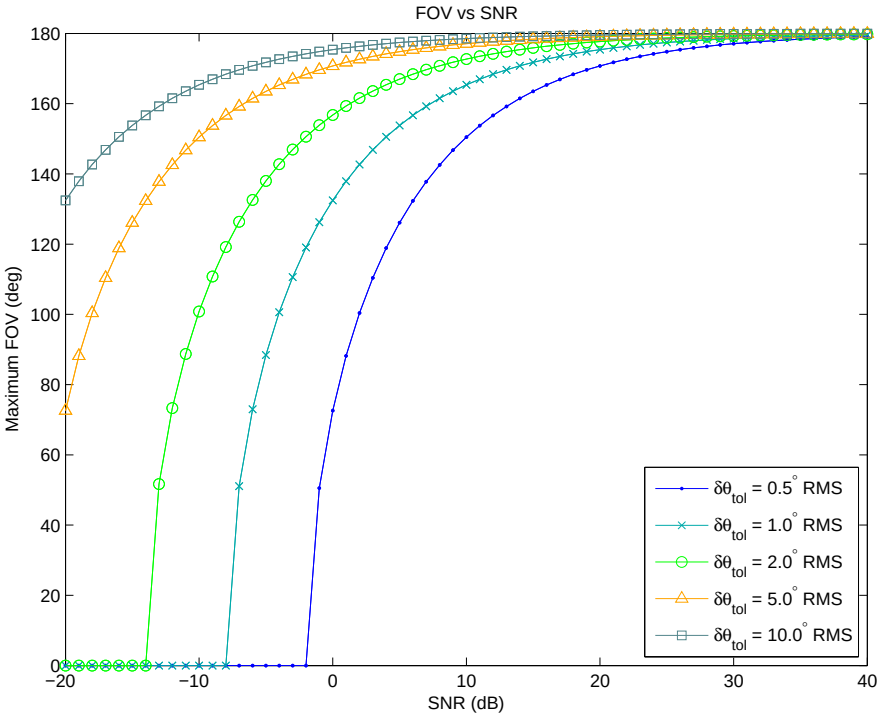

Figure 3.30: Comparison of the FOV of an interferometer as a function of SNR at various error tolerances. Simulation parameters: $f = 18$ GHz, $d = \lambda/2$, $\lambda = 16.67$ mm, $N = 2048$ samples, and $t_s = 750$ ps.

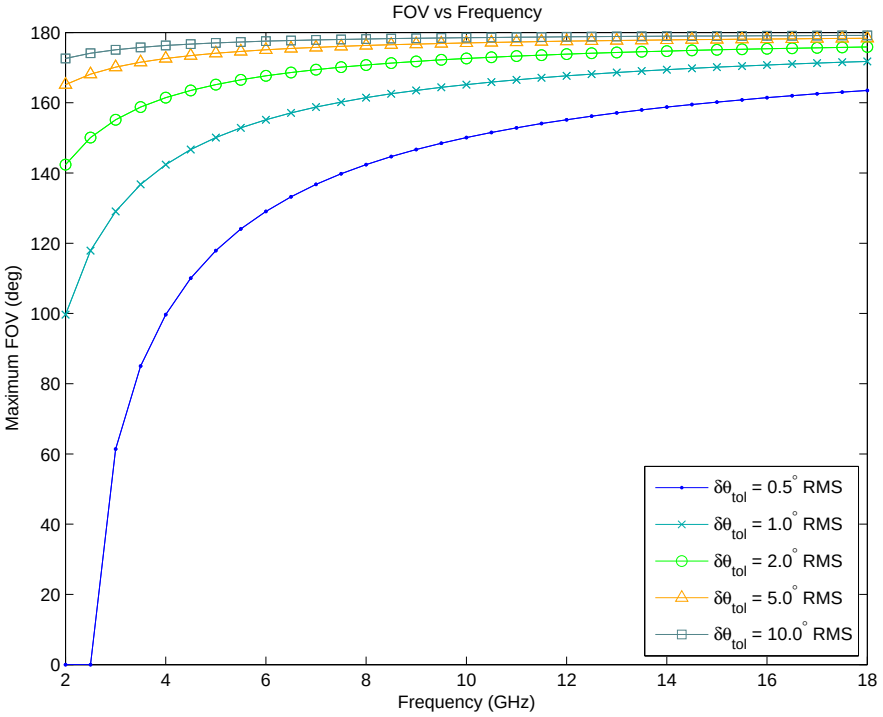

Figure 3.31: Comparison of the FOV of an interferometer as a function of frequency at various error tolerances. Simulation parameters: $\eta = 15$ dB, $d = \lambda/2$, $\lambda = 16.67$ mm, $N = 2048$ samples, and $t_s = 750$ ps.

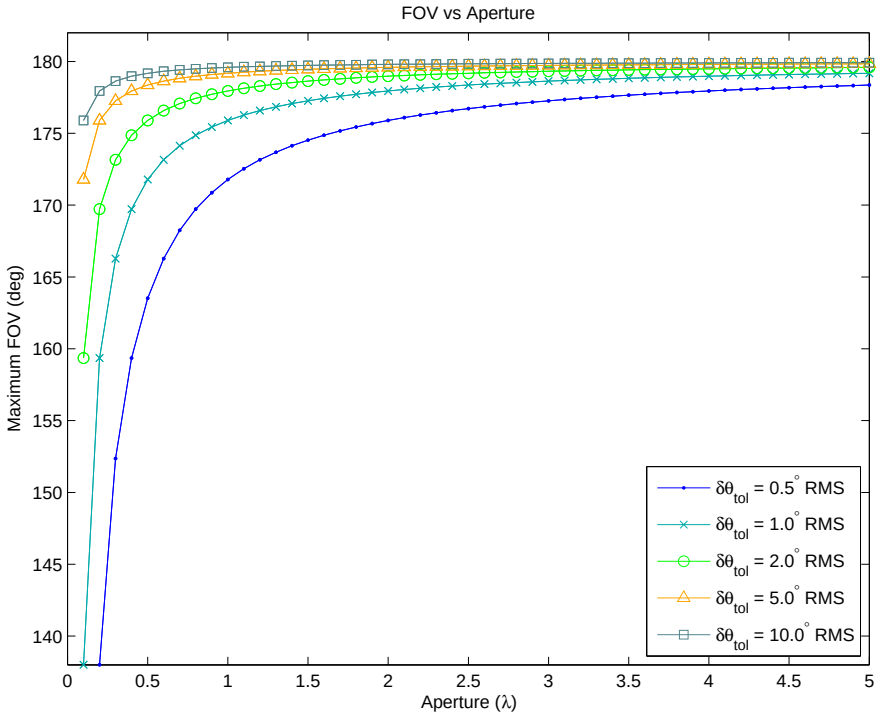

Figure 3.32: Comparison of the FOV of an interferometer as a function of the array aperture with various error tolerances. Simulation parameters: $\eta = 15$ dB, $f = 18$ GHz, $N = 2048$ samples, and $t_S = 750$ ps.

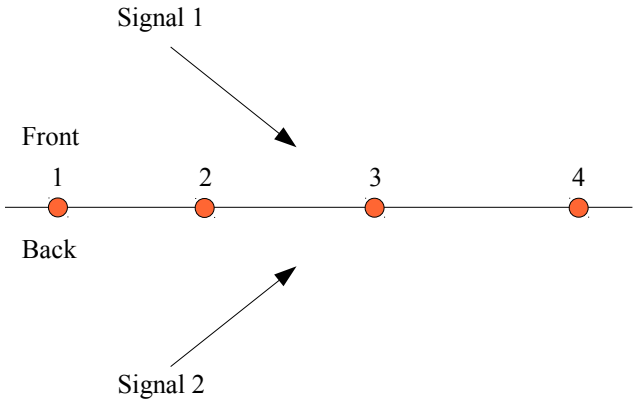

Figure 3.33: Linear arrays are unable to distinguish between signals arriving from the "front" or "back" hemispheres due to the geometric symmetry.

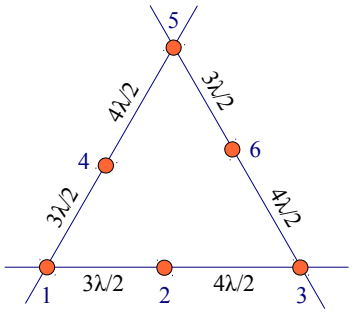

Figure 3.34: Multiple independent linear arrays are required to obtain a 360° field-of-view.

depicted in Figure 3.34. For these systems, the AOA estimation of each "arm" may be considered as a self-contained direction finding system, or may include the phase delay measurements from different arms. The ambiguity resolution algorithms described in this chapter can still be applied to these systems. When combining the phase delay or AOA estimates from different arms, the rotational offset angles must be taken into account. That is, the phase delay relationship with the AOA becomes

$$\psi_m = \frac{2\pi f d_m}{c} \sin(\theta - \vartheta_{\text{arm}}), \tag{3.174}$$

where ϑ_{arm} is the rotation angle of the interferometer arm relative to some reference.

360° FOV Using Circular Arrays

The 180° geometric ambiguity problem of linear arrays can be avoided by using non-linear array geometries. For radar intercept receivers, uniform circular arrays are often used to achieve a 360° field-of-view. Unlike linear arrays which have a non-uniform performance between broadside and endfire, the uniform geometry of circular arrays have a more consistent performance at all azimuth angles.

3.10 Summary

This chapter has discussed the theory of contemporary interferometry. For short-baseline interferometers, the maximum likelihood estimator and two time-domain estimators were presented and their performance in noise was evaluated. All estimators were shown to be asymptotically efficient, i.e. they achieve the root-CRLB at high SNR. The maximum likelihood estimator offered the best AOA estimation performance at low SNR and can estimate the AOA of multiple signals simultaneously provided the signals are sufficiently separated in frequency. The two time-domain methods were computationally faster but can only estimate the AOA of one narrowband signal at a time and only work well at high SNR.

This chapter has also shown that long baseline interferometers offer improved AOA accuracy in the presence of noise. However, due to the circular nature of phase measurements, long baseline interferometers suffer from phase ambiguities which must be resolved with ambiguity resolution algorithms using either independent AOA estimation

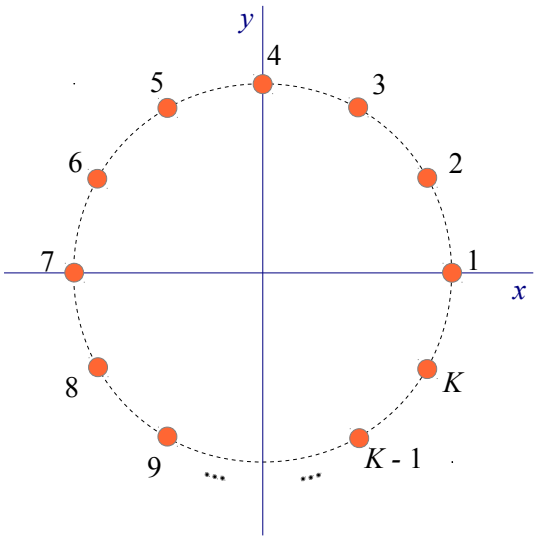

Figure 3.35: A circular array geometry.

algorithms or multiple interferometer baselines. Independent AOA estimation methods, such as amplitude comparison or TDOA, can be used to resolve the phase ambiguities. Alternatively, a short-baseline interferometer may be included to resolve the ambiguities. However, such methods impose further design constraints on the antenna array which may not be achievable in practice.

Alternatively, multiple carefully-chosen, long baseline interferometers can be used to resolve the ambiguities. A number of contemporary ambiguity resolution algorithms were presented and compared. The correlative interferometer (and maximum likelihood estimator) was shown to be able to coherently exploit the phase delay measurements from all antenna baselines to give a asymptotically efficient AOA estimation performance that achieves the root-CRLB at high SNR. However, the correlative interferometer was also shown to be a computationally intensive algorithm and is generally one or more orders of magnitude slower than other slightly sub-optimal methods.

The CAS algorithm is computationally faster, however, the AOA estimation performance only achieves the d_{41}-root-CRLB corresponding to the widest antenna pair. While this performance degradation is statistically significant, the absolute degradation is typically less than a fraction of a degree for large apertures and may be acceptable in practical systems which require computationally fast algorithms, such as ES systems.

The look-up-table implementation of the LF algorithm was shown to be the most computationally efficient algorithm and achieves the same AOA estimation accuracy as the CAS algorithm at high SNR. However, any errors in the ambiguity resolution (either due to noise or quantisation errors) can cause significant AOA estimation errors.

The performance comparison of the long baseline interferometers suggests that the LF and CAS algorithms are computationally fast and near-optimal AOA estimators at high SNR. Hence, these algorithms are ideally suited for implementation in ES and ELINT

systems to provide near real-time surveillance using physically large wideband antennas and sparse array geometries. Additional auxiliary antennas may be required to maintain good performance at low SNR. Alternatively, the correlative interferometers may be used to obtain better performance at low SNR at the expense of a greater computation time and so is suited for offline or less time-critical systems, such as ELINT systems.

Chapter 4

Interferometry Using Second Order Difference Arrays

4.1 Introduction

In the previous chapter, some contemporary multi-baseline interferometric implementations suitable for ES and ELINT systems were discussed. It was shown that while a short-baseline interferometer can provide unambiguous AOA estimation in a computationally efficient manner, the accuracy of short baseline interferometers are relatively coarse. Longer baselines offer greater accuracies but require the use of ambiguity resolution algorithms. At high SNR, statistically optimal methods can significantly increase the computation time of the algorithm while slightly sub-optimal methods can be one or two orders of magnitude faster.

In this chapter, an alternative interferometric algorithm based on a *second-order difference array* (SODA) is considered. This so-called *SODA interferometer* will be shown to be a computationally fast algorithm that provides unambiguous AOA estimation using two long baselines with an AOA estimation performance comparable to a short-baseline interferometer. It will also be shown that the accuracy of the AOA estimation can further be improved by combining the SODA interferometer with some of the conventional ("first-order") ambiguity resolution methods discussed in the previous chapter.

The use of SODA geometries for unambiguous AOA estimation is not a new concept. In [3], Jones *et al.* used a similar interferometric architecture to perform meteorological studies. The wide antenna spacings allowed the authors to reduce the effects of mutual coupling by using longer baselines. However, the authors only considered relatively short apertures. More recently, Ballal and Bleakley [84–86] provided a rigorous mathematical proof to show that the principles of second-order differences can be used to unambiguously estimate the time delay between three sensors. The authors noted that the unambiguous time delay can be readily translated to an equivalent phase delay for AOA estimation. Finally, many studies have been undertaken in the array processing literature on the topic of virtual interpolated arrays for beamforming and array processing techniques [45, 87–89]

While the use of SODA geometries has been previously considered in other applications,

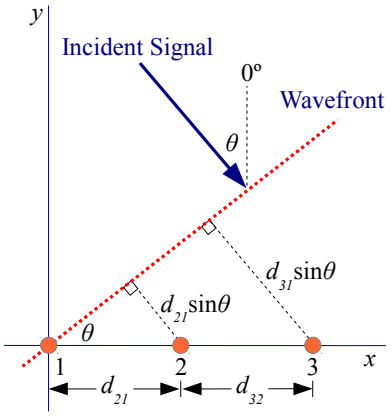

Figure 4.1: A collinear array with three antennas.

to the knowledge of the author an extensive study of the AOA estimation performance and algorithm complexity of the SODA interferometer has not been considered before. Furthermore, the enhancement of the AOA estimation performance by combining the SODA interferometer with conventional "first-order" ambiguity resolution methods to derive optimal AOA estimates in a computationally efficient manner has not been considered before. Finally, the application of SODA interferometry to the electronic surveillance problem introduces a number of practical considerations that have not been previously addressed, such as its performance over a wide frequency range and its ability to obtain unambiguous AOA estimation using sparse large aperture arrays.

4.2 SODA Interferometry

4.2.1 Unambiguous AOA Estimation

Consider a collinear array with three antennas as depicted in Figure 4.1. The unambiguous "first-order" phase delays for the d_{21} and d_{32} baselines, i.e. ψ_{21} and ψ_{32} respectively, are given by

$$\psi_{21} = \frac{2\pi f d_{21}}{c}\sin\theta, \tag{4.1}$$

$$\psi_{32} = \frac{2\pi f d_{32}}{c}\sin\theta, \tag{4.2}$$

where it is assumed that $d_{32} > d_{21} \gg \lambda_{\min}/2$ and $\lambda_{\min}$ corresponds to the wavelength of the highest frequency of interest. The long baselines suggest that the phase delays are highly ambiguous.

The "second-order" phase delay, ψ_Δ, can be calculated as the difference between the first-order phase delays as follows,

$$\psi_\Delta = \psi_{32} - \psi_{21} = \frac{2\pi f(d_{32} - d_{21})}{c}\sin\theta = \frac{2\pi f d_\Delta}{c}\sin\theta, \tag{4.3}$$

where

$$d_\Delta = d_{32} - d_{21}, \tag{4.4}$$

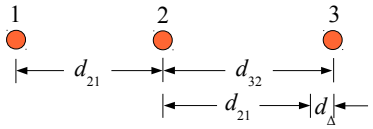

Figure 4.2: Array geometry for a SODA interferometer.

and is termed the *second-order baseline*. Since the expression for ψ_Δ has the same mathematical form as the first-order phase delays, the second-order phase delay can be unambiguous, i.e. $\psi_\Delta \in [-\pi, \pi]$, provided that the second-order baseline is sufficiently short in the sense that the following constraint is satisfied,

$$0 < d_\Delta \leq \frac{\lambda_{\min}}{2}, \tag{4.5}$$

where $\lambda_{\min}$ is the wavelength of the highest frequency of interest. This constraint is depicted graphically in Figure 4.2. Provided that (4.5) is satisfied, the AOA of the signal can be unambiguously estimated using the so-called SODA interferometer as follows

$$\hat{\theta} = \arcsin\left(\frac{c\psi_\Delta}{2\pi f d_\Delta}\right). \tag{4.6}$$

In this thesis, the terms "second-order" and "SODA" will be used interchangeably and so the parameters, ψ_Δ and d_Δ, may also be referred to as the *SODA phase delay* and *SODA baseline* respectively.

4.2.2 Correction for Ambiguous Phase Delay Measurements

In the above formulation, the signs of the unambiguous first-order phase delays, ψ_{21} and ψ_{32}, are expected to be the same for any given AOA. That is, ψ_{21} and ψ_{32} are both positive for positive AOA and are both negative for negative AOA. Furthermore, since it is assumed that $d_{32} > d_{21}$, it is expected that the magnitude of ψ_{32} will be greater than ψ_{21}, i.e. $|\psi_{32}| > |\psi_{21}|$. These two properties will ensure that the second-order phase delay, as computed by (4.3), will be in the interval $\psi_\Delta \in [-\pi, \pi]$.

However, in practice, the second-order phase delay, ψ_Δ, must be estimated from the measured, ambiguous first-order phase delays, $\tilde{\psi}_{21} \in [-\pi, \pi]$ and $\tilde{\psi}_{32} \in [-\pi, \pi]$, where

$$\tilde{\psi}_{21} = [\psi_{21}]_{2\pi}, \tag{4.7}$$
$$\tilde{\psi}_{32} = [\psi_{32}]_{2\pi}, \tag{4.8}$$

and $[\,\cdot\,]_{2\pi}$ represents the modulo 2π operation. Due to the effects of phase wrapping, the signs of $\tilde{\psi}_{21}$ and $\tilde{\psi}_{32}$ may differ and the magnitude of $\tilde{\psi}_{32}$ may not necessarily be greater than $\tilde{\psi}_{21}$. The combination of these two effects may cause the difference between the measured first-order phase delays, i.e. $\tilde{\psi}_{32} - \tilde{\psi}_{21}$, to fall outside the interval $[-\pi, \pi]$. The following correction is therefore required to ensure that the estimated second-order phase delay, $\tilde{\psi}_\Delta$, lies in the interval $[-\pi, \pi]$,

$$\tilde{\psi}_\Delta = \left[\tilde{\psi}_{32} - \tilde{\psi}_{21}\right]_{2\pi}. \tag{4.9}$$

Even though a modulo 2π operation is used, $\tilde{\psi}_\Delta$ is still guaranteed to be unambiguous since the corresponding second-order baseline is short, i.e. $d_\Delta \leq \lambda_{\min}/2$. The expression (4.9) can be considered as the SODA ambiguity resolution algorithm since its purpose is to convert the ambiguous first-order phase delays to an unambiguous second-order phase delay.

4.2.3 Algorithm Complexity

As with conventional interferometry, a typical execution of the SODA interferometer requires that the phase delays of each first-order interferometer baseline to be estimated. Assuming that a FFT is performed to estimate the phase delays in the frequency domain as described by (3.17), the algorithm complexity to estimate the phase delays is $O(\Phi + M)$, where $\Phi = KN \log_2 N$ represents the number of operations to perform the FFT on each antenna output, K is the number of antennas, N is the number of samples and M is the number of baselines.

The SODA ambiguity resolution algorithm is very fast since it only involves a single difference operation and an interval test to ensure that ψ_Δ lies within $[-\pi, \pi]$. This has an algorithm complexity of $O(1)$. The approximate total algorithm complexity for the SODA interferometer is therefore $O(\Phi + M + 1)$.

4.2.4 Alternate Expressions for the SODA Baseline Constraint

For the purposes of designing SODA geometries, it is sometimes convenient to re-express the SODA baseline constraint (4.4) in terms of other first-order baselines. For a given d_{21} baseline, a SODA geometry requires

$$d_{32} = d_{21} + d_\Delta. \tag{4.10}$$

Alternatively, since $d_{31} = d_{21} + d_{32}$, a SODA geometry requires that

$$d_{31} = 2d_{21} + d_\Delta. \tag{4.11}$$

With this notation, the second-order phase delay is given by $\tilde{\psi}_\Delta = [\tilde{\psi}_{31} - 2\tilde{\psi}_{21}]_{2\pi} = [\tilde{\psi}_{32} - \tilde{\psi}_{21}]_{2\pi}$. Provided that (4.5) is satisfied, then regardless of the physical lengths of d_{21}, d_{32} and d_{31}, the same unambiguous second-order baseline, d_Δ, is formed. In other words, the AOA estimation performance of the SODA interferometer is independent of the physical first-order baselines (and hence physical array aperture) because the same virtual aperture is formed.

Example 4.1
Consider the same two-baseline interferometer described in Example 3.3, where $d_{21} = 3\lambda/2$, $d_{31} = 7\lambda/2$, $\lambda = 16.67$ mm, $f = 18$ GHz and $\theta = 23.42°$. In this exaple, d_{21} and d_{31} satisfy the SODA baseline constraint in (4.11) with $d_\Delta = \lambda/2$, i.e.

$$d_{31} = 7\lambda/2 = 2(3\lambda/2) + \lambda/2 = 2d_{21} + \lambda/2. \tag{4.12}$$

For $\theta = 23.42°$, the measured first-order ambiguous phase delays are given by

$$\tilde{\psi}_{21} = [\psi_1]_{2\pi} = [214.63°]_{2\pi} = -145.37°, \quad (4.13)$$

$$\tilde{\psi}_{31} = [\psi_2]_{2\pi} = [500.81°]_{2\pi} = 140.81°. \quad (4.14)$$

The second-order phase delay can therefore be calculated as

$$\tilde{\psi}_\Delta = \left[\tilde{\psi}_{31} - 2\tilde{\psi}_{21}\right]_{2\pi} = [140.81° - 2 \times (-145.37°)]_{2\pi} = 71.55°. \quad (4.15)$$

Applying the second-order variables to the SODA interferometer gives

$$\hat{\theta} = \arcsin\left(\frac{c\tilde{\psi}_\Delta}{2\pi f d_\Delta}\right) = 23.42°. \quad \blacksquare \quad (4.16)$$

4.2.5 RMS Error of the SODA Interferometer

The SODA interferometer is able to perform unambiguous AOA estimation using a sparse array geometry because the first-order interferometric baselines have been specifically chosen so that the ambiguities in the first-order interferometers cancel each other to leave a residual phase delay that is unambiguously related to the signal's AOA. This is equivalent to the creation of a virtual pair of antennas with a baseline of d_Δ as depicted in Figure 4.3.

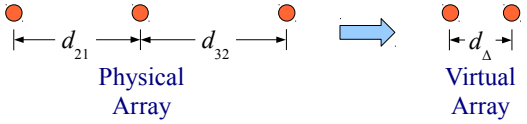

Figure 4.3: A SODA interferometer effectively creates a virtual short-baseline interferometer from a sparse antenna array.

The RMS error of the SODA interferometer is expected to be slightly worse than an equivalent first-order interferometer with a physical baseline of d_Δ. This performance degradation is attributed to the fact that three antenna outputs are used to estimate the phase delay of a (virtual) 2-antenna interferometer. The extra antenna output is expected to introduce more noise to the phase delay estimation and hence lead to a reduced AOA estimation performance.

Consider a 2-antenna first-order interferometer with a physical baseline of $d_{21,\text{first-order}} = \lambda_{\min}/2$. For a given AOA, the first-order phase delay is computed as the difference between two phase measurements (as discussed in Section 3.4), as follows,

$$\tilde{\psi}_{21,\text{first-order}} = \angle X_2(f) X_1^*(f) = [\angle X_2(f) - \angle X_1(f)]_{2\pi} = \left[\tilde{\Phi}_2 - \tilde{\Phi}_1\right]_{2\pi}, \quad (4.17)$$

where $\tilde{\Phi}_1 = \angle X_1(f)$ and $\tilde{\Phi}_2 = \angle X_2(f)$ are the phase measurements of each channel and are assumed to have an associated variance $\sigma^2_{\Phi_1}$ and $\sigma^2_{\Phi_2}$ respectively. For a multi-channel system with identical components in each channel, it is reasonable to assume that the variance of the phase measurements is the same for each channel, i.e., let

$$\sigma^2_\Phi = \sigma^2_{\Phi_1} = \sigma^2_{\Phi_2}. \quad (4.18)$$

From (4.18) and (3.25), the corresponding variance of the first-order phase delay estimate, $\sigma^2_{\psi_{21},\text{first-order}}$, can then be written as

$$\sigma^2_{\psi_{21},\text{first-order}} = \sigma^2_{\Phi_1} + \sigma^2_{\Phi_2} = 2\sigma^2_{\Phi} \equiv \frac{1}{\eta N}, \tag{4.19}$$

Now consider a 3-antenna SODA interferometer with a virtual baseline of $d_\Delta = \lambda_{\min}/2$. For a given angle, the second-order phase delay is computed as the difference between the first-order phase delays as follows,

$$\begin{aligned} \tilde{\psi}_\Delta &= \left[\tilde{\psi}_{32} - \tilde{\psi}_{21}\right]_{2\pi}, && (4.20)\\ &= \left[(\tilde{\Phi}_3 - \tilde{\Phi}_2) - (\tilde{\Phi}_2 - \tilde{\Phi}_1)\right]_{2\pi}, && (4.21)\\ &= \left[\tilde{\Phi}_3 - 2\tilde{\Phi}_2 + \tilde{\Phi}_1\right]_{2\pi}, && (4.22) \end{aligned}$$

where $\tilde{\Phi}_1 = \angle X_1(f)$, $\tilde{\Phi}_2 = \angle X_2(f)$ and $\tilde{\Phi}_3 = \angle X_3(f)$ are the phase measurements in the first, second and third channels respectively and are assumed to have an associated variance $\sigma^2_{\Phi_1}$, $\sigma^2_{\Phi_2}$ and $\sigma^2_{\Phi_3}$ respectively. In [90], it was shown that the coefficients of a linear combination of independent random variables is squared when computing the variance of the linear combination. That is, given $W = \alpha_1 X_1 + \alpha_2 X_2 + \alpha_3 X_3$, where X_1, X_2 and X_3 are independent random variables and α_1, α_2 and α_3 are constant coefficients, the variance of W, is given by

$$\text{Var}\{W\} = \alpha_1^2 \text{Var}\{X_1\} + \alpha_2^2 \text{Var}\{X_2\} + \alpha_3^2 \text{Var}\{X_3\}. \tag{4.23}$$

Applying (4.23) to (4.22) gives the variance of the second-order phase delay estimate, $\sigma^2_{\psi_\Delta}$, as follows

$$\sigma^2_{\psi_\Delta} = \sigma^2_{\Phi_3} + 4\sigma^2_{\Phi_2} + \sigma^2_{\Phi_1}. \tag{4.24}$$

Again, assuming that the variance of the phase measurements in each channel are the same, i.e. let

$$\sigma^2_{\Phi} = \sigma^2_{\Phi_1} = \sigma^2_{\Phi_2} = \sigma^2_{\Phi_3}, \tag{4.25}$$

the variance of the second-order phase delay estimate, $\sigma^2_{\psi_\Delta}$, simplifies to

$$\sigma^2_{\psi_\Delta} = \sigma^2_{\Phi_3} + 4\sigma^2_{\Phi_2} + \sigma^2_{\Phi_1} = 6\sigma^2_{\Phi} \equiv 3 \cdot \frac{1}{\eta N}. \tag{4.26}$$

Since the physical first-order interferometer and the virtual SODA interferometer have the same aperture, i.e. $d_{21,\text{first-order}} = d_\Delta = \lambda_{\min}/2$, it is expected that the RMS errors of both interferometers will be comparable. However, inspection of (4.19) and (4.26) shows that the variance of the second-order phase delay estimate is three times higher than the equivalent first-order phase delay estimate, i.e.

$$\frac{\sigma^2_{\psi_\Delta}}{\sigma^2_{\psi_{21},\text{first-order}}} = 3. \tag{4.27}$$

Thus, the standard deviation (or RMS error) of the second-order phase delay is a factor of $\sqrt{3}$ times higher than the RMS error of the equivalent first-order phase delay. From

(3.27), it is expected that the equivalent physical first-order interferometer will have a RMS error, $\delta\theta_{\text{RMS, first-order}}$, given by

$$\delta\theta_{\text{RMS, first-order}} \approx \frac{1}{\sqrt{\eta N}} \cdot \frac{c}{2\pi f d_\Delta \cos\theta}, \tag{4.28}$$

where $d_{21,\text{first-order}} = d_\Delta$ and $1/\sqrt{\eta N}$ represents the RMS error of the phase delay estimation. On the other hand, the SODA interferometer is expected to have a RMS error, $\delta\theta_{\text{RMS, SODA}}$, given by

$$\delta\theta_{\text{RMS, SODA}} \approx \sqrt{3} \cdot \frac{1}{\sqrt{\eta N}} \cdot \frac{c}{2\pi f d_\Delta \cos\theta} \equiv \sqrt{3} \cdot \delta\theta_{\text{RMS, first-order}}. \tag{4.29}$$

4.2.6 Performance Evaluation

In this section, Monte Carlo simulations are used to evaluate the AOA estimation performance of the SODA interferometer and the equivalent first-order interferometer with the same physical baseline, d_Δ. In these simulations, the SODA baseline is assumed to be $d_\Delta = \lambda/2$, where λ is the wavelength of the signal frequency. The first-order baseline, d_{21}, has been arbitrarily chosen to be $3\lambda/2$, and so from (4.11), $d_{31} = 7\lambda/2$.

Figure 4.4 shows the RMS error performance of the interferometers as a function of AOA at a SNR of $\eta = 15$ dB and signal frequency of $f = 18$ GHz using 10,000 Monte Carlo receiver noise realisations. The RMS errors are compared against the square-root of the Cramér-Rao Lower Bound (CRLB) obtained using (a) the d_Δ baseline, and (b) all available antennas. These bounds are referred to as the "d_Δ-root-CRLB" and the "3-antenna root-CRLB" respectively.

This example shows that while the RMS errors of the equivalent first-order interferometer achieves the d_Δ-root-CRLB, the RMS errors of the SODA interferometer is consistently a factor of $\sqrt{3}$ worse than the first-order interferometer. However, in absolute terms, this performance degradation is less than 1° RMS within the interval $\theta \in [-82°, 82°]$. This figure also shows that the performance of the SODA interferometer is approximately 12 times worse than the 3-antenna root-CRLB.

Figure 4.5 shows the AOA estimation performance of the interferometers at $\theta = 70°$ as a function of frequency. The angle, $\theta = 70°$, is chosen to correspond to the expected limit of the FOV at 2 GHz with a maximum error tolerance of 2° RMS (see Figure 3.31). This simulation verifies that the relative performance of the SODA interferometer and equivalent first-order interferometer are consistent at all frequencies.

Finally, Figure 4.6 shows the AOA estimation performance of the SODA interferometer as a function of both frequency and the d_{31} baseline. In this simulation, the RMS errors are calculated over all angles between $-70°$ and 70° in 1° intervals using 100 Monte Carlo receiver noise realisations at each angle. This simulation verifies that the AOA estimation performance of the SODA interferometer is independent of the first-order baselines.

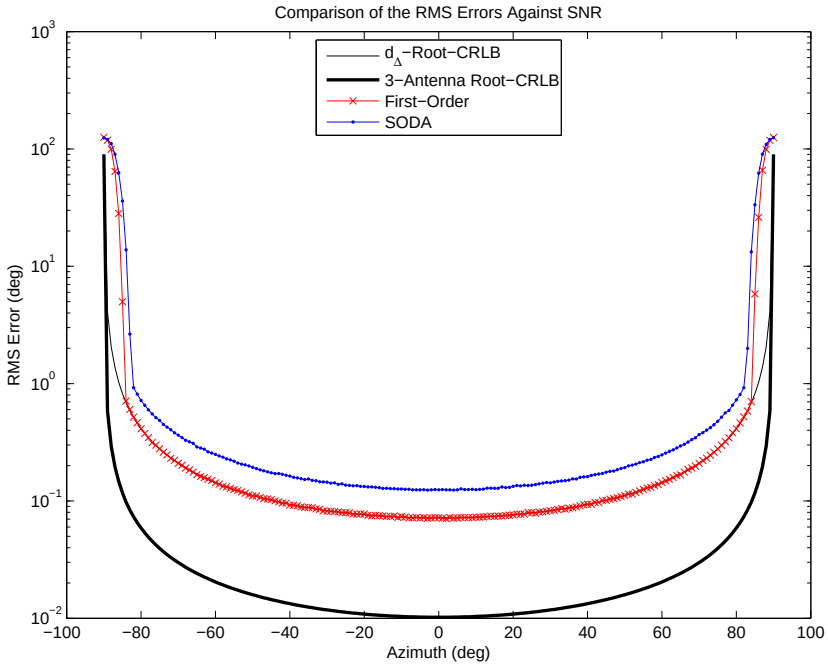

Figure 4.4: Comparison of the AOA estimation performance of the SODA interferometer and the equivalent first-order interferometer as a function of AOA. Simulation parameters: $\eta = 15$ dB, $f = 18$ GHz, $\lambda = 16.67$ mm, $d_{21} = 3\lambda/2$, $d_{32} = 7\lambda/2$, $N = 2048$ samples, $t_s = 750$ ps, and $\mathcal{Q} = 10,000$ realisations.

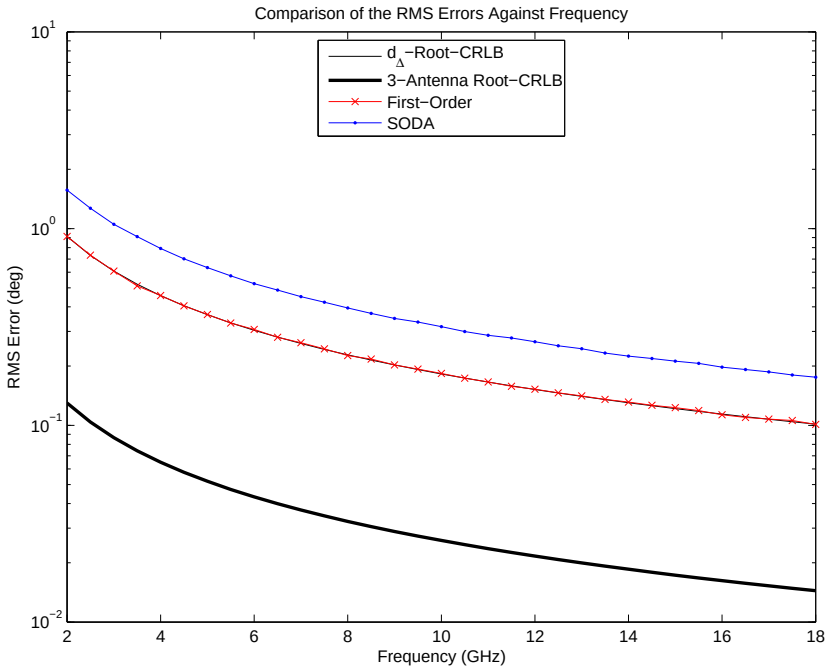

Figure 4.5: Comparison of the AOA estimation performance of the SODA interferometer and the equivalent first-order interferometer as a function of frequency. Simulation parameters: $\eta = 15$ dB, $\theta = 70°$, $\lambda = 16.67$ mm, $d_{21} = 3\lambda/2$, $d_{32} = 7\lambda/2$, $N = 2048$ samples, $t_s = 750$ ps, and $\mathcal{Q} = 10,000$ realisations.

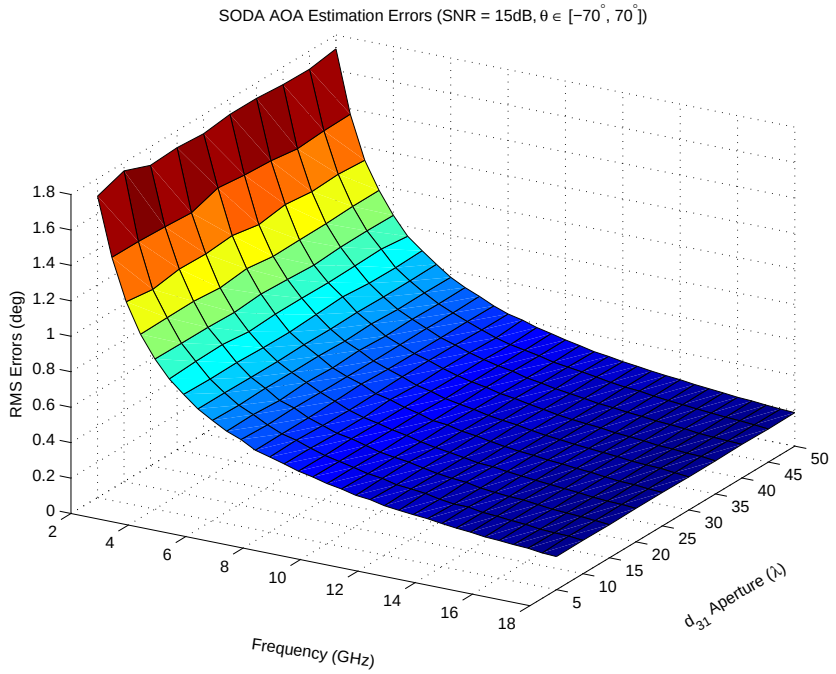

Figure 4.6: The angular accuracy of a SODA interferometer is independent of the physical first-order baselines.

4.3 SODA-Cued Ambiguity Resolution

The previous section demonstrated that the unambiguous AOA estimation performance of the SODA interferometer is limited to a virtual, short-baseline, d_Δ, and does not take advantage of the higher accuracy offered by the longer physical first-order baselines, i.e. d_{21}, d_{32} or d_{31}. By comparing (4.29) with (4.28), the longest first-order baseline, d_{31}, is expected to offer an improvement in the AOA estimation by a factor of

$$\text{Improvement} = \sqrt{3} \cdot \frac{d_{31}}{d_\Delta}. \tag{4.30}$$

Alternatively, if all three first-order baselines are used, then using (4.11) and (4.29) with the expressions for the CRLB, as described by (3.168), the improvement in the AOA estimation is given by

$$\text{Improvement} = 2 \cdot \sqrt{3\left(\frac{d_{21}}{d_\Delta}\right)^2 + 3\left(\frac{d_{21}}{d_\Delta}\right) + 1}. \tag{4.31}$$

The significant improvement in the AOA estimation provides a motivation to use the relatively coarse SODA AOA estimate to cue the conventional first-order ambiguity resolution methods discussed in Section 3.6 and Section 3.7. Such methods will allow high accuracy AOA estimates to be obtained in a computationally efficient manner.

Example 4.2
Consider the 3-antenna interferometer discussed in Example 4.1 where $d_\Delta = \lambda/2$, $d_{21} = 3\lambda/2$ and $d_{31} = 7\lambda/2$. In this example, the first-order baseline, d_{31}

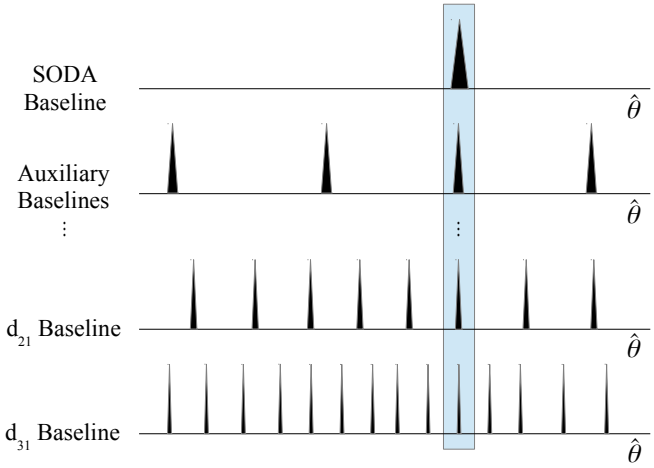

Figure 4.7: The unambiguous second-order phase delay can be used to successively resolve the ambiguities of the longer first-order baselines.

is expected to offer an improvement in the RMS error of the AOA estimation of the SODA interferometer by a factor of

$$\text{Improvement} = \sqrt{3}\frac{7\lambda/2}{\lambda/2} \approx 12.12. \tag{4.32}$$

If all three antennas are used, the RMS error can be improved by a factor of

$$\text{Improvement} = 2 \cdot \sqrt{3\left(\frac{3\lambda/2}{\lambda/2}\right)^2 + 3\left(\frac{3\lambda/2}{\lambda/2}\right) + 1} \approx 12.17. \tag{4.33}$$

These figures are consistent with the simulation results observed in Figure 4.4. ∎

4.3.1 SODA-Based Inference (SBI) Interferometer

One method of improving the SODA AOA estimate is to use the virtual short baseline of the SODA interferometer as the unambiguous short-baseline interferometer as described in Section 3.6.2. In this case, the unambiguous second-order phase delay is used to successively resolve the ambiguities of the first-order baselines, which are assumed to be sorted into ascending order. In other words, the ambiguities of the long first-order baselines can be resolved using the following phase delay set, $\Psi = \{\tilde{\psi}_\Delta, \tilde{\psi}_{21}, \tilde{\psi}_{31}\}$, and their corresponding baselines, $D = \{d_\Delta, d_{21}, d_{31}\}$, with the algorithm described in Section 3.6.2. The final AOA estimate can then be obtained from the resolved phase delay of the d_{31} baseline. This process is depicted in Figure 4.7 and shall be referred to as the *SODA-Based Inference* (SBI) interferometer.

While the AOA estimation performance of the SODA interferometer is independent of the first-order baselines, the coarse accuracy of the SODA interferometer places an upper limit on the maximum length of the d_{21} baseline for the SBI interferometer. From (3.49) and (4.29), the upper limit for the d_{21} baseline is given by

$$d_{21} \leq d_\Delta \cdot \frac{\pi}{3\sqrt{3}} \cos\theta_{\max} \sqrt{\eta N}. \tag{4.34}$$

This suggests that the maximum aperture of the array will also be constrained through (4.11). If a large aperture is desired and the corresponding d_{21} baseline cannot satisfy (4.34), additional auxiliary antennas may be used to provide shorter intermediate baselines to satisfy (4.34). However, this performance improvement comes at the expense of additional receiver channels.

Since the SBI interferometer needs to resolve the ambiguity in each successively longer baseline, this ambiguity resolution method has an algorithm complexity of $O(M)$, where M is the number of interferometer baselines. In the simplest case, $M = 3$ which comprises of the SODA baseline, d_Δ, and two first-order baselines, d_{21} and d_{31}. Additional auxiliary antennas may be used to improve the ambiguity resolution performance of the SBI interferometer at low SNR, in which case, $M > 3$. Since the estimation of the phase delays has an algorithm complexity of $O(\Phi + M)$, the total algorithm complexity for the SBI interferometer is therefore $O(\Phi + 2M)$, where $\Phi = KN \log_2 N$, K is the number of antennas and N is the number of samples.

The SBI interferometer is computationally faster than the first-order common angle search (CAS) algorithm and correlative interferometers discussed in the previous chapter. However, the SBI interferometer is also more sensitive to noise errors since any resolution errors in the shorter baselines will be compounded with each successive inference. When an ambiguity resolution error occurs, the error of the SBI interferometer will be comparable to the SODA AOA estimate.

4.3.2 SODA-Cued Correlative Interferometer

The SODA AOA estimate can also be used to reduce the search space (and hence computation time) of the correlative interferometer. For very sparse arrays, the SODA-cued search space may also improve the AOA estimation performance of the correlative interferometer by ignoring ambiguous angles with high sidelobes in the correlation cost function.

For a linear array, the search interval of a correlative interferometer will typically be $[-90°, 90°]$. With the SODA AOA estimate, $\hat{\theta}_{\text{SODA}}$, this search space can be reduced to the interval $[\hat{\theta}_{\text{SODA}} - \delta\theta_{\text{search}}, \hat{\theta}_{\text{SODA}} + \delta\theta_{\text{search}}]$, where $\delta\theta_{\text{search}}$ is the number of angles either side of $\hat{\theta}_{\text{SODA}}$ to search. While the full search interval spans 180°, the reduced interval only spans $2\delta\hat{\theta}_{\text{search}}$ degrees. As a rule of thumb, a reasonable limit for the search angle would be three times the RMS error of the SODA AOA estimate, i.e. $\delta\theta_{\text{search}} = 3\delta\theta_{\text{RMS,SODA}}$.

Example 4.3
Consider the same array geometry as described in Example 3.5, where $d_{21} = 3\lambda/2$, $d_{31} = 7\lambda/2$ and $\lambda = 16.67$ mm. Figure 4.8 shows the output of the correlative interferometer using a cosine cost function when the signal AOA is $\theta = 23.42°$. Assuming a SNR of $\eta = 15$ dB, signal frequency of $f = 18$ GHz and $N = 2048$ samples, the RMS error of the SODA AOA estimate can be calculated from (4.29) to be about 0.14°. In one particular realisation, the SODA interferometer estimates the AOA of the signal to be $\hat{\theta}_{\text{SODA}} = 23.48°$. The corresponding search space for the correlative interferometer

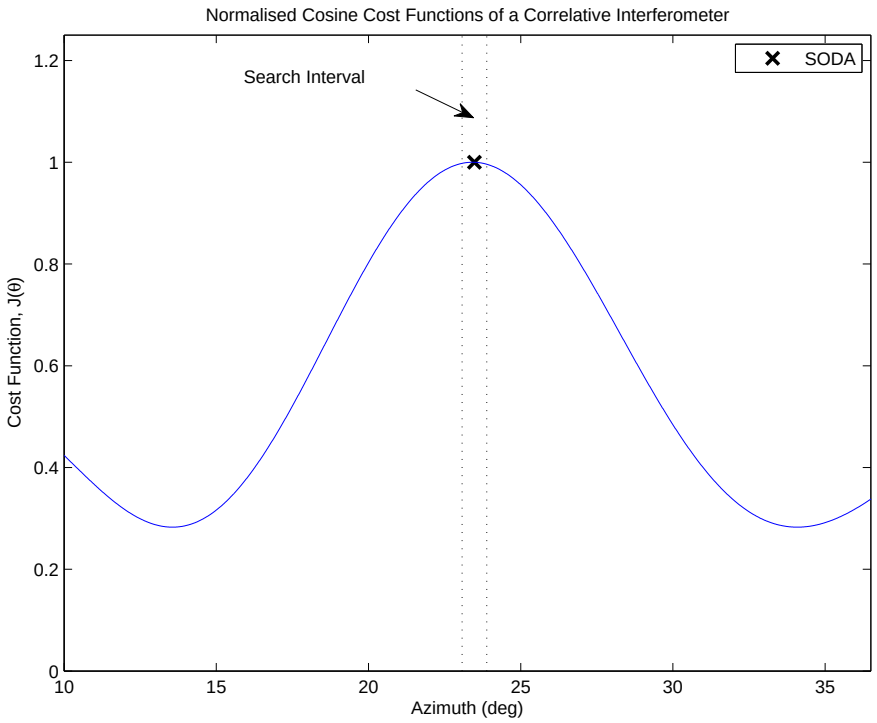

Figure 4.8: The SODA AOA estimate can be used to reduce the search range of the correlative interferometer.

can therefore be reduced from $[-90°, 90°]$ to $[23.06°, 23.90°]$. This means that only 0.46% of the full search space needs to be searched. ∎

In general, the grid search estimate of the SODA-cued correlative interferometer will still need to be refined using an optimisation algorithm, such as Newton's Method, to further improve the AOA estimation. At high SNR, it is reasonable to expect that the RMS error of the SODA AOA estimate is sufficiently small that the AOA estimate falls within the main lobe of the correlative interferometer's cost function. If this the case, an alternative implementation of the SODA-cued correlative interferometer is to bypass the grid search altogether and simply use the SODA AOA estimate as the initial estimate to the optimisation algorithm.

The complexity of the SODA-cued correlative interferometer is $O(\Phi+M(G'+\Gamma+1)+1)$, where $\Phi = KN\log_2 N$, K is the number of antennas, N is the number of samples, M is the number of baselines, G' represents the number of search angles in the reduced search space and Γ represents the number of iterations used by Newton's Method. If the grid search is not performed, the algorithm complexity of the SODA-cued optimisation algorithm is $O(\Phi + M(\Gamma + 1) + 1)$.

4.3.3 SBI-Cued Correlative Interferometer

Since the SBI interferometer provides higher accuracy than the SODA interferometer but is also computationally fast, an alternative is to use the SBI interferometer's AOA estimate to cue the correlative interferometer or directly cue its optimisation algorithm.

Since the SBI interferometer can exploit auxiliary antennas, the SBI-cued correlative interferometer is expected to have a better AOA estimation performance than the SODA-cued correlative interferometer at low SNRs when auxiliary antennas are available.

The complexity of the SODA-cued correlative interferometer is $O(\Phi+M(G'+\Gamma+2)+1)$, where $\Phi = KN\log_2 N$, K is the number of antennas, N is the number of samples, M is the number of baselines, G' represents the number of search angles in the reduced search space and Γ represents the number of iterations used by Newton's Method. If the grid search is not performed, the algorithm complexity of the SBI-cued optimisation algorithm is $O(\Phi + M(\Gamma + 2) + 1)$.

4.4 Performance Comparison

In this section, Monte Carlo simulations are used to evaluate the AOA estimation performance of the discussed SODA-based algorithms using the same array geometry as described in Section 3.8.2. Antennas 1, 3 and 4 of this array geometry forms a 3-antenna SODA geometry designed to operate up to 16 GHz. In the interest of finding fast algorithms, the SODA-cued and SBI-cued correlative interferometers are implemented using the coarse AOA estimates to directly cue the optimisation algorithm of the interferometric maximum likelihood estimator (MLE), i.e. the grid search of the correlative interferometer is not performed. For notational convenience, these algorithms are labelled as "SODA-Cued Opt." and "SBI-Cued Opt." respectively.

For comparison, the AOA estimation performance of the algorithms will be compared against the square-root of the Cramér-Rao Lower Bound (CRLB). Three different CRLBs are defined to reflect the bounds obtained using (a) the physical d_Δ baseline, (b) the d_{41} baseline, and (c) all available antennas. The square-root of these bounds shall be referred to as the "d_Δ-root-CRLB", "d_{41}-root-CRLB" and "K-antenna root-CRLB" respectively.

In order to allow direct comparison with the conventional ambiguity resolution algorithms discussed in the previous chapter, these simulations assume the same parameters as described in Section 3.8.3. That is, the intercepted signal is a single-tone with a frequency and initial phase of $f = 9410$ MHz and $\varphi = 0°$ respectively. The signal is assumed to arrive from an AOA of $\theta = 23.42°$. The RMS error performance of each algorithm is evaluated using $\mathcal{Q} = 10,000$ receiver noise realisations. For each noise realisation, it is assumed that $N = 2048$ digital samples are collected at a sample interval of $t_s = 750$ ps. In these simulations, the phase delays are estimated using the FFT maximum likelihood estimator implemented using a 2048-point FFT. No scalloping losses are expected to occur in these simulations. Newton's Method optimisation of the SODA and SBI AOA estimates is allowed to perform a maximum of $\Gamma_{\max} = 100$ iterations and the convergence tolerance is set to $\delta\theta_{\text{tol}} = 1° \times 10^{-5}$.

RMS Error Comparison

Figure 4.9 and Figure 4.10 show the RMS error performance of each algorithm when implemented using the 3-antenna array geometry. For this particular array geometry

no noticeable difference is observed between the d_Δ-root-CRLB and the 3-antenna root-CRLB.

As expected, this simulation shows that the RMS errors of the SODA interferometer is a factor of $\sqrt{3}$ above the d_Δ-root-CRLB and approximately a factor of 175 above the d_{41}-root-CRLB and 3-antenna root-CRLB. These results are consistent with the expected values obtained from (4.29), (4.30) and (4.31). While the AOA estimation performance of the SODA interferometer is clearly sub-optimal, in absolute terms, the RMS errors are still below 1° RMS at SNRs above 2 dB.

On the other hand, the SBI interferometer achieves the d_{41}-root-CRLB from 8 dB SNR and the SODA-cued and SBI-cued optimisation algorithms achieve the 3-antenna root-CRLB from 22 dB and 8 dB respectively. While the maximum number of iterations was set to $\Gamma_{\max} = 100$ iterations, the actual number of iterations taken in these simulations was on average $\Gamma_{\text{actual}} = 2$.

Interestingly, below 20 dB SNR, the SODA-cued optimisation algorithm has a worse AOA estimation performance than the SODA interferometer. This performance degradation is attributed to the SODA interferometer having insufficient accuracy at low SNRs to estimate the AOA to within the main lobe of the cost function of the correlative interferometer (see Figure 3.20). As a result, the poor initial estimate provided to Newton's Method caused the optimisation algorithm to fail. In these simulations, the correlative interferometer's grid search was intentionally not performed to increase the computational speed of the algorithm. It is expected that the SNR thresholds of these algorithms can be significantly improved by explicitly performing the grid search prior to the optimisation algorithm.

Figure 4.11 and Figure 4.12 shows that with the inclusion of a fourth auxiliary antenna, the SNR threshold of the SBI and SBI-cued optimisation algorithms are both reduced to -4 dB. As discussed in Section 3.8.2, there is a small but statistically significant difference between the d_{41}-root-CRLB and the 4-antenna root-CRLB. Since the SBI-cued optimisation algorithm achieves the 4-antenna root-CRLB but the SBI interferometer only achieves the d_{41}-root-CRLB, the SBI-cued optimisation algorithm is generally preferred since it achieves an optimal AOA estimation performance at high SNR with the same SNR threshold. Not surprisingly, the inclusion of the auxiliary antenna has no effect on the performance of the SODA or SODA-cued correlative interferometers since the SODA algorithm does not utilise the outputs of the auxiliary antennas.

Relative Execution Time

Table 4.1 shows the average relative execution time of each algorithm while performing a single AOA estimation using the 4-antenna array geometry. These execution times are normalised to the execution time of the SODA interferometer. The algorithms are presented in the order of increasing execution time, i.e. from fastest to slowest.

In the previous chapter, it was shown that the line fitting algorithm was the fastest conventional ambiguity resolution technique. Directly comparing the relative execution

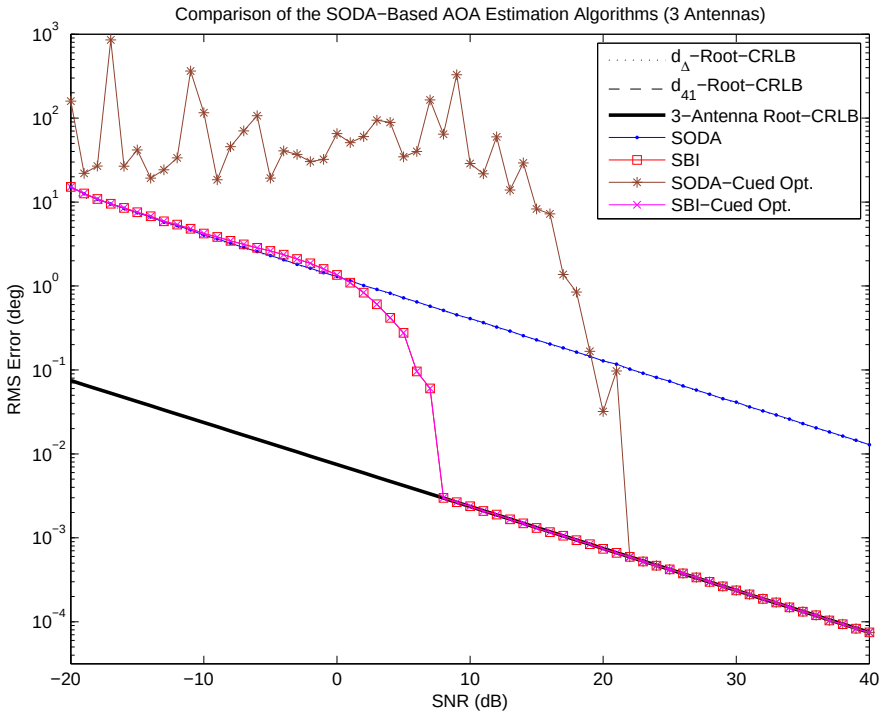

Figure 4.9: RMS error performance of each algorithm as a function of SNR. Simulation parameters: $K = 3$ antennas, $\theta = 23.42°$, $f = 9410$ MHz, $\varphi = 0°$, $N = 2048$ samples, $t_s = 750$ ps and $\mathcal{Q} = 10,000$ realisations.

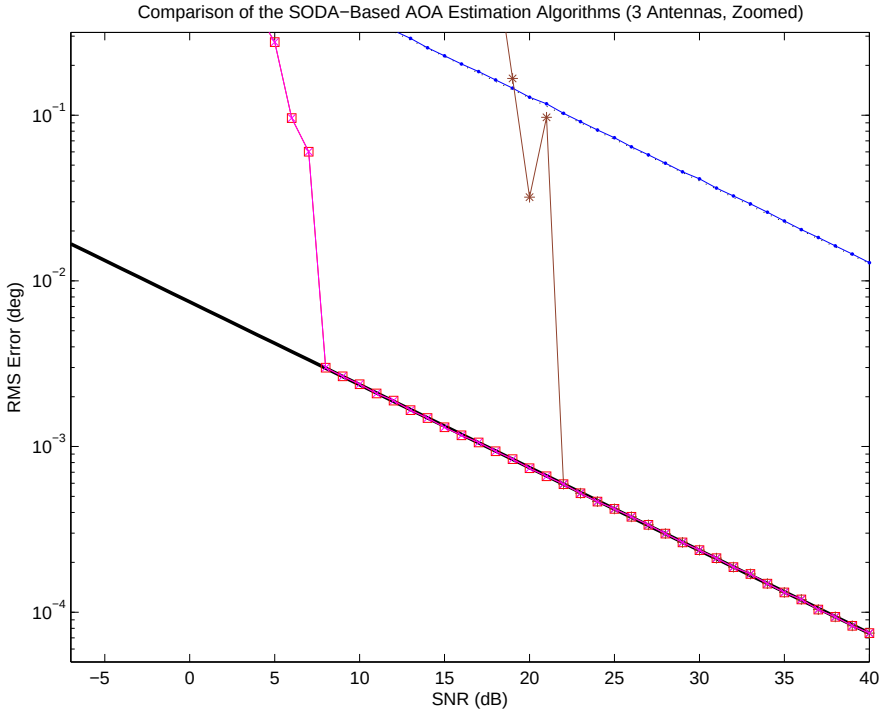

Figure 4.10: RMS error performance of each algorithm as a function of SNR. Simulation parameters: $K = 3$ antennas, $\theta = 23.42°$, $f = 9410$ MHz, $\varphi = 0°$, $N = 2048$ samples, $t_s = 750$ ps and $\mathcal{Q} = 10,000$ realisations.

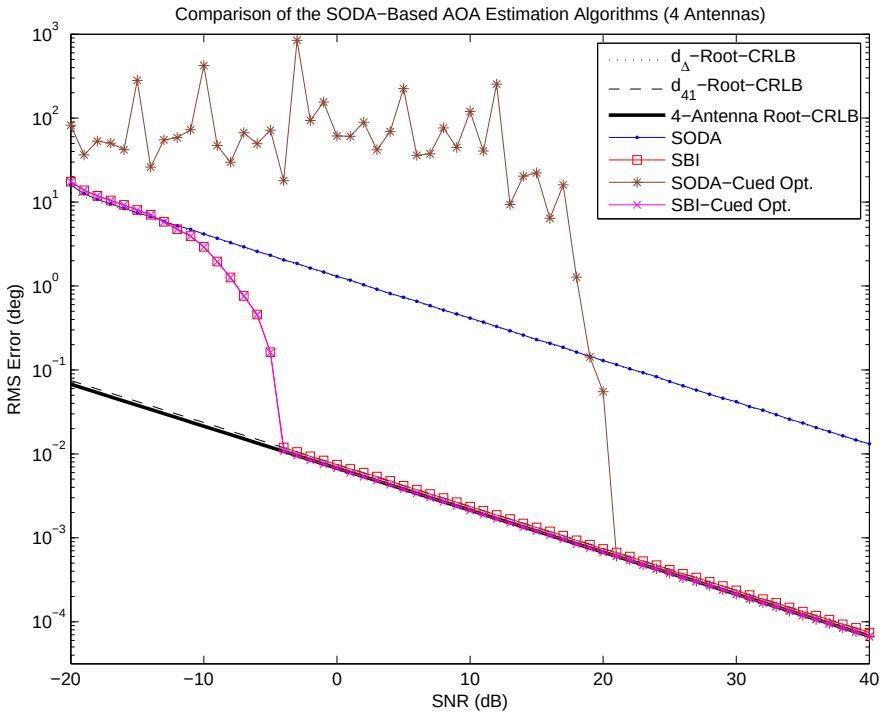

Figure 4.11: RMS error performance of each algorithm as a function of SNR. Simulation parameters: $K = 4$ antennas, $\theta = 23.42°$, $f = 9410$ MHz, $\varphi = 0°$, $N = 2048$ samples, $t_s = 750$ ps and $\mathcal{Q} = 10,000$ realisations.

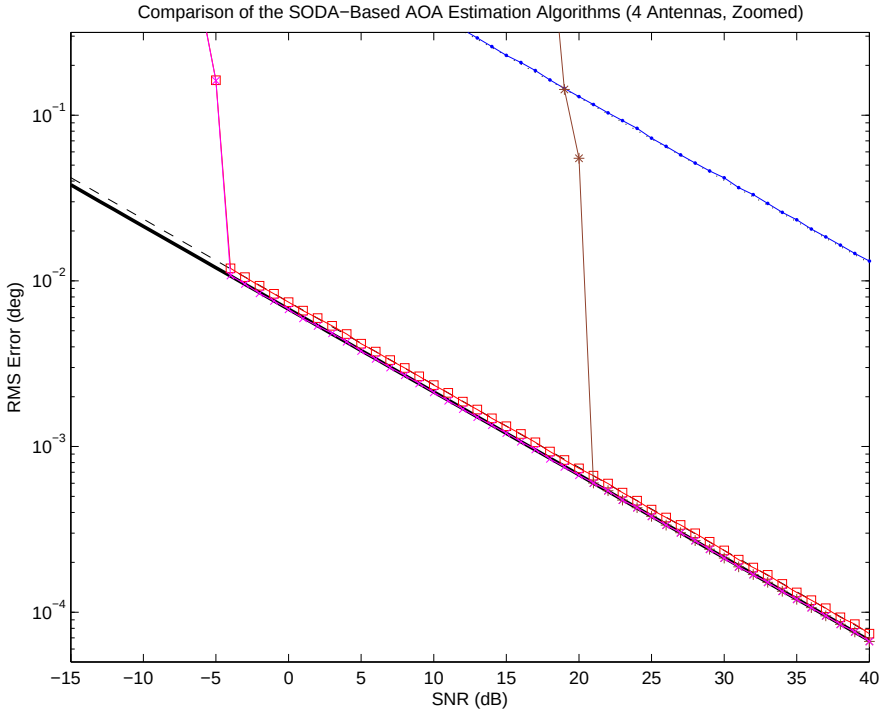

Figure 4.12: RMS error performance of each algorithm as a function of SNR. Simulation parameters: $K = 4$ antennas, $\theta = 23.42°$, $f = 9410$ MHz, $\varphi = 0°$, $N = 2048$ samples, $t_s = 750$ ps and $\mathcal{Q} = 10,000$ realisations.

Algorithm	Algorithm Complexity	Execution Time
SODA	$O(\Phi + M + 1)$	1.00
SBI	$O(\Phi + 2M)$	1.01
SODA-Cued Opt.	$O(\Phi + M(\Gamma + 2))$	1.16
SBI-Cued Opt.	$O(\Phi + M(\Gamma + 2))$	1.12

Table 4.1: Relative execution times for the SODA-based algorithms.

times in Table 4.1 with Table 3.4 shows that the SODA and SBI interferometers are marginally faster than the line fitting algorithm. These algorithms will therefore be preferred for time-critical applications. On the other hand, the SODA-cued and SBI-cued optimisation methods are only marginally slower than the SODA interferometer. Since they achieve optimal AOA estimation performance at high SNR, these algorithms will generally be preferred for optimal AOA estimation.

4.5 Other Considerations

4.5.1 Other Linear Combinations of First-Order Phase Delays

The SODA interferometer presented thus far forms two first-order interferometer baselines, d_{21} and d_{32}, using three physical antennas with one antenna common between the two baselines. A linear combination of the two first-order phase delays obtained from these baselines, $\tilde{\psi}_{21}$ and $\tilde{\psi}_{32}$, are then used to obtain an unambiguous second-order phase delay, $\tilde{\psi}_{\Delta}$, i.e.

$$\tilde{\psi}_{\Delta} = \left[\tilde{\psi}_{32} - \tilde{\psi}_{31}\right]_{2\pi}. \tag{4.35}$$

It should be noted that the above is not the only possible linear combination of first-order phase delays and that it is possible to obtain the same second-order phase delay using other linear combinations of the first-order phase delays. Furthermore, the number of possible linear combinations increases as the number of available antennas increase. However, it is important to note that increasing the number of first-order phase delays and/or using high magnitude coefficients in the linear combination will also increase the variance of the second-order phase delay estimate. In other words, using a large number of antennas or using a linear combination of first-order phase delays with large coefficients may in fact result in a RMS error that is worse than the 3-antenna SODA interferometer presented in Section 4.2.

Example 4.4
Consider a 6-antenna SODA interferometer whose first-order baselines, d_{21}, d_{54} and d_{63}, are chosen such that a second-order baseline, $d_{\Delta,\text{6-Ant}}$, can be formed using the following linear combination,

$$d_{\Delta,\text{6-Ant}} = d_{63} - d_{54} - 2d_{21}, \tag{4.36}$$

and that $d_{\Delta,\text{6-Ant}}$ is unambiguous in the sense that it satisfies (4.5). The

corresponding second-order phase delay, $\tilde{\psi}_{\Delta,\text{6-Ant}}$, can be computed as

$$\begin{aligned}\tilde{\psi}_{\Delta,\text{6-Ant}} &= \left[\tilde{\psi}_{63} - \tilde{\psi}_{54} - 2\tilde{\psi}_{21}\right]_{2\pi}, &(4.37)\\ &= \left[(\tilde{\Phi}_6 - \tilde{\Phi}_3) - (\tilde{\Phi}_5 - \tilde{\Phi}_4) - 2(\tilde{\Phi}_2 - \tilde{\Phi}_1)\right]_{2\pi}, &(4.38)\\ &= \left[\tilde{\Phi}_6 - \tilde{\Phi}_5 + \tilde{\Phi}_4 - \tilde{\Phi}_3 - 2\tilde{\Phi}_2 + 2\tilde{\Phi}_1\right]_{2\pi}, &(4.39)\end{aligned}$$

where $\tilde{\Phi}_1$, $\tilde{\Phi}_2$, $\tilde{\Phi}_3$, $\tilde{\Phi}_4$, $\tilde{\Phi}_5$ and $\tilde{\Phi}_6$ are the phase measurements of each channel and are assumed to have an associated variance $\sigma^2_{\Phi_1}$, $\sigma^2_{\Phi_2}$, $\sigma^2_{\Phi_3}$, $\sigma^2_{\Phi_4}$, $\sigma^2_{\Phi_5}$ and $\sigma^2_{\Phi_6}$ respectively. From (4.23), the variance of the second-order phase delay estimate, $\sigma^2_{\psi_{\Delta,\text{6-Ant}}}$, is given by

$$\sigma^2_{\psi_{\Delta,\text{6-Ant}}} = \sigma^2_{\Phi_6} + \sigma^2_{\Phi_5} + \sigma^2_{\Phi_4} + \sigma^2_{\Phi_3} + 4\sigma^2_{\Phi_2} + 4\sigma^2_{\Phi_1}. \tag{4.40}$$

Assuming that the variance of the phase measurements in each channel are the same, i.e. $\sigma^2_\Phi = \sigma^2_{\Phi_1} = \sigma^2_{\Phi_2} = \sigma^2_{\Phi_3} = \sigma^2_{\Phi_4} = \sigma^2_{\Phi_5} = \sigma^2_{\Phi_6}$, the variance of the second-order phase delay estimate, $\sigma^2_{\psi_{\Delta,\text{6-Ant}}}$, simplifies to

$$\sigma^2_{\psi_{\Delta,\text{6-Ant}}} = 10\sigma^2_\Phi \equiv 5 \cdot \frac{1}{\eta N}. \tag{4.41}$$

In Section 4.2.5, it was shown that the phase delay of a 2-antenna first-order interferometer with a physical baseline of d_Δ has a variance given by (4.19) as follows

$$\sigma^2_{\psi_{21},\text{first-order}} = 2\sigma^2_\Phi \equiv \frac{1}{\eta N}, \tag{4.42}$$

Inspection of (4.41) and (4.42) suggests that the variance of the second-order phase delay obtained using the 6-antenna implementation of the SODA interferometer is five times higher than the equivalent first-order phase delay estimate. This further suggests that the RMS error in the AOA estimation performance of the 6-antenna SODA interferometer will be a factor of $\sqrt{5}$ higher than the RMS error of the equivalent first-order interferometer.

In this particular example, the RMS error of the 6-antenna SODA interferometer is actually higher than the RMS error of the 3-antenna SODA interferometer as discussed in Section 4.2.5. Thus, this example shows that implementing a SODA interferometer with more antennas and a more complex linear combination of first-order phase delays does not necessarily improve the AOA estimation and may even be worse than the 3-antenna implementation. ∎

A drawback of the 3-antenna SODA interferometer is that one of the antennas is common between the two first-order baselines. This introduces a correlated noise component which ultimately leads to a larger than necessary RMS error in the AOA estimation. With four or more antennas, a linear combination of first-order phase delays that avoids the use of a common antenna can be chosen which may result in a lower RMS error.

Example 4.5
Consider a 4-antenna SODA interferometer whose first-order baselines, d_{21} and d_{43}, are chosen such that a second-order baseline, $d_{\Delta,\text{4-Ant}}$, can be formed using the following linear combination,

$$d_{\Delta,\text{4-Ant}} = d_{43} - d_{21}, \tag{4.43}$$

and that $d_{\Delta,\text{4-Ant}}$ is unambiguous in the sense that it satisfies (4.5). Using a similar analysis to Example 4.4, it can be shown that the RMS error of the 4-antenna implementation of the SODA interferometer is a factor of $\sqrt{2}$ higher than the RMS error of the equivalent first-order interferometer and is lower than the RMS error of the 3-antenna SODA interferometer by a factor of

$$\left(1 - \frac{\sqrt{2}}{\sqrt{3}}\right) \times 100\% = 18.35\%. \quad \blacksquare \tag{4.44}$$

Example 4.5 shows that the RMS error of the SODA interferometer can be slightly improved by choosing a linear combination of first-order phase delays that avoids the use of a common antenna. However, such an implementation requires the use of four antennas and so this performance improvement comes at the expense of additional hardware costs.

In Section 4.3, it was shown that the 3-antenna SODA AOA estimate can be used with the conventional first-order ambiguity resolution methods discussed in Section 3.6 and Section 3.7 to provide a more significant improvement in the AOA estimation performance. Since these methods provide a better performance with a smaller number of antennas, and hence at a reduced cost, the remainder of this thesis shall only consider the 3-antenna SODA interferometer.

4.5.2 Non-Collinear SODA Interferometer

The SODA interferometer presented thus far has assumed a collinear array. In this section, it will be shown that the collinearity requirement can be relaxed for smaller apertures to allow slightly non-linear arrays to be constructed. This may allow a conformal mounting of the antennas onto a platform, such as the hull of an aircraft or the mast of a ship.

In general, any non-linear array comprising of three antennas can be considered as a triangle. For mathematical convenience, a mathematical polar coordinate system (see Figure 3.3) can be defined so that Antennas 1 and 3, and hence the the d_{31} baseline, are aligned to the 0° axis. Antenna 2 can be positioned so that the d_{21} baseline interferometer is rotated by an angle, α, counter-clockwise away from the 0° axis. This array geometry is depicted in Figure 4.13.

The unambiguous first-order phase delays for the d_{21} and d_{31} baselines, i.e. ψ_{21} and ψ_{31}, are given by

$$\psi_{21} = \frac{2\pi f d_{21}}{c} \sin(\theta + \alpha), \tag{4.45}$$

$$\psi_{31} = \frac{2\pi f d_{31}}{c} \sin\theta, \tag{4.46}$$

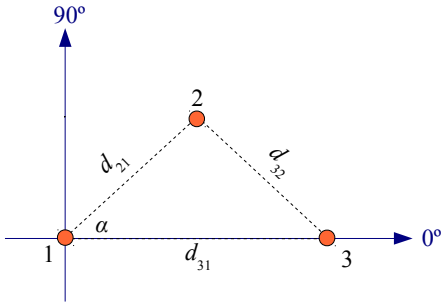

Figure 4.13: A 3-antenna non-linear array can be considered as a triangular array.

where $0 \leq \alpha \leq \pi/2$, and it is assumed that $d_{31} > d_{21} \gg \lambda_{\min}/2$, and where $\lambda_{\min}$ is the wavelength of the highest frequency of interest. It can be shown that the second-order phase delay is given by

$$\psi_\Delta = \psi_{31} - 2\psi_{21} = \frac{2\pi f d_\Delta}{c} \sin(\theta + \Theta), \tag{4.47}$$

where d_Δ is the second-order baseline and Θ is a rotation angle defined as follows

$$d_\Delta = \sqrt{d_{31}^2 + 4d_{21}^2 - 4d_{21}d_{31}\cos\alpha}, \tag{4.48}$$

$$\Theta = \arctan\left(\frac{-2d_{21}\sin\alpha}{d_{31} - 2d_{21}\cos\alpha}\right). \tag{4.49}$$

Like the collinear case, the second-order phase delay, ψ_Δ, can be made unambiguous if the following constraint is satisfied,

$$0 < d_\Delta \leq \frac{\lambda_{\min}}{2}. \tag{4.50}$$

The second-order phase delay, ψ_Δ, therefore corresponds to a virtual antenna pair with a second-order baseline, d_Δ, that is rotated by an angle Θ. The AOA of the signal can then be unambiguously estimated using the so-called *non-collinear SODA interferometer* as follows

$$\hat{\theta} = \arcsin\left(\frac{c\tilde{\psi}_\Delta}{2\pi f d_\Delta}\right) - \Theta. \tag{4.51}$$

Note that while the physical triangular array is not a linear array, the virtual array as described above is still a linear array and so the AOA estimation still limited to a 180° field-of-view (FOV). Hence, the non-collinear SODA interferometer is only useful for mounting purposes and does not provide any increase in the FOV of the system.

For an arbitrary aperture, d_{31}, the non-collinear SODA interferometer requires corresponding d_{21} baseline interferometer to be

$$d_{21} = \frac{1}{2}d_{31}\cos\alpha + \frac{1}{2}\sqrt{d_\Delta^2 - d_{31}^2\sin^2\alpha}. \tag{4.52}$$

Since d_{21} and d_{31} are physical lengths, their values must be real and positive. This implies that the term under the square root sign in (4.52) must also be real and so it can be shown that the d_{21} baseline rotation angles, α, must satisfy

$$\alpha \leq \arcsin\left(\frac{d_\Delta}{d_{31}}\right). \tag{4.53}$$

The constraint (4.53) effectively limits the maximum value of α and hence also limits the extent of non-collinearity that can be tolerated for a given aperture. Figure 4.14 plots the maximum value of α when $d_\Delta = \lambda/2$ as a function of the array aperture, i.e. the d_{31} baseline. This figure shows that for larger apertures, α rapidly tends towards zero and so the array becomes increasingly collinear. However, for smaller apertures, the maximum value of α may be as high as 30°.

Due to the non-collinear nature of the array geometry, the 'broadside or "looking" direction of the SODA virtual antenna pair is rotated by an angle, Θ. Figure 4.15 plots Θ as a function of α when $d_{31} = 50\lambda$ and $d_\Delta = \lambda/2$. This figure shows that as α increases to its maximum value as specified by (4.53), Θ rapidly approaches 90°. This implies that care must be taken to correctly orientate the non-collinear SODA interferometer to offset the rotation angle of the virtual array.

4.5.3 Field-of-View

Since the collinear and non-collinear SODA interferometer both create a virtual antenna pair from three antennas, then regardless of the array geometry, the virtual array is effectively a linear array with a field-of-view (FOV) limited to $[-90°, 90°]$. Hence, the discussion in Section 3.9.3 regarding the FOV for linear arrays is equally relevant for SODA interferometers. That is, in order to construct a SODA-based direction finding system that is capable of a 360° FOV, multiple arms of linear SODA interferometers will need to be orientated at different rotation angles as illustrated in Figure 3.34.

4.6 Summary

This chapter introduced the concept of using second-order processing to obtain the output from a virtual antenna pair for unambiguous AOA estimation in a computationally fast manner from highly ambiguous, long baseline interferometers. The AOA estimation performance of the SODA interferometer was shown to be independent of the physical first-order baselines. Rather, the AOA estimation performance of the SODA interferometer was shown to be a factor of $\sqrt{3}$ worse than an equivalent physical first-order short-baseline interferometer. However, in absolute terms, the SODA interferometer is still able to achieve sub-degree RMS errors at high SNR and so is a good candidate for implementation in real-time radar intercept receivers, such as ES systems, where fast AOA estimation is necessary and relatively coarse AOA accuracies can be tolerated.

In order to take advantage of the higher accuracies offered by the physical first-order interferometers that make up the SODA interferometer, it was shown that the SODA AOA estimate can be used to cue the first-order ambiguity resolution methods. These techniques are referred to as the SBI, SODA-cued and SBI-cued correlative interferometers. At high SNRs, the SODA-cued and SBI-cued correlative interferometers can be more efficiently implemented by bypassing the grid search to directly cue the optimisation algorithm.

The SBI and SBI-cued correlative interferometers are asymptotically efficient at high SNR and strikes a good balance between the AOA estimation accuracy and computation time. The SODA-cued and SBI-cued correlative interferometer were shown to

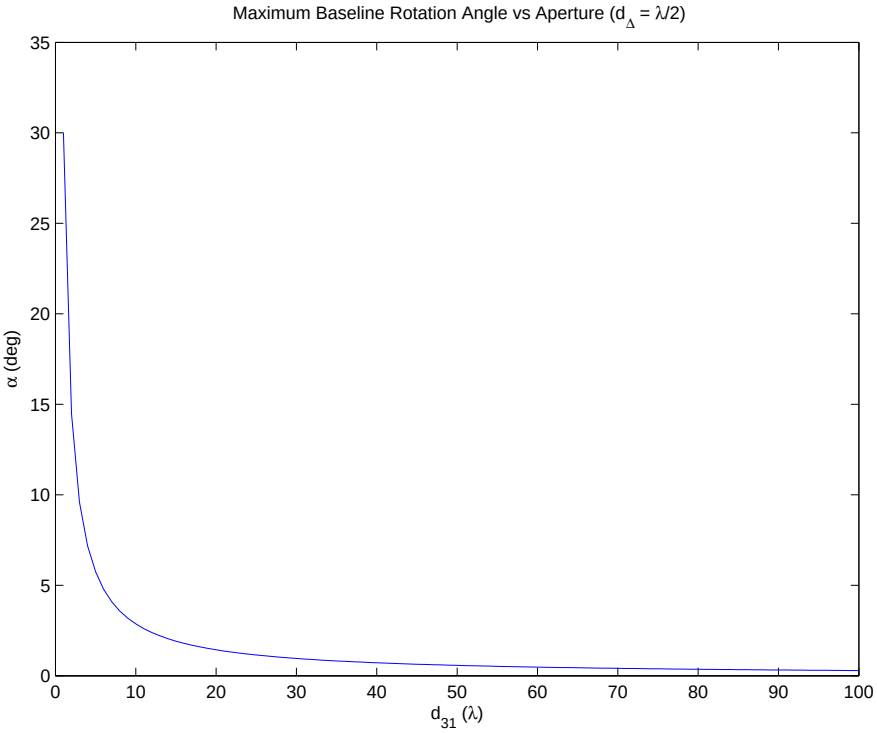

Figure 4.14: d_{21} baseline rotation angle, α, vs the array aperture for $d_\Delta = \lambda/2$.

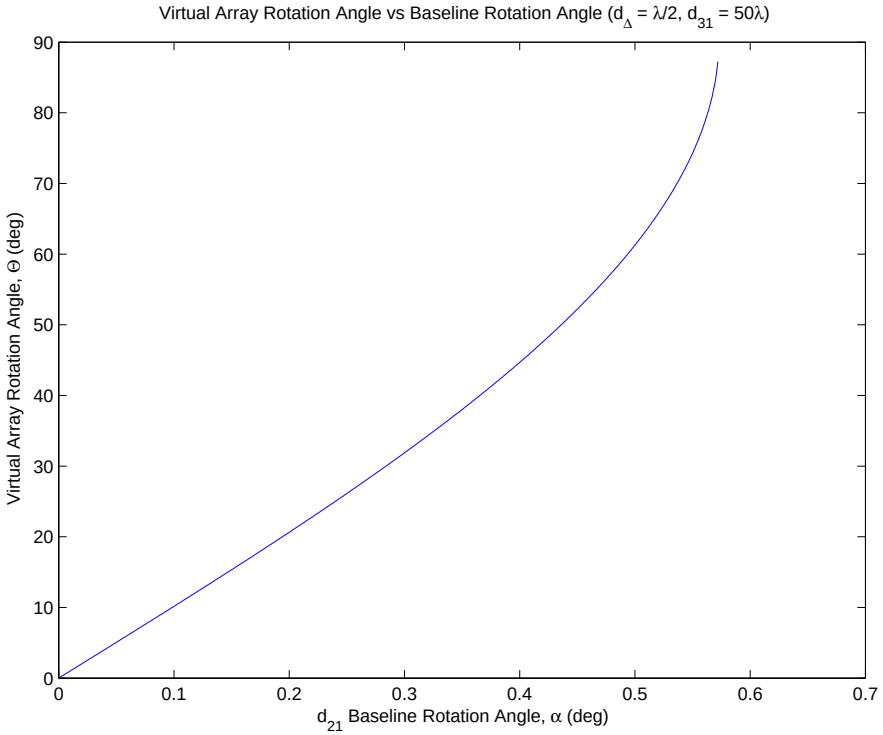

Figure 4.15: Virtual array rotation angle, Θ, vs the d_{21} rotation angle, α, for $d_{31} = 50\lambda$ and $d_\Delta = \lambda/2$.

provide better AOA estimation performance than the SBI interferometer since they achieve the K-antenna root-CRLB while the SBI interferometer only achieves the d_{K1}-root-CRLB corresponding to the widest antenna pair. When the grid search is bypassed, the SBI-cued optimisation algorithm exhibits a significantly lower SNR threshold than the SODA-cued optimisation algorithm and so will generally be preferred. These results suggest that the SBI and SBI-cued correlative interferometers are good candidates for implementation in real-time radar intercept receivers, such as ES or ELINT receivers, where higher AOA accuracies are required.

Finally, non-collinear SODA geometries were considered. This study showed that while it was possible to implement a SODA interferometer using non-collinear geometries, the extent of non-collinearity that could be tolerated is generally very small, particularly for long first-order baselines. Furthermore, the orientation of the virtual array generated from a non-collinear SODA geometry is rotated in azimuth and so care must be taken to correctly orientate the array. Finally, since the non-collinear SODA interferometer does not provide any improvement in the field-of-view of the system, the use of non-collinear arrays is mainly useful for conformal mounting purposes.

Chapter 5

Array Processing Using Second Order Difference Arrays

Array processing algorithms simultaneously exploit the amplitude and phase delay information from all available antennas in a coherent fashion to perform AOA estimation. This is in contrast to the operation of interferometers which only exploit the phase delay information. Interferometers ignore the signal's amplitude and so effectively give equal weighting to all phase delay measurements.

It would be remiss of this thesis to only discuss AOA estimation in the context of interferometry without any discussion on array processing techniques. This chapter shall introduce two common array processing techniques, namely the conventional phaseshift beamformer (CBF) and multiple signal classification (MUSIC) algorithms, and focus on their application to second-order difference array (SODA) geometries for unambiguous AOA estimation. The intention of this chapter is not to produce new array processing algorithms, but rather to evaluate the performance of the conventional algorithms using a SODA geometry. Since SODA geometries are linear arrays, the array processing methods discussed in this chapter will be confined to linear arrays.

5.1 Beamforming and Array Processing

5.1.1 Signal Model

Consider a single, narrowband signal incident upon a linear array of K antennas as depicted in Figure 5.1. As described in Section 3.2.2, the noiseless, narrowband signal model, $s(t)$, can be written as a function of time, t, as specified in (3.7) as follows

$$s(t) = Ae^{j(2\pi ft+\varphi)}, \tag{5.1}$$

where A, f and φ represent the signal's peak amplitude, carrier frequency and initial phase respectively. In practical systems, the ideal signal is corrupted by an additive noise component, $\epsilon(t)$. Taking the position of the first antenna as an arbitrary reference, the noisy antenna output of the k-th antenna with respect to the first antenna can be written as

$$x_{k1}(t) = s(t+\tau_{k1}) + \epsilon_k(t) = Ae^{j(2\pi ft+\varphi+\psi_{k1}(\theta))} + \epsilon_k(t), \tag{5.2}$$

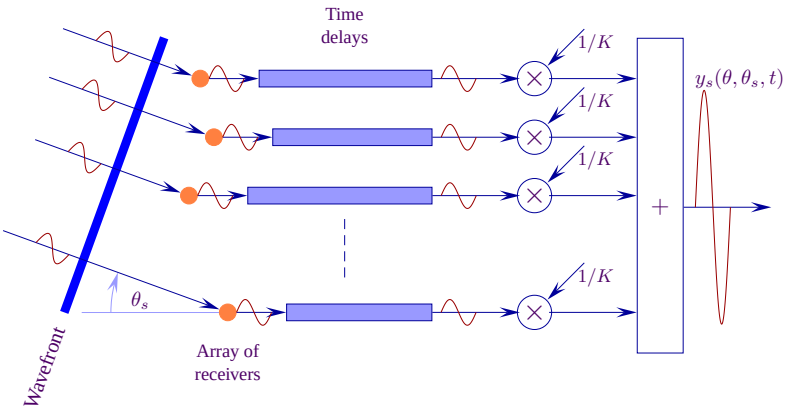

Figure 5.1: Array processing algorithms exploit the propagation delays in a coherent manner.

where $k = 1, 2, \ldots, K$, τ_{k1} is the propagation time delay for the signal to reach the k-th antenna after arriving at the first antenna, and $\epsilon_k(t)$ represents the independent receiver noise in the k-th channel. The equivalent propagation phase delay between the k-th antenna and the first antenna, $\psi_{k1}(\theta)$, is given by

$$\psi_{k1}(\theta) = 2\pi f \tau_{k1} = \frac{2\pi f d_{k1}}{c} \sin\theta. \tag{5.3}$$

As described in Section 3.2.2, the propagation time, τ_{kl}, is actually a time advance for positive θ and a time delay for negative θ. Similarly, the propagation phase, ψ_{kl} is a phase advance for positive θ and a phase delay for negative θ. However, for notational brevity, this thesis will generally refer to τ_{kl} and ψ_{kl} as the propagation time delay and phase delay respectively. In this chapter the phase delay is explicitly written as a function of the AOA to highlight the relationship between the phase delays and the AOA of the signal.

The narrowband signal component of the antenna output can be separated into a time-varying component, $s(t)$, and an independent phase delay, $e^{j\psi_{k1}(\theta)}$, as follows,

$$x_{k1}(t) = s(t)e^{j\psi_{k1}(\theta)} + \epsilon_k(t). \tag{5.4}$$

For a multi-channel digital receiver, the digital sampling of the signal occurs at regular, discrete time intervals, t_s. For a collection of N digital samples, the n-th sample of the narrowband signal model can be re-written as

$$x_{k1}[n] = s[n]e^{j\psi_{k1}(\theta)} + \epsilon_k[n], \tag{5.5}$$

which corresponds to the time instance, $t = nt_s$, and $n = 0, 1, \ldots, N-1$. The output from all K antennas can be expressed more compactly in vector notation as

$$\boldsymbol{x}[n] = s[n] \begin{pmatrix} e^{j\psi_{11}(\theta)} \\ e^{j\psi_{21}(\theta)} \\ \vdots \\ e^{j\psi_{K1}(\theta)} \end{pmatrix} + \begin{pmatrix} \epsilon_1[n] \\ \epsilon_2[n] \\ \vdots \\ \epsilon_K[n] \end{pmatrix} = s[n]\,\boldsymbol{v}(\theta) + \boldsymbol{\epsilon}[n], \tag{5.6}$$

where $\boldsymbol{x}[n]$ is a $K \times 1$ vector representing the K antenna outputs of the n-th sample, $\boldsymbol{\epsilon}[n]$ is a $K \times 1$ vector representing the noise in each channel, and $\boldsymbol{v}(\theta)$ is a $K \times 1$ vector representing the propagation phase delays of the signal with respect to the first antenna and is defined as

$$\boldsymbol{v}(\theta) = \begin{pmatrix} e^{j\psi_{11}(\theta)} \\ e^{j\psi_{21}(\theta)} \\ \vdots \\ e^{j\psi_{K1}(\theta)} \end{pmatrix} = \begin{pmatrix} e^{j2\pi f d_{11} \sin\theta/c} \\ e^{j2\pi f d_{21} \sin\theta/c} \\ \vdots \\ e^{j2\pi f d_{K1} \sin\theta/c} \end{pmatrix}. \tag{5.7}$$

The aim of the array processors is to search for the AOA whose corresponding propagation phase delay vector best matches the signal's propagation phase delay vector. This search is the electronic equivalent of a mechanically steered directional antenna and is hence termed *electronic steering*. The AOA and propagation phase delay vector corresponding to the currently steered direction are termed the *steering angle* and *steering vector* respectively. The steering parameters are controlled by the AOA estimation algorithm and are not to be confused with the signal parameters. The subscript $_s$ will be used to distinguish the steering parameters from the signal parameters.

The antenna array effectively has a beampattern associated with the steering angle that is given by

$$P_{\text{beampattern}}(\theta, \theta_s) = \frac{1}{K^2} \left| \boldsymbol{v}^H(\theta)\, \boldsymbol{v}(\theta_s) \right|^2, \tag{5.8}$$

where $P_{\text{beampattern}}(\theta, \theta_s)$, represents the received power from a unit amplitude plane wave incident upon the array from an angle θ when the array is steered to an angle, θ_s. Figure 5.2 shows the beampattern for an 8-antenna uniform linear array (ULA) with a $\lambda/2$ spacing between the antennas and when the steering angle is $\theta_s = 0°$. Since a narrow "beam" is formed in the direction of the steered angle, algorithms which exploit the beampattern are generally termed *beamformers*.

5.1.2 Conventional Phaseshift Beamformer

A straightforward implementation of a beamformer is to search for the AOA that produces the propagation phase delays that most closely match the signal's measured propagation phase delays [2, 45, 91]. For the steering angle, θ_s, the corresponding beamformer output, $\boldsymbol{y}[\theta_s, n]$, is given by

$$\boldsymbol{y}[\theta_s, n] = \frac{1}{K} \boldsymbol{v}^H(\theta_s)\, \boldsymbol{x}[n], \tag{5.9}$$

where the superscript ^{H} represents the Hermitian (complex conjugate transpose) operation. Since it is conventional to express the array output in terms of power, the array output power of the conventional phaseshift beamformer (CBF), $P_{\text{CBF}}(\theta_s)$, can be

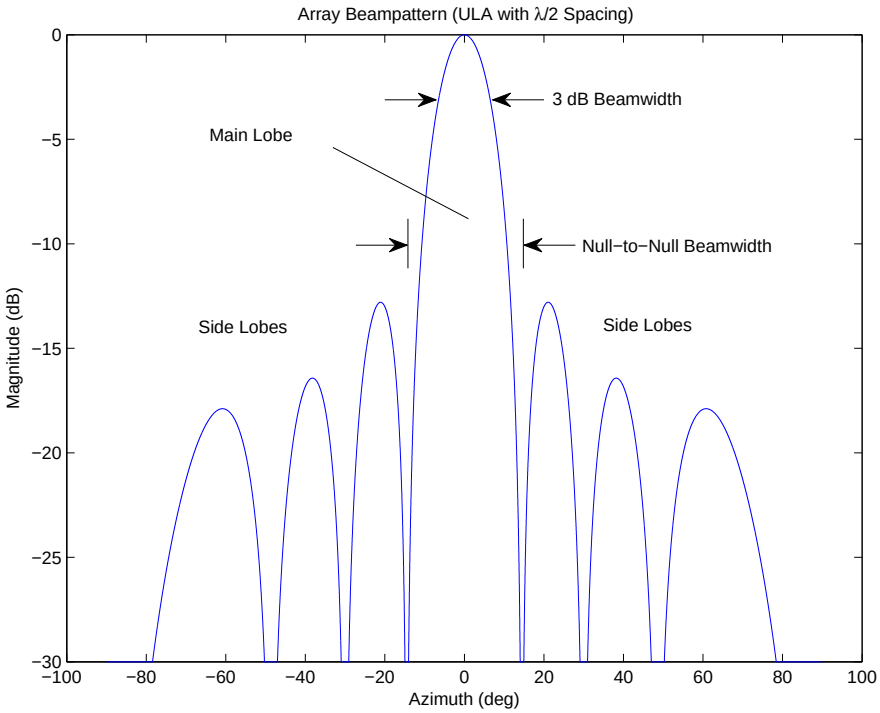

Figure 5.2: Beampattern of an 8-antenna uniform linear array with a $\lambda/2$ antenna spacing and steered at $\theta_s = 0°$.

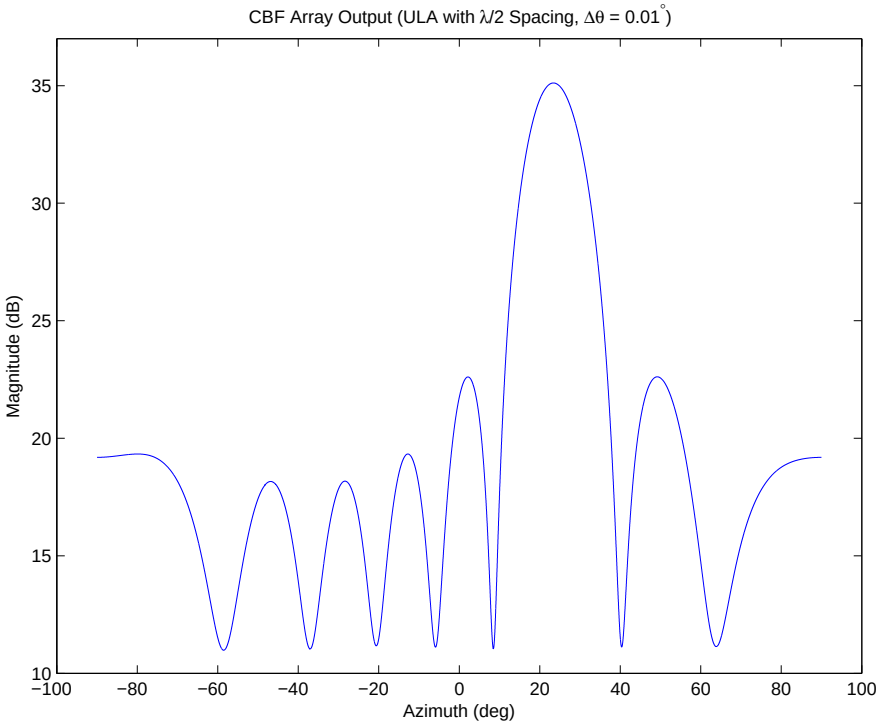

Figure 5.3: Array output of the CBF algorithm using an 8-antenna uniform linear array with a $\lambda/2$ antenna spacing when $\theta = 23.42°$. Simulation parameters: $\eta = 15$ dB, $f = 16$ GHz, $N = 2048$ samples, and $\Delta\theta = 0.01°$.

defined as follows

$$\begin{aligned} P_{\mathrm{CBF}}(\theta_s) &= E\left\{ |\, \boldsymbol{y}\,[\theta_s, n]|^2 \right\} && (5.10)\\ &= E\left\{ \left| \frac{1}{K}\, \boldsymbol{v}^{\,H}(\theta_s)\, \boldsymbol{x}\,[n] \right|^2 \right\} && (5.11)\\ &= \frac{1}{K^2}\, \boldsymbol{v}^{\,H}(\theta_s) E\left\{ \boldsymbol{x}\,[n]\, \boldsymbol{x}^{\,H}[n] \right\}\, \boldsymbol{v}\,(\theta_s) && (5.12)\\ &= \frac{1}{K^2}\, \boldsymbol{v}^{\,H}(\theta_s)\, \boldsymbol{R}\, \boldsymbol{v}\,(\theta_s), && (5.13) \end{aligned}$$

where $E\{\cdot\}$ represents the expectation operator, and $\boldsymbol{R} = E\left\{ \boldsymbol{x}\,[n]\, \boldsymbol{x}\,[n]^H \right\}$ is a $K \times K$ matrix termed the *covariance matrix*, or *cross-spectral matrix*.

Using the CBF algorithm, the AOA estimation can be performed by searching for the peaks in the beamformer output. For L signal arrivals, the AOA of the signals will generally correspond to the steering angles of the L highest peaks of the beamformer output. In general, a K-antenna array can estimate the AOA of up to $K-1$ signals simultaneously incident upon the array. In the special case of a single signal, i.e. $L = 1$, the AOA estimation can be written as

$$\hat{\theta} = \underset{\theta_s}{\arg\max}\, P_{\mathrm{CBF}}(\theta_s) = \underset{\theta_s}{\arg\max}\, \frac{1}{K^2}\, \boldsymbol{v}^{\,H}(\theta_s)\, \boldsymbol{R}\, \boldsymbol{v}\,(\theta_s). \tag{5.14}$$

Figure 5.3 shows the array output of the CBF algorithm using an 8-antenna uniform linear array with a $\lambda/2$ spacing. In this example, the AOA of the signal is $\theta = 23.42°$ and the electronic scanning is performed with a resolution of $\Delta\theta = 0.01°$. This figure shows that there is a distinct peak in the array output in the direction of the signal's AOA.

In practice, the cross-spectral matrix can be estimated by averaging over a number of samples in the time-domain, namely,

$$\hat{\boldsymbol{R}} = \frac{1}{N} \sum_{n=0}^{N-1} \boldsymbol{x}\,[n]\, \boldsymbol{x}^{\,H}[n]. \tag{5.15}$$

Alternatively, frequency-domain beamforming can be performed by estimating the cross-spectral matrix in the frequency-domain. The element in the k-th row and l-th column of the cross spectral matrix, R_{kl}, can be written as

$$\hat{R}_{kl} = \frac{1}{W} \sum_{w=1}^{W} X_{k,f,w} X^*_{l,f,w}, \tag{5.16}$$

where $X_{k,f,w}$ and $X_{l,f,w}$ represent the Fourier coefficients of the w-th snapshot for the k-th and l-th receiver evaluated at the signal frequency, f, respectively. The estimate of the cross spectral matrix may be improved by averaging over W independent snapshots.

Optimisation Using Newton's Method

The CBF algorithm is another example of a grid search algorithm. As discussed in 3.7.5, all practical implementations of a grid search algorithm will have a discrete search

resolution and so the resolution of the AOA estimation will be quantised. Newton's Method can be used to refine the AOA estimate as follows [71]

$$\hat{\theta}^{(\gamma+1)} = \hat{\theta}^{(\gamma)} - \frac{P'_{\text{CBF}}(\hat{\theta}^{(\gamma)})}{P''_{\text{CBF}}(\hat{\theta}^{(\gamma)})}, \tag{5.17}$$

where the initial estimate is set to the AOA estimate that corresponds to the maximum output of the CBF algorithm as described by (5.14), i.e. $\hat{\theta}^{(1)} = \hat{\theta}_{\text{CBF}}$, Γ is the number of iterations, $\gamma = 1, 2, \ldots, \Gamma$, and $P'_{\text{CBF}}(\hat{\theta}^{(\gamma)})$ and $P''_{\text{CBF}}(\hat{\theta}^{(\gamma)})$ represent the first and second derivatives of $P_{\text{CBF}}(\hat{\theta}^{(\gamma)})$ with respect to $\theta^{(\gamma)}$ and are given by

$$P'_{\text{CBF}}(\hat{\theta}^{(\gamma)}) = \sum_{k=1}^{K}\sum_{l=1}^{K} j v_l^* C_{lk} v_k \left(\frac{\partial \psi_{k1}}{\partial \theta} - \frac{\partial v_l}{\partial \theta}\right) \tag{5.18}$$

$$P''_{\text{CBF}}(\hat{\theta}^{(\gamma)}) = \sum_{k=1}^{K}\sum_{l=1}^{K} v_l^* C_{lk} v_k \left(2\frac{\partial \psi_{k1}}{\partial \theta}\frac{\partial \psi_{l1}}{\partial \theta} + j\left(\psi_{l1} - \psi_{k1}\right) - \left(\frac{\partial \psi_{k1}}{\partial \theta}\right)^2 - \left(\frac{\partial \psi_{l1}}{\partial \theta}\right)^2\right). \tag{5.19}$$

In the above expressions, $C_{lk} = \hat{R}_{lk}$, which represents the element at the l-th row and k-th column of the estimated cross spectral matrix, $\hat{\boldsymbol{R}}$, and v_k and v_l represent the k-th and l-th elements of the steering vector evaluated at $\hat{\theta}^{(\gamma)}$, i.e. $\boldsymbol{v}(\hat{\theta}^{(\gamma)})$. The optimisation algorithm is terminated when the specified maximum number of iterations has been completed or once the difference between iterative estimates falls below a specified tolerance, i.e. $|\hat{\theta}^{(\gamma+1)} - \hat{\theta}^{(\gamma)}| \leq \delta\theta_{\text{tol}}$, where $\delta\theta_{\text{tol}}$ is the chosen tolerance.

Algorithm Complexity

A typical execution of the CBF algorithm requires that the cross-spectral matrix be estimated. Assuming that a FFT is used to estimate the cross-spectral matrix in the frequency domain as described by (5.16), the algorithm complexity to estimate the cross-spectral matrix is $O(W(\Phi + K^2))$, where $\Phi = KN\log_2 N$ represents the number of operations to perform the FFT on each antenna output, K is the number of antennas, N is the number of samples and W is the number of snapshots.

The next part of the CBF algorithm is the grid search. For each steering angle, the steering vector is computed from (5.7) and has an algorithm complexity of $O(K)$. The CBF array output is then computed from (5.13) using matrix multiplications and so has an algorithm complexity of $O(K^2)$. A search must then be performed to determine which angle produces the largest array output. For G steering angles, this will be an $O(G)$ operation. The algorithm complexity of the entire grid search is therefore approximately $O(G(K^2 + K + 1))$.

Finally, Newton's Method is used to refine the grid search estimate. For each iteration, Newton's Method requires calculating the derivatives of the array output from (5.18) and (5.19) which are $O(K^2)$ operations. For Γ iterations, the algorithm complexity of the optimisation is then approximately $O(K^2\Gamma)$.

The total algorithm complexity of the CBF algorithm is therefore approximately $O(W\Phi + K^2(W + G + \Gamma) + GK + G)$. It should be noted that the algorithm complexity presented here is effectively an approximation of the number of loops performed by the algorithm and does not represent a detailed analysis for all operations in the algorithm. Furthermore, it does not distinguish between the speed of individual operations, such as addition and multiplication.

5.1.3 Optimal Beamformers and Super-Resolution Methods

Since its inception there have been many variations to the beamforming concept. In particular, so-called *optimal beamformers* were developed by applying carefully chosen weights to meet certain criteria of optimality [2, 45, 91, 92]. Some well-known optimal beamformers include the *maximum-likelihood beamformer*, which maximises the likelihood function of the array output [2, 45, 92, 93], the *maximum gain beamformer*, which maximises the array gain [92, 94], the *minimum mean square error beamformer*, which minimises the mean square error [2], and the *minimum variance distortionless response* (MVDR) beamformer, which minimises the output power of the array while normalising the beampattern in the steered direction [92, 94–96]. For applications with known signal waveforms, beamformers can also be developed to explicitly exploit the signal's waveform to give improved performance [97]. Examples of such beamformers include *chirp beamformers* [98–100] and *binary phase shift keyed (BPSK) beamformers* [101–103].

More recently, eigenanalysis of the cross-spectral matrix have shown that the signal and noise components of the array output spans different subspaces if they are uncorrelated. This gave rise to a new class of very powerful AOA estimation techniques generally known as subspace, or super-resolution, techniques. Some well-known super-resolution techniques include the *multiple signal classification* (MUSIC) [104], *estimation of signal parameters via rotational invariance principles* (ESPRIT) [105], and *min-norm* [106] algorithms. Strictly speaking, these methods are not beamformers since they do not form "beams" in the conventional sense. Furthermore, unlike beamformers whose array output power is related to the signal power, the output of super-resolution techniques have no physical meaning and are only used to indicate the AOA of a signal. As such, these methods are generally referred to as *array processors*.

5.1.4 Multiple Signal Classification (MUSIC)

MUSIC [2, 45, 91, 104] is a well-known array processing technique that is often used in high resolution AOA estimation problems. This technique exploits the orthogonality between the signal and noise subspaces of the cross-spectral matrix, $\boldsymbol{R}$.

The first step of the MUSIC algorithm is to perform an eigen-decomposition of the cross-spectral matrix to obtain the set of eigenvalues, $\{\gamma_1, \gamma_2, \ldots, \gamma_K\}$, and corresponding eigenvectors, $\{\boldsymbol{q}_1, \boldsymbol{q}_2, \ldots, \boldsymbol{q}_K\}$. It is assumed that the eigenvalues, and their corresponding eigenvectors, are sorted into descending order so that

$$\gamma_1 \geq \gamma_2 \geq \cdots \geq \gamma_K. \tag{5.20}$$

The output of the MUSIC algorithm, $P_{\text{MUSIC}}(\theta_s)$, can then be written as [2, 45, 104]

$$P_{\text{MUSIC}}(\theta_s) = \frac{1}{\sum_{k=L+1}^{K} |\, \boldsymbol{v}^{\,H}(\theta_s)\, \boldsymbol{q}_{\,k}|^2}, \tag{5.21}$$

where L is the number of signals simultaneously illuminating the array. In practice, L must either be known or estimated from the data [2, 91]. For the purposes of this thesis, it is assumed that only one signal is illuminating the array and so it is assumed that $L = 1$.

Figure 5.4 shows the array output of a MUSIC array processor when applied to the same AOA estimation problem as Figure 5.3. This figure shows that the array output has a single distinct peak in the direction of the signal's AOA. In contrast to the CBF algorithm, the array output of the MUSIC array processor has a very narrow mainlobe width and exhibits very low sidelobes. These highly desirable characteristics have led to the popularity of using the MUSIC array processor for AOA estimation problems. As previously stated, the peaks of the MUSIC array output only indicate the AOA of signals; the magnitude of the peaks are not related to the signal's power.

Optimisation Using Newton's Method

Newton's Method can also be used to optimise the quantised AOA estimate from the MUSIC grid search and can be obtained by replacing the derivatives, $P'_{\text{CBF}}(\theta^{(\gamma)})$ and $P''_{\text{CBF}}(\theta^{(\gamma)})$, in (5.17)–(5.19) with the corresponding MUSIC derivatives, $P'_{\text{MUSIC}}(\theta^{(\gamma)})$ and $P''_{\text{MUSIC}}(\theta^{(\gamma)})$, respectively. The MUSIC derivatives can be computed from (5.18) and (5.19), by setting $C_{lk} = \Lambda_{lk}$ which represents the element at the l-th row and k-th column of the matrix, $\boldsymbol{\Lambda}$, where

$$\boldsymbol{\Lambda} = \boldsymbol{Q}\, \boldsymbol{Q}^{\,H}, \tag{5.22}$$

and

$$\boldsymbol{Q} = \left[\; \boldsymbol{q}_{\,L+1} \quad \boldsymbol{q}_{\,L+2} \quad \cdots \quad \boldsymbol{q}_{\,K} \;\right]. \tag{5.23}$$

Algorithm Complexity

A typical execution of the MUSIC algorithm follows a similar sequence of operations to the CBF algorithm. However, the MUSIC algorithm requires an additional step to compute the eigenvalue decomposition of the cross-spectral matrix. For an array of K antennas, the algorithm complexity of an eigenvalue decomposition of a $K \times K$ matrix will be $O(K^3)$. The total algorithm complexity of the MUSIC algorithm is therefore approximately $O(W\Phi + K^3 + K^2(W + G + \Gamma) + GK + G)$.

5.2 Sparse Large Aperture Arrays

Inspection of the Cramér-Rao Lower Bound (CRLB) for the AOA estimation using a non-uniform linear array (NULA), as specified by (3.168), suggests that better AOA estimation performance can be obtained with large aperture arrays. This statement is consistent with the use of long baselines in interferometry to improve the AOA estimation performance. However, for a uniform linear array, unambiguous AOA estimation can

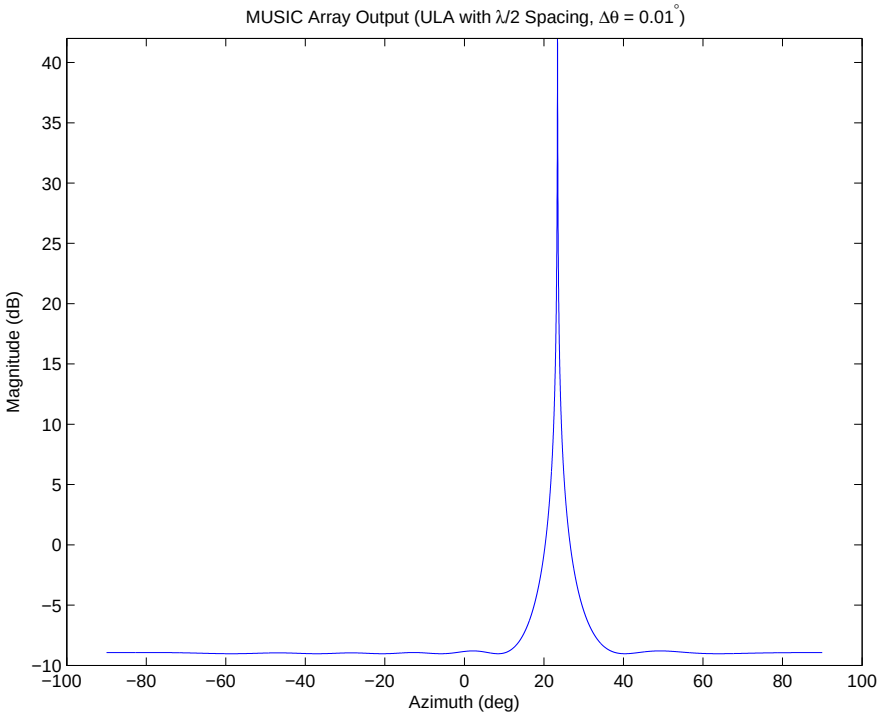

Figure 5.4: Array output of a MUSIC array processor using an 8-antenna uniform linear array with a $\lambda/2$ antenna spacing when $\theta = 23.42°$. Simulation parameters: $\eta = 15$ dB, $f = 16$ GHz, $N = 2048$ samples, $W = 1$ snapshot, and $\Delta\theta = 0.01°$.

only be obtained if the inter-element spacing between the antennas, d, is less than or equal to $\lambda_{\min}/2$ apart, i.e.

$$d \leq \frac{\lambda_{\min}}{2}, \tag{5.24}$$

where $\lambda_{\min}$ is the wavelength of the highest frequency of interest. This condition is the spatial equivalent of the Nyquist rate from digital sampling theory, and so is sometimes called the *spatial Nyquist rate* in array processing.

As with the interferometric case, this thesis assumes that physically large wideband antennas need to be used for wide spectrum electronic surveillance and so the spatial Nyquist rate will not be satisfied, i.e. $d > \lambda_{\min}/2$. As a result, *spatial aliasing* occurs and manifests in the array beampattern as so-called *grating lobes*. Grating lobes are peaks in the array beampattern that are indistinguishable from the main lobe and hence give rise to ambiguities in the AOA estimation. In terms of interferometry, spatial aliasing manifests as ambiguities in the phase delay measurements as described in Section 3.5.

Example 5.1
Figure 5.5 shows the beampattern for an 8-antenna uniform linear array with a 7.1429λ spacing between the antennas to form a 50λ physical aperture. This figure shows that when the array is steered to $\theta_s = 0°$, a main lobe forms at $0°$, however there also exists a number of grating lobes at $\pm 8.05°$, $\pm 16.26°$, $\pm 24.84°$, $\pm 34.06°$, $\pm 44.43°$, $\pm 57.15°$ and $\pm 78.55°$ respectively due

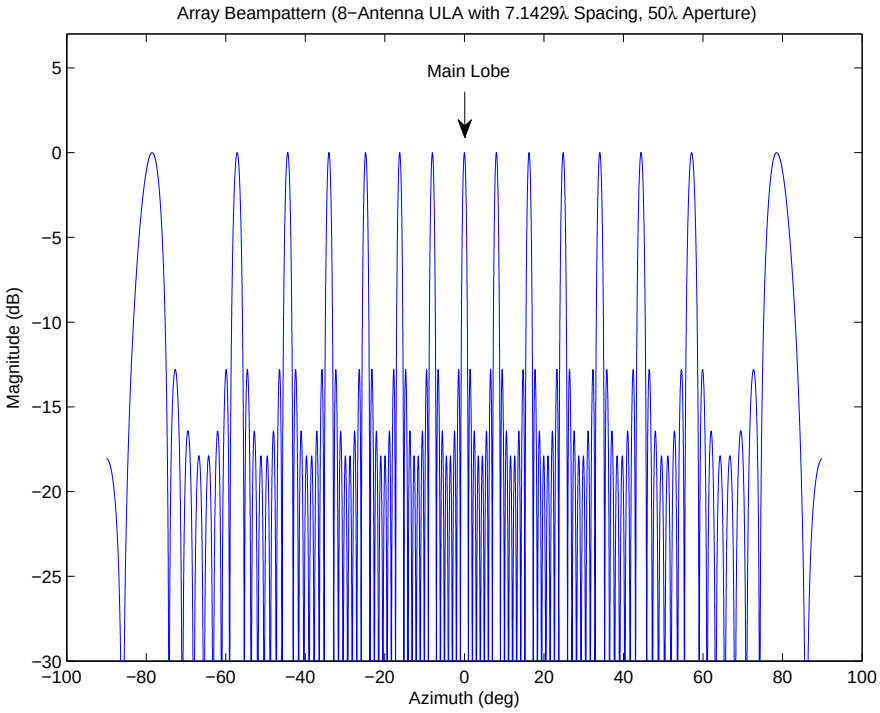

Figure 5.5: Beampattern of an 8-antenna uniform linear array with a uniform antenna spacing of 7.1429λ (50λ aperture).

to spatial aliasing.

Figure 5.6 and Figure 5.7 show the corresponding array outputs of CBF and MUSIC algorithms for a signal arriving from $\theta = 23.42°$. These figures show that the array outputs have a peak corresponding to the true AOA at $\theta = 23.42°$ as well as a number of grating lobes at $-90°$, $-59.60°$, $-46.26°$, $-35.63°$, $-26.27°$, $-17.61°$, $-9.35°$, $-1.29°$, $6.75°$, $14.92°$, $32.51°$, $42.65°$, $54.83°$, and $73.23°$ respectively. Based on these array outputs, it is not possible to distinguish which peak corresponds to the true AOA of the signal and so the AOA estimation is ambiguous. ∎

As with the interferometric case, non-uniform antenna spacings are required to overcome the ambiguities associated with grating lobes [79]. With non-uniform antenna spacings, the spatially aliased copies of the main lobe do not sum in a fully coherently manner and so technically do not give rise to grating lobes. This will allow unambiguous AOA estimation to be performed. However, it should be noted that depending on the sparsity of the non-uniform array, partial uniformity among some of the antennas may cause a partially coherent summation at some angles which gives rise to high sidelobes. As with the previous chapters, this chapter shall assume that no pair of antennas satisfy the spatial Nyquist rate.

The relationship between the lack of grating lobes and the non-uniform antenna spacings is related to the discussion in Section 3.7.1. That is, when the antenna separations are non-uniform (i.e. not integer multiples of each other), a unique set of ambiguous phase

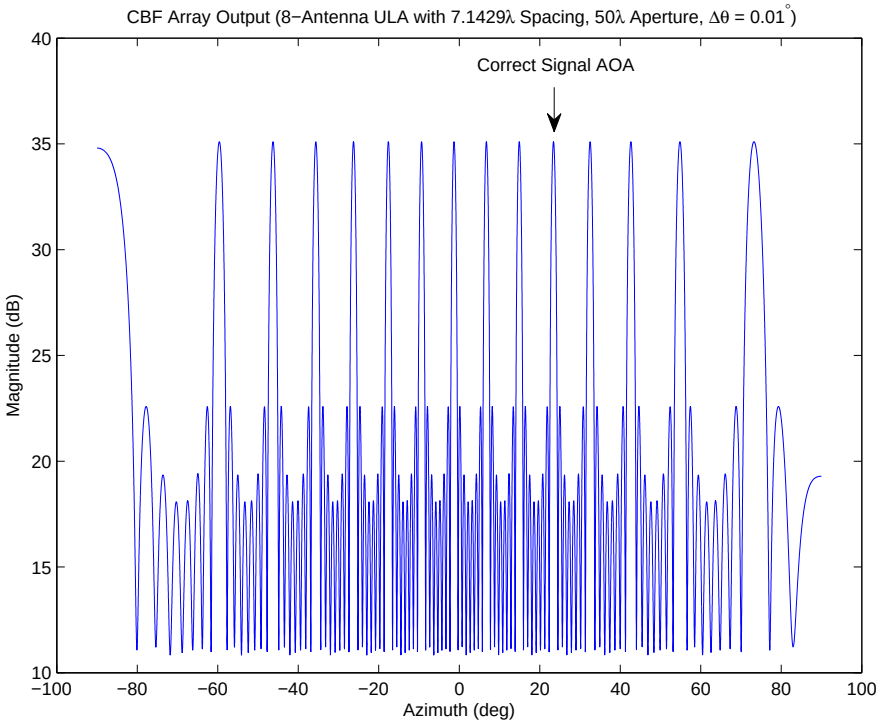

Figure 5.6: CBF array output using an 8-antenna uniform linear array with a uniform antenna spacing of 7.1429λ (50λ aperture) when $\theta = 23.42°$. Simulation parameters: $\eta = 15$ dB, $f = 16$ GHz, $N = 2048$ samples, $W = 1$ snapshot, and $\Delta\theta = 0.01°$.

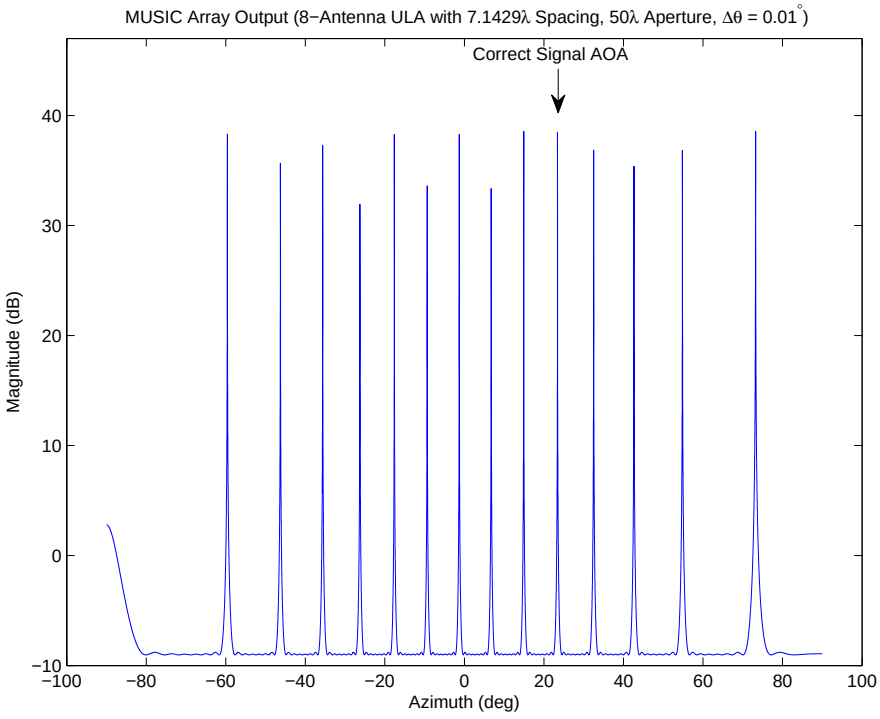

Figure 5.7: MUSIC array output using an 8-antenna uniform linear array with a uniform antenna spacing of 7.1429λ (50λ aperture) when $\theta = 23.42°$. Simulation parameters: $\eta = 15$ dB, $f = 16$ GHz, $N = 2048$ samples, $W = 1$ snapshot, and $\Delta\theta = 0.01°$.

Figure 5.8: An 8-antenna non-uniform linear array.

delays will be measured for each AOA. In terms of array processing, this translates to a unique set of propagation phase delays which will ensure that the array output will only coherently sum in the direction of the signal.

Example 5.2
Consider an 8-antenna non-uniform linear array with a 50λ aperture as illustrated in Figure 5.8. Figure 5.9 shows the beampattern for this array when the steering angle is $\theta_s = 0°$ with an AOA search resolution arbitrarily chosen to be $\Delta\theta = 0.01°$. This figure shows that there is one distinct main lobe at $\theta_s = 0°$. While there are also a number of high sidelobes, the magnitudes of the side lobes are distinctly smaller than the main lobe and so are technically not considered grating lobes.

Figure 5.10 shows the corresponding beamformer output of the CBF algorithm for a signal arriving from $\theta = 23.42°$. This figure shows that there is one distinct peak at the true AOA at $\theta = 23.42°$ and so the AOA of the signal can be unambiguously estimated if it is known that there is only one signal arrival. In this example, a number of sidelobes exist within 3 dB of the peak of the main lobe. The largest sidelobe occurs at $\theta = -67.52°$ and is only 1.19 dB below the peak of the main lobe.

Note that the beamformer output is not simply a circularly rotated version of the array beampattern. The difference between the beamformer output and the rotated array beampattern is attributed to the fact these outputs are related to the AOA, θ, in a non-linear arcsine fashion as described in (5.3). However, the beamformer output will be a circularly rotated array beampattern if the beamformer output is plotted against $\sin\theta$ instead of θ.

Figure 5.11 shows the corresponding array output of the MUSIC algorithm. In this example, the MUSIC array processor has managed to suppress many of the sidelobes that are exhibited in the array beampattern while maintaining a very narrow mainlobe width. Furthermore, while the CBF algorithm has a large sidelobe at $\theta = -67.52°$, the MUSIC algorithm significantly suppresses the array output in this direction. ▮

5.2.1 Grid Search Resolution

Beamforming and array processing algorithms use a grid search to find the steering angle which produces a large peak in the array output that corresponds to the direction of a signal arrival. The Rayleigh resolution limit [2] suggests that the resolution of the grid search should be less than or equal to one-half of the null-to-null beamwidth of the array beampattern. The null-to-null beamwidth, $\mathrm{BW_{NN}}$, is the angular width between

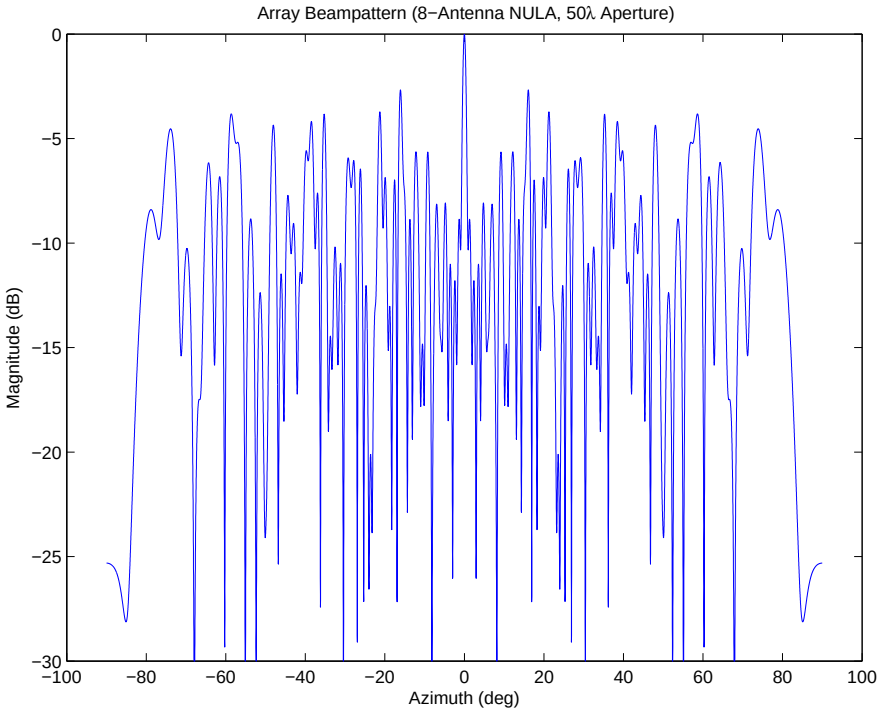

Figure 5.9: Beampattern of a 8-antenna non-uniform linear array with a 50λ aperture at 16 GHz.

the first nulls from the peak of the main lobe of the array beampattern and is illustrated in Figure 5.2. For a uniform linear array with $\lambda/2$ spacing, the null-to-null beamwidth, $\mathrm{BW}_{\mathrm{NN,ULA}}$, may be approximated by [2]

$$\mathrm{BW}_{\mathrm{NN,\ ULA}} \approx 2 \arcsin\left(\frac{\lambda}{\text{aperture}}\right), \tag{5.25}$$

where it is assumed that the aperture is significantly greater than λ. The grid search resolution of a uniform linear array should therefore be

$$\Delta\theta_{\mathrm{ULA}} \leq \frac{1}{2}\mathrm{BW}_{\mathrm{NN,ULA}} \approx \arcsin\left(\frac{\lambda}{\text{aperture}}\right). \tag{5.26}$$

However, for non-uniform linear arrays, the null-to-null beamwidth, $\mathrm{BW}_{\mathrm{NN,NULA}}$, is often smaller than but similar to $\mathrm{BW}_{\mathrm{NN,ULA}}$. Since (5.25) is only an approximation and $\mathrm{BW}_{\mathrm{NN,NULA}} \leq \mathrm{BW}_{\mathrm{NN,ULA}}$, this thesis shall arbitrarily choose the search resolution for non-uniform linear array geometries to be one-quarter of $\mathrm{BW}_{\mathrm{NN,ULA}}$ as follows,

$$\Delta\theta_{\mathrm{NULA}} = \frac{1}{4} \times \mathrm{BW}_{\mathrm{NN,ULA}} \approx \frac{1}{2} \arcsin\left(\frac{\lambda}{\text{aperture}}\right). \tag{5.27}$$

The choice of the grid search resolution is particularly important for sparse non-uniform linear array geometries due to the combined effect of scalloping losses and high sidelobes. As with all grid search algorithms, scalloping losses can occur if the AOA of the signal lies between two search bins. Since sparse array geometries have high sidelobes, the presence of scalloping losses can lead to incorrect AOA estimation as one of the sidelobes may be mistaken to indicate the signal's AOA. Using a finer search resolution will

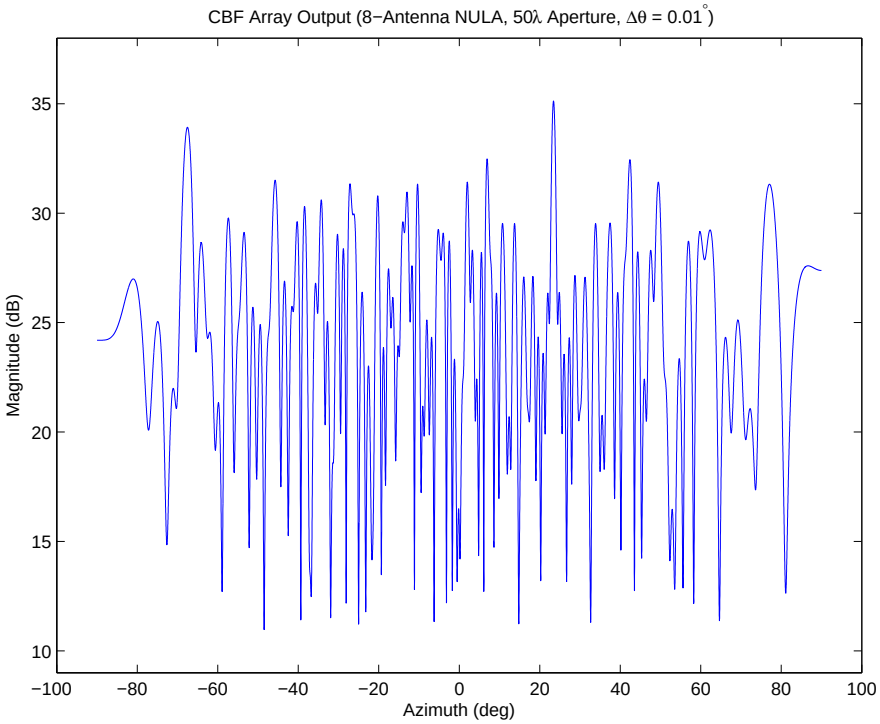

Figure 5.10: CBF array output using an 8-antenna non-uniform linear array with a 50λ aperture when $\theta = 23.42°$. Simulation parameters: $\eta = 15$ dB, $f = 16$ GHz, $N = 2048$ samples, $W = 1$ snapshot, and $\Delta\theta = 0.01°$.

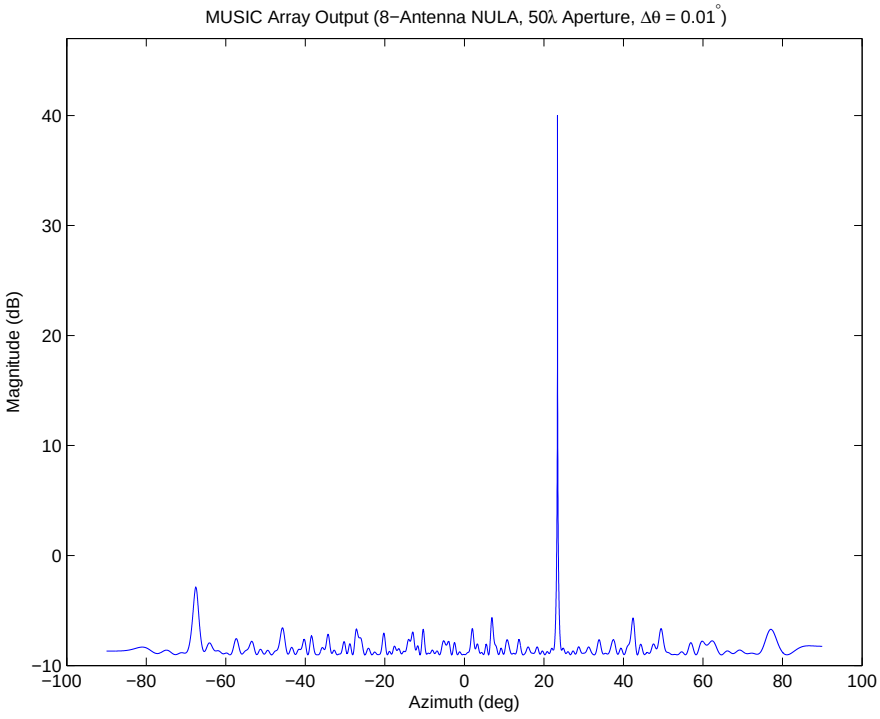

Figure 5.11: MUSIC array output using an 8-antenna non-uniform linear array with a 50λ aperture when $\theta = 23.42°$. Simulation parameters: $\eta = 15$ dB, $f = 16$ GHz, $N = 2048$ samples, $W = 1$ snapshot, and $\Delta\theta = 0.01°$.

provide a more robust performance against scalloping losses as well as improve the AOA estimation accuracy. However, these improvements come at the expense of increased computations.

Example 5.3
This example will demonstrate the importance of choosing an appropriate search resolution. Consider the array geometry used in Example 5.2. This array geometry has an aperture of 50λ at 16 GHz and so $\text{BW}_{\text{NN, ULA}}$ is approximately

$$\text{BW}_{\text{NN, ULA}} \approx 2 \arcsin\left(\frac{\lambda}{50\lambda}\right) \approx 2.292^\circ. \tag{5.28}$$

Consider setting the grid search resolution to $\Delta\theta = 1.146^\circ$, which is intentionally chosen to not satisfy (5.27). Inspection of the array beampattern in Figure 5.9 suggests that with this resolution, the maximum scalloping loss is 4.77 dB when the signal's AOA lies exactly halfway between two search bins. Furthermore, this array beampattern has 14 sidelobes with magnitudes within 4.77 dB of the magnitude of the main lobe. Thus, when scalloping losses occur, the peak of the array output may be attenuated to a level that is indistinguishable from the sidelobes. Figure 5.12 and Figure 5.13 confirm that the array output of the CBF and MUSIC algorithms do not yield an unambiguous peak at the signal's true AOA at $\theta = 23.42^\circ$. In fact, the sidelobes at $-67.61^\circ, 6.88^\circ$, and 42.40° have a higher peak than the main lobe at 22.92° for both algorithms.

In order to overcome the problem of scalloping losses, a finer search resolution is required. Using a search resolution of $\Delta\theta = 0.573^\circ$ to satisfy (5.27), would yield a maximum scalloping loss of 1.19 dB if the signal lies exactly halfway between two search bins. Since the magnitude of the highest sidelobe is 2.675 dB below the magnitude of the main lobe, the signal's peak is guaranteed to be higher than the sidelobe peaks even when scalloping losses occur. This search resolution would therefore be adequate to yield an unambiguous peak in the array output as confirmed by Figure 5.14 and Figure 5.15. ∎

In the AOA estimation problems considered in this thesis, the sensitivity of the grid search resolution to scalloping losses is further accentuated by the presence of high sidelobes due to the use of sparse large aperture arrays. The number of sidelobes and the extent of their magnitudes tend to increase as the sparsity of the array increases, i.e. when the spacing between antennas become longer. In the ideal unambiguous case, the 50λ aperture in Example 5.3 will be formed using 100 antennas with a uniform spacing of $\lambda/2$. However, in the example, only 8 antennas are used to form an array of the same aperture and so the spatial data is effectively undersampled by a factor of 12.5 and ultimately resulted in high sidelobes appearing in the array beampattern.

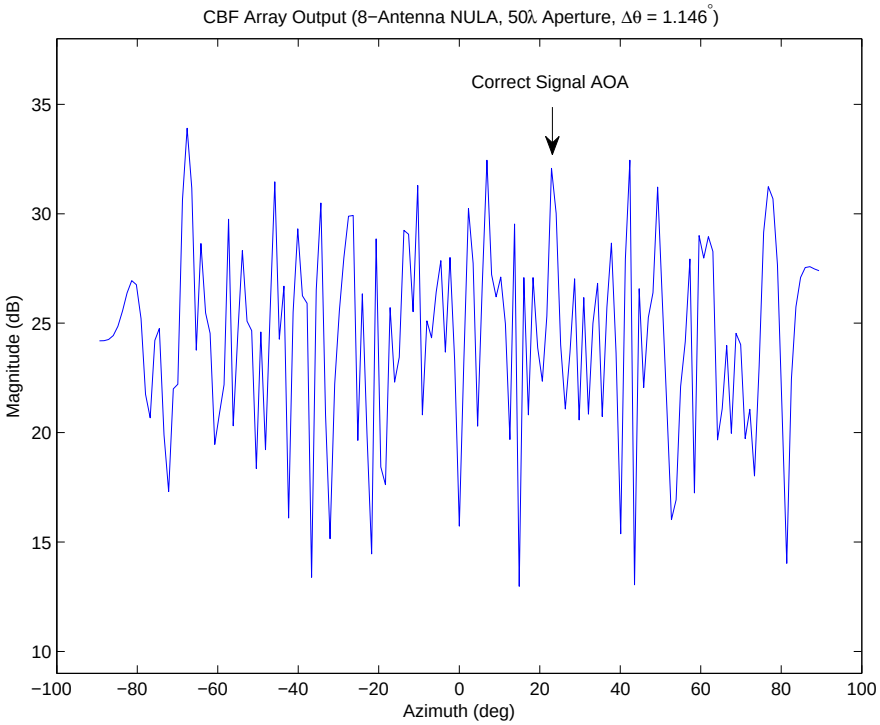

Figure 5.12: CBF array output using an 8-antenna non-uniform linear array with a 50λ aperture when $\theta = 23.42°$. Simulation parameters: $\eta = 15$ dB, $f = 16$ GHz, $N = 2048$ samples, $W = 1$ snapshot, and $\Delta\theta = 1.146°$.

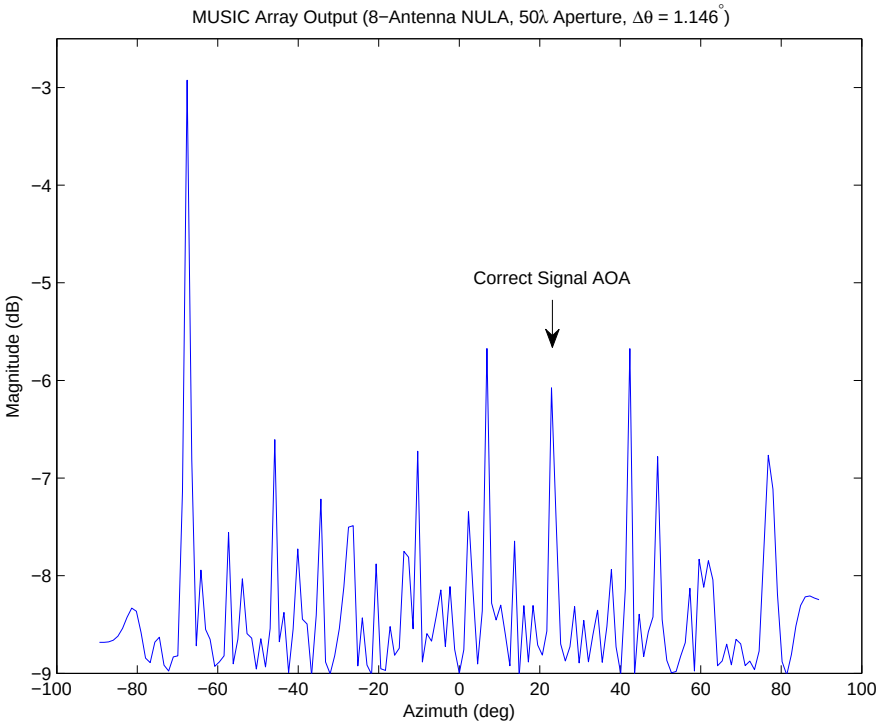

Figure 5.13: MUSIC array output using an 8-antenna non-uniform linear array with a 50λ aperture when $\theta = 23.42°$. Simulation parameters: $\eta = 15$ dB, $f = 16$ GHz, $N = 2048$ samples, $W = 1$ snapshot, and $\Delta\theta = 1.146°$.

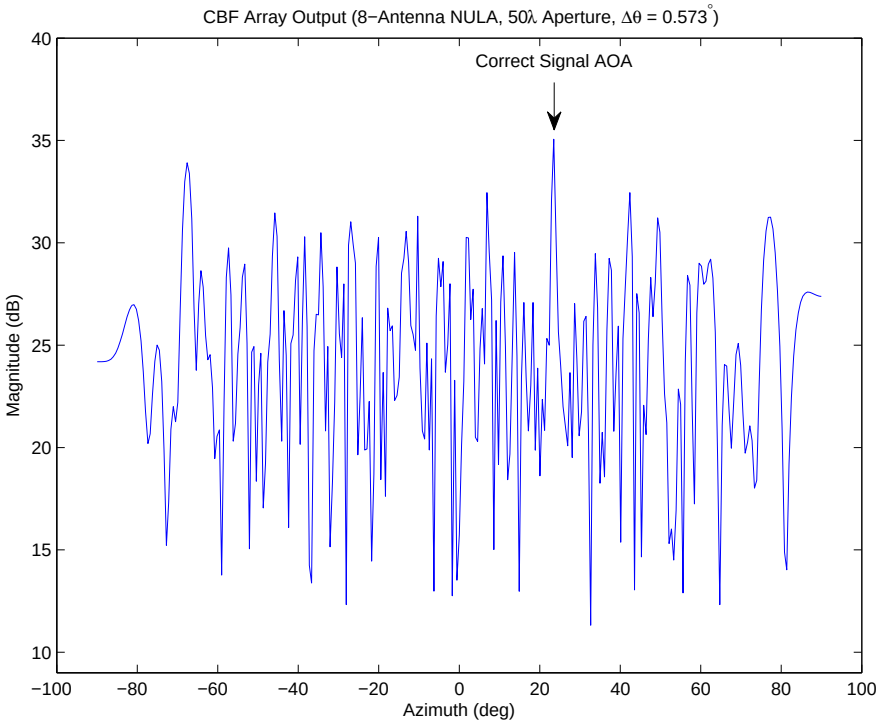

Figure 5.14: CBF array output using an 8-antenna non-uniform linear array with a 50λ aperture when $\theta = 23.42°$. Simulation parameters: $\eta = 15$ dB, $f = 16$ GHz, $N = 2048$ samples, $W = 1$ snapshot, and $\Delta\theta = 0.573°$.

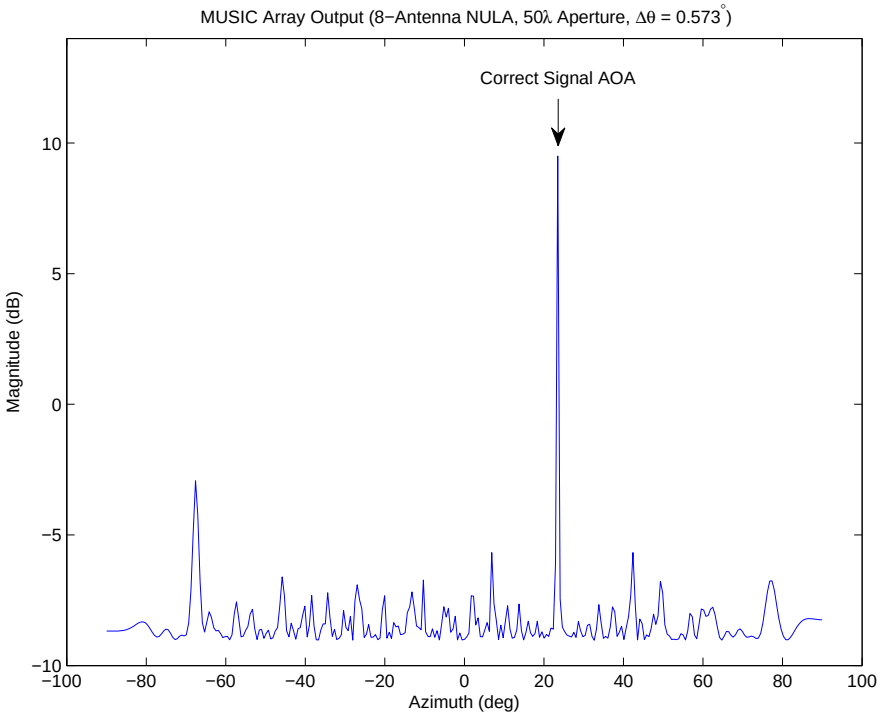

Figure 5.15: MUSIC array output using an 8-antenna non-uniform linear array with a 50λ aperture when $\theta = 23.42°$. Simulation parameters: $\eta = 15$ dB, $f = 16$ GHz, $N = 2048$ samples, $W = 1$ snapshot, and $\Delta\theta = 0.573°$.

Many studies have attempted to investigate "optimal" non-uniform array geometries that exhibit an unambiguous main lobe with good sidelobe behaviour [78–83]. Furthermore, in an analogous manner to spectral analysis, it is possible to use spatial windowing functions to further control the sidelobe behaviour [2]. However, these studies are beyond the intended scope of this thesis. Instead, in the subsequent section it will be shown that the second-order processing introduced in the previous chapter can be exploited to provide unambiguous AOA estimation in the presence of high sidelobes for sparse SODA geometries.

5.3 Array Processing with SODA Geometries

5.3.1 SODA-Cued Array Processing

In the previous section, it was shown that a sparse large aperture non-uniform linear array has an unambiguous main lobe in its array beampattern but also exhibits high sidelobe levels which can be problematic when scalloping losses occur. In order to avoid incorrect AOA estimation, a very fine grid search resolution as specified by (5.27) should be used. For large apertures, the null-to-null beamwidth, $\mathrm{BW_{NN}}$, is very small and so the number of steering angles that need to be searched is very large. This can lead to computationally intensive grid searches.

On the other hand, it was established in Section 4.2 that a SODA interferometer can provide a coarse AOA estimate in a computationally fast manner. The SODA interferometer can therefore be used to reduce the search space of the array processor in a similar manner to the SODA-cued correlative interferometer as described in Section 4.3.2. For a linear array, the search interval of the array processor will typically be $[-90°, 90°]$. As a rule of thumb, the SODA AOA estimate can be used to reduce the search interval to $[\hat{\theta}_{\mathrm{SODA}} - 3\delta\theta_{\mathrm{RMS,SODA}}, \hat{\theta}_{\mathrm{SODA}} + 3\delta\theta_{\mathrm{RMS,SODA}}]$. While the full search interval spans 180°, the reduced interval only spans $6\delta\hat{\theta}_{\mathrm{RMS,SODA}}$.

In this implementation, the SODA interferometer acts as an independent technique that reduces the search space of the array processor. This has the benefit of ignoring sidelobes outside the search space as well as reducing the number of computations that need to be performed for each AOA estimation. However, the independent use of the SODA interferometer does not change the array beampattern or array output and so AOA estimation errors can still occur if the array beampattern exhibits high sidelobes within the reduced search space.

Example 5.4
Consider the array output of the CBF algorithm when applied to the same 8-antenna non-uniform linear array as illustrated in Figure 5.8. In this example, it is assumed that the SNR is $\eta = 15$ dB, signal frequency is $f = 16$ GHz, AOA is $\theta = 23.42°$, $N = 2048$ samples and $W = 1$ snapshot.

The first three antennas of this array, positioned at 0, 3.1429λ and 6.7857λ re-

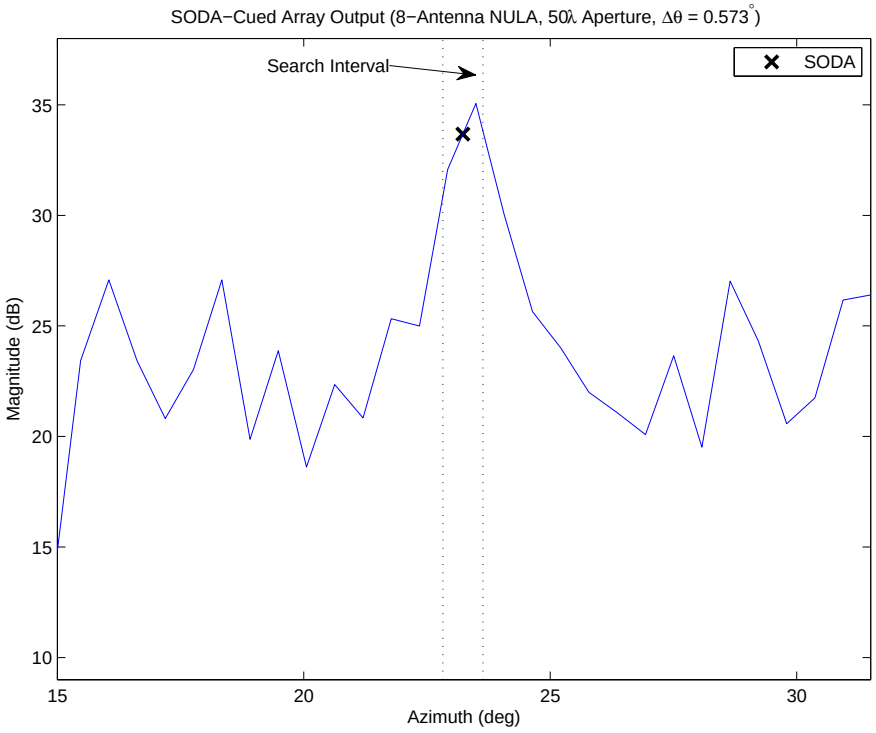

Figure 5.16: The SODA AOA estimate can be used to reduce the search range of the conventional beamformer.

spectively, satisfy the SODA baseline requirements specified by (4.11), since

$$d_{21} = 3.1429\lambda, \tag{5.29}$$
$$d_{31} = 6.7857\lambda = 2d_{21} + \lambda/2. \tag{5.30}$$

With this array geometry, (4.29) suggests that the SODA interferometer will be able to estimate the AOA of the signal with a RMS error of approximately $0.14°$. Figure 5.16 shows one realisation of this scenario. In this particular example, the SODA interferometer estimated the AOA of the signal to be $\hat{\theta}_{\text{SODA}} = 23.26°$ and so the SODA-cued beamformer only needs to search grid points in the interval $[22.84°, 23.68°]$. For a grid search resolution of $\Delta\theta = 0.573°$, this means that only $1 - 2$ grid points need to be considered. This is in contrast to the 315 grid points that need to be considered to conduct a full search in the interval $[-90°, 90°]$. In other words, when cued by the SODA AOA estimate, less than 0.63% of the total search space needs to be considered and so the computation time of the CBF algorithm is significantly improved. ∎

In a similar manner to the SODA-cued correlative interferometer, the grid search estimate of the SODA-cued array processor will still need to be refined using an optimisation algorithm, such as Newton's Method, to further improve the AOA estimation. At high SNR, it is reasonable to expect that the RMS error of the SODA AOA estimate is sufficiently small that the AOA estimate lies within the main lobe of the array output. If this is the case, an alternative implementation of the SODA-cued array processor is to

bypass the grid search altogether and simply use the SODA AOA estimate as the initial estimate to the optimisation algorithm of the array processor.

Algorithm Complexity

The algorithm complexity of the SODA-cued CBF algorithm is the sum of the algorithm complexities for the SODA interferometer and the CBF algorithm and is given by $O(W\Phi + K^2(W + G' + \Gamma) + G'K + G' + 1)$, where $\Phi = KN \log_2 N$ represents the number of operations to perform the FFT on each antenna output, K is the number of antennas, N is the number of samples and W is the number of snapshots, G' is the number of angles in the reduced search space and Γ is the number of iterations used by Newton's Method. If the grid search is not performed, the algorithm complexity of the SODA-cued CBF optimisation algorithm reduces to $O(W\Phi + K^2(W + \Gamma) + 1)$.

Similarly, the algorithm complexity for the SODA-cued MUSIC algorithm is the sum of the algorithm complexities for the SODA interferometer and the MUSIC algorithm and is given by $O(W\Phi + K^3 + K^2(W + G' + \Gamma) + G'K + G' + 1)$. If the grid search is not performed, the algorithm complexity of the SODA-cued MUSIC optimisation algorithm reduces to $O(W\Phi + K^3 + K^2(W + \Gamma) + 1)$.

5.3.2 SBI-Cued Array Processing

In Section 4.3.1, it was shown that the SBI interferometer is a computationally fast algorithm that can exploit the SODA AOA estimate to provide higher accuracy AOA estimates. Thus, the higher accuracy SBI AOA estimate can be used to cue the array processing for better performance. Since the SBI interferometer can exploit auxiliary antennas to improve its ambiguity resolution at low SNRs, the SBI-cued array processors are expected to have a better AOA estimation performance than the SODA-cued array processors at low SNRs and when auxiliary antennas are available.

Algorithm Complexity

The algorithm complexity of the SBI-cued CBF algorithm is the sum of the algorithm complexities for the SBI interferometer and the CBF algorithm and is given by $O(W\Phi + K^2(W + G' + \Gamma) + G'K + G' + 2M)$, where M is the number of interferometer baselines. If the grid search is not performed, the algorithm complexity of the SBI-cued CBF optimisation algorithm reduces to $O(W\Phi + K^2(W + \Gamma) + 2M)$.

Similarly, the algorithm complexity for the SBI-cued MUSIC algorithm is the sum of the algorithm complexities for the SBI interferometer and the MUSIC algorithm and is given by $O(W\Phi + K^3 + K^2(W + G' + \Gamma) + G'K + G' + 2M)$. If the grid search is not performed, the algorithm complexity of the SODA-cued MUSIC optimisation algorithm reduces to $O(W\Phi + K^3 + K^2(W + \Gamma) + 2M)$.

5.3.3 SODA Array Processing

The exploitation of the second-order processing to create a virtual pair for SODA interferometry can be generalised to an arbitrary number of antennas to create a virtual uniform linear array. Any beamforming and array processing algorithm can then be applied to the virtual array outputs to perform AOA estimation.

In this thesis, the terms "first-order" and "physical" will be used interchangeably to describe the parameters associated with the first-order physical array. Similarly, the terms "second-order" and "virtual" will be used to describe the parameters associated with the second-order virtual array.

Antenna Positions

The SODA interferometer takes a linear combination of the phases of three appropriately positioned antennas to generate the equivalent phase delay of two virtual antennas. For three antennas, this is achieved with the following constraint on the physical antenna separations,

$$d_{32} - d_{21} = d_{\Delta}, \tag{5.31}$$

where d_{21} and d_{32} are the first-order physical baselines and d_{Δ} is the baseline for the virtual antenna pair. Unambiguous AOA estimation can then be performed using interferometry by ensuring that $d_{\Delta} \leq \lambda_{\min}/2$, where $\lambda_{\min}$ is the wavelength of the highest frequency of interest.

Synthesis of the virtual antenna pair can be generalised to a greater number of antennas to create a virtual uniform linear array. While many combinations of the first-order phase delays are possible to generate a virtual array output, this chapter shall specifically focus on an array design that generalises the antenna positions of the 3-antenna SODA interferometer to a larger number of antennas as depicted in Figure 5.17 and Figure 5.18. The advantage of such an array geometry is that the first three antennas can be used as a 3-antenna SODA interferometer for coarse AOA estimation. For $K \geq 3$ antennas, this is achieved with the following constraint on the physical antenna separations,

$$d_{\Delta,k-1,1} = d_{k,k-1} - d_{k-1,k-2} = (k-2)d_{\Delta}, \tag{5.32}$$

where $k = 3, 2, \ldots, K$ and d_{Δ} is the uniform inter-element spacing between the virtual antennas. Unambiguous AOA estimation can then be performed by using any beamforming or array processing technique by ensuring that $d_{\Delta} \leq \lambda_{\min}/2$.

For the purposes of designing SODA geometries, it is convenient to rewrite (5.32) in terms of antenna positions. The antenna separation between the k-th and $(k-1)$-th antennas can be written as follows

$$d_{k,k-1} = u_k - u_{k-1}, \tag{5.33}$$

where u_k and u_{k-1} are the physical antenna positions of the k-th and $(k-1)$-th antennas respectively. Using this notation, the antennas for a K-antenna SODA geometry can then be re-written as

$$u_k = 2u_{k-1} - u_{k-2} + (k-2)d_{\Delta}, \tag{5.34}$$

where $u_1 = 0$ and u_2 is an arbitrarily chosen length.

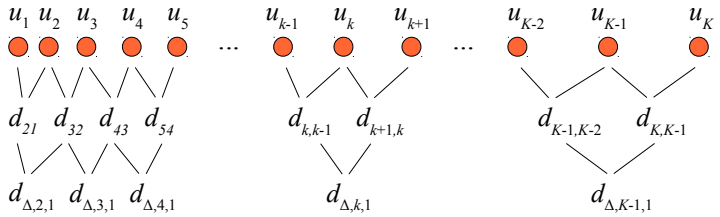

Figure 5.17: The second-order differences between the physical antenna positions of a sparse large aperture array can be used to synthesise the baselines of an unambiguous virtual uniform linear array.

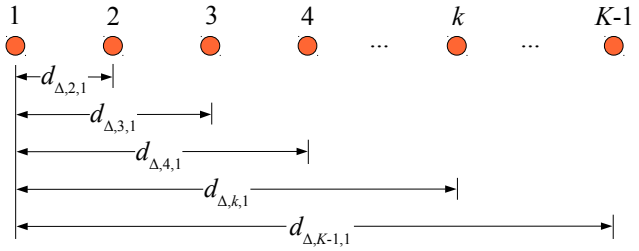

Figure 5.18: The antenna positions of a virtual uniform linear array formed from the second-order differences of the physical antenna positions.

k	$2u_{k-1}$	u_{k-2}	$(k-2)d_\Delta$	u_k
1	–	–	–	0
2	–	–	–	3.1429λ
3	6.2858λ	0	0.5λ	6.7858λ
4	13.5716λ	3.1429λ	λ	11.4287λ
5	22.8574λ	6.7858λ	1.5λ	17.5716λ
6	35.1432λ	11.4287λ	2λ	25.7145λ
7	51.429λ	17.5716λ	2.5λ	36.3574λ
8	72.7148λ	25.7145λ	3λ	50λ

Table 5.1: Antenna positions for an 8-antenna SODA geometry with $d_\Delta = \lambda/2$, $u_1 = 0$ and $u_2 = 3.1429\lambda$.

Example 5.5
Consider the design of an 8-antenna SODA geometry with $d_\Delta = \lambda/2$. In this example, $u_1 = 0$ and u_2 is arbitrarily chosen to be $u_2 = 3.1429\lambda$. The antenna positions for all remaining antennas can be computed from (5.34) and are listed in Table 5.1. These antenna positions correspond to the antenna array depicted in Figure 5.8. ∎

Second-Order Signal Model

In order to apply the conventional array processing algorithms to the virtual array, a vector representation of the virtual array signal model is required. This can be achieved by deriving a "second-order signal model" as described below.

Consider the first-order signal model of the k-th antenna of a physical K-antenna linear

array, $x_{k1}[n]$, as follows,

$$x_{k1}[n] = Ae^{j(2\pi fnt_s+\varphi+\psi_{k1}(\theta))} + \epsilon_k[n] = s[n]e^{j\psi_{k1}(\theta)} + \epsilon_k[n], \tag{5.35}$$

where $k = 1, 2, \ldots, K$, $s[n] = Ae^{j(2\pi fnt_s+\varphi)}$ represents the time-varying signal waveform, $e^{j\psi_{k1}(\theta)}$ represents the propagation phase delay and $\epsilon_k[n]$ represents the independent receiver noise in the k-th channel.

The corresponding second-order signal model can be formed from the outputs of each consecutive triplet of physical antennas. The second-order signal model of the v-th antenna of the V-antenna virtual array, $\chi_{v1}[n]$, can be written as

$$\begin{aligned} \chi_{v1}[n] &= x_{v+1,1}[n]x^*_{v,1}[n]x^*_{v,1}[n]x_{v-1,1}[n], & (5.36)\\ &= A^4e^{j(\psi_{v+1,1}(\theta)-2\psi_{v,1}(\theta)+\psi_{v-1,1}(\theta))} + \epsilon'_v[n], & (5.37)\\ &= A^4e^{j\psi_{\Delta,v1}} + \epsilon'_v[n], & (5.38) \end{aligned}$$

where the second-order phase delay, $\psi_{\Delta,v1}$, is given by

$$\psi_{\Delta,v1} = \psi_{v+1,v} - \psi_{v,v-1} = \frac{2\pi f(v-1)d_\Delta}{c}\sin\theta, \tag{5.39}$$

and $V = K-1$, $v = 2, \ldots, V$, $\psi_{\Delta,v1}(\theta)$ is the second-order phase delay which corresponds to the virtual antenna separation, $d_{\Delta,v1}$, and $\epsilon'_v[n]$ represents the "noise" component of the v-th virtual antenna which consists of the first-order receiver noise components from the $(v-1)$-th, v-th and $(v+1)$-th physical antennas and their corresponding cross-terms with the first-order signals, $x_{v-1}[n]$, $x_v[n]$ and $x_{v-1}[n]$. The phase delay of the first (reference) virtual antenna is expected to be $\psi_{\Delta,11} = 0$ and so the signal model for the first virtual antenna can be written as $\chi_{11}[n] = |x_{11}[n]|^4 = A^4 + \epsilon'_1[n]$.

Following (5.6), the n-th sample from all $V = K-1$ virtual antennas can be expressed more compactly in vector notation as follows

$$\boldsymbol{\chi}[n] = A^4\begin{pmatrix} e^{j\psi_{\Delta,11}(\theta)} \\ e^{j\psi_{\Delta,21}(\theta)} \\ \vdots \\ e^{j\psi_{\Delta,V1}(\theta)} \end{pmatrix} + \begin{pmatrix} \epsilon'_1[n] \\ \epsilon'_2[n] \\ \vdots \\ \epsilon'_V[n] \end{pmatrix} = s'[n]\,\boldsymbol{\nu}(\theta) + \boldsymbol{\epsilon}'[n], \tag{5.40}$$

where $\boldsymbol{\chi}[n]$ is a $V \times 1$ vector representing the V virtual antenna outputs, $s'[n] = A^4$ is a non-time-varying component that is only related to the signal amplitude, $\boldsymbol{\epsilon}'$ is a $V \times 1$ vector representing the noise in each virtual channel, and $\boldsymbol{\nu}(\theta)$ is a $V \times 1$ vector representing the propagation phase delays of the signals with respect to the first (reference) virtual antenna and is defined as

$$\boldsymbol{\nu}(\theta) = \begin{pmatrix} e^{j\psi_{\Delta,11}(\theta)} \\ e^{j\psi_{\Delta,21}(\theta)} \\ e^{j\psi_{\Delta,31}(\theta)} \\ \vdots \\ e^{j\psi_{\Delta,V1}(\theta)} \end{pmatrix} = \begin{pmatrix} e^{0\times j2\pi fd_\Delta\sin\theta/c} \\ e^{1\times j2\pi fd_\Delta\sin\theta/c} \\ e^{2\times j2\pi fd_\Delta\sin\theta/c} \\ \vdots \\ e^{(V-1)\times j2\pi fd_\Delta\sin\theta/c} \end{pmatrix}. \tag{5.41}$$

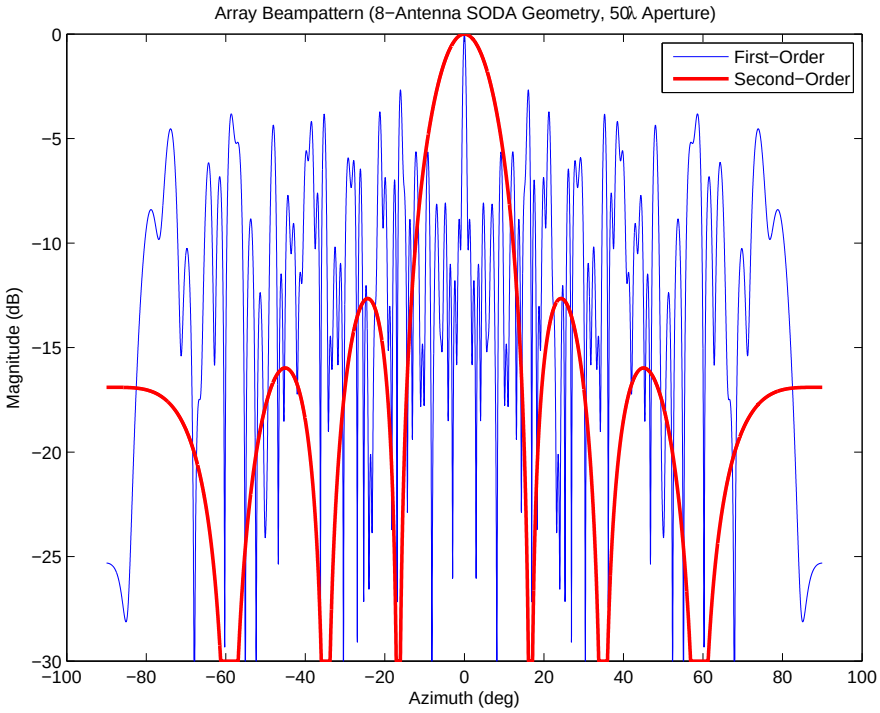

Figure 5.19: Beampattern of a 7-antenna virtual uniform linear array derived from an 8-antenna physical SODA geometry with a 50λ aperture.

Since the second-order array signal model described by (5.40) has the same functional form as the first-order signal model described by (5.6), the conventional beamforming and array processing algorithms can be applied to the second-order signal model for AOA estimation. However, the second-order signal, $s'[n] = A^4$, no longer contains the signal waveform component. Furthermore, while the first-order signal has a magnitude of A, the second-order signal has a magnitude of A^4. This suggests that the output power of a beamformer applied to the virtual array will be a factor of A^6 higher than the equivalent array processor applied to the physical first-order array.

Example 5.6

The 8-antenna non-uniform linear array illustrated in Figure 5.8 is an 8-antenna SODA geometry which has antenna positions tabulated in Table 5.1. With this array geometry, a 7-antenna virtual uniform linear array can be formed with an inter-element spacing of $\lambda/2$ at 16 GHz. In this example, it is assumed that the SNR is $\eta = 15$ dB, signal frequency is $f = 16$ GHz, AOA is $\theta = 23.42°$, $N = 2048$ digital samples and $W = 1$ snapshot.

Figure 5.19 shows the array beampattern for the first-order 8-antenna physical non-uniform linear array (with a 50λ aperture) and the second-order 7-antenna virtual uniform linear array (with a 3λ aperture) respectively. This figure shows that the physical array beampattern has a very narrow null-to-null beamwidth of approximately $\text{BW}_{\text{NN,first-order}} \approx 2.292°$ but also exhibits very high sidelobes. The magnitude of the highest sidelobe peak is only 2.675 dB below the mainlobe peak. This beampattern suggests that

high precision AOA estimation can be performed using the physical array, however, the AOA estimation may be erroneous due to the high sidelobes. In contrast, the virtual array beampattern has a much wider beamwidth of $\text{BW}_{\text{NN,second-order}} \approx 38.94°$ but also exhibits much lower sidelobes. The magnitude of the highest sidelobe peak is 12.65 dB below the mainlobe peak. This beampattern suggests that while the precision of the AOA estimation is lower than the physical array, the virtual array is also less prone to AOA estimation errors associated with high sidelobes. In order to reduce the number of computations but also avoid scalloping losses, (5.27) suggests that grid search resolution of the array processors be set to $\Delta\theta_{\text{first-order}} = 0.573°$ and $\Delta\theta_{\text{second-order}} = 9.736°$ for the physical and virtual arrays respectively.

Figure 5.20 shows the array output of the CBF algorithm for the physical and virtual arrays respectively. Due to the discrete search resolution, neither arrays have a peak at the true AOA at $\theta = 23.42°$. The first-order array has an unambiguous peak at $\hat{\theta}_{\text{first-order}} = 23.49°$, while the second-order virtual array has an unambiguous peak at $\hat{\theta}_{\text{second-order}} = 19.47°$. Using Newton's Method to optimise the grid search estimate, the AOA estimates can be refined to $\hat{\theta}_{\text{first-order}} = 23.4088°$ and $\hat{\theta}_{\text{second-order}} = 23.3874°$ respectively and so the estimation errors are therefore $-0.0112°$ and $-0.0326°$ respectively.

Similarly, Figure 5.21 shows the array output of the MUSIC algorithm for the physical and virtual arrays. In this case, the MUSIC grid search estimates the AOA as $\hat{\theta}_{\text{first-order}} = 23.38°$ and $\hat{\theta}_{\text{second-order}} = 19.47°$ respectively. Using Newton's Method to optimise the grid search estimate, the AOA estimates can be refined to $\hat{\theta}_{\text{first-order}} = 23.4088°$ and $\hat{\theta}_{\text{second-order}} = 23.3845°$ respectively and so the estimation errors are therefore $-0.0112°$ and $-0.0355°$ respectively.

While the AOA estimation error of the CBF and MUSIC algorithms are about three times higher using the virtual array than using the physical array, it should be noted that the performance degradation is small in an absolute sense. Furthermore, the number of computations required to estimate the AOA using the virtual array is significantly less than using the physical array. Since the virtual array only requires a grid search resolution of $\Delta\theta_{\text{second-order}} = 9.736°$, the algorithms only need to search through 19 possible angles within the interval $[-90°, 90°]$. On the other hand, the physical array requires a a search resolution of $\Delta\theta_{\text{first-order}} = 0.573°$ and so the algorithms need to search through 315 possible angles in the same interval. Thus, by using second-order processing, the algorithms exploiting the virtual array are able to reduce the number of computations by a factor of approximately 16.6 compared to using the physical array at the expense of a small performance degradation. ∎

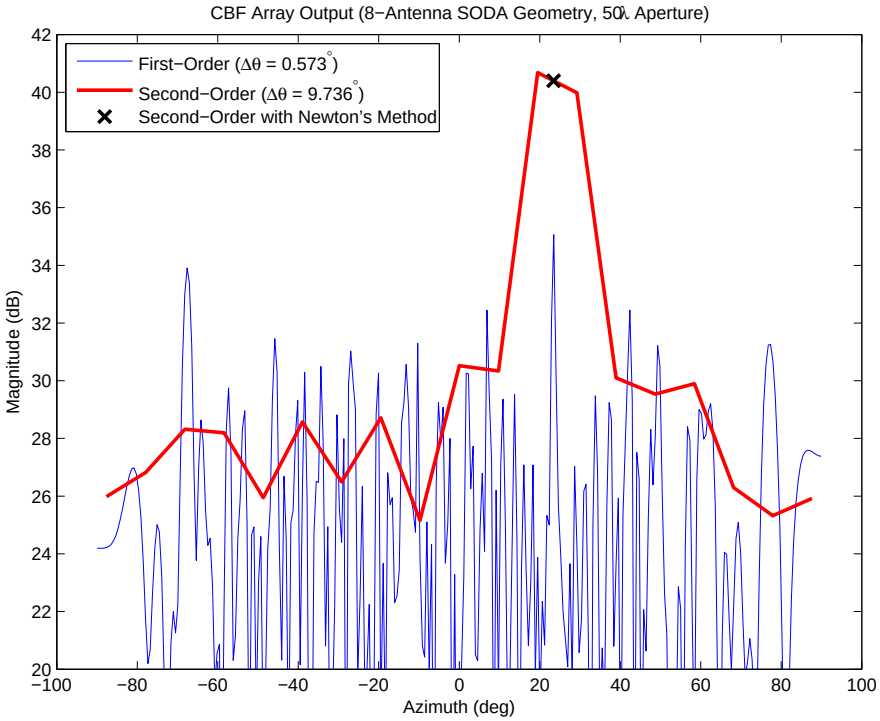

Figure 5.20: Comparison of the first-order and second-order array outputs for a 8-antenna SODA geometry using the CBF algorithm. Simulation parameters: $\theta = 23.42°$, $\eta = 15$ dB, $f = 16$ GHz, $N = 2048$ samples, $W = 1$ snapshot, $\Delta\theta_{\text{first-order}} = 0.573°$ and $\Delta\theta_{\text{second-order}} = 9.736°$.

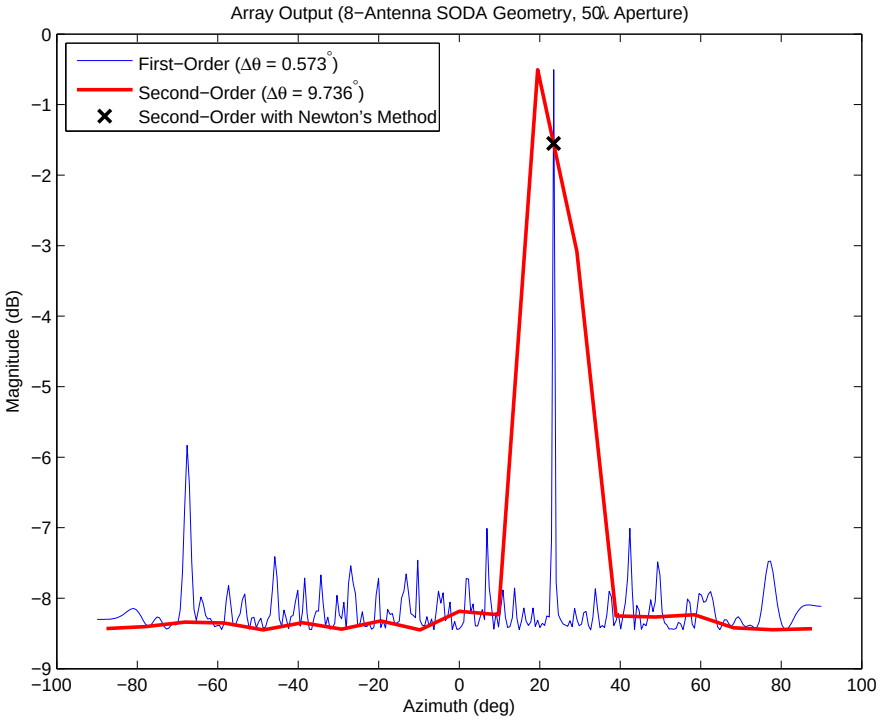

Figure 5.21: Comparison of the first-order and second-order array outputs for a 8-antenna SODA geometry using the MUSIC algorithm. Simulation parameters: $\theta = 23.42°$, $\eta = 15$ dB, $f = 16$ GHz, $N = 2048$ samples, $W = 1$ snapshot, $\Delta\theta_{\text{first-order}} = 0.573°$ and $\Delta\theta_{\text{second-order}} = 9.736°$.

Algorithm Complexity

The algorithm complexity for the second-order CBF and MUSIC algorithms are similar to the complexities for first-order algorithms with the difference that an additional K operations are required to generate the outputs of the virtual array and that the number of angles in the grid search is reduced. The algorithm complexity for the second-order CBF algorithm can therefore be written as $O(W\Phi+K^2(W+G''+\Gamma)+K(G''+1)+G'')$, where G'' represents the reduced number of steering angles. Similarly, the algorithm complexity for the second-order MUSIC algorithm is $O(W\Phi + K^3 + K^2(W + G'' + \Gamma) + K(G'' + 1) + G'')$.

5.4 Performance Comparison

In this section, the AOA estimation performance of the CBF and MUSIC algorithms will be evaluated using the physical and virtual arrays of the SODA geometry described in Section 3.8.2. These algorithms will also be evaluated using the 8-antenna SODA geometry described in Example 5.5 designed for 16 GHz. For comparison, the AOA estimation performance of these algorithms will be compared against some of the interferometric algorithms described in the previous chapters.

5.4.1 Array Beampatterns

Figure 5.22 shows the physical and virtual array beampatterns for the 3-antenna array geometry (i.e. when Antennas 1, 3 and 4 are used) at 9410 MHz. Due to the sparsity of the array geometry, the first-order array beampattern exhibits very high sidelobes and the highest sidelobe is immediately adjacent to the main lobe and is located approximately 3.9° away from the main lobe. These sidelobes are technically not grating lobes since they have a lower magnitude than the main lobe, however, the difference between the magnitude of the main lobe and highest sidelobe is extremely small (about 3.811×10^{-3} dB) and so it is expected that the 3-antenna physical array geometry may still exhibit grating lobe like effects. That is, at low SNR, the array output at the sidelobes may be higher than the mainlobe due to the effects of noise or scalloping losses and so lead to erroneous AOA estimation.

Figure 5.23 shows the physical and virtual array beampatterns for the 4-antenna array geometry at 9410 MHz. This array geometry uses the same 3-antenna array geometry above but also includes an additional auxiliary antenna (Antenna 2) to provide an intermediate baseline to reduce the sparsity of the array. The inclusion of the auxiliary antenna changes the physical array beampattern by suppressing some of the sidelobes exhibited in Figure 5.22. The highest sidelobe is now located 15.7° away from the main lobe and is no longer immediately adjacent to the main lobe. The difference between the magnitude of the main lobe and highest sidelobe has increased to about 0.2238 dB. While this magnitude difference is very small in an absolute sense, it is still two-orders of magnitude better than the physical array beampattern of the 3-antenna array geometry and so algorithms using the 4-antenna array geometry are expected to provide better AOA estimation performance at low SNR. Note that since the position of Antenna 2 does not adhere to the SODA constraint specified by (5.34), this antenna is not used to form the virtual array and so the virtual array beampattern remains unchanged.

Figure 5.24 shows the physical and virtual array beampatterns for the 8-antenna array geometry at 9410 MHz. Note that the first-order array beampattern shown in this figure differs slightly from Figure 5.19 which shows the first-order array beampattern of the same array at 16 GHz. Since the 8-antenna array uses more antennas to form the same aperture (i.e. 29.41λ at 9410 MHz), the sparsity of the 8-antenna array is much lower than the 3-antenna array. As a result, the first-order beampattern for the 8-antenna array is expected to have lower sidelobes than the 3-antenna array. For the 8-antenna array, the highest sidelobe is located 28.1° away from the main lobe and the difference between the magnitude of the main lobe and highest sidelobe is about 2.676 dB. Thus, it is expected that the 8-antenna array will provide better AOA estimation performance at low SNR.

5.4.2 Grid Search Resolutions

Since the 3-antenna, 4-antenna and 8-antenna array geometries considered in this section are all designed to have an aperture of 29.41λ at 9410 MHz, the null-to-null beamwidth of the physical beampatterns of all three antenna arrays will be approximately the same. From (5.25), it can be shown that

$$\mathrm{BW}_{\mathrm{NN,first\text{-}order}} \approx 2\arcsin\left(\frac{\lambda}{\mathrm{aperture}}\right) = 2\arcsin\left(\frac{\lambda}{29.41\lambda}\right) \approx 3.8971^\circ, \tag{5.42}$$

and so (5.27) suggests that the search resolution for the first-order CBF and MUSIC algorithms should be set to $\Delta\theta_{\text{first-order}} = 0.974^\circ$.

For the 3-antenna array geometry, Figure 5.22 suggests that the corresponding 2-antenna virtual array beampattern has a null-to-null beamwidth of $\mathrm{BW}_{\mathrm{NN,second\text{-}order,2\text{-}Ant}} = 180^\circ$. This suggests that the search resolution for the virtual array should be less than 45°, i.e. $\Delta\theta_{\text{second-order, 2-Ant}} \leq 45^\circ$. Note that since the virtual array aperture is less than λ, (5.25) cannot be used to estimate $\mathrm{BW}_{\mathrm{NN,second\text{-}order,2\text{-}Ant}}$.

For the 8-antenna physical array, visual inspection of Figure 5.24 suggests that the array beampattern of the corresponding 7-antenna virtual array has a null-to-null beamwidth of $\mathrm{BW}_{\mathrm{NN,second\text{-}order,7\text{-}Ant}} \approx 58.20^\circ$ and so (5.27) suggests that the search resolution for the second-order CBF and MUSIC algorithms using the 7-antenna virtual array should be set to $\Delta\theta_{\text{second-order, 7-Ant}} = 14.55^\circ$. Note that since the 7-antenna virtual array has a small aperture, (5.25) will tend to overestimate the null-to-null beamwidth.

Since $\Delta\theta_{\text{second-order, 2-Ant}}$ and $\Delta\theta_{\text{second-order, 7-Ant}}$ are both rather coarse, this performance comparison shall arbitrarily choose a finer grid search resolution of $\Delta\theta_{\text{second-order}} = 5^\circ$ for both virtual arrays to improve the performance of the grid search estimation. While this grid search resolution is smaller than that required by (5.27), the increase in the number of computations is not significant and is still approximately 5 times less than the first-order grid search resolutions.

5.4.3 Monte Carlo Simulations

Monte Carlo simulations were used to evaluate the AOA estimation performance of the CBF and MUSIC algorithms when applied to the physical and virtual arrays of the

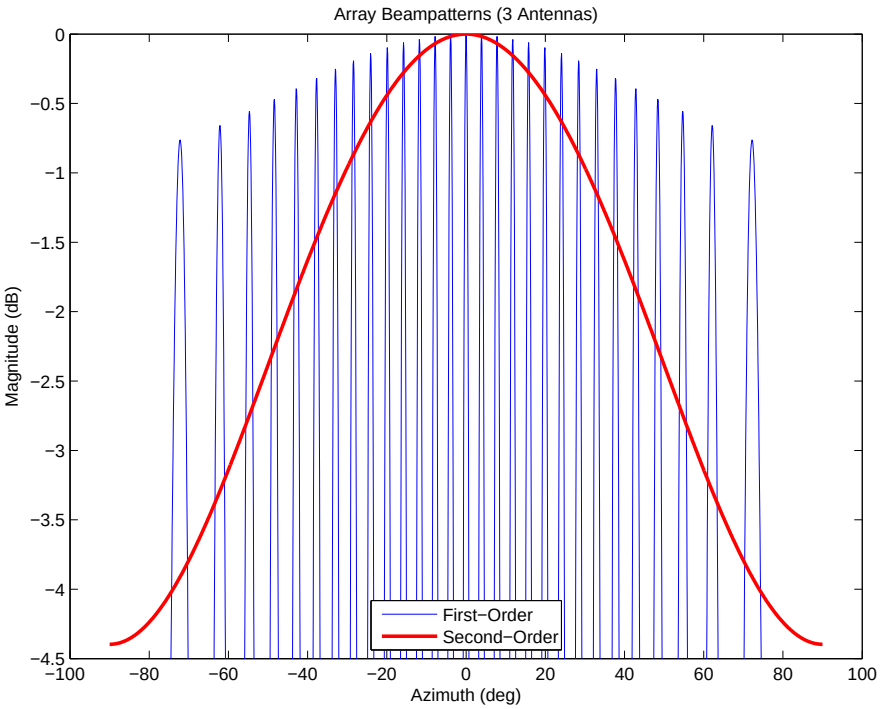

Figure 5.22: Array beampatterns for the physical and virtual arrays using the 3-antenna array geometry at $f = 9410$ MHz.

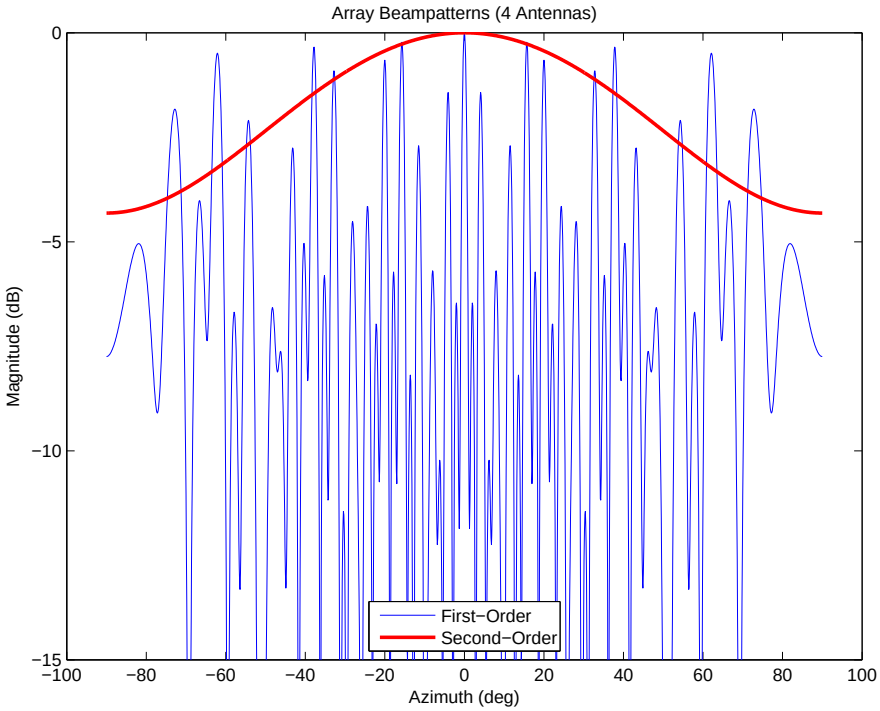

Figure 5.23: Array beampatterns for the physical and virtual arrays using the 4-antenna array geometry at $f = 9410$ MHz.

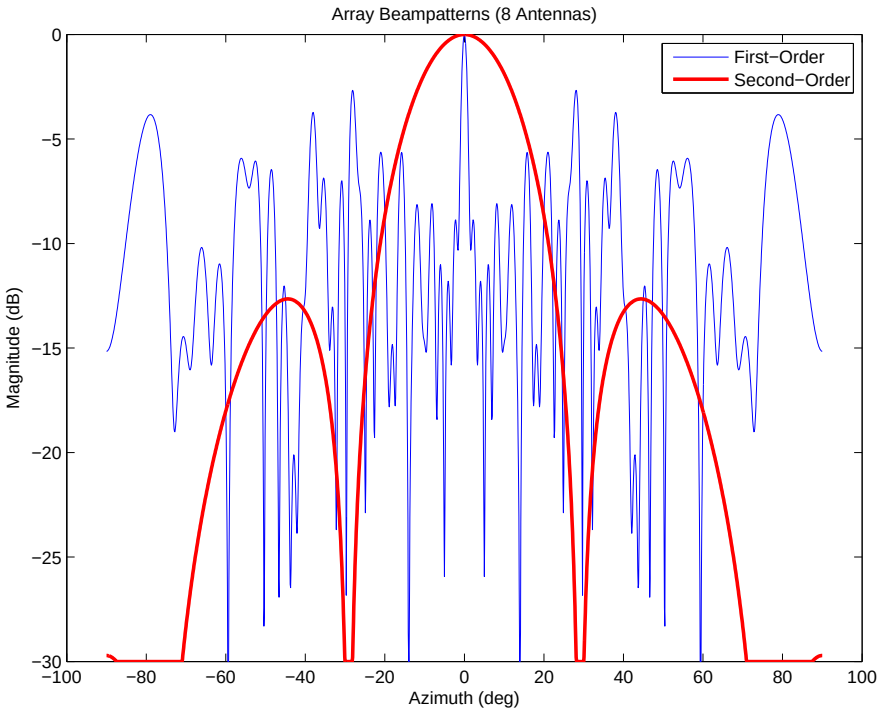

Figure 5.24: Array beampatterns for the physical and virtual arrays using the 8-antenna array geometry at $f = 9410$ MHz.

discussed SODA geometries. Since it was shown in Section 4.4 that the SBI-cued and SODA-cued optimisation algorithms have comparable execution times, but the SBI-cued optimisation algorithms generally have superior AOA estimation performance, these simulations will not consider the performance of the SODA-cued algorithms. These algorithms are labelled as "SBI-Cued CBF Opt." and "SBI-Cued MUSIC Opt." respectively. For comparison, the AOA estimation performance of the MLE, SODA and SBI interferometers will also be evaluated.

These simulations assume the same parameters as the comparisons performed in Section 3.8.3 and Section 4.4 to allow direct comparison with the previous results. That is, the intercepted signal is assumed to be a single-tone with a frequency and initial phase of $f = 9410$ MHz and $\varphi = 0°$ respectively. The signal is assumed to arrive from an AOA of $\theta = 23.42°$. The RMS error performance of each algorithm is evaluated using $\mathcal{Q} = 10,000$ receiver noise realisations. For each noise realisation, it is assumed that $N = 2048$ digital samples are collected at a sample interval of $t_s = 750$ ps. In these simulations, the phase delays and cross-spectral matrix are estimated in the frequency domain using a 2048-point FFT and a single snapshot, i.e. $W = 1$. No scalloping losses are expected to occur in these simulations. Newton's Method optimisation of the CBF and MUSIC algorithms is allowed to perform a maximum of $\Gamma_{\max} = 100$ iterations and the convergence tolerance is set to $\delta\theta_{\text{tol}} = 1° \times 10^{-5}$.

RMS Error Comparison

Figure 5.25 and Figure 5.26 show the RMS error performance of each algorithm when implemented using the 3-antenna array geometry. In this example, the performance of the first-order CBF and MUSIC algorithms have an identical performance. The first-order CBF and MUSIC algorithms, MLE interferometer, and SBI-cued CBF and MUSIC optimisation algorithms all achieve the 3-antenna root-CRLB. The first-order CBF and MUSIC algorithms have a SNR threshold of 0 dB, while the MLE interferometer has a SNR threshold of 3 dB and the SBI-cued CBF and MUSIC optimisation algorithms have a SNR threshold of 8 dB. It is interesting to note that the first-order CBF and MUSIC algorithms have a lower SNR threshold than the MLE interferometer. While all of the algorithms exploit the phase component of the signal, only the array processing algorithms additionally exploit the amplitude component of the signal and so provides them with a small, but statistically significant, performance improvement at low SNR.

The SBI-cued optimisation algorithms have a significantly higher SNR threshold compared to the first-order CBF and MUSIC algorithms and the MLE interferometer. This is because the SBI-cued optimisation algorithms rely on accurate AOA estimates from the SBI interferometer. Since the SBI interferometer has a SNR threshold of 8 dB, the performance of the SBI-cued optimisation algorithms will be limited to the same SNR threshold. Note that it is expected that if the grid search of the CBF and MUSIC algorithms is performed, the SNR threshold is expected to be identical to the first-order CBF and MUSIC algorithms.

The second-order CBF and MUSIC algorithms approach the same performance as the SODA interferometer from about 5 dB SNR and achieve the same performance from about 20 dB SNR. Like the SODA interferometer, the performance of the second-order array processors is a factor of $\sqrt{3}$ above the d_{Δ}-root-CRLB. Interestingly, below the SNR threshold, the performance of the SODA interferometer is actually better than the second-order array processors.

Figure 5.27 and Figure 5.28 show that with the inclusion of the fourth auxiliary antenna, the SNR threshold for the first-order CBF and MUSIC algorithms and the MLE interferometer are reduced to -11 dB and the SNR threshold for the SBI and SBI-cued algorithms are reduced to -4 dB. Since the position of the auxiliary antenna does not satisfy the requirements of a SODA geometry, as specified by (5.34), its output cannot be used by the SODA interferometer and second-order CBF and MUSIC algorithms and so the performance of these algorithms remain unchanged.

As discussed in Section 3.8.2, with the 3-antenna array, there is no noticeable difference between the d_{41}-root-CRLB and the 3-antenna root-CRLB. However, there is a small but statistically significant difference between the d_{41}-root-CRLB and the 4-antenna root-CRLB. As a result, this example shows that while the AOA estimation performance of the SBI interferometer is not statistically optimal, the performance of the SBI-cued CBF and MUSIC algorithms do achieve the 4-antenna root-CRLB and hence are statistically optimal at high SNR.

Figure 5.29 shows the RMS error performance of each algorithm using the 8-antenna ar-

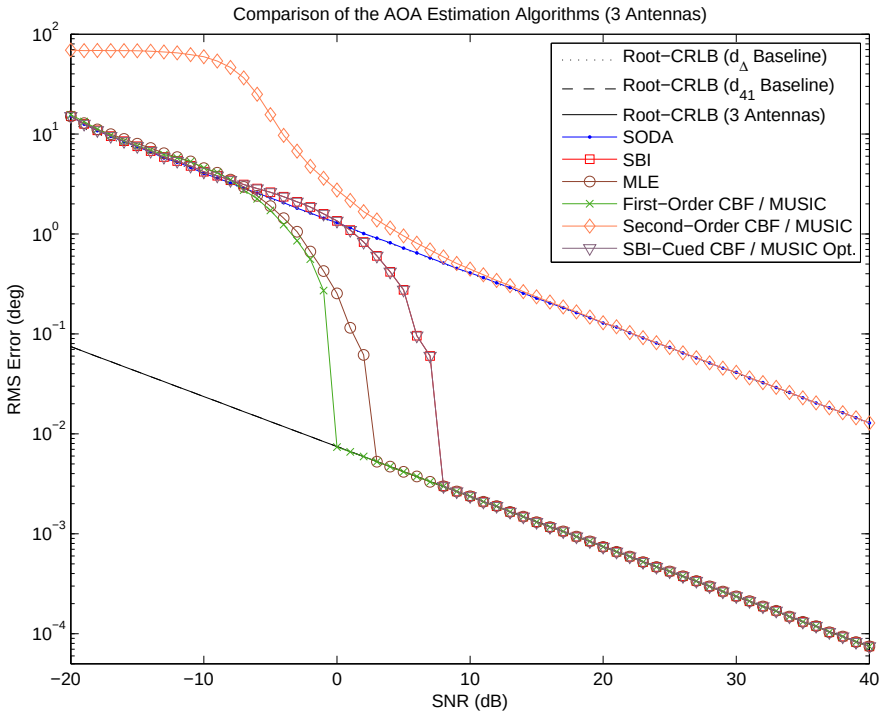

Figure 5.25: RMS error performance of each algorithm as a function of SNR. Simulation parameters: $K = 3$ antennas, $\theta = 23.42°$, $f = 9410$ MHz, $\varphi = 0°$, $N = 2048$ samples, $W = 1$ snapshot, $t_s = 750$ ps and $\mathcal{Q} = 10,000$ realisations.

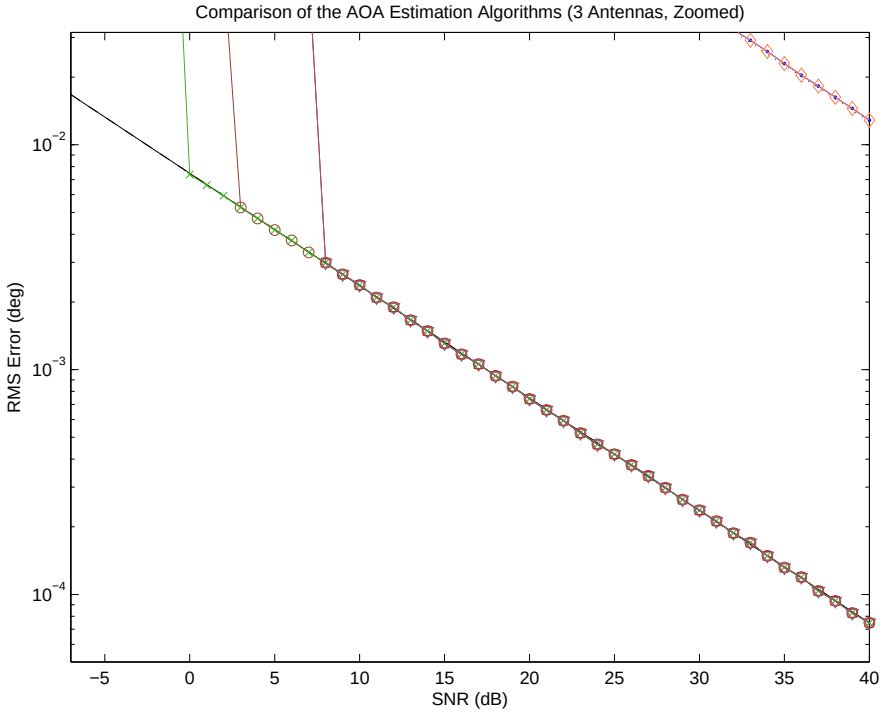

Figure 5.26: RMS error performance of each algorithm as a function of SNR. Simulation parameters: $K = 3$ antennas, $\theta = 23.42°$, $f = 9410$ MHz, $\varphi = 0°$, $N = 2048$ samples, $W = 1$ snapshot, $t_s = 750$ ps and $\mathcal{Q} = 10,000$ realisations.

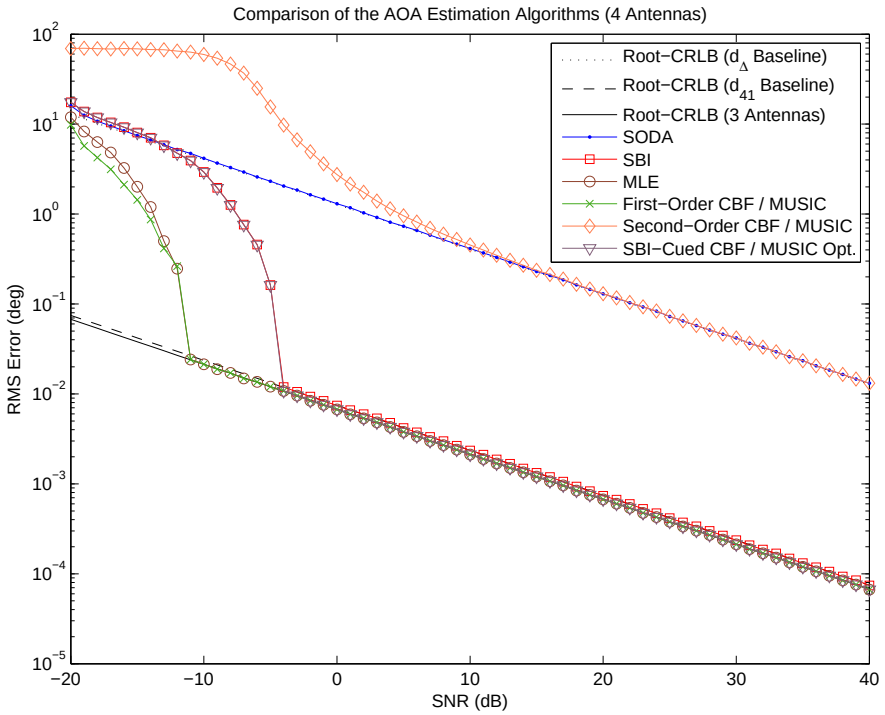

Figure 5.27: RMS error performance of each algorithm as a function of SNR. Simulation parameters: $K = 4$ antennas, $\theta = 23.42°$, $f = 9410$ MHz, $\varphi = 0°$, $N = 2048$ samples, $W = 1$ snapshot, $t_s = 750$ ps and $\mathcal{Q} = 10,000$ realisations.

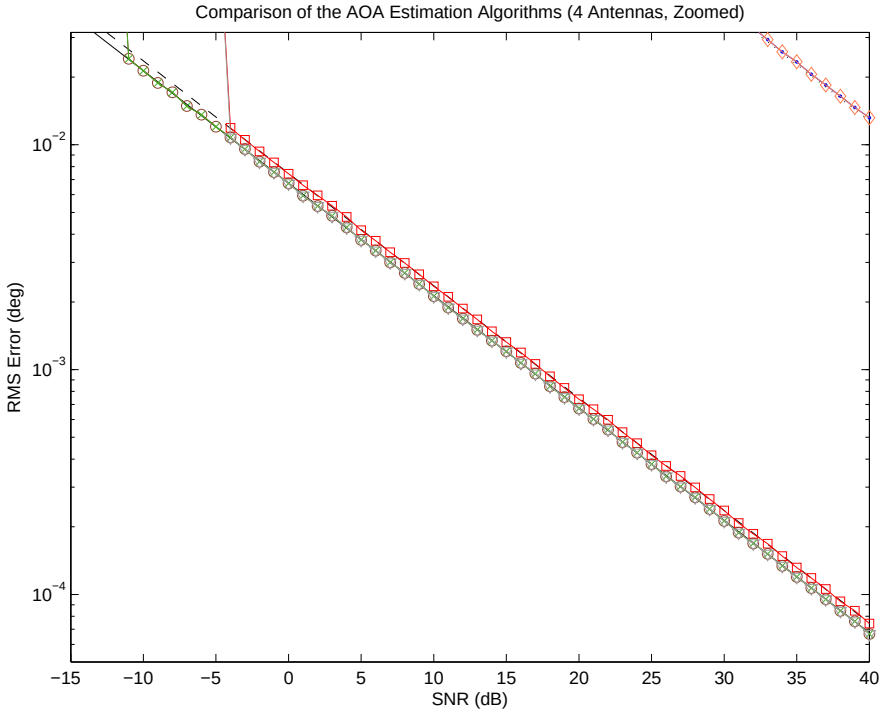

Figure 5.28: RMS error performance of each algorithm as a function of SNR. Simulation parameters: $K = 4$ antennas, $\theta = 23.42°$, $f = 9410$ MHz, $\varphi = 0°$, $N = 2048$ samples, $W = 1$ snapshot, $t_s = 750$ ps and $\mathcal{Q} = 10,000$ realisations.

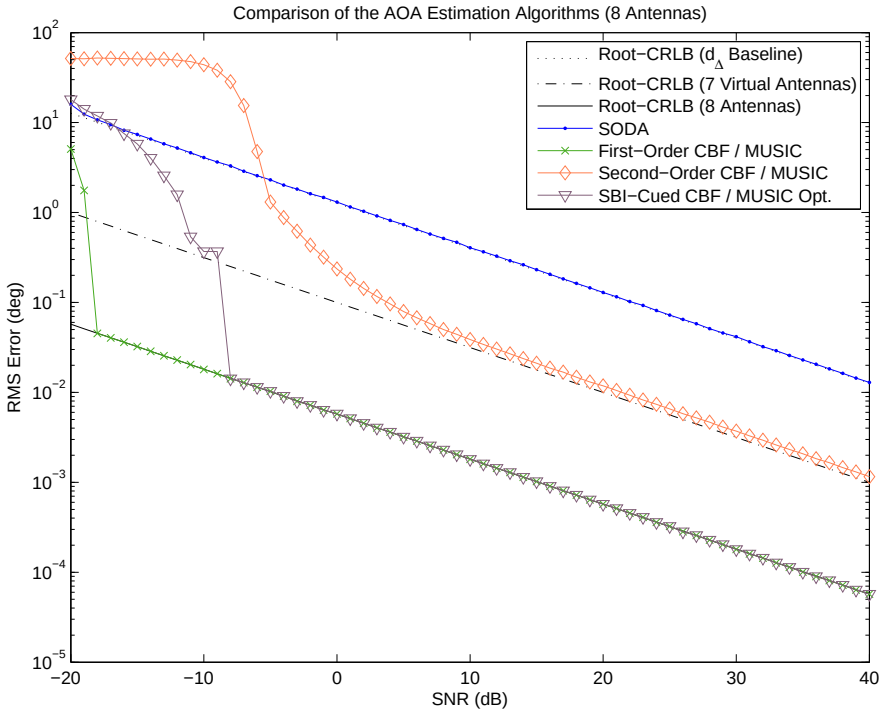

Figure 5.29: RMS error performance of each algorithm as a function of SNR. Simulation parameters: $K = 8$ antennas, $\theta = 23.42°$, $f = 9410$ MHz, $\varphi = 0°$, $N = 2048$ samples, $W = 1$ snapshot, $t_s = 750$ ps and $\mathcal{Q} = 10,000$ realisations.

ray geometry described in Example 5.5. This simulation verifies that SODA geometries with more than three antennas can be used to synthesise a virtual array with a larger aperture than can be achieved by a 3-antenna SODA interferometer. With a larger aperture, the AOA estimation performance of the second-order CBF and MUSIC algorithms is able to exceed the performance of the SODA interferometer from about -5 dB SNR and is consistently a factor of about 1.16 times higher the 7-antenna root-CRLB of the virtual array. Again, this performance degradation is the result of using the output from consecutive triplets of antennas to estimate the second-order phase delays.

This simulation shows that the first-order and SBI-cued CBF and MUSIC algorithms all achieve the 8-antenna root-CRLB. The SNR thresholds for the first-order and SBI-cued algorithms are -18 dB and -8 dB respectively.

Relative Execution Time

Table 5.2 shows the average relative execution time of each algorithm to perform a single AOA estimation using the 4-antenna array geometry. These execution times are normalised to the execution time of the SODA interferometer to allow direct comparison with the execution times in Table 3.4 and Table 4.1. The algorithms are presented in the order of increasing execution time, i.e. from fastest to slowest.

This table verifies that the SODA and SBI interferometers are the fastest algorithms in

Algorithm	Algorithm Complexity	Execution Time
SODA	$O(\Phi + M + 1)$	1.00
SBI	$O(\Phi + 2M)$	1.01
SBI-Cued MUSIC Opt.	$O(W\Phi + K^2(W + \Gamma) + 2M)$	2.72
SBI-Cued CBF Opt.	$O(W\Phi + K^3 + K^2(W + \Gamma) + 2M)$	2.73
Second-Order CBF	$O(W\Phi + K^2(W + G'' + \Gamma)$ $+K(G'' + 1) + G'')$	7.82
Second-Order MUSIC	$O(W\Phi + K^3 + K^2(W + G'' + \Gamma)$ $+K(G'' + 1) + G'')$	7.87
MLE	$O(\Phi + M(G + \Gamma + 1))$	12.55
First-Order CBF	$O(W\Phi + K^2(W + G + \Gamma) + GK + G)$	45.83
First-Order MUSIC	$O(W\Phi + K^3 + K^2(W + G + \Gamma) + GK + G)$	48.79

Table 5.2: Relative execution time factor for the array processing and interferometric algorithms.

these simulations. This is followed by the SBI-cued algorithms which are approximately 2.7 times slower and then the second-order CBF and MUSIC algorithms which are approximately 7.8 times slower. Finally, the first-order CBF and MUSIC algorithms are the slowest algorithms and are about $45.8-48.8$ times slower than the SODA interferometer.

These relative execution times confirm that while the first-order CBF and MUSIC algorithms offer the best performance in terms of the lowest RMS errors and SNR thresholds, they are nearly 50 times slower than the SODA interferometer. For time-critical applications, such as tactical ES systems, these algorithms are undesirable as they are computationally slow and only offer a marginal improvement in the AOA estimation in an absolute sense. It will often be more desirable to implement the SODA or SBI interferometers to obtain the fastest, but sub-optimal, AOA estimation performance. Alternatively, the SBI-cued optimisation methods (for either the MLE interferometer or the first-order CBF or MUSIC algorithm) can provide optimal AOA estimation performance at the expense of a marginal increase in the computation time.

5.5 Summary

This chapter presented the AOA estimation problem in the context of a multi-channel array processor. Two popular array processing methods, namely the conventional phase-shift beamformer (CBF) and Multiple Signal Classification (MUSIC) algorithms, were presented. It was also shown that the AOA estimate obtained from each algorithm's grid search can be further improved by using an optimisation algorithm, such as Newton's Method.

Since the array processing algorithms are grid search algorithms, correct estimation of a signal's AOA will require that a distinct peak be detected at the correct search bin. However, due to the scalloping losses that can occur when the signal's AOA lies between two search bins, the magnitude of the main lobe can be significantly attenuated. In the context of ES applications, it was shown that the requirement to use physically large wideband antennas in turn requires the use of sparse large aperture arrays for AOA

estimation. While ambiguities (or grating lobes) can be avoided by using non-uniform arrays, the sparsity of the antenna array causes high sidelobes to appear in the array beampattern. If scalloping losses causes the peak of the main lobe to fall below the magnitude of one or more sidelobes, the AOA of the signal will be incorrectly estimated. To avoid erroneous AOA estimation, a very small grid search resolution must be used to minimise the scalloping losses. In general, the grid search resolution should be set to a value less than or equal to one-half of the null-to-null beamwidth of the array beampattern. Since large aperture arrays have very narrow beamwidths, the grid search resolution required by the array processors will be very small and hence translates to a large number of computations. This will generally mean that the computational speed of the array processing algorithms is slow in comparison to interferometers.

In order to address the slow computation time of the array processing algorithms, this chapter proposes to use the AOA estimates from the SODA or SBI interferometer to reduce the search space of the array processing algorithms. Furthermore, at high SNR, the AOA estimates from the SODA and SBI interferometers may have sufficient accuracy to be directly applied to the array processor's optimisation algorithm and so further improvements can be made to the computation time as the grid search is not performed. While the AOA estimates from the SODA and SBI interferometers are sub-optimal, the final AOA estimate from the hybrid algorithms come from the optimal first-order array processors and so the AOA estimation performance of these algorithms are statistically optimal at high SNR.

Alternatively, it was shown that second-order processing can be used to translate a sparse large aperture physical antenna array to a non-sparse uniform virtual array with a smaller unambiguous aperture. Conventional array processing algorithms can then be applied to the virtual array. By virtue of its smaller aperture, the beampattern of the virtual array has a wider beamwidth and exhibits lower sidelobes than the beampattern of the physical array. This suggests that the virtual array can make use of a coarser grid search resolution and so the computational speed of these so-called second-order array processors is significantly improved at the expense of a reduced AOA estimation accuracy. Since it was shown that the SBI-cued array processors are statistically optimal at high SNR and are computationally faster than the second-order array processors, the SBI-cued array processors will generally be preferred.

Chapter 6

Calibration

6.1 Introduction

All of the AOA estimation algorithms discussed in the previous chapters have assumed a perfect signal model with well-behaved independent receiver noise. In practice, a number of imbalances may disproportionately distort one or more parameters of the measured signal in each channel of a multi-channel digital receiver. Some common sources of channel imbalance include:

- **Hardware Imperfections -** All hardware components, such as antennas, tuners, filters, amplifiers, and cables, will add some distortion to the signal as the signal propagates through the component. These distortions will manifest as gain and phase errors and may be dependent on the signal frequency and operating temperature of the receiver. In the case of antennas, the distortions may also be dependent on the AOA of the signal.

- **Imperfect Antenna Separations -** The antenna separation between two antennas is often assumed to be the distance between the physical (geometric) centre of the antenna. However, in general, the electrical phase centre (where the signal frequency actually resonates on the antenna) may differ from the antenna's physical centre. This is particularly true for wideband antennas, such as cavity-backed spiral antennas, where different parts of the antenna are designed to resonate at different frequencies. The effect of a mismatch between the physical and electrical phase centres of antennas is that the effective interferometer baselines may differ from the physical antenna separations. This means that the effective interferometer baselines will differ from the physical baselines and so will introduce an AOA dependent error.

- **Mutual Coupling -** Mutual coupling is a phenomenon that occurs when a signal received at an antenna is re-radiated to adjacent antennas. The extent of mutual coupling is dependent on the received signal power, antenna directivity and the antenna separations. In general, mutual coupling may introduce gain, frequency and AOA dependent imbalances to the received signals.

- **Crosstalk -** Crosstalk is a form of electromagnetic interference which occurs when a strong signal in one channel induces a current in other channels. The extent of crosstalk depends on the received signal power, proximity of RF paths and the

effectiveness of any electromagnetic shielding between the channels. Crosstalk may introduce gain, frequency and phase imbalances to the received signals.

Hardware developers will generally attempt to minimise channel imbalances through careful engineering design, such as using the same types of components in each channel and ensuring identical signal path lengths. However, the nature of imperfect hardware will mean that channel imbalances cannot be completely eliminated. Fortunately, these imbalances behave in a consistent and repeatable manner and so calibration methods can be applied to mitigate their effects.

In this chapter, the effect of the channel imbalances on interferometric AOA estimation will be considered. Some calibration methods that are suited for long baseline interferometers will also be presented.

6.2 Effect of Channel Imbalances

While there may be many different sources of channel imbalances, their combined effect on the output signals of the multi-channel digital receiver can be aggregated into four distinct sources of error, namely,

- phase imbalance,
- frequency imbalance,
- baseline errors, and
- gain imbalance.

These are systematic errors in the sense that they are consistent and repeatable imbalances that arise from the specific hardware implementation. The presence of systematic errors will introduce bias errors to the AOA estimation and must be mitigated to allow high accuracy and unbiased AOA estimation to be performed. Since this thesis is focused on interferometry, this section will discuss the systematic errors in the context of a two-channel interferometer, however, the results can also be generalised to multi-channel interferometry and array processing.

6.2.1 Phase, Frequency and Baseline Errors

In Chapter 3, it was shown that the AOA estimate of an interferometer is given by

$$\hat{\theta} = \arcsin\left(\frac{c\hat{\psi}}{2\pi f d}\right). \tag{6.1}$$

This expression suggests that accurate AOA estimation depends on accurate measurements of the phase delay between the channels, ψ, signal frequency, f, and antenna separation, d. Any errors in the measurement of these parameters will manifest as bias errors in the AOA estimation. These bias errors can be quantified through a perturbation analysis where the AOA estimate obtained from an ideal, noiseless signal model is subtracted from the AOA estimate obtained from an uncalibrated, noiseless signal model, $\hat{\theta}^u$. The uncalibrated signal model is obtained by introducing an imbalance

of $\delta\psi$, δf and δd to the measured values for the phase delay, frequency, and baseline respectively. The AOA bias errors can be respectively written as

$$\delta\theta_{\delta\psi} = \hat{\theta}^u(\psi + \delta\psi, f, d) - \theta(\psi, f, d), \tag{6.2}$$

$$\delta\theta_{\delta f} = \hat{\theta}^u(\psi, f + \delta f, d) - \theta(\psi, f, d), \tag{6.3}$$

$$\delta\theta_{\delta d} = \hat{\theta}^u(\psi, f, d + \delta d) - \theta(\psi, f, d), \tag{6.4}$$

where the $\hat{}$ accent denotes an estimated parameter and the subscript on the AOA bias error, $\delta\theta$, keeps track of the parameter causing the error. Several authors [5, 36, 41] have attempted to approximate the error contributions by performing a differential analysis on (6.1) as follows,

$$\delta\theta_{\delta\psi,\text{diff}} \approx \frac{\delta\psi}{\psi} \cdot \frac{c\psi}{2\pi f d \cos\theta} = \frac{\delta\psi}{\psi} \cdot \varepsilon, \tag{6.5}$$

$$\delta\theta_{\delta f,\text{diff}} \approx -\frac{\delta f}{f} \cdot \frac{c\psi}{2\pi f d \cos\theta} = -\frac{\delta f}{f} \cdot \varepsilon, \tag{6.6}$$

$$\delta\theta_{\delta d,\text{diff}} \approx -\frac{\delta d}{d} \cdot \frac{c\psi}{2\pi f d \cos\theta} = -\frac{\delta d}{d} \cdot \varepsilon, \tag{6.7}$$

where $\varepsilon = c\psi/2\pi f d \cos\theta$. In fact, (6.5) is the expression for the error contributions of the phase delay error and is identical to the approximate expression for the RMS error of the AOA estimation obtained by taking the square-root of the Cramér-Rao Lower Bound, i.e. (3.27). However, it will be shown by example that the differential analysis is only a good approximation of the AOA bias errors when the AOA is approximately broadside to the array (i.e. $\theta \sim 0°$) and can differ significantly from the true errors (obtained through perturbation analysis) when the AOA approaches endfire (i.e. $\theta \sim \pm 90°$).

Example 6.1
Figure 6.1 to Figure 6.3 show the AOA bias error obtained using both perturbation and differential analysis for some typical systematic errors that may be encountered by a modern digital microwave radar intercept receiver, namely a phase error of $\delta\psi = 5°$, frequency error of $\delta f = 1$ MHz, and a baseline error of $\delta d = 1$ mm. To avoid confusion with noise errors and phase ambiguities, these plots assume an ideal, noiseless signal model with a signal frequency of $f = 18$ GHz and an unambiguous antenna separation of $d = \lambda/2 = 8.3333$ mm, where λ is the signal wavelength.

The perturbation curves show that the systematic errors introduce AOA-dependent bias errors to the AOA estimation. These bias errors are lowest about broadside and rise exponentially towards endfire. This angle-dependency suggests that the extent of the AOA bias error can be reduced by limiting the field-of-view of the interferometer to a smaller angular region about broadside.

These figures also show that the frequency imbalance has the least significant effect on the AOA estimation. In this example, a 1 MHz frequency imbalance introduces a maximum AOA bias error of 0.60° at endfire. In comparison, a

1 mm baseline error has the most significant effect on the AOA estimation with a maximum AOA bias error of 26.77° at endfire. A 5° phase delay error has an intermediate effect on the AOA estimation with a maximum AOA bias error of 13.54° at endfire.

These figures also illustrate the difference between the perturbation and differential methods of computing the bias errors. While the differential method is insightful and can be useful for quick and approximate calculations, they can differ significantly from the true errors obtained through perturbation analysis. This is particularly true at endfire where the differential analysis calculates the AOA error to be infinite (although, in practice, the AOA error will be limited to 180° due to phase wrapping).

While the differential analysis of the AOA bias errors may not be accurate in an absolute sense, the differential method is still useful to understand the relative extent of the AOA bias errors. Given that $\delta\psi = 5°$, $\delta f = 1$ MHz and $\delta d = 1$ mm, the corresponding AOA bias errors, given by (6.5) - (6.7), are approximately

$$\delta\theta_{\delta\psi,\text{diff}} \approx \frac{5°}{360°} \times \varepsilon \approx 1.39\% \times \varepsilon, \tag{6.8}$$

$$\delta\theta_{\delta f,\text{diff}} \approx -\frac{1 \text{ MHz}}{18000 \text{ MHz}} \times \varepsilon \approx -0.0056\% \times \varepsilon \tag{6.9}$$

$$\delta\theta_{\delta d,\text{diff}} \approx -\frac{1 \text{ mm}}{8.3333 \text{ mm}} \times \varepsilon \approx -12.00\% \times \varepsilon. \tag{6.10}$$

These calculations confirm that the baseline error introduces the most significant AOA bias errors because a 1 mm error is relatively large compared to the antenna separation. On the other hand, the frequency error introduces the least significant AOA bias errors because a 1 MHz error is small compared to the signal frequency. ∎

6.2.2 Gain Imbalance

Gain imbalances cause the signal power, and hence signal-to-noise ratio (SNR), of the measured signal in each channel to be different. These imbalances manifest as a performance degradation in the AOA estimation in the presence of independent receiver noise. In Section 3.8.1, the Cramér-Rao Lower Bound (CRLB) for the AOA estimation using a linear array was shown to be inversely proportional to the SNR as follows

$$\text{CRLB}(\theta) \propto \frac{1}{\eta}, \tag{6.11}$$

where $\eta = A^2/2\sigma^2$ represents the SNR of the signal, A represents the signal amplitude, A^2 represents the signal power and $2\sigma^2$ represents the receiver noise power of the real and imaginary components. This expression implicitly assumes that the SNR of the signal is identical in all channels.

Under the assumption that the receiver noise is white and that all channels are designed to have the same noise power, it is reasonable to assume that any differences in the SNR

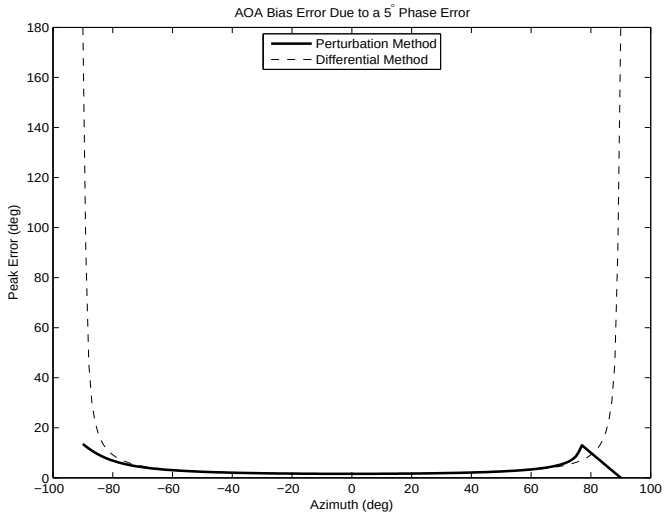

Figure 6.1: AOA bias error due to a 5° bias error in the phase delay estimate. The signal frequency is assumed to be $f = 18$ GHz and the antenna separation is $d = \lambda/2$.

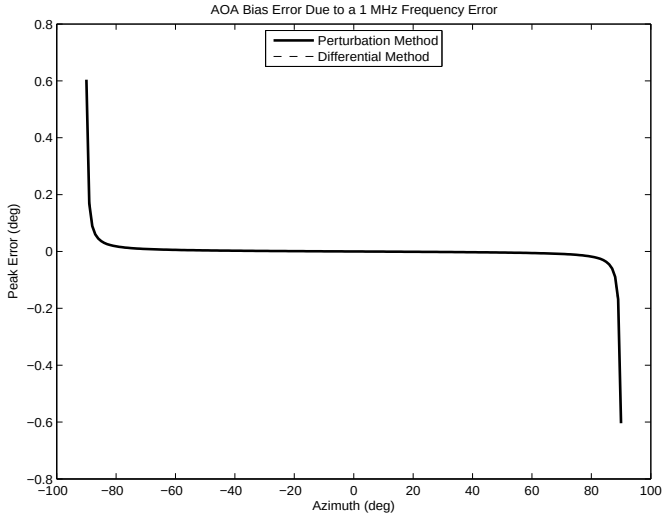

Figure 6.2: AOA bias error due to a 1 MHz bias error in the frequency estimate. The signal frequency is assumed to be $f = 18$ GHz and the antenna separation is $d = \lambda/2$.

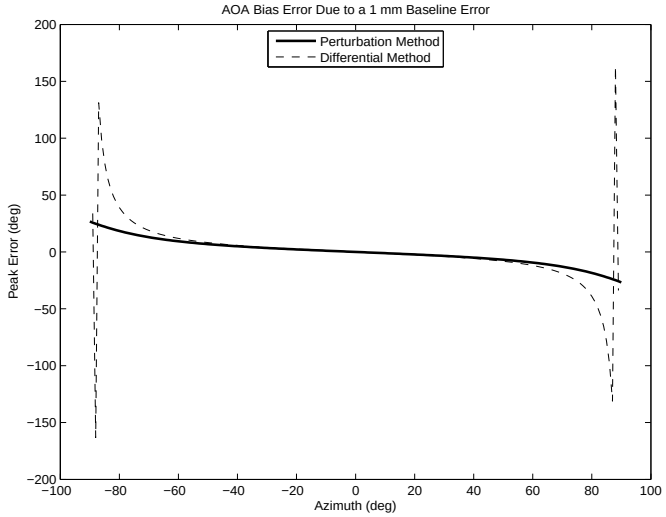

Figure 6.3: AOA bias error due to a 1 mm bias error in the interferometer baseline. The signal frequency is assumed to be $f = 18$ GHz and the antenna separation is $d = \lambda/2$.

of each channel is entirely due to amplitude (or gain) imbalances. The amplitude of the signal in the k-th channel, A_k, can be modelled as a gain imbalance applied to the true signal amplitude as follows

$$A_k = \alpha_k A, \tag{6.12}$$

where α_k represents the scaling effect of the gain imbalance. This suggests that the SNR of the k-th channel can be written as

$$\eta_k = \frac{A_k}{2\sigma^2} = \alpha_k^2 \eta. \tag{6.13}$$

From (A.61), when the SNR of the signal differs in each channel, the CRLB can be shown to be proportional to

$$\text{CRLB}(\theta) \propto K \frac{1}{\sum_{k=1}^{K} \eta_k} = \left(K \frac{1}{\sum_{k=1}^{K} \alpha_k} \right) \cdot \frac{1}{\eta}. \tag{6.14}$$

Comparing (6.14) with (6.11) shows that in the presence of amplitude imbalances, the CRLB is scaled by a factor of $K \left(\sum_{k=1}^{K} \alpha_k \right)^{-1}$. This suggests that amplitude imbalances do not introduce a bias error to the AOA estimation but rather scales the RMS error of the AOA estimation performance in noise by a factor of $\sqrt{K \left(\sum_{k=1}^{K} \alpha_k \right)^{-1}}$.

6.3 Signal Models

In this section, the signal models that will be used to discuss the calibration methods will be established.

6.3.1 Calibrated Signal Model

From Section 3.2.2, the ideal, noiseless narrowband signal can be modelled as

$$s^c(t) = Ae^{j(2\pi f t + \varphi)}. \tag{6.15}$$

Since the purpose of calibration methods is to attempt to recover the ideal signal from the uncalibrated signal, the above expression can also be considered the calibrated signal model. The superscript ^{c} will be used to distinguish the calibrated signal model and its parameters from the uncalibrated signal.

For an array of K antennas, the propagation time delay between the k-th and l-th antennas, τ_{kl}, is given by

$$\tau_{kl}^c = \frac{d_{kl}}{c} \sin\theta. \tag{6.16}$$

The calibrated signal received at the k-th antenna relative to the l-th antenna can therefore be expressed as

$$s_{kl}^c(t) = Ae^{j(2\pi f(t+\tau_{kl}^c)+\varphi)} = Ae^{j(2\pi f t + \varphi + \psi_{kl}^c)}, \tag{6.17}$$

where $\psi_{kl}^c = 2\pi f d_{kl} \sin\theta / c$ represents the ideal phase delay of the calibrated signal measured at the k-th antenna with respect to the l-th antenna.

6.3.2 Uncalibrated Signal Model

For an array of K antennas, the uncalibrated signal from the k-th antenna relative to the l-th antenna can be modelled as

$$s^u_{kl}(t) = \alpha_{kl} A e^{j(2\pi(f+\delta f_{kl})(t+\tau^c_{kl}+\delta\tau_{kl})+(\varphi+\delta\varphi_{kl}))}, \tag{6.18}$$

where α_{kl}, δf_{kl} and $\delta\varphi_{kl}$ represent the aggregated amplitude, frequency and phase imbalances of the k-th channel relative to the l-th channel respectively. A propagation time delay error, $\delta\tau_{kl}$, is also introduced to the uncalibrated signal model as a result of the additional time required to travel from the k-th antenna to the l-th antenna due to a baseline error, δd_{kl}. The propagation time delay error and baseline error are related by

$$\delta\tau_{kl} = \frac{\delta d_{kl}}{c} \sin\theta. \tag{6.19}$$

The superscript ^{u} is used to distinguish the uncalibrated signal model and its parameters from the calibrated signal.

The uncalibrated signal model can be written in terms of the calibrated signal model as

$$s^u_{kl}(t) = \alpha_{kl} s^c_{kl}(t) e^{j\beta'_{kl}(A,f,\theta,T,t)}, \tag{6.20}$$

where $\beta'_{kl}(A, f, \theta, T, t)$ represents a time-varying phase delay bias error that arises due to the channel imbalances and is defined as

$$\begin{aligned} \beta'_{kl}(A, f, \theta, T, t) &= 2\pi\delta f_{kl} t + 2\pi(f+\delta f_{kl})\delta\tau_{kl} + 2\pi\delta f_{kl}\tau^c_{kl} + \delta\varphi_{kl}, & (6.21)\\ &= \beta''_{kl}(A, f, \theta, T, t) + \beta_{kl}(A, f, \theta, T), & (6.22) \end{aligned}$$

where $\beta''_{kl}(A, f, \theta, T, t) = 2\pi\delta f_{kl} t$ is the time-varying component and $\beta_{kl}(A, f, \theta, T) = 2\pi(f+\delta f_{kl})\delta\tau_{kl} + 2\pi\delta f_{kl}\tau^c_{kl} + \delta\varphi_{kl}$ is a constant phase offset. The arguments to the phase delay error components, A, f, θ and T, represent the dependency of the systematic errors on the signal's amplitude, carrier frequency, AOA, and receiver operating temperature respectively.

In practice, frequency imbalances arise mainly due to the use of independent local oscillators to down-convert the radio frequency (RF) signals in each channel to a more manageable intermediate frequency (IF). This major source of frequency imbalance can be mitigated by using a single common local oscillator for all channels. While hardware components may also introduce frequency imbalances, these imbalances are often small compared to the operating frequency. Furthermore, from Section 6.2.1, it was shown that the bias error introduced by a small frequency imbalance is small and so the effects of the frequency imbalance can be considered negligible. This assumption implies that $\beta''_{kl}(A, f, \theta, T, t) \approx 0$, and so the phase delay error, $\beta'_{kl}(A, f, \theta, T, t)$, will be dominated by $\beta_{kl}(A, f, \theta, T)$, i.e.,

$$\beta'_{kl}(A, f, \theta, T, t) \approx \beta_{kl}(A, f, \theta, T). \tag{6.23}$$

In other words, the combined effect of phase and baseline errors introduces a constant offset to the phase delay estimation. For phase-based AOA estimation algorithms, such as interferometry and array processing, this phase delay offset must be removed prior to, or incorporated into, the AOA estimation algorithm.

6.4 Calibration Methodology

6.4.1 Calibration Tables

Calibration techniques attempt to remove the effects of channel imbalances from the uncalibrated signals. To facilitate this process, calibration look-up-tables are used to store the difference between the measured, uncalibrated signals and the theoretical signals derived from the signal model. Sometimes, it may be possible to represent the calibration data more efficiently as a mathematical function.

For phase-based AOA estimation algorithms, the phase delay errors, $\beta_{kl}(A, f, \theta, T)$, must be quantified for all possible signal amplitudes, carrier frequencies, AOAs and receiver operating temperatures that are of interest. However, in practice, the calibration tables will be generated at discrete intervals and interpolation methods will be used to derive the calibration data at intermediate values.

The calibration data needs to be captured using the full antenna array structure connected to the microwave digital receiver and a known transmission source. This data must be collected in a "quiet" RF environment, such as an anechoic chamber or an isolated RF environment, to ensure that no other RF signals or multi-path interferences affect the data.

Since this thesis is primarily concerned with AOA estimation, it is the AOA-dependency of the phase delay error that is of most interest. The calibration look-up-tables can therefore be arranged as a number of one-dimensional, AOA-dependent phase delay errors that belong to a specific combination of signal amplitude, carrier frequency and receiver operating temperature. Since the signal amplitude and carrier frequency can be estimated from the output of a single uncalibrated channel, and since the operating temperature can be directly measured at the receiver, the appropriate look-up-table can be readily determined for a given intercept. When the calibration data is arranged in this way, the AOA-dependent phase delay errors can simply be written as $\beta_{kl}(\theta)$ and so the the calibrated phase delay, $\psi^c_{kl}(\theta)$, can be obtained by simply removing the phase delay error as follows

$$\hat{\psi}^c_{kl}(\theta) = \tilde{\psi}^u_{kl}(\theta) - \beta_{kl}(\theta). \tag{6.24}$$

In practice, fielded direction finding systems often need to be re-calibrated regularly to adapt to changing signal environments, such as a change in physical location or temperature variations over time. Since it is often not practical to perform a full calibration in the field, practical systems often utilise a built-in, partial calibration process where a RF signal is directly injected into the RF chain after the antennas. This allows the calibration algorithm to characterise the digital receiver chain and remove any channel imbalances immediately after the antennas. This method also allows the temperature dependency of the calibration data to be ignored since the calibration data is generated dynamically at the current receiver operating temperature. However, this partial calibration method cannot be used to characterise the channel imbalances from the antenna array. These distortions can only be characterised prior to deployment using over-the-air transmissions from a source with a known AOA.

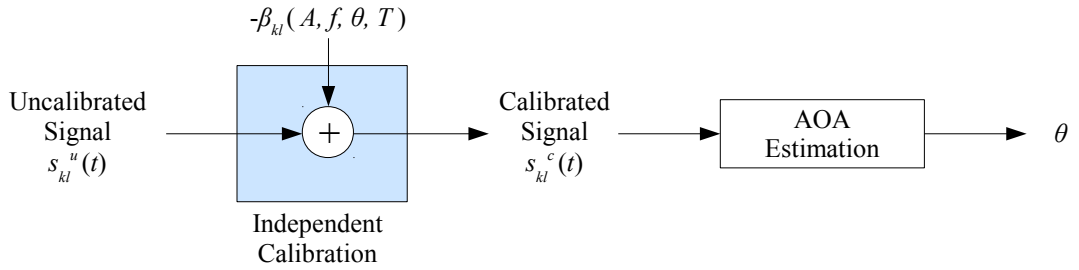

Figure 6.4: A simple calibration method. The signals are calibrated prior to AOA estimation.

6.4.2 Simple Calibration

A simple calibration method would be to subtract the appropriate channel imbalance, $\beta_k(A, f, \theta, T)$, from the phase delay of the uncalibrated signal, $\tilde{\psi}_{kl}^{u}(\theta)$, as described by (6.24), prior to the AOA estimation. This simple calibration method is illustrated in Figure 6.4.

However, in order to apply this simple calibration method, the signal's amplitude, carrier frequency, AOA and the receiver operating temperature must first be known so that the appropriate compensation values can be determined from the calibration tables. While the signal amplitude, carrier frequency and receiver operating temperature can be readily measured, the requirement to know the AOA prior to determining the appropriate compensation values presents a circular dependency problem. That is, the AOA of the signal must be known *prior* to determining the appropriate calibration values that need to be applied, however, the AOA of the signal can only be estimated *after* the system has been calibrated. Thus, this simple calibration method cannot be used to calibrate a multi-channel phase-based direction finding system when the AOA of the signal is not known in advance.

6.4.3 Joint Calibration and AOA Estimation

The circular dependency problem described above can be overcome by modifying the AOA estimation algorithms to directly operate on the uncalibrated data. This method effectively incorporates the calibration process into the AOA estimation algorithm. This joint calibration and AOA estimation methodology is illustrated in Figure 6.5 and will be described in more detail in the subsequent section.

While this integrated calibration methodology is sufficient for AOA estimation, the channel outputs remain uncalibrated. If calibrated signal outputs are desired for subsequent processing, the estimated AOA can be used to cue the simple calibration method discussed in the previous section.

6.5 Short-Baseline Calibration

Unambiguous AOA estimation using a single short-baseline interferometer requires a unique relationship between the measured (calibrated or uncalibrated) phase delays and the AOA. This in turn requires that the relationship be monotonic and that the phase

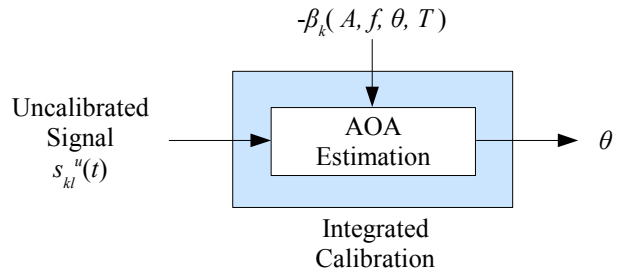

Figure 6.5: The AOA estimation algorithms can be modified to allow AOA estimation directly from the uncalibrated data.

delays lie entirely in the interval $\psi \in [-\pi, \pi]$.

For the calibrated case, the relationship between the calibrated phase delay, ψ^c_{kl}, and the AOA is given by (3.10). For short baselines, i.e. $d_{kl} \leq \lambda_{\min}/2$, the limits of the measured phase delays will be monotonic lie wholly within the interval $\psi^c_{kl}(\theta) \in [-\pi, \pi]$ and so unambiguous AOA estimation can be performed.

For the uncalibrated case, the additive phase delay bias error, $\beta_{kl}(\theta)$, can affect the uniqueness and monotonicity of the relationship between the measured phase delay and the AOA as follows

- $\psi^u_{kl}(\theta)$ remains monotonic and unique for all θ,
- $\psi^u_{kl}(\theta)$ remains monotonic but is not unique for all θ,
- $\psi^u_{kl}(\theta)$ is neither monotonic nor unique for all θ.

In the first case, where $\psi^u_{kl}(\theta)$ maintains a monotonic and unique relationship with all θ, unambiguous AOA estimation can still be performed using a single baseline. Such scenarios can occur when the phase delay errors are a constant value or when the actual interferometer baseline is shorter than the assumed interferometer baseline. However, in the latter two cases, the relationship between ψ^u_{kl} and θ is no longer unique and so unambiguous AOA estimation cannot be performed for all angles using a single baseline. Such scenarios can occur when the interferometer's electrical baseline is longer than its physical baseline or when the antenna elements have a non-monotonic phase response with respect to θ. The following examples will further illustrate these behaviours in more detail.

Example 6.2
Consider a constant phase delay bias error of $\beta_{kl}(\theta) = 50°$ for all θ as illustrated in Figure 6.6. Figure 6.7 shows the corresponding relationship between the uncalibrated phase delay and the AOA. While the uncalibrated phase delays are now offset and discontinuous due to phase wrapping, its relationship with the AOA remains unique and so unambiguous AOA estimation can still be performed with the appropriate compensation.

In this example, the calibration function is not dependent on the AOA and so the calibrated phase delay can be obtained as follows,

$$\hat{\psi}_{kl}^{c}(\theta) = \left[\tilde{\psi}_{kl}^{u}(\theta) - 50^{\circ}\right]_{2\pi}. \tag{6.25}$$

Unambiguous AOA estimation can then be obtained by applying the short-baseline interferometric algorithm to the calibrated phase delay. ∎

Example 6.3
Consider the AOA-dependent phase delay errors that arise due to a shorter than expected interferometer baseline as illustrated in Figure 6.8. Such a situation can occur due to a mismatch between the electrical and physical phase centres of the antennas. In this example, Figure 6.9 shows that the uncalibrated phase delays are a scaled version of the calibrated phase delays and their limits are within the interval $\psi_{kl}^{u} \in [-\pi, \pi]$. Since the relationship between the uncalibrated phase delays and AOAs remains unique, unambiguous AOA estimation can be performed with the appropriate unambiguous compensation.

In this example, the calibration value can be determined directly from the uncalibrated phase delay and does not require direct knowledge of the AOA. That is, the unique relationship between the uncalibrated phase delay and AOA can be exploited to obtain a calibration function to determine the appropriate phase delay error as follows

$$f(\psi_{kl}^{u}) = \beta_{kl}(\theta). \tag{6.26}$$

The calibrated phase delay can be obtained from

$$\hat{\psi}_{kl}^{c}(\theta) = \left[\tilde{\psi}_{kl}^{u}(\theta) - f(\psi_{kl}^{u})\right]_{2\pi}. \tag{6.27}$$

Unambiguous AOA estimation can then be obtained by applying the short-baseline interferometric algorithm to the calibrated phase delay. ∎

Example 6.4
Consider the AOA-dependent phase delay errors that arise due to a longer than expected interferometer baseline as depicted in Figure 6.10. Such a situation can occur due to a mismatch between the electrical and physical phase centres of the antennas. In this example, Figure 6.11 shows that the uncalibrated phase delays are a scaled version of the calibrated phase delays and their limits exceed the interval $[-\pi, \pi]$. Since there is no longer a unique relationship between the uncalibrated phase delays and the AOAs, unambiguous AOA estimation cannot be performed for all angles.

In other words, due to the ambiguous relationship between the uncalibrated phase delay and the AOA, the appropriate phase delay compensation may also be ambiguous. Since the AOA of the signal is not known *a priori*, the appropriate phase delay compensation cannot be determined using a single

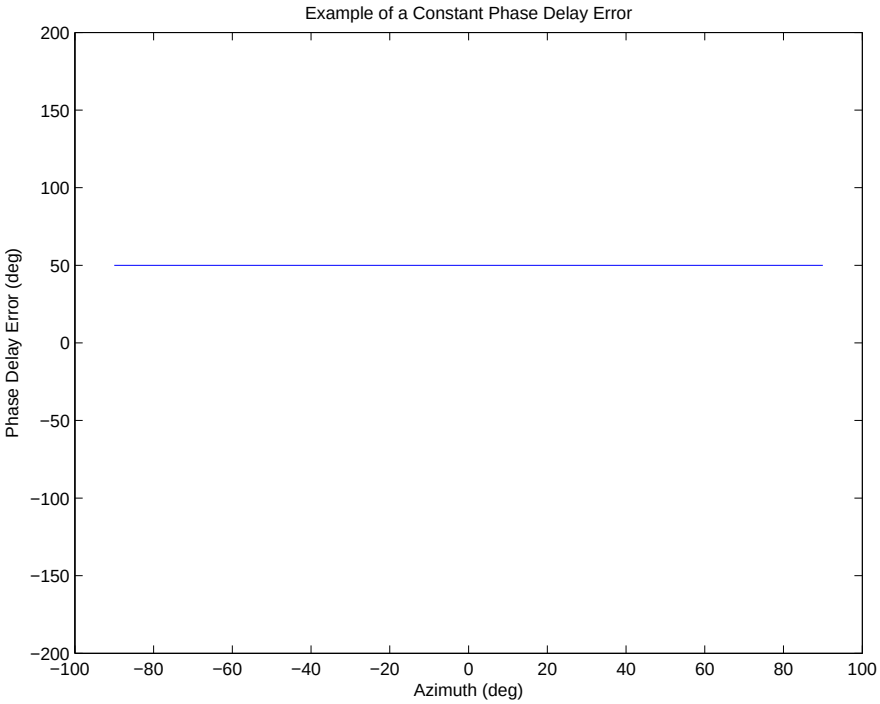

Figure 6.6: Example of a constant phase delay error of 50°.

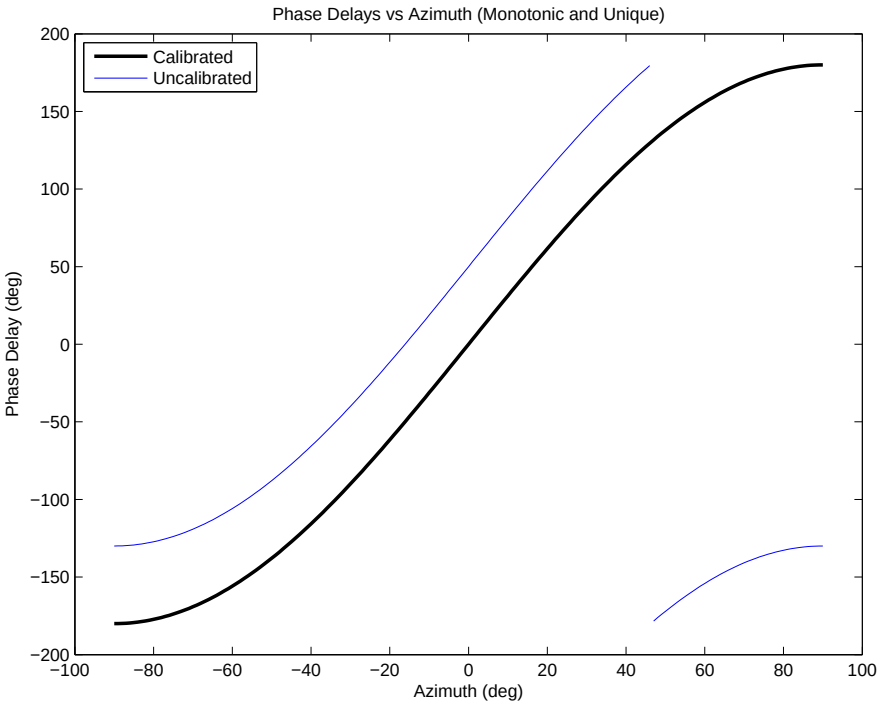

Figure 6.7: The relationship between the uncalibrated phase delays and the AOA remains unique when there is a constant phase delay error.

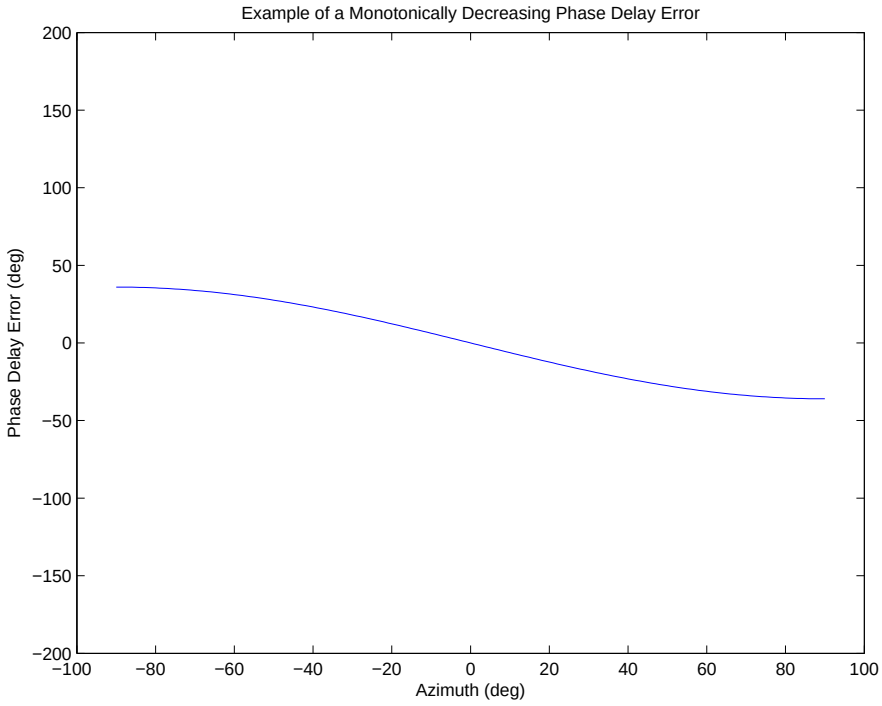

Figure 6.8: Example of a monotonically decreasing phase delay error arising from a shorter than expected interferometer baseline.

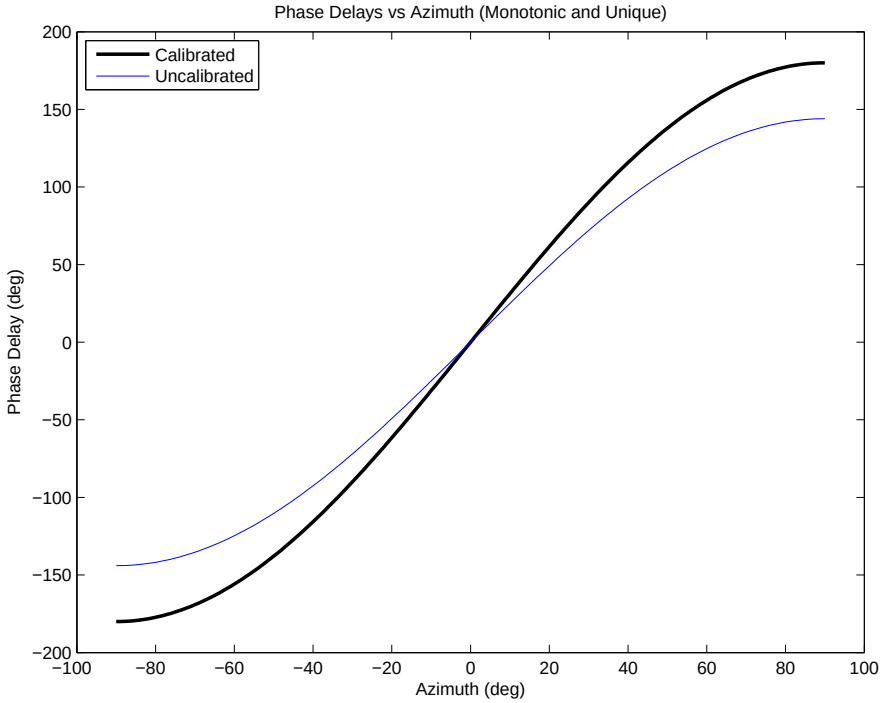

Figure 6.9: The relationship between the uncalibrated phase delays and the AOA remains monotonic and unique and so unambiguous AOA estimation can be performed.

baseline and so unambiguous AOA estimation cannot be performed.

In this example, the uncalibrated phase delays can still be uniquely measured between the interval $\psi_{kl}^u \in [-144°, 144°]$ which corresponds to the AOA interval $\theta \in [-42°, 42°]$. Unambiguous AOA estimation can therefore be performed within a field-of-view of 85°. ∎

Example 6.5
Consider a non-monotonic phase delay error that may arise due to non-linearities in the antenna responses as depicted in Figure 6.12. In this example, the limits of the uncalibrated phase delays are entirely within the interval $\psi_{kl}^u \in [-\pi, \pi]$, however, due to the non-monotonic behaviour, the relationship between the uncalibrated phase delays and the AOAs is ambiguous and so unambiguous AOA estimation cannot be performed for all angles.

In this example, the uncalibrated phase delays can still be uniquely measured between the interval $\psi_{kl}^u \in [-94°, 94°]$ which corresponds to the AOA interval $\theta \in [-20°, 20°]$. Unambiguous AOA estimation can therefore be performed within a field-of-view of 41°. ∎

6.5.1 Implementation Using a 1-D Look-Up-Table

The AOA estimation methodology discussed in this section has thus far assumed a two-step process where calibration is first applied to remove the effects of channel imbalances, followed by the application of the AOA estimation algorithm on the calibrated phase delays. However, for digital, short-baseline interferometers, the AOA estimation can be more efficiently implemented in a single-step using a one-dimensional look-up-table. Provided that the uncalibrated phase delays maintain a monotonic and unique relationship with the AOA, the calibration look-up-table (or an equivalent calibration function) can be used to directly map the uncalibrated phase delays, ψ_{kl}^u, to the appropriate AOA, θ. When an uncalibrated phase delay is measured, the look-up-table can be consulted to give the corresponding AOA estimate. Figure 6.14 depicts such a look-up-table graphically. The advantage of this technique is that the calibration process and AOA estimation can be performed in a single step and has an algorithm complexity of $O(1)$.

6.6 Long-Baseline Calibration

For long baselines, the calibration problem is complicated by the additional ambiguity in the phase delay measurements. If the phase delay error, $\beta_{kl}(\theta)$, is a constant value in all channels, and hence independent of AOA, then this phase delay error can readily be removed prior to applying the AOA estimation algorithm. However, if the phase delay error varies with the AOA, then each uncalibrated phase delay measurement, ψ_{kl}^u, may correspond to multiple ambiguous AOAs, e.g. $\theta_1^a, \theta_2^a, \theta_3^a, \ldots$, etc. and each ambiguous AOA has a different phase delay error, e.g. $\beta_{kl}(\theta_1^a), \beta_{kl}(\theta_2^a), \beta_{kl}(\theta_3^a), \ldots$ etc. Without a unique relationship between the uncalibrated phase delays and the AOA, the short-baseline calibration methods discussed in the previous section cannot be applied.

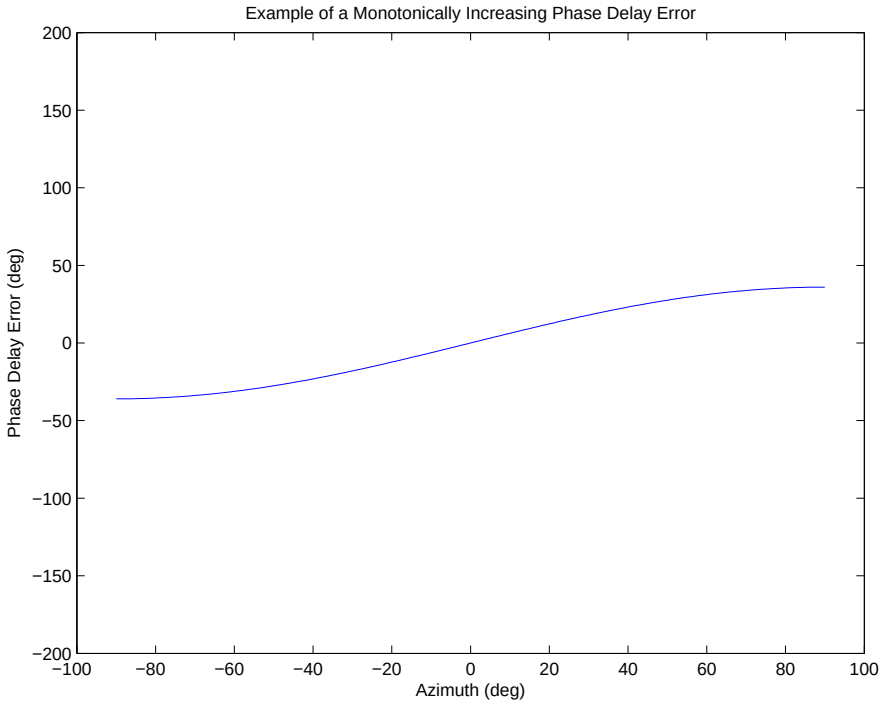

Figure 6.10: Example of a monotonically increasing phase delay error arising from a longer than expected interferometer baseline.

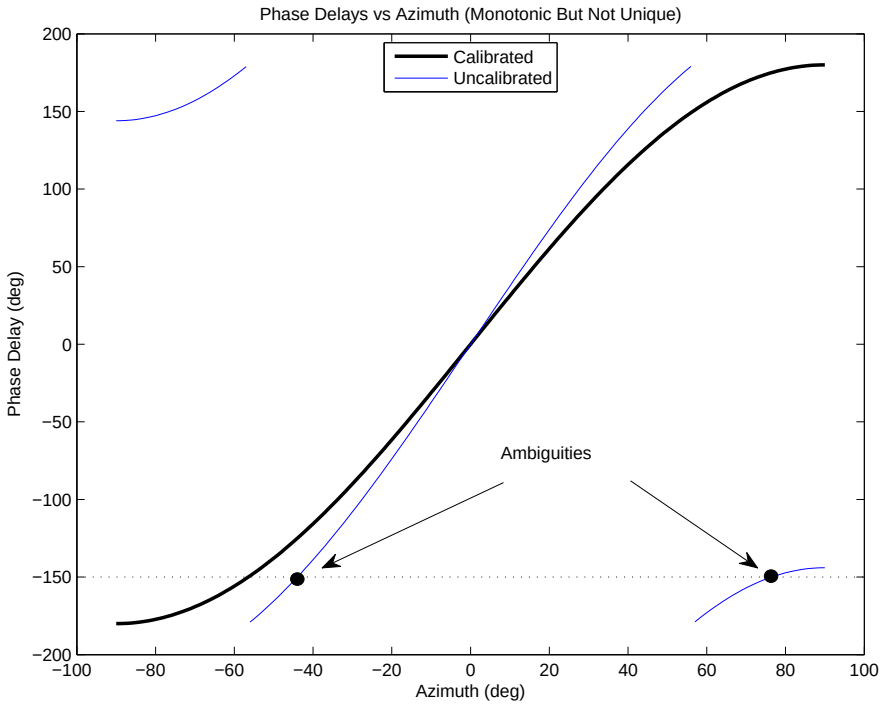

Figure 6.11: The relationship between the uncalibrated phase delays and the AOA remains monotonic but is not unique, and so unambiguous AOA estimation cannot be performed at all angles.

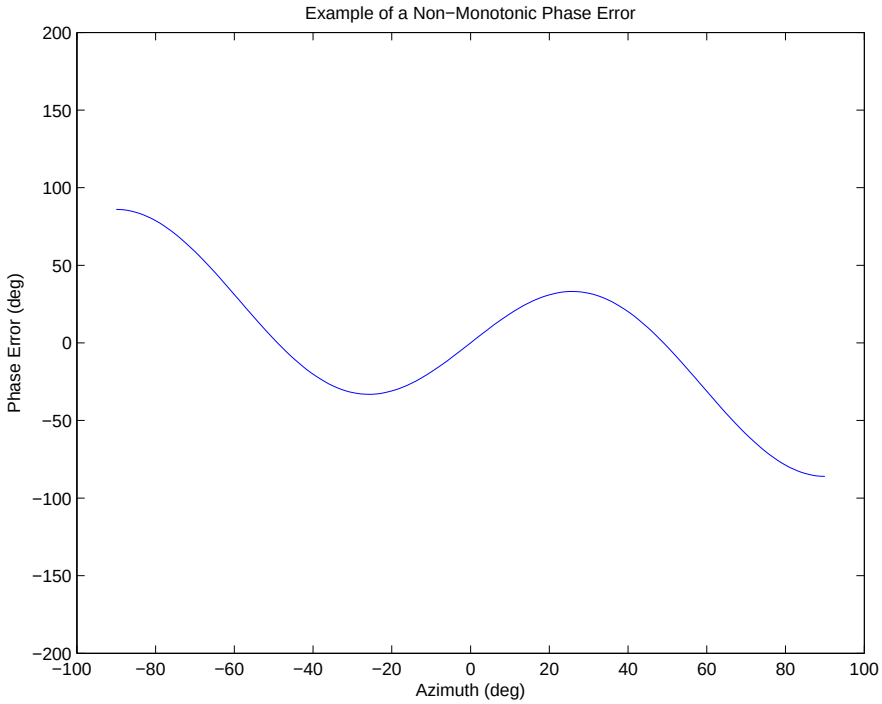

Figure 6.12: Example of a non-monotonic phase delay error.

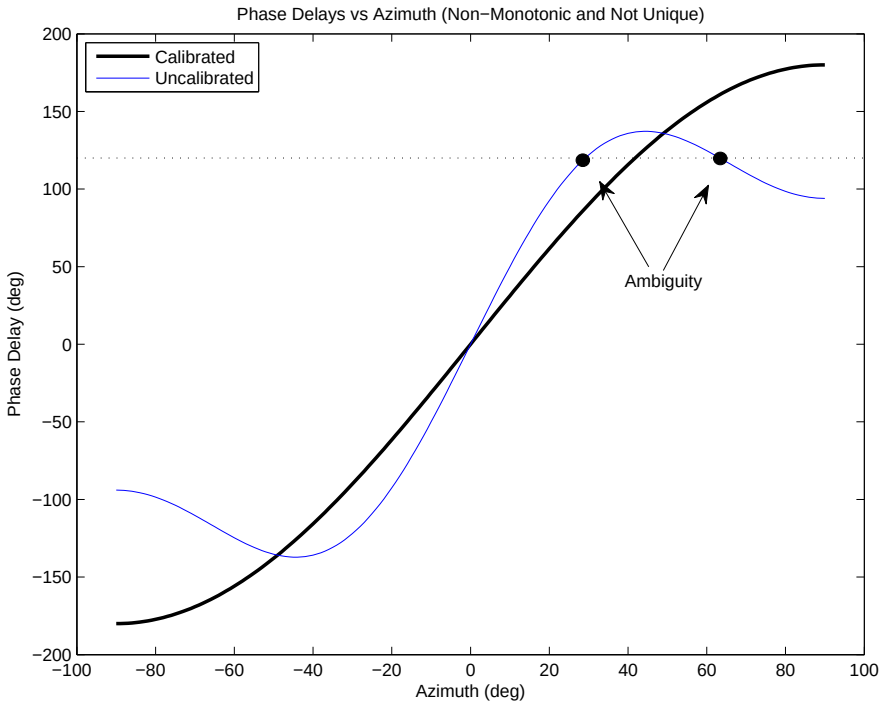

Figure 6.13: Relationship between the uncalibrated phase delays and the AOA is ambiguous if the phase delay error is non-monotonic.

Address	$\psi^u(\theta_1)$	$\psi^u(\theta_2)$	$\psi^u(\theta_3)$	$\psi^u(\theta_4)$	$\psi^u(\theta_5)$	$\psi^u(\theta_6)$	$\psi^u(\theta_7)$	$\psi^u(\theta_8)$	$\psi^u(\theta_9)$	$\psi^u(\theta_{10})$	$\psi^u(\theta_{11})$
LUT Value	θ_1	θ_2	θ_3	θ_4	θ_5	θ_6	θ_7	θ_8	θ_9	θ_{10}	θ_{11}

Figure 6.14: A look-up-table can be used to map the uncalibrated phase delays to the AOA.

In this section, it will be shown that for two or more long baselines, the set of uncalibrated phase delays from all interferometric baselines will be unique for each AOA with appropriate antenna spacings. This allows the long baseline ambiguity resolution algorithms discussed in Section 3.7 to be adapted to incorporate the channel imbalances.

Relationship Between the Uncalibrated, Ambiguous Phase Delays at θ

Consider the uncalibrated, unambiguous phase delays, $\psi^u_{kl}(\theta)$ and $\psi^u_{ml}(\theta)$, of two long interferometric baselines, d_{kl} and d_{ml}, such that

$$\psi^u_{kl}(\theta) = \frac{2\pi f d_{kl}}{c}\sin\theta + \beta_{kl}(\theta) = \tilde{\psi}^u_{kl}(\theta) + \rho_{kl}2\pi, \tag{6.28}$$

$$\psi^u_{ml}(\theta) = \frac{2\pi f d_{ml}}{c}\sin\theta + \beta_{ml}(\theta) = \tilde{\psi}^u_{ml}(\theta) + \rho_{ml}2\pi, \tag{6.29}$$

where $\tilde{\psi}^u_{kl}(\theta), \tilde{\psi}^u_{ml}(\theta) \in [-\pi, \pi]$ are the uncalibrated, ambiguous phase delays and ρ_{kl}, ρ_{ml} are integers representing the ambiguity numbers and are constrained by (3.34). In this section, all phase delay notations have been explicitly written as a function of θ to distinguish between the phase delay measurements from different AOAs. The above expressions can be re-arranged to give the following equality,

$$\frac{2\pi f}{c}\sin\theta = \frac{\tilde{\psi}^u_{kl}(\theta) + \rho_{kl}2\pi - \beta_{kl}(\theta)}{d_{kl}} = \frac{\tilde{\psi}^u_{ml}(\theta) + \rho_{ml}2\pi - \beta_{ml}(\theta)}{d_{ml}}. \tag{6.30}$$

This can be further arranged to give an expression that describes the relationship between the uncalibrated, ambiguous phase delays of each baseline at θ as follows

$$\tilde{\psi}^u_{kl}(\theta) = \frac{d_{kl}}{d_{ml}}\tilde{\psi}^u_{ml}(\theta) + 2\pi\left(\frac{d_{kl}}{d_{ml}}\rho_{ml} - \rho_{kl}\right) - \left(\frac{d_{kl}}{d_{ml}}\beta_{ml}(\theta) - \beta_{kl}(\theta)\right). \tag{6.31}$$

Uncalibrated, Ambiguous Phase Delays at a Different AOA, θ'

Consider the phase delays of the same interferometer baselines at a different AOA, θ'. The unambiguous phase delays are

$$\psi^u_{kl}(\theta') = \frac{2\pi f d_{kl}}{c}\sin\theta' + \beta_{kl}(\theta') = \tilde{\psi}^u_{kl}(\theta') + \rho'_{kl}2\pi, \tag{6.32}$$

$$\psi^u_{ml}(\theta') = \frac{2\pi f d_{ml}}{c}\sin\theta' + \beta_{ml}(\theta') = \tilde{\psi}^u_{ml}(\theta') + \rho'_{ml}2\pi, \tag{6.33}$$

where $\tilde{\psi}^u_{kl}(\theta'), \tilde{\psi}^u_{ml}(\theta') \in [-\pi, \pi]$ are the uncalibrated, ambiguous phase delays and ρ'_{kl}, ρ'_{ml} are integers representing the ambiguity numbers and are constrained by (3.34). Note that the parameters $\tilde{\psi}^u_{kl}(\theta')$, $\tilde{\psi}^u_{ml}(\theta')$, ρ'_{kl} and ρ'_{ml} for θ' are generally different from the parameters $\tilde{\psi}^u_{kl}(\theta)$, $\tilde{\psi}^u_{ml}(\theta)$, ρ_{kl} and ρ_{ml} for θ.

Uniqueness of the Set of Uncalibrated, Ambiguous Phase Delays at Different AOAs

Let $\Psi(\theta)$ denote the set of uncalibrated, ambiguous phase delays from each interferometer baseline for an AOA, θ, as follows,

$$\Psi^u(\theta) = \{\psi^u_{kl}(\theta), \psi^u_{ml}(\theta)\}. \tag{6.34}$$

In order to ensure that the set of ambiguous phase delays from all baselines is unique for all AOAs, the set of uncalibrated, ambiguous phase delays, $\Psi^u(\theta)$, for θ must not be the same as the set of measured phase delays, $\Psi^u(\theta')$, for a different AOA, θ', i.e.

$$\Psi^u(\theta) \neq \Psi^u(\theta'). \tag{6.35}$$

This expression requires that the elements of each set to not be simultaneously pairwise equal. In other words, uniqueness requires at least one of the following conditions to be true,

$$\psi^u_{kl}(\theta) \neq \psi^u_{kl}(\theta'), \qquad \text{or} \tag{6.36}$$
$$\psi^u_{ml}(\theta) \neq \psi^u_{ml}(\theta'). \tag{6.37}$$

While the unambiguous phase delays measured at θ and θ' will be different, it is possible that the measured, ambiguous phase delays of one baseline to be the same due to phase wrapping. As an example, consider that an ambiguity exists in the d_{ml} baseline such that the same ambiguous phase delay is measured at θ and θ'. While the unambiguous phase delays are unique, i.e. $\psi^u_{ml}(\theta) \neq \psi^u_{ml}(\theta')$, it is possible that for this particular pair of AOAs, the measured phase delays are ambiguous such that

$$\tilde{\psi}^u_{ml}(\theta) \equiv \tilde{\psi}^u_{ml}(\theta'). \tag{6.38}$$

When this occurs, the ambiguity numbers will differ, i.e. $\rho_{ml} \neq \rho'_{ml}$, however these values cannot be directly measured. In this example, (6.37) is not satisfied and so (6.36) must be satisfied in order to ensure that $\Psi^u(\theta)$ and $\Psi^u(\theta')$ are unique.

For the d_{kl} baseline, the corresponding uncalibrated, ambiguous phase delay due to θ' can be determined by substituting θ', ρ'_{kl} and ρ'_{ml} into (6.31) to give

$$\tilde{\psi}^u_{kl}(\theta') = \frac{d_{kl}}{d_{ml}}\tilde{\psi}^u_{ml}(\theta') + 2\pi\left(\frac{d_{kl}}{d_{ml}}\rho'_{ml} - \rho'_{kl}\right) - \left(\frac{d_{kl}}{d_{ml}}\beta_{ml}(\theta') - \beta_{kl}(\theta')\right). \tag{6.39}$$

Since it is assumed that $\tilde{\psi}^u_{ml}(\theta) \equiv \tilde{\psi}^u_{ml}(\theta')$, the above expression can be re-written as

$$\begin{aligned}\tilde{\psi}^u_{kl}(\theta') &= \frac{d_{kl}}{d_{ml}}\tilde{\psi}^u_{ml}(\theta) + 2\pi\left(\frac{d_{kl}}{d_{ml}}\rho'_{ml} - \rho'_{kl}\right) - \left(\frac{d_{kl}}{d_{ml}}\beta_{ml}(\theta') - \beta_{kl}(\theta')\right), \\ &= \tilde{\psi}^u_{kl}(\theta) + 2\pi\left(\frac{d_{kl}}{d_{ml}}(\rho'_{ml} - \rho_{ml}) - (\rho'_{kl} - \rho_{kl})\right) - \Lambda(\theta, \theta'),\end{aligned} \tag{6.40}$$

where

$$\Lambda(\theta, \theta') = \left(\frac{d_{kl}}{d_{ml}}(\beta_{ml}(\theta') - \beta_{ml}(\theta)) - (\beta_{kl}(\theta') - \beta_{kl}(\theta))\right). \tag{6.41}$$

Inspection of (6.40) suggests that the ambiguous phase delays, $\tilde{\psi}^u_{kl}(\theta)$ and $\tilde{\psi}^u_{kl}(\theta')$, will only be the same if $\Lambda(\theta, \theta')$ is an integer multiple of 2π *and* either d_{kl} is an integer

multiple of d_{ml} *or* $(\rho'_{ml} - \rho_{ml})$ is an integer multiple of d_{ml}. In practice, d_{ml} can be readily chosen to ensure that $(\rho'_{ml} - \rho_{ml})$ is not an integer multiple of d_{ml}. Thus, if d_{kl} is also chosen to not be an integer multiple of d_{ml} then (6.36) is satisfied and so this guarantees that the set of phase delays is unique for each AOA, i.e. $\Psi(\theta) \neq \Psi(\theta')$. This unique relationship can be exploited to unambiguously estimate the AOA of the signal by modifying the ambiguity resolutions methods discussed in Section 3.7 to estimate the AOA from the uncalibrated data. In contrast to the short-baseline interferometer, the long-baseline interferometer can perform unambiguous AOA estimation without requiring the uncalibrated phase delays in each channel to have a monotonic and unique relationship with the AOA for all angles. Finally, note that unlike the ideal (calibrated) case, a unique relationship between the set of uncalibrated, ambiguous phase delays and the AOA may still exist if d_{kl} is an integer multiple of d_{ml} provided that $\Lambda(\theta, \theta')$ is not an integer multiple of 2π.

6.6.1 Ambiguity Resolution Using Multiple Baselines and Uncalibrated Data

In order to perform unambiguous AOA estimation using uncalibrated data, the ambiguity resolution methods described in Section 3.7 need to be modified to allow them to operate directly on the uncalibrated data. This section will show the necessary modifications for the correlative, common angle search (CAS) and SODA interferometer.

Correlative Interferometers

For correlative interferometers, the required modification involves changing the computation of the cost function, $J(\theta_s)$, to compare the measured, uncalibrated, ambiguous phase delays against the expected uncalibrated, ambiguous phase delays obtained through the calibration process. For example, for a calibrated system, the maximum likelihood cost function is

$$J^c_{\text{MLE}}(\theta_s) = \sum_{m=1}^{M} \cos\Big(\tilde{\psi}^c_m - \psi^c_m(\theta_s)\Big), \tag{6.42}$$

where $\tilde{\psi}^c_m \in [-\pi, \pi]$ is the calibrated, ambiguous phase delay and $\psi^c_m(\theta_s)$ is the calibrated, unambiguous phase delay at θ_s. For an uncalibrated system, the modified cost function can be written as follows

$$J^u_{\text{MLE}}(\theta_s) = \sum_{m=1}^{M} \cos\Big(\tilde{\psi}^u_m - \psi^u_m(\theta_s)\Big), \tag{6.43}$$

where $\tilde{\psi}^u_m \in [-\pi, \pi]$ is the uncalibrated, ambiguous phase delay measured using the hardware and $\psi^u_m(\theta_s)$ is the uncalibrated, unambiguous phase delay measured at θ_s obtained from the calibration data.

Since the above implementation merely swaps the calibrated data with the uncalibrated data, the performance of the correlative interferometer using uncalibrated data remains the same. From Section 3.7.5, the algorithm complexity of the uncalibrated correlative interferometer is $O(\Phi + M(G + 2\Gamma + 1))$, where $\Phi = KN \log_2 N$, K is the number of antennas, N is the number of samples, M is the number of baselines, G is the number of search angles, and Γ is the number of iterations used by Newton's Method.

Common Angle Search

For a calibrated system, the CAS algorithm can be written as a search for the combination of ambiguity numbers that minimise the following cost function,

$$J^c_{\text{CAS}}(\boldsymbol{\rho}^q) = \sum_{m=1}^{M} \left| \frac{\tilde{\psi}^c_m + \rho^q_m 2\pi}{d_m} - \frac{\tilde{\psi}^c_M + \rho^q_M 2\pi}{d_M} \right|, \tag{6.44}$$

where $\tilde{\psi}^c_m \in [-\pi, \pi]$ is the calibrated, ambiguous phase delay, $\boldsymbol{\rho}^q = \{\rho^q_1, \rho^q_2, \ldots, \rho^q_M\}$ is a vector representing the q-th combination of ambiguity numbers corresponding to the AOA, θ^q, from the set of valid ambiguity numbers, Ω_{subset}, ρ^q_m represents the ambiguity number of the d_m baseline for the q-th combination, and $q = 1, 2, \ldots, Q_{\text{subset}}$, where Q_{subset} is the length of the set Ω_{subset}. For an uncalibrated system, this cost function becomes,

$$J^u_{\text{CAS}}(\boldsymbol{\rho}^q) = \sum_{m=1}^{M} \sum_{g=1}^{G} \left| \frac{\tilde{\psi}^u_m + \rho^q_m 2\pi - \beta_m(\theta^g)}{d_m} - \frac{\tilde{\psi}^u_M + \rho^q_M 2\pi - \beta_M(\theta^g)}{d_M} \right|, \tag{6.45}$$

where $\tilde{\psi}^u_m \in [-\pi, \pi]$ is the uncalibrated, ambiguous phase delay measured using the hardware, G is the number of possible angles. Since the AOA of the signal is not known *prior* to the AOA estimation, (6.45) must search for the global minimum of the cost function for all possible AOAs. That is, in addition to searching for the correct combination of ambiguity numbers, the CAS algorithm must also compensate the phase delay errors for every possible angle for each ambiguity number combination. The algorithm complexity of the CAS algorithm applied to the uncalibrated phase delays is therefore $O(\Phi + M(GQ_{\text{subset}} + 1))$ and is significantly higher than the calibrated case.

SODA Interferometry

Consider the uncalibrated, unambiguous phase delays of two long interferometer baselines, d_{21} and d_{32}, such that

$$\psi^u_{21} = \frac{2\pi f d_{21}}{c} \sin\theta + \beta_{21}(\theta), \tag{6.46}$$

$$\psi^u_{32} = \frac{2\pi f d_{32}}{c} \sin\theta + \beta_{32}(\theta). \tag{6.47}$$

The uncalibrated SODA phase delay can be calculated as

$$\psi^u_\Delta = [\psi^u_{32} - \psi^u_{21}]_{2\pi} = \psi^c_\Delta + \beta_{32}(\theta) - \beta_{21}(\theta). \tag{6.48}$$

This expression shows that the SODA phase delay has the same functional form as a short baseline interferometer with an additive, AOA-dependent phase delay error. Hence, the discussion on short-baseline calibration in Section 6.5 is equally applicable to the SODA interferometer and so a simple one-dimensional look-up-table can be implemented to uniquely map ψ^u_Δ to θ provided that the uncalibrated SODA phase delay maintains a unique relationship with the AOA, i.e. the SODA phase delay errors $\beta_{32}(\theta) - \beta_{21}(\theta)$ is monotonic and ψ^u_Δ does not exceed the interval $[-\pi, \pi]$. From Section 4.2.3, the algorithm complexity for the uncalibrated SODA interferometer is $O(\Phi + M + 1)$.

6.7 Summary

In this chapter, it was shown that practical systems will suffer from a number of non-idealities, such as hardware imperfections, imperfect antenna separations, mutual couping, and crosstalk. The aggregated effect of these non-idealities introduces gain, frequency and phase imbalances and baseline errors to the measured phase delays.

The purpose of the calibration process is to remove the channel imbalances to allow unambiguous AOA estimation to be performed. For phase-based AOA estimation methods, such as interferometry, beamforming and array processing, it is the AOA dependency of the phase imbalance that is of most concern. A circular dependency exists since the AOA is required *prior* to calibration to determine the correct phase compensation to apply to the uncalibrated data. However, the AOA is not known until it is estimated *after* calibration. Fortunately, this circular dependency can be eliminated by modifying the AOA estimation algorithms to operate directly on the uncalibrated data. In effect, this latter process integrates the calibration process and AOA estimation into a single step.

For a single short-baseline interferometer, unambiguous AOA estimation can be performed provided that the additive phase delay bias errors are such that the uncalibrated phase delays maintain a monotonic and unique relationship with the AOA. For multiple, long-baseline interferometers, unambiguous AOA estimation can be performed directly on the uncalibrated data using the ambiguity resolution algorithms discussed in Section 3.7 after modifying their cost functions to exploit the uncalibrated phase delays rather than the calibrated phase delays.

Finally, a modified correlative and SODA interferometer can be applied to uncalibrated data with any significant difference in the algorithm complexity and hence computation time. However, when the modified CAS algorithm is applied to uncalibrated data, the algorithm complexity increases significantly and so the algorithm is also slower than the calibrated case.

Chapter 7

The Electronic Support Testbed

7.1 Introduction

The Electronic Support (ES) Testbed is a digital microwave radar intercept receiver that was developed in conjunction with the author's colleagues at the Defence Science and Technology Organisation (DSTO) of Australia. The ES Testbed exists in single-channel and multi-channel configurations and was developed to demonstrate and evaluate signal processing algorithms, such as AOA estimation, for ES and ELINT applications. The multi-channel configuration of the ES Testbed was developed with the express purpose of evaluating the AOA estimation algorithms proposed in this thesis.

It is acknowledged that most of the digital receiver design and implementation of the ES Testbed was performed by DSTO colleagues. The author's contribution to the development of the ES Testbed are as follows:

- providing advice about the architecture and implementation of the multi-channel ES Testbed, particularly in regards to timing and phase coherency between the channels,
- testing and debugging the multi-channel ES Testbed,
- developing a data alignment method to correct for timing mismatches between the hardware components,
- phase calibration of the ES Testbed to allow high-accuracy AOA estimation,
- developing the software front-end for data collection and analysis, and
- validating the performance of the ES Testbed through experimentation by organising and actively participating in a number of field trials and through extensive analysis of the trial data.

In this chapter, the design objectives and hardware specifications of the ES Testbed will be presented.

7.2 Hardware Design

7.2.1 Design Objectives

The objective of the ES Testbed is to provide a research and development platform to implement and evaluate new algorithms and architectures for next-generation microwave radar intercept receivers. The current implementation of the ES Testbed is designed to meet the specifications described in Section 1.4.1 as follows,

- be able to intercept radar signals between $2 - 18$ GHz,
- be able to simultaneously monitor a wide frequency range (up to 500 MHz),
- be able to intercept narrowband and wideband signals (up to 500 MHz)
- be able to exploit multiple, simultaneously illuminating signals,
- maintain near real-time operation in a high signal density environment,
- maintain a high probability of intercept (POI) at all times, and
- be cost effective.

The ES Testbed is implemented in a modular fashion using commercial, off-the-shelf (COTS) components. A modular architecture was intentionally chosen to allow the system to be scaled to an arbitrary number of channels for AOA estimation. The use of COTS components reduces the risk, cost and development time of the system compared to the development of custom hardware.

7.2.2 Sampling Architecture

The signal models and associated AOA estimation theory discussed in this thesis have assumed a complex signal model. In practice, the digital representation of the complex signal consists of an in-phase (real) and a quadrature (imaginary) component. Both components must be available prior to the application of the AOA estimation algorithms. While reception of the in-phase component is straightforward, reception of the quadrature component can either be explicitly performed using *quadrature sampling* techniques or generated from the in-phase component using *real-signal sampling* or *bandpass sampling* techniques. The sampling architecture of the ES Testbed was chosen to implement a bandpass sampling architecture to achieve the computational efficiencies in quadrature generation, filter design and basebanding.

Bandpass Sampling

For a band-limited signal with a non-zero centre frequency of f_c and a bandwidth of B MHz, bandpass sampling recognises that the frequency range of interest only extends from $(f_c - B/2)$ MHz to $(f_c + B/2)$ MHz. With appropriate filtering, the Nyquist criterion for bandpass sampling requires a sample rate of at least $2B$ MSPS [48]. This sampling architecture is depicted in Figure 7.1.

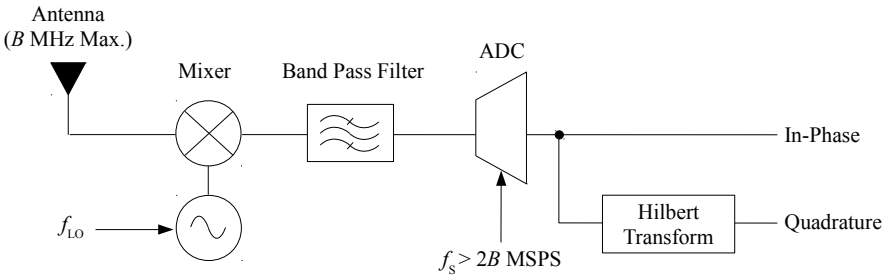

Figure 7.1: Simplified block diagram of a bandpass sampling architecture.

Greater computational efficiencies can be obtained in the signal processing that typically occurs immediately after digitisation, such as quadrature generation, filtering and basebanding, when the signal of interest is centred at $f_s/4$. An efficient signal processing "trick" that can be used to shift a signal centred at f_c to $f_s/4$ is to specifically choose a sample rate that satisfies the following [48]

$$f_s = \frac{4f_c}{m_{\text{odd}}}, \tag{7.1}$$

where f_s is the sample rate, f_c is the centre frequency of the signal and m_{odd} is an odd integer. At this specific sample rate, aliasing effects are intentionally exploited to shift the signal from f_c to $f_s/4$ without any explicit frequency translation operation. Note that the choice of m_{odd} must still ensure that the Nyquist criterion is satisfied, i.e. $f_s \geq 2B$ MSPS. While the chosen sample rate in (7.1) is often faster than the minimum necessary by the Nyquist criterion, the computational advantages offered by this choice of sample rate is often a good trade-off against the cost of a faster ADC as will be discussed below.

Figure 7.2 illustrates the frequency spectrum of a typical real signal at various stages of the bandpass sampling process. In this figure, the signal is assumed to be centred at f_c with bandwidth B MHz. The sample rate is chosen to be $f_s = 4f_c/3$, i.e. $m_{\text{odd}} = 3$. Figure 7.2(a) depicts the frequency spectrum of the real signal prior to sampling. The (blue) trapezoid centred at f_c represents the signal energy at the positive frequency component and the (orange) trapezoid centred at $-f_c$ represents the signal energy at the negative frequency component. Note that the negative frequency component is spectrally inverted. After sampling at a rate of $f_s = 4f_c/3$, aliasing causes the positive frequency component to be "copied" to $-f_s/4$ and the negative frequency component to be copied to $f_s/4$. For illustrative purposes, the aliasing effects are depicted in Figure 7.2(b), however in practice, the frequency spectrum can only be unambiguously observed within the interval $[-f_s/2, f_s/2]$ as depicted in Figure 7.2(c).

One of the first operations that needs to be performed immediately after digitisation of the in-phase signal is to generate the quadrature signal to obtain the complex signal representation. When the signal is centred at $f_s/4$, the quadrature generation can be efficiently implemented as a simple finite impulse response (FIR) filter with as little as 6 taps [107]. The frequency spectrum of the complex signal is depicted in Figure 7.2(d).

Next, the spectral inversion of the aliased signal at $f_s/4$ must be corrected. This is generally achieved by multiplying the digital samples of by a factor $(-1)^n$, where n is the

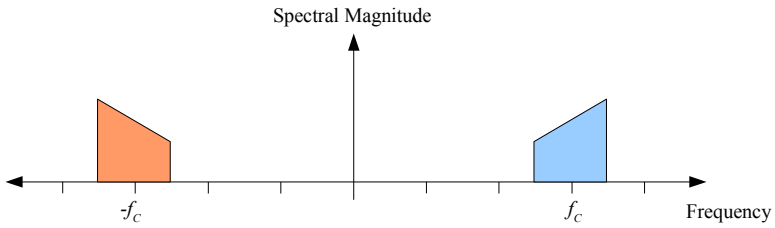

(a) Frequency spectrum of a real signal prior to sampling.

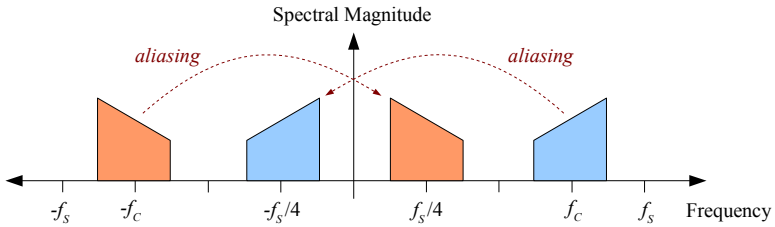

(b) Frequency spectrum of the real signal immediately after sampling

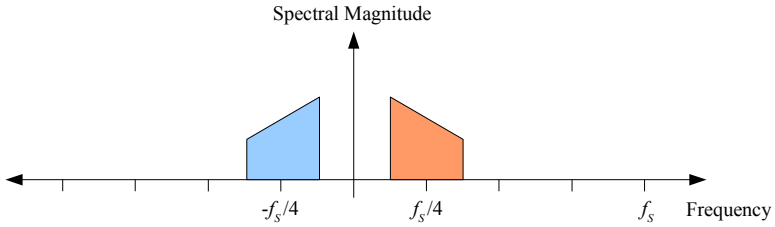

(c) Frequency spectrum of the real signal within the unambiguous interval $[-f_s/2, f_s/2]$.

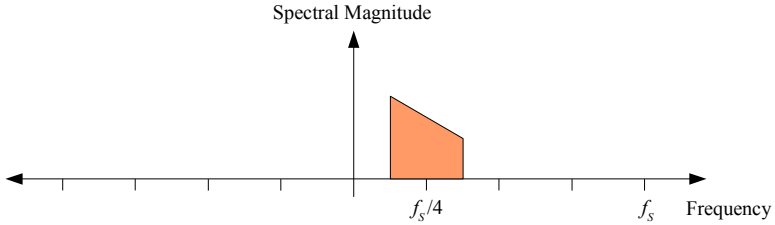

(d) Frequency spectrum of the complex signal after quadrature generation and filtering.

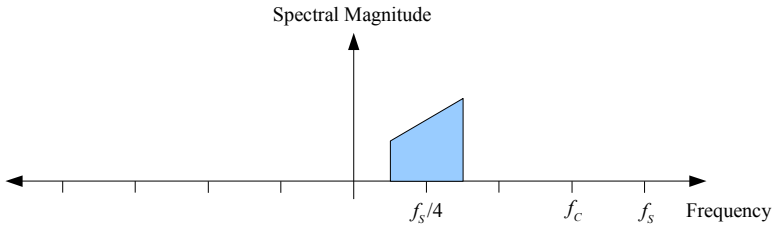

(e) Frequency spectrum of the complex signal after spectral inversion.

Figure 7.2: An appropriately selected sampling rate can shift a signal centred at f_c to $f_s/4$ without an explicit frequency shift operation.

sample number. Since this is simply a sign change of every odd sample, the spectral inversion can be implemented without the use of any multiplications. Since multiplication operations are generally computationally expensive, it is desirable to avoid multiplication operations where possible. Once the spectral inversion has been corrected, the frequency spectrum of the signal will be as depicted in Figure 7.2(e).

In signal processing, basebanding of a signal (i.e. frequency translation to 0 MHz) is a commonly performed operation. Another advantage of centring the signal at $f_s/4$ is that basebanding can also be performed without the use of any multiplications [48].

Finally, filtering is a common operation that is performed in digital signal processing. The intention of digital filters is to allow frequencies within the passband of the filter to pass through the system while rejecting all frequencies outside the passband (i.e. the stopband). In practice, all digital filter designs require some transition bandwidth between the passband and the stopband [48, 108]. The sample rate of practical digital receivers will therefore need to be faster than the Nyquist rate to provide a buffer in the frequency spectrum to allow for the transition bandwidth of digital filters. Another advantage of centring the signal at $f_s/4$ is that the maximum transition bandwidth is available for the digital filters for a given sample rate. In general, a wider transition bandwidth allows simpler digital filters to be used.

Sampling Architecture of the ES Testbed

The sampling architecture of the ES Testbed was chosen to implement bandpass sampling of the signal centred at $f_s/4$ due to the computational efficiencies it offers in quadrature generation, filter design and basebanding. Currently, many commercially-available, microwave (super-heterodyne) tuners exist which are designed to operate between $2-18$ GHz. These tuners commonly down-convert the radio frequency (RF) signal to an intermediate frequency (IF) of 1 GHz and provide an instantaneous bandwidth of 500 MHz. Using these specifications with (7.1), the sample rate of the ES Testbed was chosen to be

$$f_s = \frac{4 \times 1\text{GHz}}{3} = 1333\frac{1}{3}\text{MSPS}, \tag{7.2}$$

where the centre frequency is set to the IF of 1 GHz and $m_{\text{odd}} = 3$. For a signal with a 500 MHz instantaneous bandwidth, the Nyquist criterion requires that the sample rate be at least 1000 MSPS, and so the above sample rate satisfies the Nyquist criterion. The sample interval of the ES Testbed will therefore be $t_s = 1/f_s = 750$ ps. With this sampling rate and IF, the spectrally-inverted, aliased signal will be centred at $333\frac{1}{3}$ MHz.

Note that the down-conversion of the radar signal from RF to IF changes the measured carrier frequency of the signal, however, the signal's original RF can still be determined since the local oscillator frequency is known. The phase of the signal remains unchanged after down-conversion and so the phase delays will still be directly related to the signal's original RF.

7.2.3 Hardware Components

The ES Testbed follows a conventional digital receiver design with a bandpass sampling architecture and is illustrated in Figure 7.3. Microwave radar signals are received at the

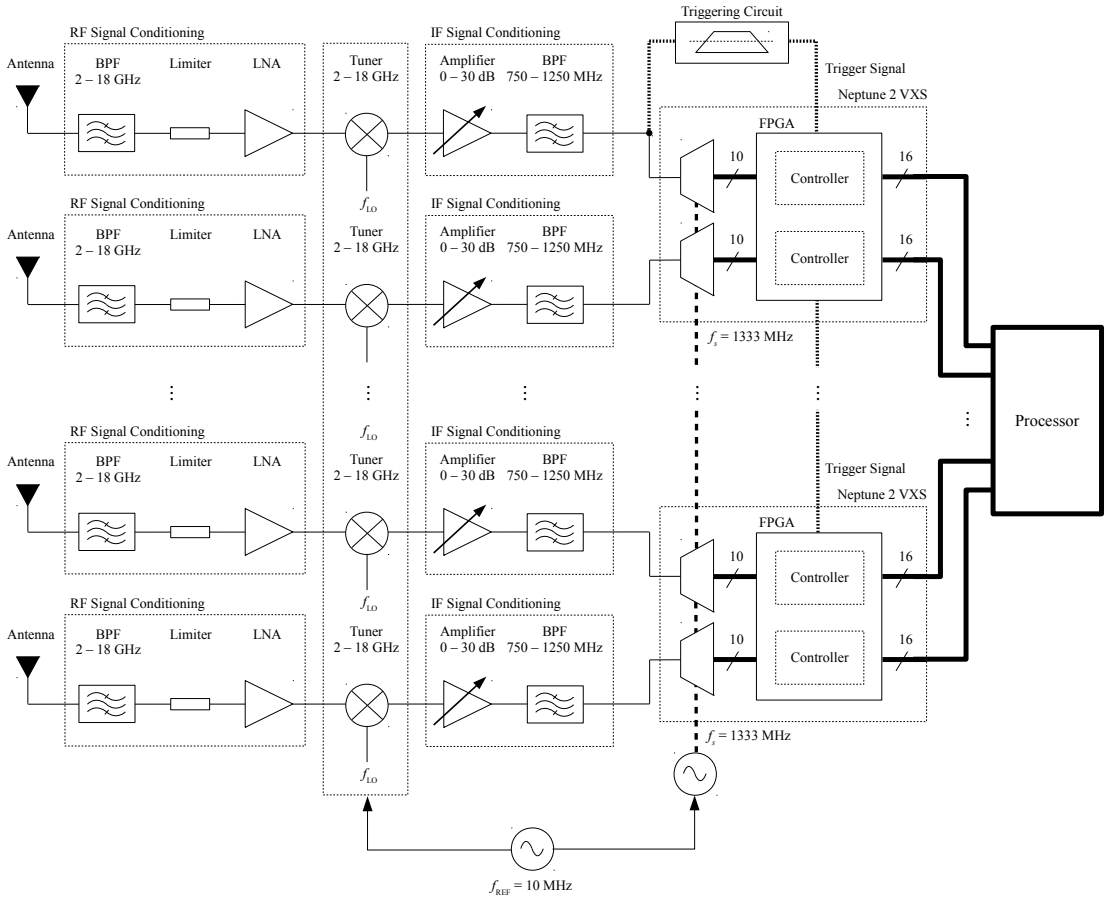

Figure 7.3: Hardware architecture for the multi-channel ES Testbed.

antennas and down-converted from RF to IF using multi-channel, wideband microwave tuners. Signal conditioning (i.e. amplification and filtering) is performed at both RF and IF to improve the fidelity of the down-conversion. The IF signal is digitised using parallel high-speed ADCs and then transferred to a computer where the calibration and AOA estimation methods are applied. All components of the ES Testbed are discrete, commercially-available components that are connected together using RF and IF cables with SMA connectors.

For the experiments conducted during this research, cavity-backed spiral antennas were used to provide wideband frequency coverage between $2-18$ GHz. These antennas (Part Number: C390-188) were manufactured by Microwave Engineering Corporation and are left-hand circularly polarised with a Gaussian-like beampattern with a 3-dB beamwidth of approximately 80°.

The microwave tuners used in these experiments was a MA/Com (now Cobham) TU-6401 SIGINT microwave tuner [109] with multiple TU-6402 slave units [110]. By combining a single TU-6401 unit with a number of TU-6402 units, a scalable, multi-channel, wideband tuner can be realised. The TU-6401 and each TU-6402 is a single-channel super-heterodyne receiver that down-converts RF signals between $2-18$ GHz with instantaneous bandwidths of up to 500 MHz to a 1 GHz IF. To facilitate the phase syn-

chronisation of the receivers, the TU-6401 accepts an external 10 MHz reference signal and shares this reference, along with its local oscillator frequency, with all slave TU-6402 units in a phase-coherent, daisy-chained fashion.

The digitisation of the IF signal is achieved through the use of multiple Neptune 2 VXS digitisation boards from TEK Microsystems, Inc [111]. These high performance signal acquisition boards consist of two independent 10-bit ADCs whose outputs are routed through a single Xilinx Virtex 2 field-programmable-gate array (FPGA). These boards are configured to independently digitise the analogue IF signal from two antennas. The sample rate of the ADCs were set to $1333\frac{1}{3}$ MSPS and was specifically chosen to produce an intentionally aliased digital IF recording centred at $333\frac{1}{3}$ MHz. Multiple Neptune 2 VXS boards can be used to expand the number of channels. The ADCs from multiple boards can be synchronised using an external clock input. This external clock is in turn synchronised using the same 10 MHz reference signal from the MA/Com TU6401 tuner.

Once the IF signal is digitised, the sampled IF data from the Neptune 2 VXS digitisation boards is transferred to a computer for further processing using fibre optic cables. The ES Testbed intentionally sign extends the 10-bit ADC outputs to 16-bit words to allow some bit growth in the subsequent processing or the potential future use of different ADCs (with up to 16-bit outputs). Aligning each sample to an integer multiple of 8-bits also facilitates the data transfer using standard computer transmission protocols. At a sample rate of $1333\frac{1}{3}$ MSPS and a data size of 16-bits per sample, this translates to a data rate of over 21 Gbps per channel if the ES Testbed were to continuously record every sample. However, in theory, the fibre optic cables used by the ES Testbed can only sustain a rate of about 2.5 Gbps per channel. This means that the ES Testbed cannot sustain the continuous recording of the IF signal for extended periods of time. To overcome this limitation, the ES Testbed makes use of an external triggering circuit so that data is only recorded when a signal is detected. Since most radar signals exhibit some sort of duty cycle, either due to its signal waveform or a scanning antenna, the use of a triggering circuit is generally appropriate for ES applications.

7.2.4 Data Encoding

Each channel of the ES Testbed is associated with a single ADC and a FPGA controller that packages the ADC output for transmission through the fibre optic cables to a computer. When no radar signals are present, the ADC continues to operate but the FPGA controller does not send any data to the computer. When a radar signal is detected through the triggering circuit, a control signal is sent to the FPGA controller which starts the data transmission. The ADC output will continue to be sent to the computer as long as the trigger signal is active.

Due to the triggered nature of the system design, it is important to keep track of when a trigger event takes place. This will allow signals from different channels to be associated, as well as inter-pulse characteristics, such as the pulse repetition interval (PRI), to be measured. To achieve this functionality, a 48-bit *time-of-burst* (TOB) value which identifies the time instance of the first sample of the triggered event is inserted into the data stream prior to its transmission to the computer. This TOB is the value of a free-running counter that is incremented at every clock cycle from the moment the

TOB	ADC Data	TOB	ADC Data	···	TOB	ADC Data

Figure 7.4: Typical data stream of one channel from the ES Testbed.

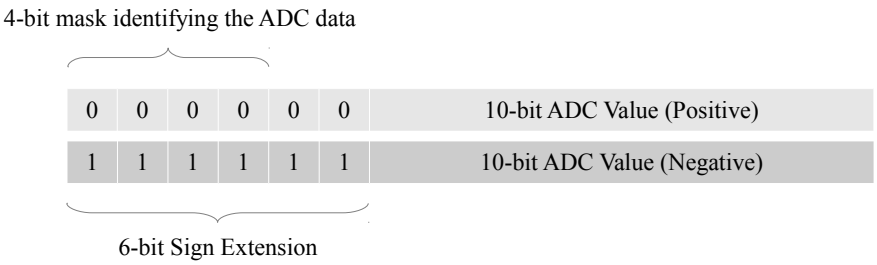

Figure 7.5: Encoding of the ADC data.

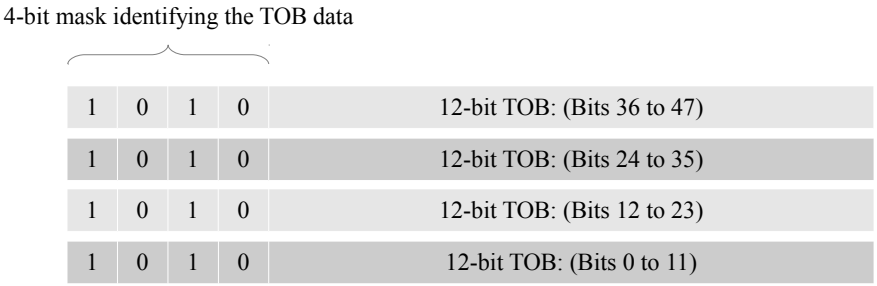

Figure 7.6: Encoding of the TOB data.

Mask (Binary)	Mask (Hexadecimal)	Data Type
1010	A	12-bit TOB Value
0000	0	In-Phase Data (Positive)
1111	F	In-Phase Data (Negative)

Table 7.1: Data masks used in the encoding of the ES Testbed data.

FPGA is turned on. Each digitisation board has its own independent TOB counter.

A typical data stream from each channel of the ES Testbed consists of a TOB value followed by a sequence of in-phase data values as depicted in Figure 7.4. All data from the ES Testbed are encoded as 16-bit words. The 10-bit ADC outputs are sign extended to 16-bits as illustrated in Figure 7.5. The 48-bit TOB value is divided into four 12-bit values. Each 12-bit value is prefixed with a 4-bit binary sequence of '1010' to form a 16-bit word as illustrated in Figure 7.6. Using this encoding scheme, the first four bits of each 16-bit word can be considered as a mask which identifies the data type as tabulated in Table 7.1.

7.3 Data Alignment

7.3.1 Sources of Data Misalignment

A design flaw exists in the current implementation of the ES Testbed where an arbitrary offset is introduced to each channel of the data stream. This data misalignment problem is specific to the current implementation of the ES Testbed and is not to be confused with the synchronisation or calibration of the multi-channel digital receiver. Synchronisation of the system refers to the synchronised timing of the hardware components, such as the local oscillator and ADCs, to ensure that the components in each channel operate at the same time and is achieved through the use of an external reference clock. Calibration of the system refers to the removal of channel imbalances that may arise due to the use of imperfect hardware. While sychronisation and calibration are general system design issues, the data misalignment discussed here is more of a "housekeeping" issue. That is, the data misalignment problem discussed in this section refers to a time and sample offset in the data stream that arises due to the specific implementation and custom firmware of the ES Testbed. The data misalignment problem may be mitigated through a more careful implementation of the ES Testbed.

A number of factors have been identified that contributes to the data misalignment. These factors include:

- TOB offset,
- trigger offset, and
- ADC sample offset.

In the remainder of this section, each factor and its corresponding correction methodology will be discussed. Once the offset in the data stream of each channel is corrected, the data streams are considered to be "aligned". Calibration and AOA estimation algorithms can then be applied to the aligned data.

TOB Offset

The ES Testbed makes use of multiple Neptune 2 VXS digitisation boards. Each digitisation board is designed with its own TOB counter this is referenced to the power-up time of the board. While it is often assumed that all hardware within a chassis will power on at the same time, in practice, there will inevitably be discrepancies in the times that each hardware receives enough electrical current from the chassis to power-up. As a result, the digitisation boards will power up at different times and so the TOB timestamps from each digitisation board to differ slightly, generally in the order of milliseconds. Since pulsed radar signals are often repeatedly transmitted at a pulse repetition interval of the order of microseconds and milliseconds, this difference in the TOB timestamps can cause different intercepts from each channel to be incorrectly associated as belonging to the same intercept.

Once the ES Testbed has been powered up, the TOB offset delay remains constant for the duration of that power cycle. However, the TOB offset delay will differ between power cycles.

Trigger Offset

An external triggering signal is used in the ES Testbed to reduce the data rate of the system by limiting the transfer of the sampled IF to occur only while a signal is detected. While the triggering circuit is designed to deliver the trigger signal to all digitisation boards at the same time, it is possible that different boards will still receive the trigger signal at slightly different times due to hardware imperfections. Furthermore, due to the asynchronous nature of the trigger signal, it is possible that the trigger event can fall exactly on the boundary of a clock cycle of the digitisation board. When this happens, it is possible that one or more digitisation boards will not begin to collect data until the next clock cycle. This means that the data from multiple channels can be offset by exactly one clock cycle (which is 16 samples, or 12 ns, in the current implementation). The trigger offset may occur on an intercept-by-intercept basis.

ADC Sample Offset

The ES Testbed is designed to sample the signal at a rate of $1333\frac{1}{3}$ MSPS (or $1333\frac{1}{3}$ MHz). Since the FPGA immediately after the ADC is unable to operate at such a high frequency, multiplexers (MUX) are used to "slow" the data down to an operating frequency of $333\frac{1}{3}$ MHz.

Since each digitisation board can power-up at different times, the ADCs will also power-up at different times. This means that a different number of samples may be present in the MUX once all of the ADCs have powered up. This sample misalignment is constant once the system has been turned on but will differ between power cycles.

7.3.2 Data Alignment Methodology

The data alignment issues in the ES Testbed can only be corrected by recording a known number of pulses in a controlled environment prior to normal operation. It is important that all components in the ES Testbed are fully powered and that no external signals are collected by the system prior to collecting the control data. The RF input into the microwave tuners of the ES Testbed is designed to allow switching between a control signal via direct injection using a signal generator and from over-the-air transmissions using the antenna array.

When collecting the control data, the output of a signal generator is split among all of the channels. The control signal must be a pulsed signal to provide a time reference for alignment. The signal characteristics, i.e. power, frequency, pulse duration and pulse repetition interval can be arbitrarily chosen, however, the signal power must be high enough to excite the triggering circuit. In the experiments conducted for this research, the parameters of the control signal were set according to Table 7.2. Approximately $100 - 1000$ control pulses should be collected each time the system is power cycled.

The process for collecting the control data is as follows:

1. Turn off the ES Testbed and signal generator.
2. Ensure that the RF switch is set to direct-injection from the signal generator. (i.e. Ensure no signal enters the system through the antennas)

Parameter	Value
Signal Power	-20 dBm
Frequency	9440 MHz
Pulse Duration	1 μs
Pulse Repetition Interval	25 ms

Table 7.2: Parameters for the control signal used for data alignment.

3. Power-up the ES Testbed.
   Wait a few seconds to ensure that all components have fully powered-up.
4. Turn on the signal generator.
5. Capture $100 - 1000$ pulses.
6. Estimate the TOB offsets in each channel.
7. Estimate the trigger offsets in each channel.
8. Estimate the ADC sample offsets in each channel.

In the following discussion, it is assumed that the control data consists of M pulses in each of the K channels of the ES Testbed. The TOB and in-phase data of the m-th pulse of the k-th channel will be denoted as $\text{TOB}(k, m)$ and $x_{k,m}(t)$ respectively.

TOB Offset Correction

The first step in the data alignment is to estimate the TOB offsets. For each pulse, the difference in the TOB values of each channel is calculated relative to an arbitrarily chosen reference channel, typically the first channel. Since the control signal is directly injected into the ES Testbed, it is expected that all channels have the same TOB value. Any differences in the TOB value can be attributed to either the power-up delays or the trigger offsets. Since the trigger offset is not expected to consistently occur, the TOB offset is estimated as the statistical mode of all of the TOB offsets for each channel.

Assuming that the first channel is the reference channel, the TOB offset of the k-th channel, $\tau_{\text{TOB}}(k)$, is calculated as follows:

for k = *2:K* **do**
  for m = *1:M* **do**
    $\text{tobOffsets}(m) = \text{TOB}(k, m) - \text{TOB}(1, m)$
  end
  $\tau_{\text{TOB}}(k) = \text{mode}\,[\text{tobOffsets}]$
end

Trigger Offset Correction

Once the TOB offset of each channel has been estimated, the trigger offset events can be detected by looking for delays between the compensated TOB values that correspond to

exactly one clock cycle of the FPGA. In the current implementation of the ES Testbed, this clock cycle corresponds to exactly 12 nanoseconds (or 16 samples). When a trigger event is detected, the leading 16 samples of each channel *without* the trigger delay is discarded.

The trigger sample offsets for the m-th pulse of the k-th channel, $\delta_{\text{TRIG}}(k, m)$, is calculated as follows:

for k = *2:K* **do**
  for m = *1:M* **do**
    $\text{TOB}_k = \text{TOB}(k, m) - \tau_{\text{TOB}}(k)$
    $\text{TOB}_1 = \text{TOB}(1, m) - \tau_{\text{TOB}}(1)$
    $\delta_{\text{TRIG}}(k, m) = \text{round}\left[\frac{\text{TOB}_k - \text{TOB}_1}{t_s}\right]$
  end
end

ADC Offset Correction

Once the TOB and trigger offsets have been taken into account, the sample offset for a single pulse can be estimated by correlating the in-phase data from each channel with the corresponding data from the first (reference) channel. The ADC sample offset for each channel can then be estimated as the statistical mode of the sample offsets for each channel.

The ADC sample offset of the k-th channel, $\delta_{\text{ADC}}(k)$, is calculated as follows,

for m = *1:M* **do**
  for k = *2:K* **do**
    $\text{TOB}_k = \text{TOB}(k, m) - \tau_{\text{TOB}}(k) + \tau_{\text{TRIG}}(k, m)$
    $x_{k,m}(t)$ = In-phase data from TOB_k until the end of the pulse
  end
  N = Common number of samples in each channel
  for k = *2:K* **do**
    $[\text{maxValue}, \text{maxIndex}] = \max\left[|\text{xcorr}(x_{k,m}(t), x_{1,m}(t))|\right]$
    $\text{adcSampleOffsets}(k, m) = N - \text{maxIndex}$
  end
end
for k = *2:K* **do**
  $\delta_{\text{ADC}}(k) = \text{mode}\left[\text{adcSampleOffsets}(k, :)\right]$
end

7.4 Summary

A significant part of this PhD research is concerned with the experimental validation of the algorithms discussed in this thesis. In this chapter, the hardware architecture

of the multi-channel ES Testbed that was used to collect the data for experimental validation was presented. A significant portion of the author's time during this PhD candidature was spent testing, debugging and calibrating the ES Testbed in order to allow multi-channel, phase-coherent data to be collected. In particular, the alignment and calibration of the data streams from multiple channels was a critical contribution to the development of a functional direction finding system.

Chapter 8

Experimental Results

8.1 Introduction

While the development of signal processing theory is important, the practical value of any algorithm can only be realised if it can be successfully transitioned into hardware. In this chapter, the AOA estimation algorithms (Chapter 3 - Chapter 5) and calibration methods (Chapter 6) will be experimentally validated using data collected from the ES Testbed (Chapter 7).

During the course of this PhD research, a total of seven separate direction finding experiments, or "field trials", were conducted between June 2008 and July 2011. The initial experiments were conducted to test and debug the ES Testbed and so the collected data has since become obsolete as the hardware and firmware was upgraded over time to overcome the errors and limitations observed in the early experiments. Of most value to this PhD research is the data from the latest experiment held in July 2011. This experiment was designated the "Gemini Trial" and was specifically conducted to capture data to experimentally validate the algorithms discussed in this thesis using the latest and most stable iteration of the ES Testbed. This chapter will therefore focus on the results obtained from the Gemini Trial.

8.2 Experimental Setup

In this section, the setup of the Gemini Trial will be presented. While this description will specifically focus on the Gemini Trial, all of the earlier experiments were conducted in a similar manner.

8.2.1 Experiment Site

The Gemini Trial was conducted at a facility owned by the Defence Science and Technology Organisation (DSTO) located at St Kilda, South Australia, Australia. The geographical location of St Kilda is illustrated by Marker A in Figure 8.1. This facility is located in an open field in a semi-rural environment and is located away from possible sources of interferences such as cars, ships, aircraft and transmission towers. In particular, there are little to no interferences at X-Band, which is the frequency band of interest in this experiment.

Figure 8.1: The Gemini Trial was conducted at St Kilda, South Australia (Marker A) in July 2011.

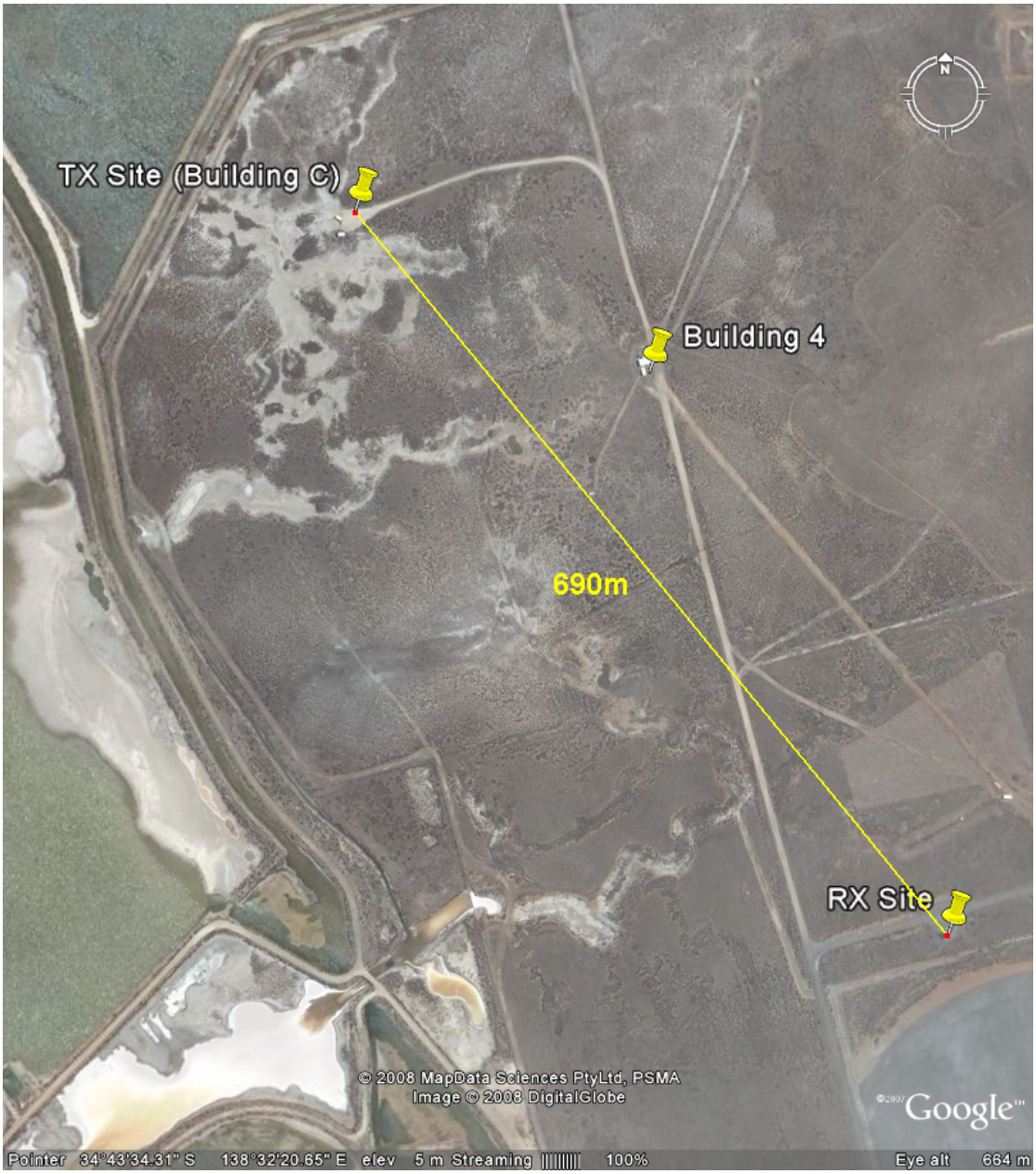

Figure 8.2: Location of the transmitting and receiving sites at St Kilda.

Within the St Kilda facility, two sites were set up to transmit and receive the radar signals respectively. The transmitting site, or "TX Site", was located at "Building C" in Figure 8.2 and the receiving site was located approximately 690 metres away at the point marked as the "RX Site". The two sites were chosen to obtain a line-of-sight between the transmitting and receiving antennas with minimal obstruction. With the exception of a small building marked as "Building 4" in Figure 8.2, there were no other significant infrastructure in the vicinity that may potentially cause RF multipath. The ground between the two sites consists of small and short vegetation and patches of sand and gravel. To avoid the problem of ground reflections, the transmission radar antenna was placed on a platform approximately 2 metres above ground level and the receiving antenna array was placed on a tripod approximately 1 metre above ground level. The receiving antennas (with directional beampatterns) were pointed away from the ground and directly towards the transmission antenna. Post-trial analysis of the experimental data verifies that the effects of ground reflections and multipath are not evident in this experiment and so may be ignored.

8.2.2 Transmission Source

The transmission source used in this experiment was an arbitrary waveform generator whose output was connected to a power amplifier and antenna. The signal waveform was chosen to be a linear FM chirp centred at 9410 MHz with a chirp rate of 510 MHz per 2.5 ms. This particular signal waveform was chosen to allow the simultaneous capture of data across the entire 500 MHz instantaneous bandwidth of the ES Testbed. The signal bandwidth was intentionally chosen to exceed the instantaneous bandwidth of the ES Testbed to observe its behaviour at the extremities of the collection bandwidth.

Linear FM chirp signals are not truly wideband signals in the sense that the frequency content of the signal is narrowband at any one instant in time and changes linearly over time as depicted in Figure 8.3. Over a short observation period of 1.536 μs, or equivalently 2048 digital samples at a sample interval of 750 ps, the rate of change in the signal frequency, Δf, is expected to be

$$\Delta f = \frac{1.536\ \mu\text{s}}{2500\ \mu\text{s}} \times 510\ \text{MHz} \approx 0.3133\ \text{MHz}. \tag{8.1}$$

At a nominal operating frequency of 9410 MHz, a signal bandwidth of 0.3133 MHz only exceeds the centre frequency by about 0.0033% and so may effectively be considered as a narrowband signal within this observation period. The slow-changing linear FM chirp signal can therefore be reasonably approximated as a sequence of short-duration, narrowband, single-tone sinusoids.

Due to the linearity of the frequency change, the instantaneous frequencies observed within a observation period are odd symmetric about the centre frequency of the observation period and so the frequency of the narrowband signal can be approximated by the average of the instantaneous frequencies. Figure 8.4 plots a segment of the instantaneous frequencies of the linear FM chirp (solid line). The dashed vertical lines represent the start and end time of each observation period. The circle markers represent the average instantaneous frequency of each observation period. The sequence of average frequencies closely match the underlying instantaneous frequencies of the linear FM chirp but

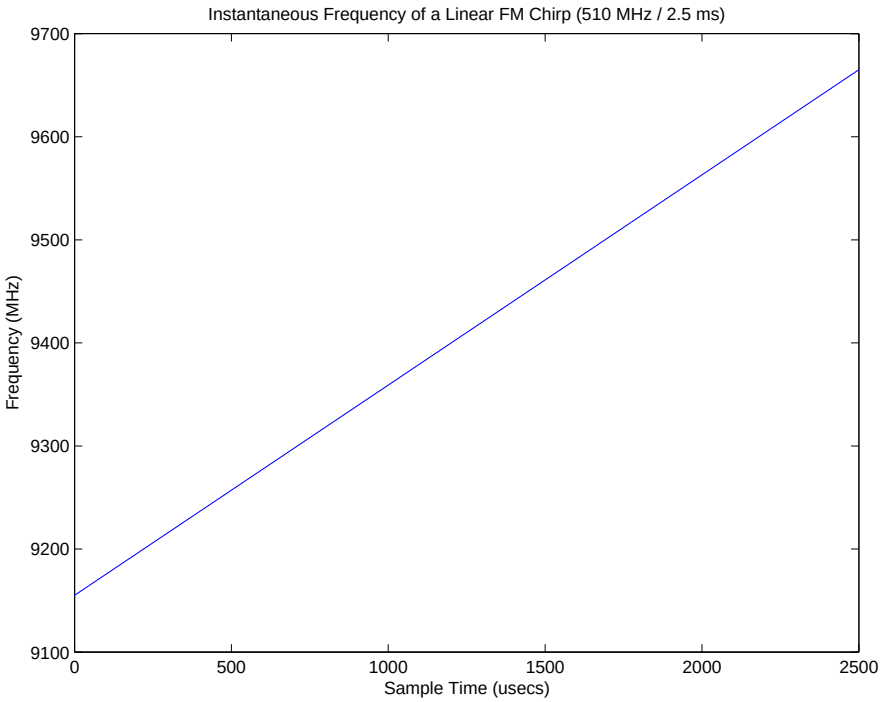

Figure 8.3: Instantaneous frequency of a linear FM chirp signal with a chirp rate of 510 MHz per 2.5 ms.

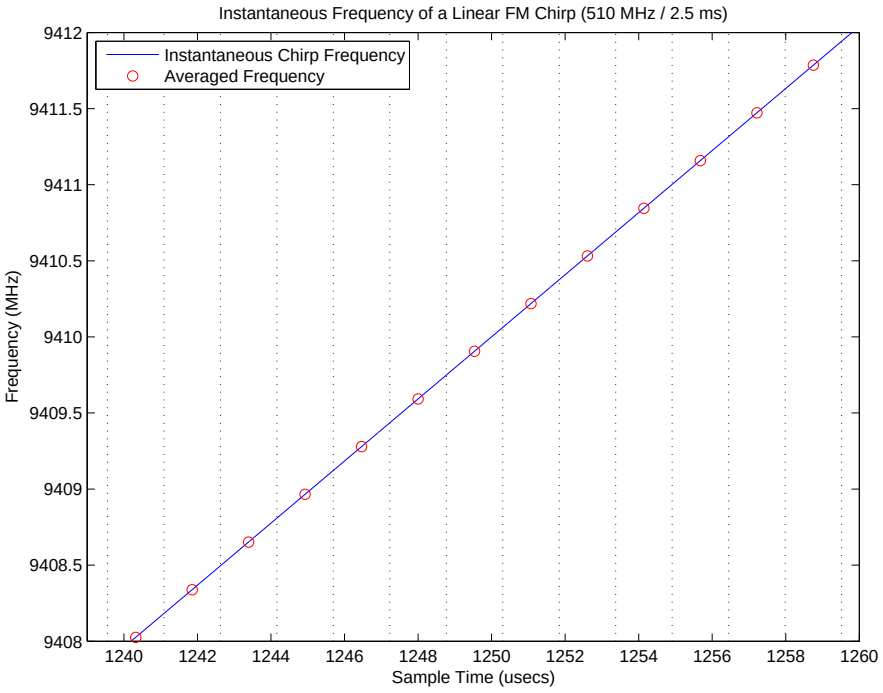

Figure 8.4: The average frequency of each observation period is plotted against the instantaneous frequency of the chirp.

suffers from a consistent bias error of -76.5 Hz as shown in Figure 8.5. Figure 8.6 shows that the corresponding bias error introduced to the AOA estimation is typically less than $2^\circ \times 10^{-5}$ for most angles and at worst is 0.0075° at endfire. Hence, the bias error introduced to the AOA estimation due to the approximation of a slow-changing linear FM chirp as a sequence of narrowband single-tone signals is effectively negligible.

In this experiment, the same signal was used for the system calibration and AOA estimation. In practice, the calibration data will generally be collected prior to the deployment of the system and will differ from the intercepted signal data. However, for the purposes of this experiment and due to time constraints, the same data is used for both system calibration and AOA estimation. The signal-to-noise ratio (SNR) of the received signal collected at the ES Testbed was approximately 5 dB.

8.2.3 Array Geometry

The array geometry of the antennas used in the Gemini Trial is depicted in Figure 8.7. This geometry was intentionally chosen to realistically reflect a practical ES and ELINT system where only a small number of independent receivers are available. Antennas 1, 3 and 4 form a 3-antenna SODA geometry with a 50λ aperture at a maximum frequency of 16 GHz. The design of this array was intentionally chosen to satisfy the objectives other DSTO experiments conducted outside the scope of this research. Antenna 2 was included as an auxiliary antenna to improve the performance of the AOA estimation at low SNR.

Since the transmission signal in this experiment is limited to 9160 MHz - 9660 MHz, and since similar results are obtained at each frequency within this range, the results presented in this chapter will only focus on 9410 MHz. At 9410 MHz, the array effectively has an aperture of 29.41λ and the interferometer baselines are $d_{21} = 3.32\lambda$, $d_{31} = 14.56\lambda$ and $d_{41} = 29.41\lambda$ respectively.

This array geometry is identical to the 3-antenna and 4-antenna array geometries used to evaluate the performance of AOA estimation algorithms in Chapter 3 to Chapter 5. The array beampatterns for the 3-antenna and 4-antenna configurations are shown in Figure 5.22 and Figure 5.23.

The antennas used in this experiment were cavity-backed spirals with a 80° beamwidth. The relatively wide antenna spacings and the directionality of the antennas helped to avoid mutual coupling effects since the antenna beampattern severely attenuates any re-radiated signals in the direction of the other antennas. Furthermore, since the antennas only have a 80° beamwidth, the experiment was constrained to AOA estimation within the interval $[-45^\circ, 45^\circ]$.

8.2.4 Data Collection Methodology

Due to the cost and safety concerns associated with a moving RF transmission source, data was collected at different azimuths by rotating the receiving antenna array while the transmitting antenna was kept stationary. To facilitate this process, the receiving antenna array was mounted on a tripod with an electronically controlled pan-and-tilt

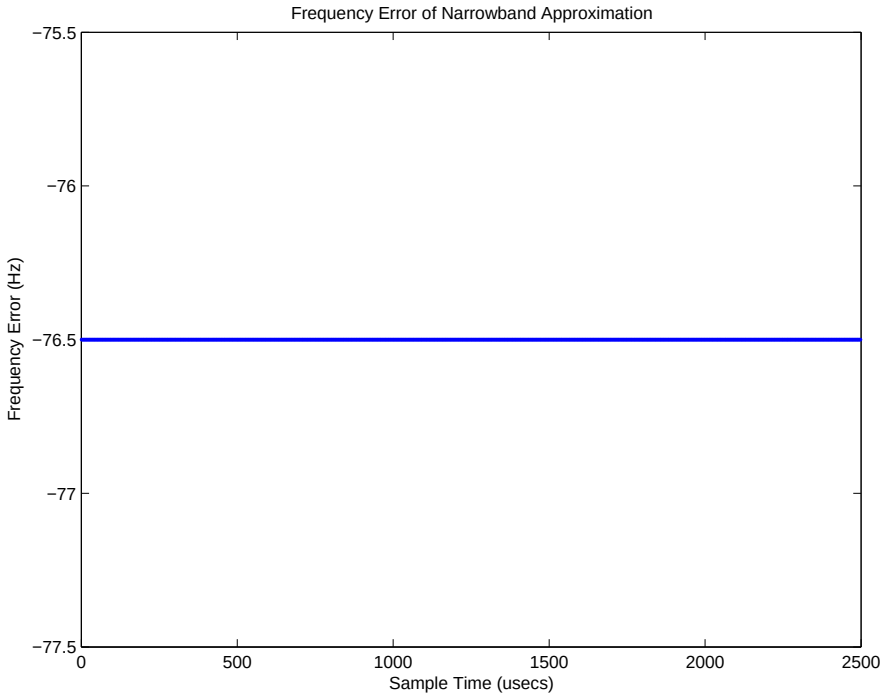

Figure 8.5: The frequency error in the approximation of the centre frequencies of each observation period by the average instantaneous frequencies.

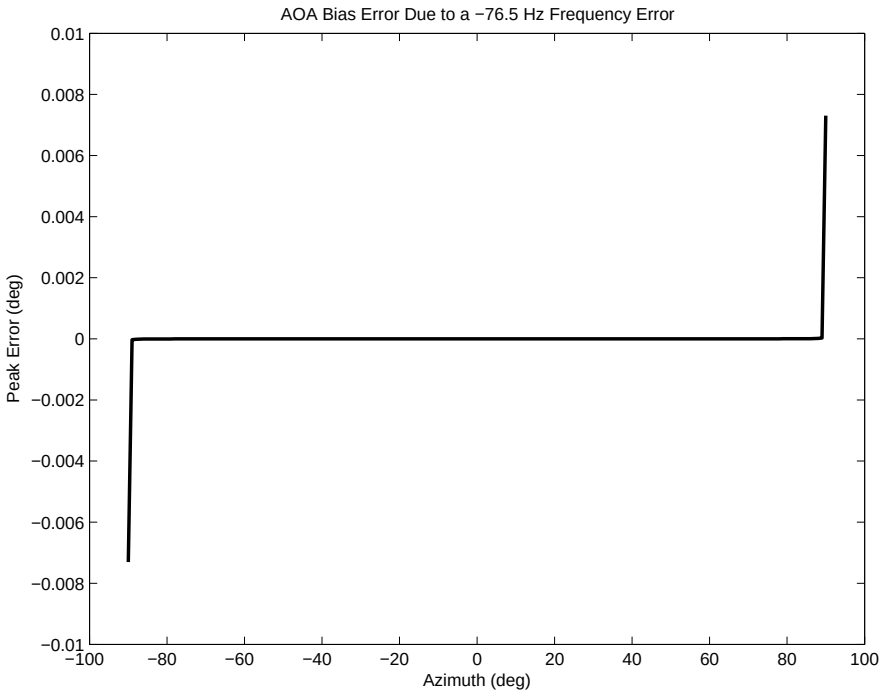

Figure 8.6: AOA bias error due to a 0.3133 MHz frequency error introduced by approximating the slow-changing linear FM chirp signal as a sequence of narrowband, single-tone signals.

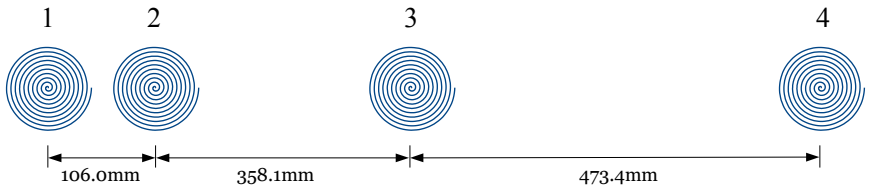

Figure 8.7: Array geometry for the Gemini Trial.

system to allow the array to be rotated in azimuth by a remote operator. Due to time constraints, the antenna array was rotated in 5° intervals. At each azimuth, approximately 48 intercepts of the linear FM chirp signal were collected.

The data was recorded using a frequency-based triggering system with a 15 ms hysteresis. This is a spectrum-based triggering system that activates a data recording when the signal energy in one or more chosen frequency bins of a FFT spectrum exceeds a specified threshold. When a trigger signal is detected, a burst of 15 ms of continuous data is recorded followed by a period of 2 seconds of inactivity to allow the data to be streamed to a computer for storage. For this particular transmission source, each trigger is expected to capture approximately six full linear FM chirp signals.

8.3 Calibration

Figure 8.8 shows the uncalibrated, unambiguous phase delays for the d_{21}, d_{31} and d_{41} interferometer baselines. In these diagrams, the 2π ambiguity of the phase delay measurements were resolved using *a priori* knowledge of the true AOA. Each (blue) dot in these plots represents the mean uncalibrated phase delay measured at a particular AOA. Approximately 20 phase delay measurements are available for each AOA. These figures confirm that the measured uncalibrated phase delays are generally offset from the theoretical phase delays due to phase imbalances in the hardware.

Figure 8.9 plots the errors between the uncalibrated, ambiguous phase delays and the theoretical phase delays. In this figure, each (red) dot represents the mean phase delay error at a particular AOA and the (blue) error bars represent the standard deviation. The mean phase delay errors may be interpreted as the calibration phase offsets, $\beta_{kl}(\theta)$, that need to be subtracted from the measured, uncalibrated phase delays to correct for the channel imbalances. Figure 8.9 can therefore be considered a visual representation of the calibration tables. These plots show that the phase delay errors vary with the AOA and so confirms the uncalibrated signal model presented in Section 6.3.2 is valid.

To illustrate the necessity to estimate the AOA directly from the uncalibrated phase delays, Figure 8.10 plots the calibration values as a function of the uncalibrated, ambiguous phase delays for the d_{41} baseline. For unambiguous AOA estimation, the relationship between the uncalibrated phase delays and the calibration values need to be unique. However, this plot shows that at some uncalibrated phase delay measurements, e.g. at $\tilde{\psi}^u_{41} = 85°$, the calibration values are ambiguous. While Figure 8.10 appears to only exhibit such ambiguities at a small number of phase delays, recall that in this experiment only 19 AOAs are considered in the interval between $[-45°, 45°]$. As more angles

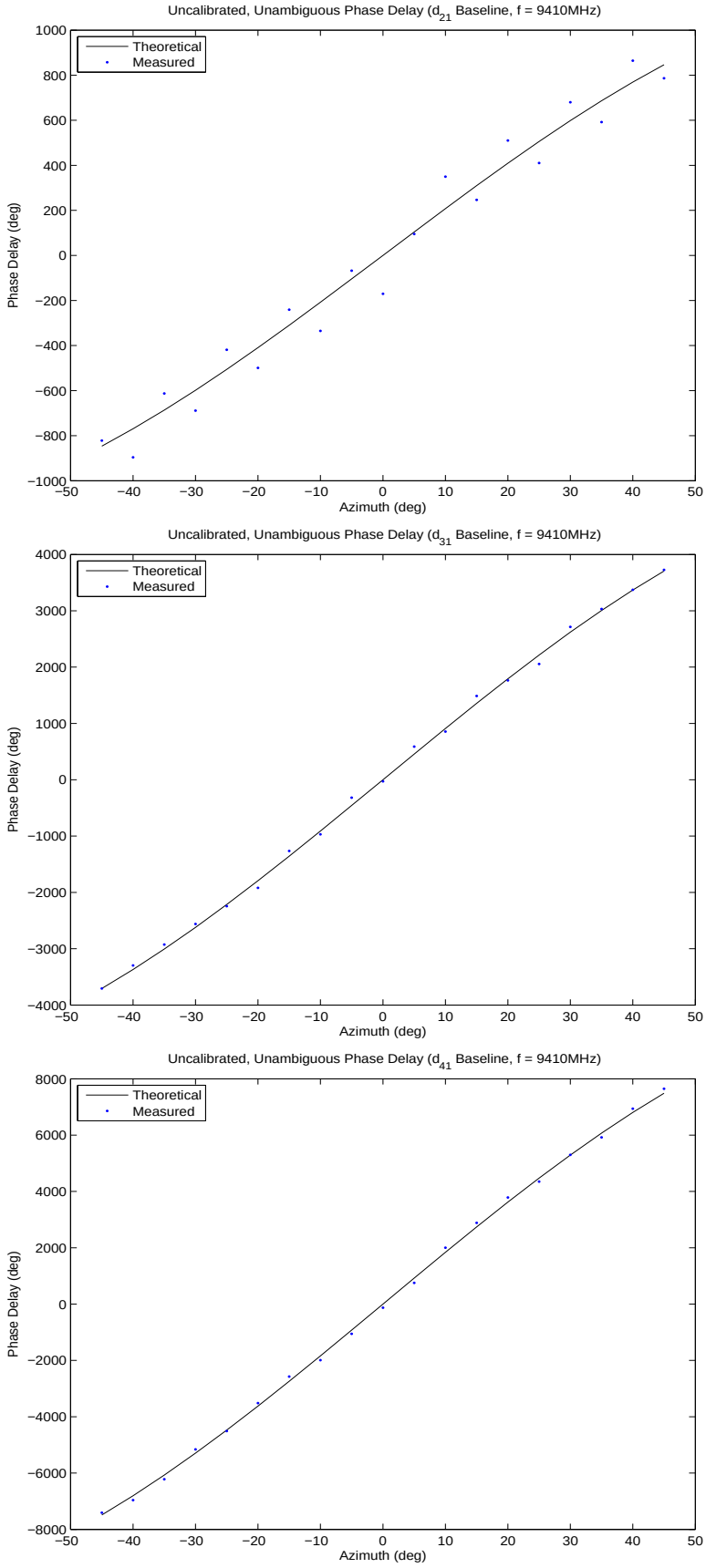

Figure 8.8: Uncalibrated, unambiguous phase delays.

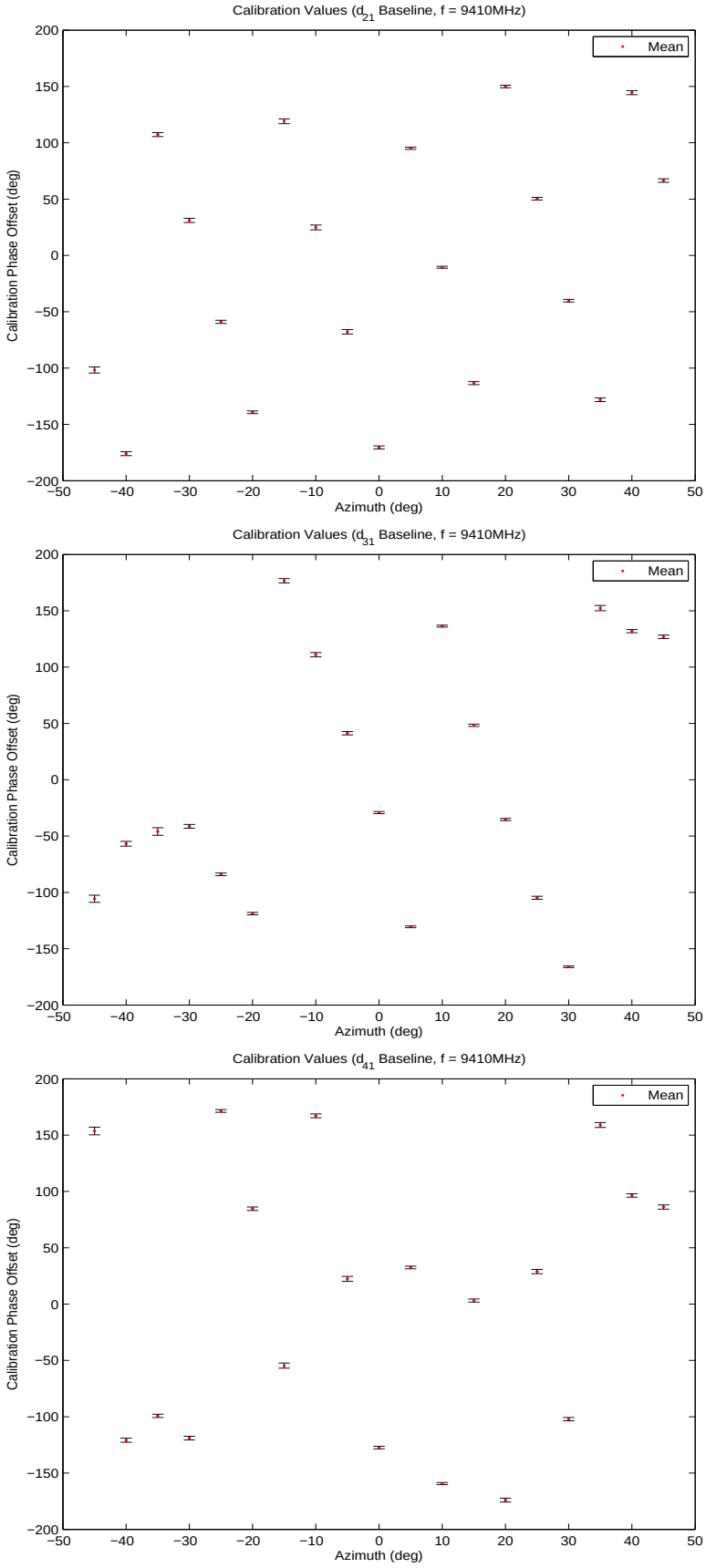

Figure 8.9: Calibration values as a function of azimuth.

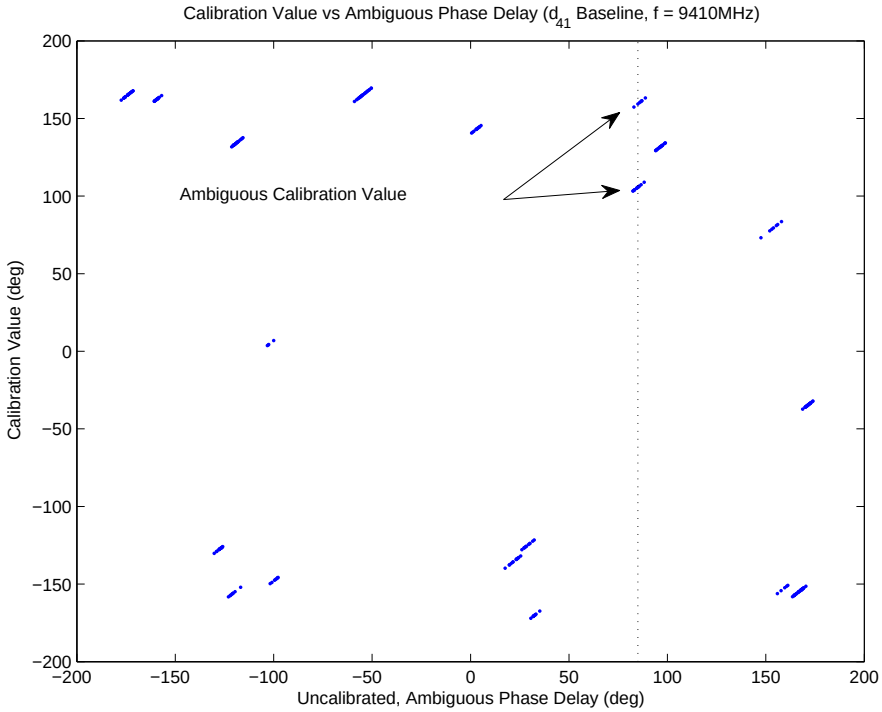

Figure 8.10: Calibration values as a function of the ambiguous, uncalibrated phase delays.

are considered, the number of ambiguities are expected to increase. Unambiguous AOA estimation must therefore be performed directly on the uncalibrated data as described in Section 6.4.3.

8.3.1 Correlative Calibration

In Section 6.6, it was shown that the set of uncalibrated, ambiguous phase delays is expected to be unique for each AOA. This claim is visually verified by Figure 8.11 which overlays the mean and standard deviation of the uncalibrated, ambiguous phase delays for each baseline as a function of AOA as dots and error bars respectively. As an example, consider that a signal arrives from $\theta = -30°$. At this AOA, the measured phase delays for the d_{31} baseline is approximately $\tilde{\psi}^u_{31}(-30°) \approx -42°$. Unfortunately, the d_{31} baseline may also measure the same phase delay when $\theta = -35°$, and so based on this phase delay measurement alone, it cannot be determined whether the AOA is $\theta = -35°$ or $\theta = -30°$. However, for $\theta = -30°$, the d_{21} and d_{41} baselines are expected to measure a phase delay of $\tilde{\psi}^u_{21}(-30°) \approx 35°$ and $\tilde{\psi}^u_{41}(-30°) \approx -116°$ respectively. On the other hand, for $\theta = -35°$, the d_{21} and d_{41} baselines are expected to measure a phase delay of $\tilde{\psi}^u_{21}(-30°) \approx 108°$ and $\tilde{\psi}^u_{41}(-30°) \approx -97°$ respectively. Thus, when the signal AOA is $\theta = -30°$, the set of phase delay measurements, $\Psi(\theta = -30°)$, will be

$$\Psi(\theta = -30°) \approx \{35°, -42°, -116°\}\,. \tag{8.2}$$

Similarly, when $\theta = -35°$, the set of phase delay measurements, $\Psi(\theta = -35°)$, will be

$$\Psi(\theta = -35°) \approx \{108°, -42°, -97°\}\,. \tag{8.3}$$

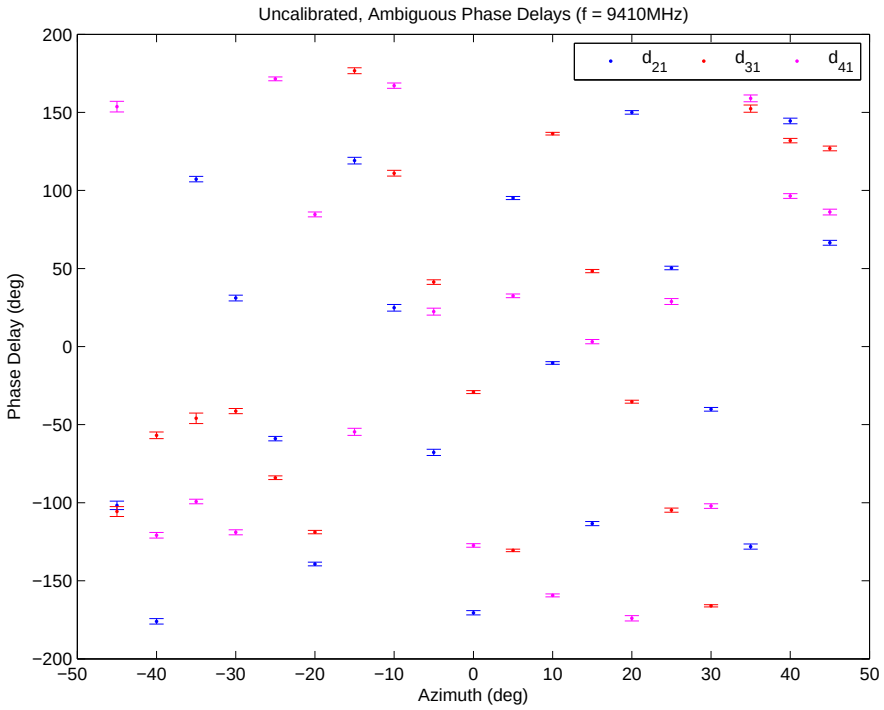

Figure 8.11: Plot of the uncalibrated, ambiguous phase delays as a function of AOA for each baseline.

Since there is a sufficient difference to distinguish $\Psi(\theta = -30°)$ from $\Psi(\theta = -35°)$, the set of uncalibrated, ambiguous phase delays is sufficiently unique that unambiguous AOA estimation can be performed using correlative interferometry as described in Section 6.6.1. The estimated AOA can then be used to determine the corresponding calibration values from the calibration tables (i.e. Figure 8.9) using the simple calibration method described in Section 6.4.2.

Figure 8.12 plots the unambiguous phase delays for the d_{21}, d_{31} and d_{41} interferometer baselines. The black line represents the expected, theoretical phase delays, the (blue) dots represent the uncalibrated phase delays and the (red) crosses represent the calibrated phase delays of each measurement using the correlation-based calibration method. Figure 8.13 shows that after calibration, the residual error in the phase delays are centred about zero and so suggests that the phase bias errors have been successfully removed. This suggests that the correlation-based calibration method is very effective at correcting the AOA-dependent phase imbalances.

8.3.2 SODA Calibration

In Section 6.6.1, it was shown that the uncalibrated SODA interferometer is equivalent to an uncalibrated short-baseline interferometer and so unambiguous AOA estimation can be performed using a one-dimensional look-up-table to map the uncalibrated phase delays to the estimated AOA as described in Section 6.5.1. Figure 8.14 plots the true AOA as a function of the uncalibrated SODA phase delays. In this figure, the (blue)

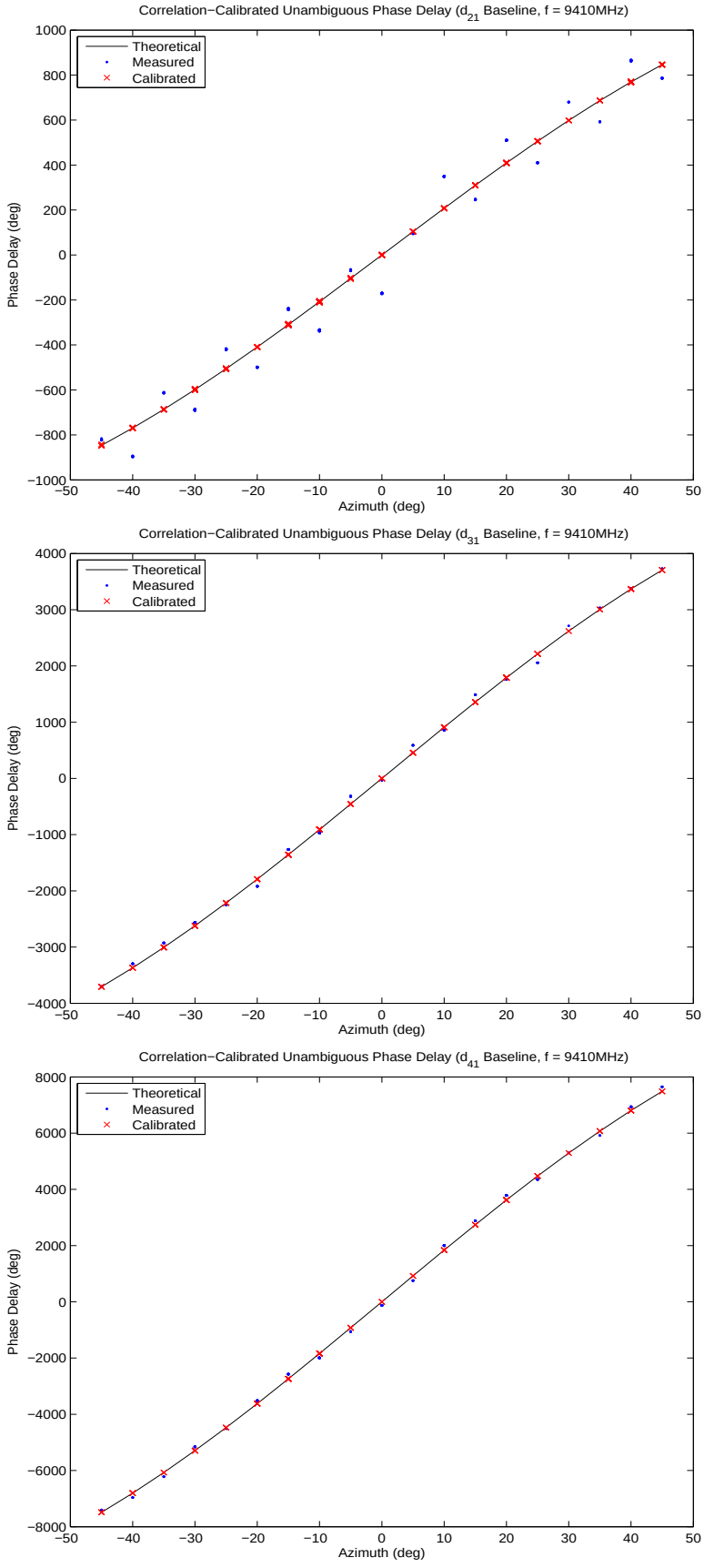

Figure 8.12: Calibrated phase delays using correlative interferometry.

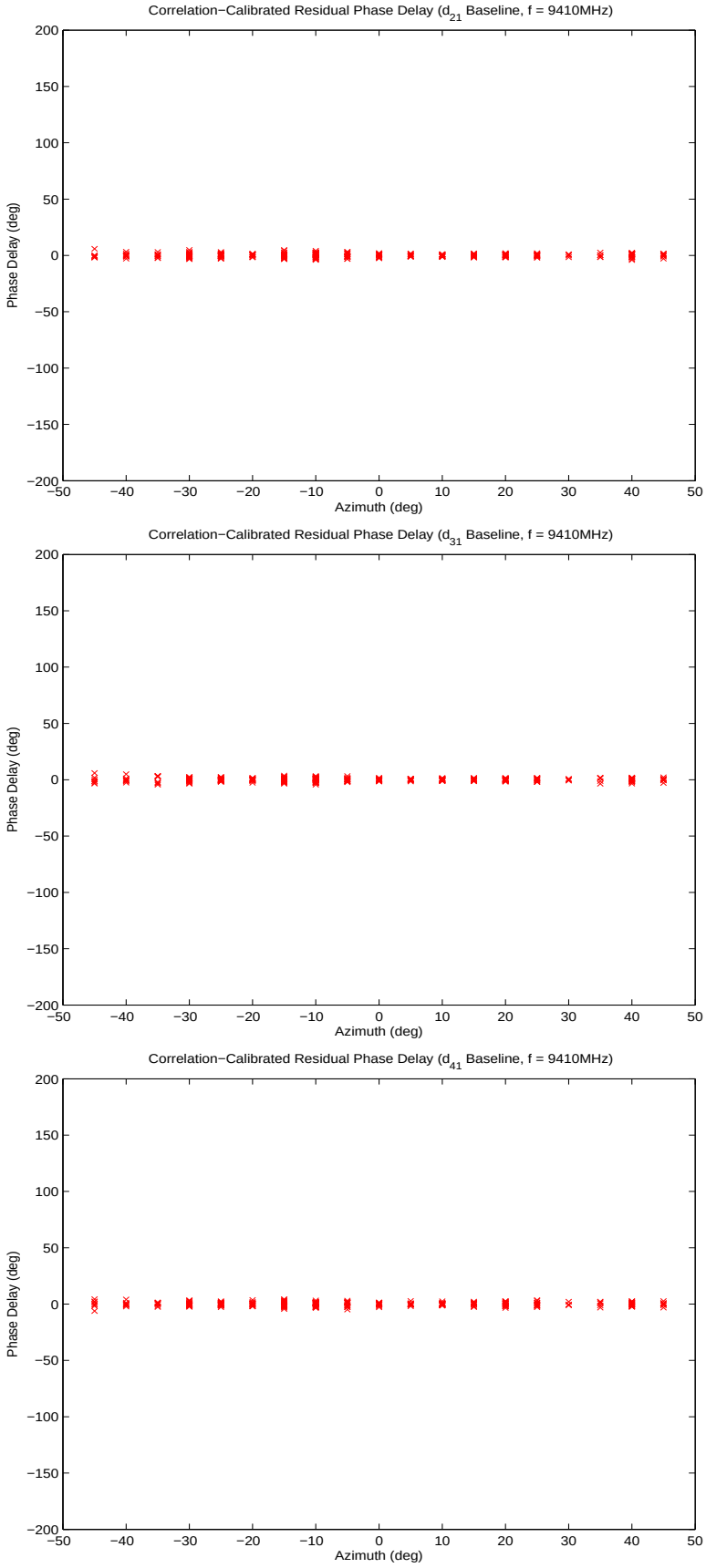

Figure 8.13: Residual phase delay offsets after calibration using correlative interferometry.

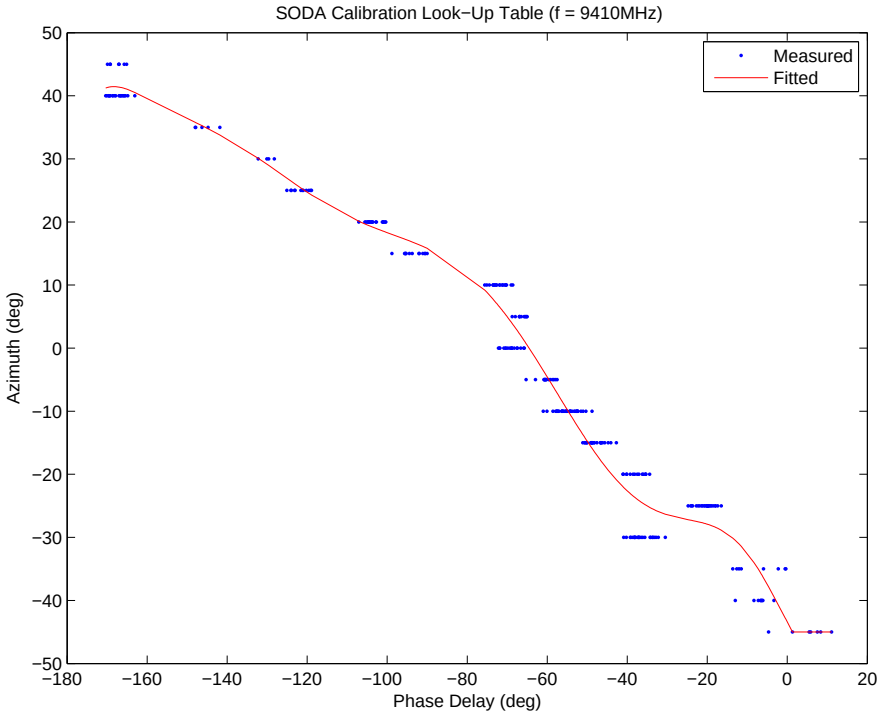

Figure 8.14: Look-up-table for SODA AOA estimation using the uncalibrated SODA phase delays.

dots represent a single uncalibrated SODA phase delay as a function of the AOA. The (red) line is a "best-fit" calibration function that succinctly describes the relationship between the uncalibrated phase delays and the estimated AOA. In this plot, the calibration function is a modified ninth-order polynomial whose end values have been modified to better reflect the limits of the experiment.

Inspection of Figure 8.14 shows that the SODA phase delays in this experiment are slightly ambiguous due to two distinct effects. Firstly, while the SODA calibration function is mostly monotonic, there is a small non-monotonic region in the interval $\psi_\Delta^u \in [-180°, -158°]$. This ambiguity can cause the wrong AOA to be estimated when $\theta = 40°$. Secondly, an additional ambiguity arises at a number of AOAs, such as $\theta = -30°$ and $\theta = 0°$, because the spread of the SODA phase delays for different AOAs overlap. This causes one SODA phase delay be to associated with multiple possible AOAs and so the AOA estimation is ambiguous. Since the variance of the SODA phase delays is dependent on the SNR of the signal, these ambiguities cannot be removed.

In this experiment, the AOA estimation error at the ambiguous angles is not expected to exceed $5° - 10°$ since the two sources of phase ambiguity described above are only ambiguous among adjacent AOAs. Despite the phase ambiguities, AOA estimation can still be performed by simply applying the uncalibrated SODA phase delays to the calibration function. The estimated AOA can then be used to determine the corresponding phase delay calibration values from the calibration tables (Figure 8.9) using the simple calibration method described in Section 6.4.2.

Figure 8.15 plots the unambiguous phase delays for the d_{21}, d_{31} and d_{41} interferometer baselines. The black line represents the theoretical phase delays, the (blue) dots represent the uncalibrated phase delays and the (red) crosses represent the calibrated phase delays using the SODA-based calibration method. This figure shows that the SODA-based calibration method can generally correctly compensate for the AOA-dependent phase imbalances, however, multiple results are obtained for some AOAs. At these AOAs, it is possible that the AOA will be incorrectly estimated and so the wrong calibration value is applied. Figure 8.16 plots the residual error in the phase delay after calibration. This figure shows that while many of the residual errors are centred about zero, a large number of phase delay measurements still contain biases due to the incorrect AOA estimation. These plots suggest that the performance of the SODA calibration is not as good as the correlative calibration method and its poorer performance is attributed to the ill-behaved (i.e. overlapping) SODA phase delays.

It should be noted that the performance of SODA calibration is related to the SNR of the signal and the nature of the phase imbalances of the specific hardware configuration. In this experiment, when the SODA calibration was applied to the ES Testbed at 5 dB SNR, the calibration process was only able to partially remove the effects of the phase imbalances. However, with a different hardware configuration, e.g. different antennas, and at higher SNR, the performance of the SODA calibration is expected to improve.

8.4 Experimental Results

In this section, the experimental performance of the following AOA estimation algorithms is compared:

- SODA interferometry,
- SBI interferometry,
- MLE interferometry,
- first-order CBF and MUSIC algorithms,
- second-order CBF and MUSIC algorithms, and
- SBI-cued and SODA-cued MLE, CBF and MUSIC algorithms.

Since the correlative calibration was shown to be more effective at removing the effects of phase imbalances, the correlative calibration method will initially be used to compare the experimental performance of the algorithms to get a sense for the best possible performance of each algorithm. However, in practice, there is little point in using the SODA interferometer with correlative calibration since the computational advantages of the SODA interferometer cannot be realised. In order to fully exploit its computational speed advantage, the SODA interferometer needs to be coupled with the SODA calibration method. The second part of this section shall evaluate the experimental performance of the SODA and SBI interferometers using SODA calibration.

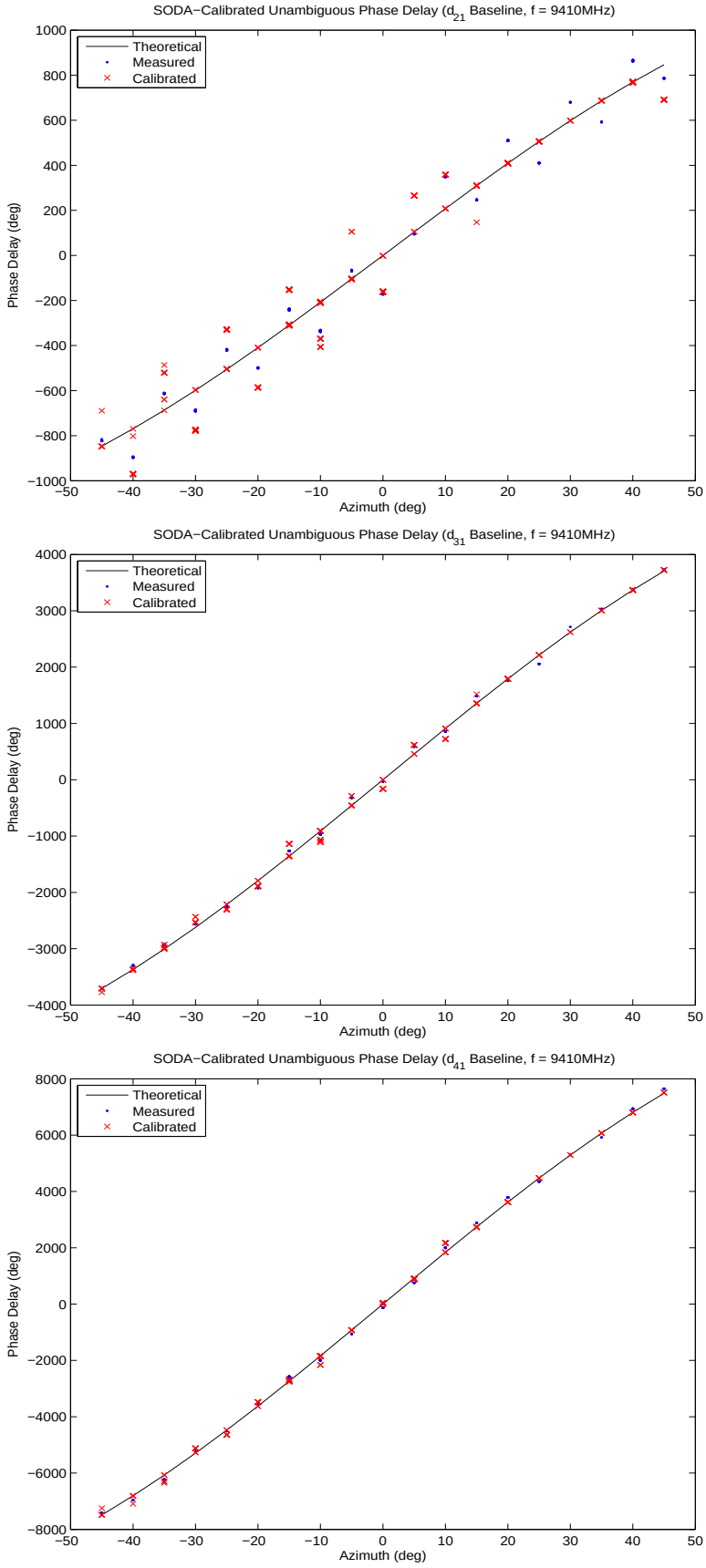

Figure 8.15: Calibrated phase delays using SODA interferometry.

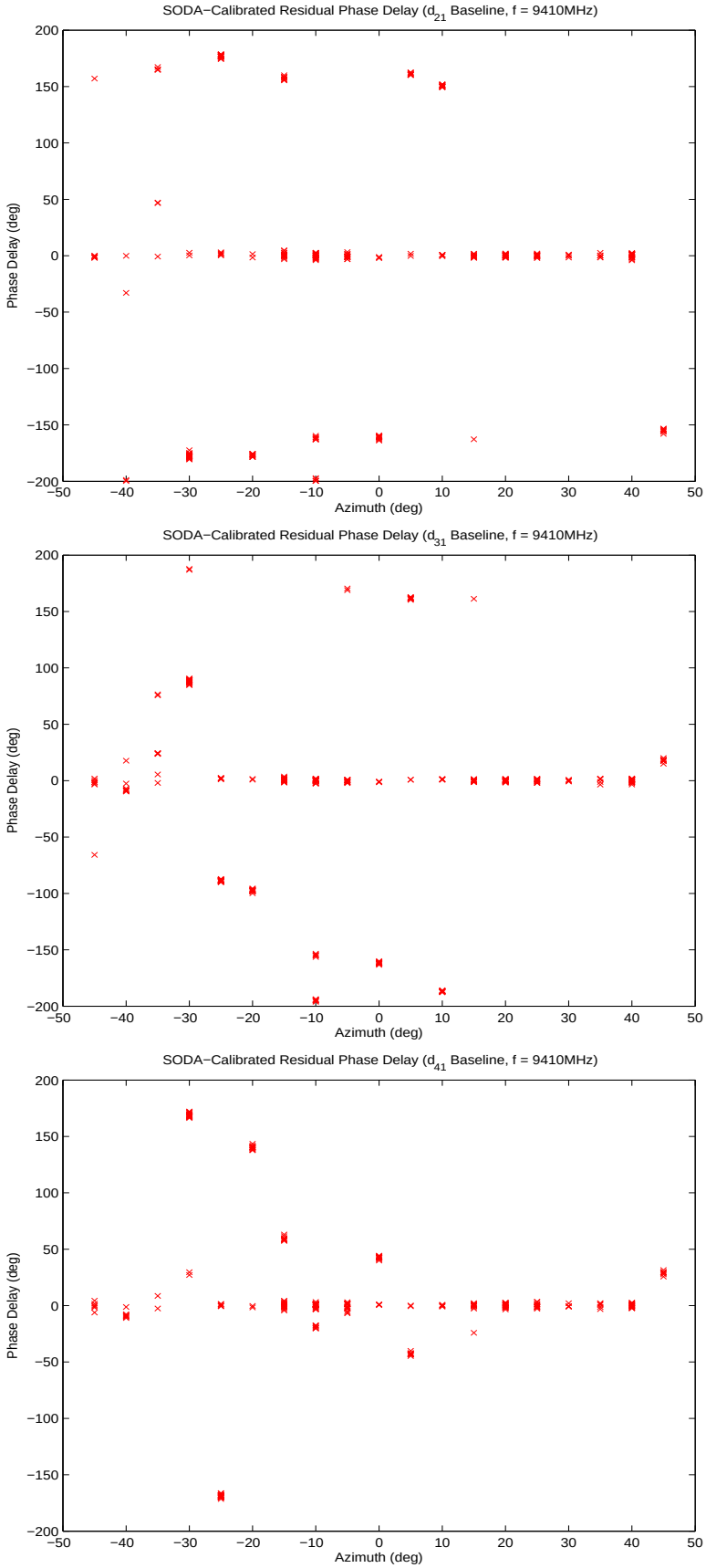

Figure 8.16: Residual phase delay offsets after calibration using SODA interferometry.

8.4.1 Experimental Performance With Correlative Calibration

Figure 8.17 shows the experimental RMS errors of the AOA estimation algorithms as a function of azimuth using the 3-antenna array geometry. In this experiment, correlative calibration method is used to remove the phase imbalances. The search resolution of the correlative interferometer is 5° which matches the rotation angle resolution of the antenna array. In contrast to the simulations in Chapter 5, it was found through trial-and-error that good AOA estimation using the first-order CBF and MUSIC algorithms required the grid search resolution to be set to one-eighth of the null-to-null beamwidth, i.e. 0.2436°. The grid search resolution of the second-order CBF and MUSIC algorithms was set to 5°. Newton's Method optimisation is used to remove the quantisation errors of all of the grid search algorithms.

In this experiment, the SODA interferometer has a RMS error of 1.518° while the SBI interferometer offers a slightly better performance with a RMS error of 1.514°. The MLE interferometer provides the best AOA estimation performance with a RMS error of 0.010° and is about two-orders of magnitude better than the SODA interferometer. Surprisingly, the first-order CBF and MUSIC algorithms have the worse performance with a RMS error of 4.538°. In this experiment, the second-order CBF and MUSIC algorithms have an identical performance to the SODA interferometer with a RMS error of 1.518°. Similarly, the SBI-cued algorithms have an identical performance to the SBI interferometer with a RMS error of 1.514°.

The simulations in Figure 5.25 suggests that at 5 dB SNR, the theoretical RMS errors of the above algorithms should be 0.7229°, 0.2761°, 0.0042°, 0.0042°, 0.9586° and 0.2761° respectively when the AOA is 23.42°. In contrast to the experimental RMS errors which are evaluated at a number of AOAs, the theoretical RMS errors presented here are only evaluated at a single AOA. However, the relative magnitude of the theoretical and experimental RMS errors are still indicative of the performance difference between the theory and the experiments. These results suggest that the experimental RMS error of the SODA and MLE interferometers are approximately 2.1 and 2.4 times higher than the theoretical values. This performance degradation is attributed to the effects of hardware imperfections that have not been completely eliminated through the calibration process.

In contrast to the simulations, the SBI and SBI-cued algorithms were not able to achieve a performance that is significantly better than the SODA interferometer. From (3.48), reliable ambiguity resolution using the SBI interferometer requires that the RMS error of the SODA interferometer to be

$$\delta\theta_{\text{SODA}} \leq \frac{c}{6fd_{31}} \approx 0.6560^\circ, \tag{8.4}$$

when $d_{31} = 464.1$ mm and $f = 9410$ MHz. Since the experimental RMS error of the SODA interferometer was shown to be 1.518°, this RMS error is not sufficiently accurate to reliably resolve the ambiguities of the first-order baselines of the 3-antenna SODA geometry and so leads to poor performance in the SBI and SBI-cued algorithms.

Furthermore, the first-order CBF and MUSIC algorithms were not able to achieve a better performance than the SODA interferometer using the sparse 3-antenna array geometry. This poor performance is attributed to the fact that the beampattern for the

3-antenna array geometry exhibits very high sidelobes and that the difference between the magnitude of the main lobe and highest sidelobe is only 3.811×10^{-3} dB. This means that the array is very sensitive to noise errors and any residual bias errors that may still exist after the calibration process. The result is that one of the adjacent sidelobes is mistaken for the AOA of the signal. Finally, in constrast to the above, the second-order CBF and MUSIC algorithms performs slightly better than expected and achieves the same performance as the SODA interferometer at 5 dB SNR.

Figure 8.18 shows that with the inclusion of the fourth auxiliary antenna, the sparsity of the array is sufficiently reduced to allow significant improvements in the experimental performance of the SBI, SBI-cued and first-order CBF and MUSIC algorithms. With four antennas, the experimental RMS error of the SBI, SBI-cued, first-order array processing and MLE algorithms are 0.010°, 0.009°, 0.009° and 0.009° respectively. In constrast, the simulation in Figure 5.27 suggests that the RMS errors of the algorithms should be 0.0042°, 0.0038°, 0.0038° and 0.0038° respectively and so the experimental RMS errors are approximately 2.4 times higher than the theoretical values. Note that since the auxiliary antenna does not conform to a SODA geometry, the RMS errors of the SODA and second-order array processsors are unchanged.

With the 4-antenna array geometry, (3.48) suggests that reliable ambiguity resolution using the SBI interferometer requires that the RMS error of the SODA interferometer to be

$$\delta\theta_{\text{SODA}} \leq \frac{c}{6fd_{21}} \approx 2.8721^\circ, \tag{8.5}$$

when $d_{21} = 106.0$ mm and $f = 9410$ MHz. Since the experimental RMS error of the SODA interferometer was shown to be 1.518°, this RMS error is sufficiently accurate to resolve the ambiguities of the first-order baselines of the 4-antenna SODA geometry. As a result, the SBI interferometer is now able to achieve a significantly lower RMS error of 0.010° and the SBI-cued algorithms are all able to further refine the SBI AOA estimate to give an even lower RMS error of 0.009°.

Furthermore, with the inclusion of the fourth antenna, the sparsity of the array is sufficiently reduced such that the beampattern of the 4-antenna array geometry suppresses the adjacent sidelobes. While the magnitude difference between the main lobe and highest sidelobe is only 0.2243 dB, in this experiment this is sufficient to allow the correct AOA to be estimated and so the RMS error of the first-order CBF and MUSIC algorithms are also 0.009°.

It should be noted that the MLE, SBI-cued and first-order CBF and MUSIC algorithms have a small, but statistically significant, performance improvement compared with the SBI interferometer of 0.001° RMS. However, this improvement is so small that it will likely be considered negligible in practice.

A summary of the AOA estimation performance of each algorithm obtained using correlative calibration is tabulated in Table 8.1.

Algorithm	Total RMS Error	
	3 Antennas	4 Antennas
MLE	0.010°	0.009°
SODA	1.518°	N/A†
SBI	1.514°	0.010°*
SBI-Cued MLE / CBF / MUSIC	1.514°*	0.009°*
First-Order CBF / MUSIC	4.538°*	0.009°*
Second-Order CBF / MUSIC	1.518°*	N/A†

Table 8.1: Experimental performance of the AOA estimation algorithms using correlative calibration at 5 dB SNR. †The fourth auxiliary antenna is unused by this algorithm.

8.4.2 Experimental Performance With SODA Calibration

Figure 8.19 shows the experimental RMS errors of the algorithms as a function of azimuth using the 3-antenna array geometry and the SODA calibration method. Since the point of using SODA calibration is to avoid the computational complexities of the MLE interferometer and the first-order array processing algorithms, the performance of these algorithms are not evaluated in this section. Furthermore, since the AOA estimation performance of the SODA interferometer will be shown to be better than the SBI interferometer in this experiment, the SODA-cued optimisation algorithms will be used in place of the SBI-cued algorithms.

With 3 antennas, the SODA and SBI interferometers have a RMS error of 3.292° and 3.526° respectively. The second-order CBF and MUSIC algorithms achieve the same performance as the SODA interferometer with a RMS error of 3.292° while the SODA-cued MLE, CBF and MUSIC algorithms have a RMS error of 11.409°. These results show that the RMS errors of the algorithms are significantly higher when using SODA calibration compared to correlative calibration. Furthermore, in this experiment, the SBI and SODA-cued algorithms perform worse than the SODA interferometer. This poor performance is attributed to the fact that the SODA calibration is not as effective as the correlative calibration in removing the phase imbalances between the channels and so residual bias errors cause significant errors in the AOA estimation. Furthermore, with a RMS error of 3.292°, the SODA interferometer does not have the required accuracy (i.e. 0.6560°) to resolve the ambiguities in the first-order baselines at 5 dB SNR and so the SBI interferometer performs poorly. Furthermore, due to the poor initial estimate, the SODA-cued algorithms also perform poorly.

Figure 8.20 shows the experimental RMS errors of the algorithms when all 4 antennas are used. This figure shows that with the inclusion of the fourth auxiliary antenna, the RMS error of the SBI and SODA-cued algorithms are in fact worse than the 3-antenna scenario with a RMS error of 6.845° and 16.154° respectively. Again, since the auxiliary antenna does not conform to a SODA geometry, the RMS errors of the SODA and second-order array processors are unchanged. Furthermore, with a RMS error of 3.292°, the SODA interferometer does not have the required accuracy (i.e. 2.8721°) to resolve the ambiguities in the first-order baselines at 5 dB SNR and so the SBI interferometer still performs poorly.

Algorithm	**Total RMS Error**	
	3 Antennas	**4 Antennas**
SODA	3.292°	N/A†
SBI	3.437°	6.845°*
SODA-Cued MLE / CBF / MUSIC	11.409°*	16.154°*
Second-Order CBF / MUSIC	3.292°*	N/A†

Table 8.2: Experimental performance of the AOA estimation algorithms using SODA calibration at 5 dB SNR. †The fourth auxiliary antenna is unused by this algorithm.

In light of the good experimental performance obtained from the same experimental data in the previous section using correlative calibration, the poor performance of the algorithms in this section is purely attributed to the poorer performance of the SODA calibration. A summary of the AOA estimation performance of each algorithm obtained using SODA calibration is tabulated in Table 8.2.

8.5 Summary

This chapter has experimentally validated that the second-order AOA estimation algorithms, namely the SODA and SBI interferometers, the SODA-cued and SBI-cued ambiguity resolution algorithms and the second-order CBF and MUSIC algorithms, can all be used to perform unambiguous AOA estimation. The performance of these algorithms were quantified at 5 dB SNR with a 3-antenna and 4-antenna array geometry and their experimental performance was compared to conventional AOA estimation methods, such as the MLE interferometer and first-order CBF and MUSIC algorithms.

The experimental results showed that with correlative calibration and the 3-antenna array geometry, the SODA, SBI, SBI-cued and second-order CBF and MUSIC algorithms can achieve a RMS error of approximately 1.5°. Using this array geometry, the first-order CBF and MUSIC algorithms were unable to achieve a better performance than SODA interferometer with a RMS error of about 4.5°, and the MLE interferometer offered the best performance with a RMS error of 0.010° and is approximately two-orders of magnitude better than the SODA interferometer. With the 4-antenna geometry, the RMS errors of the MLE, SBI, SBI-cued and first-order CBF and MUSIC algorithms were significantly improved and all algorithms achieve a RMS error of about 0.009°.

The experimental results also showed that with the current configuration of the ES Testbed, the SODA calibration method was not as effective as the correlative calibration method at 5 dB SNR. While the SODA calibration method was significantly faster, it was also significantly less effective at removing the phase imbalances between the channels. As a result, the SODA interferometer and second-order CBF and MUSIC algorithms were shown to achieve a RMS error of about 3.3°. However, in contrast to the correlative calibration, none of the other algorithms were able to achieve a better performance than the SODA interferometer. As discussed in Section 8.3.2, the performance of the SODA calibration is related to the SNR of the signal and the nature of the phase imbalances of the specific hardware configuration. While the performance of the SODA calibration

was rather poor in this particular experiment, it is expected that at higher SNR, or with different hardware configurations, such as different antennas, the performance of the SODA calibration will improve and so the AOA estimation algorithms will be able to achieve higher performance.

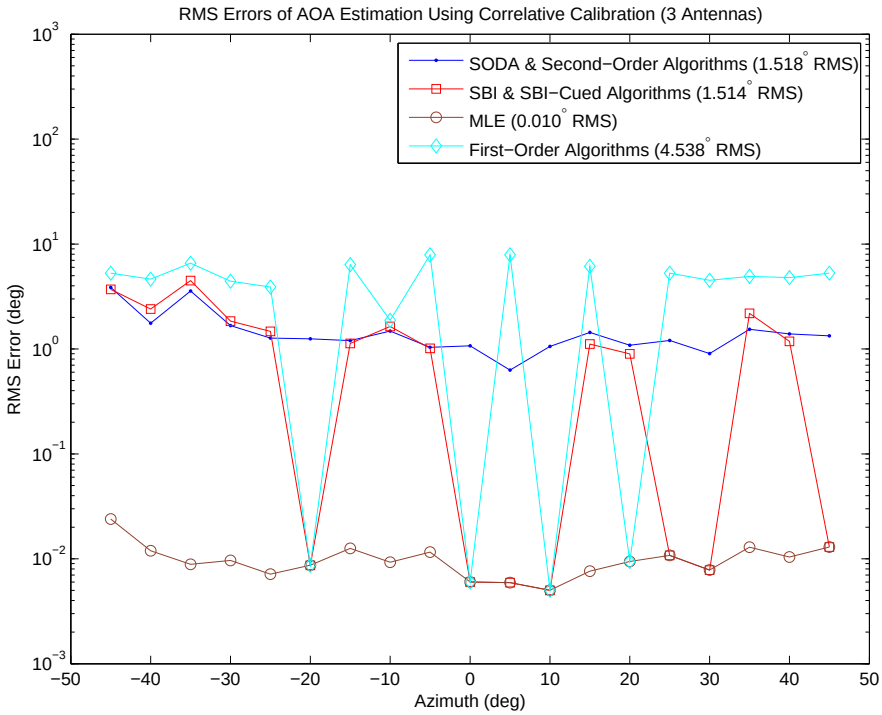

Figure 8.17: RMS errors of the AOA estimation with correlative calibration using the 3-antenna array geometry. The angular values in the labels represent the total RMS error for the algorithms.

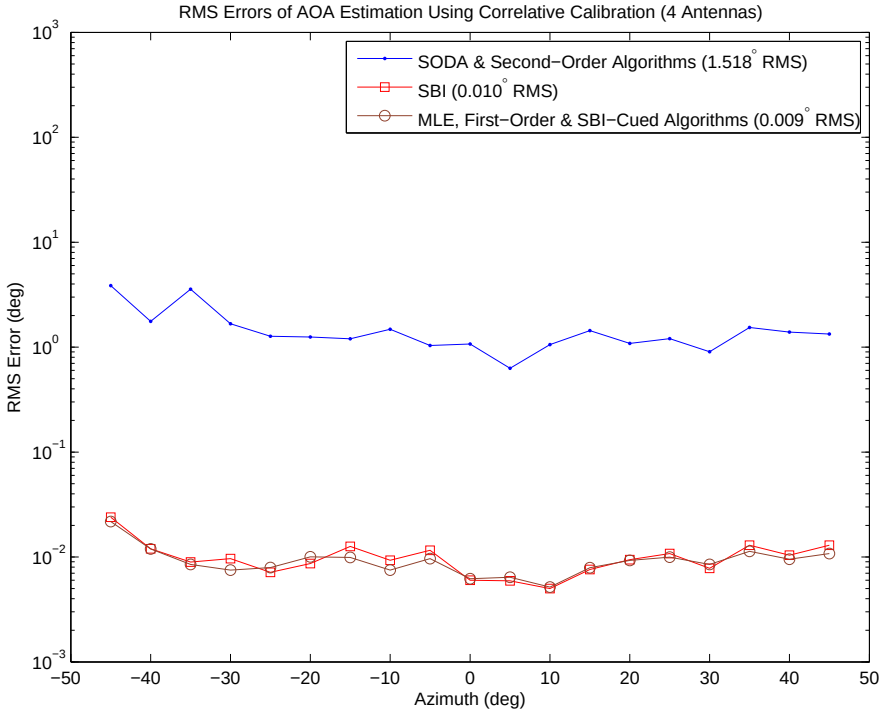

Figure 8.18: RMS errors of the AOA estimation with correlative calibration using the 4-antenna array geometry. The angular values in the labels represent the total RMS error for the algorithms.

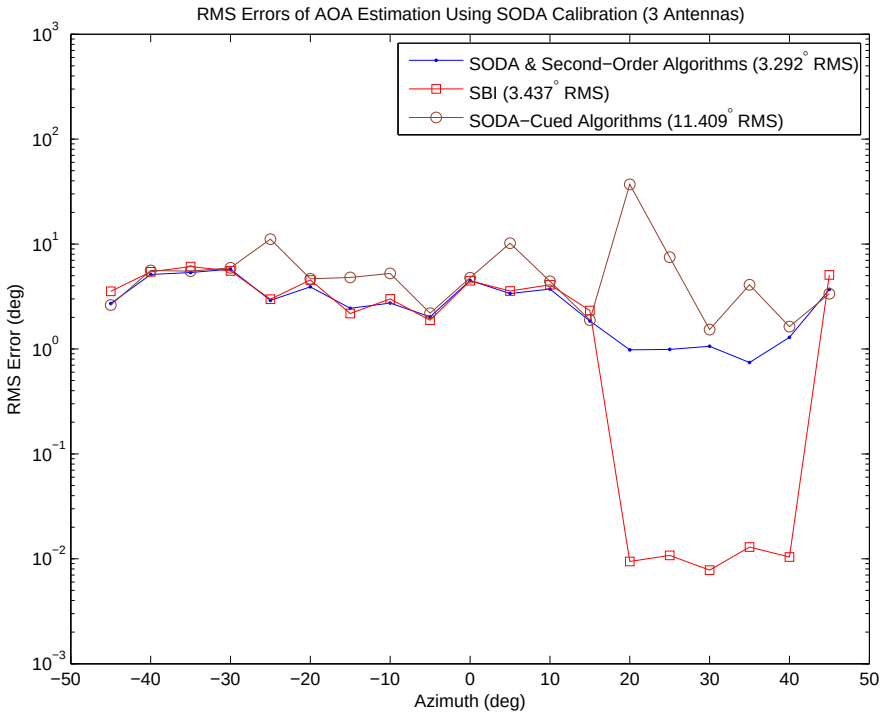

Figure 8.19: RMS errors of the AOA estimation with SODA calibration using the 3-antenna array geometry. The angular values in the labels represent the total RMS error for the algorithms.

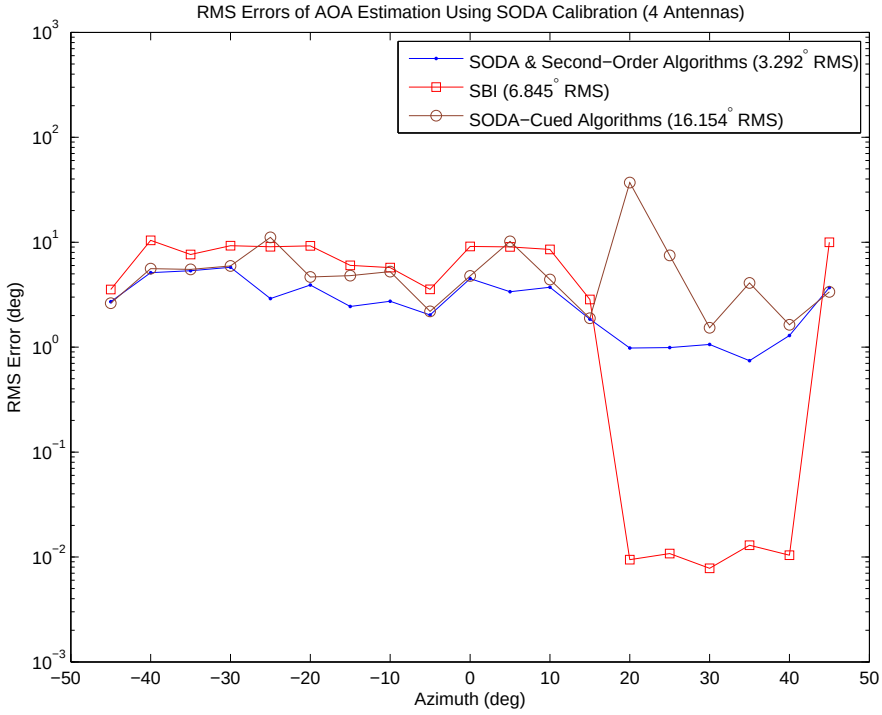

Figure 8.20: RMS errors of the AOA estimation with SODA calibration using the 4-antenna array geometry. The angular values in the labels represent the total RMS error for the algorithms.

Chapter 9

Concluding Remarks

9.1 Summary

This thesis has considered the problem of estimating the angle-of-arrival (AOA) of intercepted radar signals using digital, microwave radar intercept receivers for near real-time surveillance (Chapter 1). Due to the tactical and operational requirements of radar intercept receivers, the AOA estimation algorithms need to be computationally fast and highly accurate. The requirement for wide frequency surveillance often means that physically large wideband antennas are required which implies the use of array geometries with wide antenna spacings. Furthermore, due to the cost of wideband hardware, the number of independent channels is often limited to $2-4$ channels per quadrant of a 360° field-of-view.

Of all of the contemporary direction finding methods, interferometry is often cited as a suitable AOA estimation technique that satisfies all of the above requirements (Chapter 2). Contemporary phase-based interferometric algorithms are computationally fast and offer high accuracy AOA estimation using a small number of antennas. However, the requirement to use physically large wideband antennas for electronic surveillance applications introduces a significant ambiguity problem to the AOA estimation. In order to perform unambiguous AOA estimation, the antenna positions must be carefully chosen and coupled with ambiguity resolution algorithms (Chapter 3).

In Chapter 4, it was shown that the ambiguity problem can be completely avoided by using a second-order difference array (SODA) to create a virtual short-baseline interferometer. This algorithm was shown to be computationally efficient and operates effectively over the entire microwave frequency range between $2-18$ GHz. The performance of this algorithm was also shown to be limited to the smaller aperture but is also independent of the physical antenna spacings. While the conventional theory prefers longer baseline interferometers over shorter baselines for improved AOA accuracy, the SODA interferometer reverses this situation to derive a shorter baseline interferometer from longer baselines for the sake of unambiguous AOA estimation using physically large antennas.

The unambiguous SODA AOA estimate can also be used to cue the conventional first-order ambiguity resolution methods to obtain higher accuracy AOA estimates from the

first-order baselines with a reduced number of computations. One of the more efficient methods proposed is the SODA-Based Inference (SBI) interferometer (Section 4.3.1). The SBI interferometer was shown to be a near optimal estimator as it achieves the two-antenna Cramér-Rao Lower Bound (CRLB) corresponding to the widest antenna pair at high SNR. The SBI AOA estimate can also be used to further cue a correlative interferometer to obtain optimal performance. At high SNR, a computationally fast implementation is to use the SBI AOA estimate to directly cue to the optimisation algorithm of the correlative interferometer (i.e. bypassing the grid search).

In Chapter 5, it was shown that the concept of using second-order processing could be generalised to a larger number of antennas to create a virtual uniform linear array. Conventional beamforming and array processing algorithms can then be applied to the virtual uniform linear array to perform unambiguous AOA estimation. Like SODA interferometry, the performance of the second-order array processor is limited to the aperture of the virtual array. With three antennas, the SODA array processor has a performance that is comparable to SODA interferometry since the two algorithms effectively have the same virtual aperture. However, the second-order array processor can exploit additional antennas to form a larger virtual aperture and so can achieve a better performance than SODA interferometry if more antennas are available.

Since the SODA geometry is inherently a non-uniform linear array, the conventional first-order array processing algorithms are also able to provide unambiguous AOA estimates and are generally asymptotically efficient estimators as they achieve the CRLB at high SNR. While it is possible to apply second-order array processing to a SODA geometry, better results are usually obtained by using the equivalent first-order array processing. An exception to this occurs when using sparse large aperture arrays which tend to exhibit high sidelobes in the first-order array beampattern and so can lead to incorrect AOA estimates in the presence of noise and scalloping losses. On the other hand, since the second-order array processor synthesises the array beampattern of an unambiguous uniform linear array, the second-order array beampattern generally exhibits lower sidelobes for the same physical array geometry and so is able to correctly estimate the AOA. However, the advantage of the second-order array processor diminishes as the sparsity of the array aperture is reduced.

In Chapter 6, two calibration methods were presented to remove the effects of phase imbalance between the channels of practical hardware. The correlative calibration method was shown to be very effective at removing the phase imbalances but is computationally intensive as it requires the AOA to be estimated using correlative interferometry. The SODA calibration method was shown to be significantly faster as it uses SODA interferometry to estimate the AOA. However, in Chapter 8, it was shown that the the SODA calibration method was not able to remove the phase imbalances for all intercepts.

In Chapter 8, the calibration methods and the AOA estimation performance of the SODA interferometer, SBI interferometer and a second-order array processors were experimentally validated using the hardware developed in Chapter 7.

9.2 Future Work

This thesis has presented a number of computationally fast AOA estimation algorithms and evaluated their theoretical and experimental performance. However, a number of areas of this work may warrant further investigation. These areas will be briefly discussed below.

- **Experimental Validation at Other Frequencies -** Due to time constraints and the safety and licensing of transmitting RF signals, the experimental validation of the algorithms in this these was only performed between 9160 MHz and 9660 MHz. Since the objective is to have a radar intercept receiver that can operate between $2 - 18$ GHz, it would be desirable to experimentally validate the performance of algorithms at other frequencies.

- **Experimental Validation Using Different Transmitters -** Due to time constraints, the calibration signal was used to calibrate the system and to perform its AOA estimation. In order to fully validate the experimental performance of the algorithms, it would be desirable to use one transmitter for the calibration signal and a different transmitter for the AOA estimation.

- **Experimental Validation Using Moving Sources -** Due to time, costs and safety constraints, it was not possible to use a moving transmitting source to obtain data from different angles. In order to obtain data from different azimuths, the transmitting source was kept stationary while the receiving antenna array was rotated in azimuth. While such a collection method is reasonable in an isotropic noise environment, the rotation of the receiving antenna array may potentially expose the system to directional noise sources in a non-isotropic noise environment. While this did not appear to affect the experimental results in this thesis, it would be desirable for future experiments to utilise moving transmitting sources.

- **Wideband Signals -** This thesis assumed that the signal observed by the radar intercept receiver was narrowband. While this assumption is generally valid for the types of signals considered in this thesis, radars with wideband characteristics, such as fast chirps, do exist. It would be desirable to extend the SODA and SODA-based algorithms to operate against wideband signals.

- **Compressive Sampling -** This thesis assumed that digital radar intercept receivers sample radar signals with a uniform sampling rate that satisfies the Nyquist criterion. For modern wideband radar signals, sampling at the Nyquist rate can lead to a significant amount of data that needs to be stored, processed and transferred. In recent years, considerable work has been undertaken in the area of *compressive sampling* which allow so-called "sparse signals" to be sampled below the Nyquist rate with minimal distortion. Digital radar intercept receivers that use compressing sampling techniques have the potential to significantly reduce the amount of data that is generated and so can help to alleviate hardware design problems associated with the high-speed transfer and storage of large volumes of data. A reduced data rate may also offer improvements to the computational speed of the signal processing algorithms. In the context of this thesis, it would be interesting to investigate the performance and computational speeds of unambigu-

ous AOA estimation algorithms using data obtained from compressive sampling methods.

Appendix A

Derivations

A.1 Signal Model

Consider the signal model for a single-tone narrowband signal. For a digital collection of N samples, the digital model for the n-th sample of the k-th antenna output of a K antenna non-uniform linear array is given by

$$x_k[n] = A_k e^{j[2\pi f n t_s + \varphi + \psi_{k1}(\theta)]} + \epsilon_k[n], \tag{A.1}$$

where $k = 1, 2, \ldots, K$ and $n = 0, 1, \ldots, N-1$. The parameters A_k, f and φ are the signal's peak amplitude, carrier frequency and initial phase respectively. In this model, the peak amplitude is allowed to differ in each channel. The parameter t_s represents the sample interval of the receiver and

$$\psi_{k1}(\theta) = \frac{2\pi f d_{k1}}{c} \sin\theta, \tag{A.2}$$

is the spatial phase delay of the signal measured at the k-th antenna with respect to the first antenna. Note that with this definition, the baseline and spatial phase delay of the first antenna are $d_{11} = 0$ and $\psi_{11}(\theta) = 0$.

The additive term, $\epsilon_k[n] \sim \mathcal{N}(0, \sigma_\epsilon^2)$, represents random noise and is modelled as an independent, and identically distributed, complex-valued, zero-mean, white Gaussian random variable with variance, σ_ϵ^2. The receiver noise is also assumed to be independent for each receiver.

The noisy complex signal, $x_k[n]$, can be re-written in terms of a real, $r_k[n]$, and imaginary, $i_k[n]$, component using Euler's formula as follows,

$$x_k[n] = r_k[n] + j i_k[n], \tag{A.3}$$

where

$$\begin{aligned}
r_k[n] &= \mu_k[n] + \Re\{\epsilon_k[n]\}, && \text{(A.4)}\\
i_k[n] &= \nu_k[n] + \Im\{\epsilon_k[n]\}, && \text{(A.5)}\\
\mu_k[n] &= A_k \cos(2\pi f n t_s + \varphi + \psi_{k1}(\theta)), && \text{(A.6)}\\
\nu_k[n] &= A_k \sin(2\pi f n t_s + \varphi + \psi_{k1}(\theta)), && \text{(A.7)}
\end{aligned}$$

where $\Re\{\epsilon_k[n]\}$ and $\Im\{\epsilon_k[n]\}$ are the real and imaginary components of $\epsilon_k[n]$ and have an equal variance of $\sigma^2 = \sigma_\epsilon^2/2$.

Let $\boldsymbol{x}_k$ represent the time series of the signal in the k-th channel, such that

$$\boldsymbol{x}_k = [x_k[0], x_k[1], \ldots, x_k[N-1]]^T, \tag{A.8}$$

where $k = 1, 2, \ldots, K$ and ^{T} denotes the matrix transpose operation.

The joint probability density function, $p(\boldsymbol{x}_1, \ldots, \boldsymbol{x}_K|\boldsymbol{\alpha})$, is given by

$$p(\boldsymbol{x}_1, \ldots, \boldsymbol{x}_K|\boldsymbol{\alpha}) = \left(\frac{1}{2\pi\sigma^2}\right)^{NK} \exp\left\{-\frac{1}{2\sigma^2}\sum_{k=1}^{K}\sum_{n=0}^{N-1}(r_k[n]-\mu_k[n])^2 + (i_k[n]-\nu_k[n])^2\right\} \tag{A.9}$$

where

$$\boldsymbol{\alpha} = \begin{bmatrix} \omega & \varphi & \theta & A_1 & A_2 & \cdots & A_K \end{bmatrix}^T, \tag{A.10}$$

represents a vector of parameters that characterise the signal model and $\omega = 2\pi f$ is the angular frequency. The log-likelihood function of the signal model, $L(\boldsymbol{\alpha})$, is defined as

$$L(\boldsymbol{\alpha}) = \ln\left(p(\boldsymbol{x}_1, \ldots, \boldsymbol{x}_K|\boldsymbol{\alpha})\right). \tag{A.11}$$

A.2 Maximum Likelihood Estimation

A.2.1 Maximum Likelihood Estimator for a Non-Uniform Linear Array

The derivation of the maximum likelihood estimator (MLE) of the AOA for a non-uniform linear array has been considered many times in the literature [56, 112]. The derivation presented below generalises the derivation of the two-antenna interferometer in [112].

The log-likelihood function of the signal model is given by (A.11). Since this derivation is only concerned with AOA estimation, the log-likelihood function may be written as only being a function of θ. Hence, the log-likelihood function, $L(\theta)$, is given by

$$\begin{aligned} L(\theta) = L_0 \quad &+ \quad \frac{1}{\sigma^2}\sum_{k=1}^{K}\sum_{n=0}^{N-1} A_k r_k[n]\cos\left(2\pi f n t_s + \varphi + \psi_{k1}(\theta)\right) \\ &+ \quad \frac{1}{\sigma^2}\sum_{k=1}^{K}\sum_{n=0}^{N-1} A_k i_k[n]\sin\left(2\pi f n t_s + \varphi + \psi_{k1}(\theta)\right) \end{aligned} \tag{A.12}$$

where

$$L_0 = NK\ln\left(\frac{1}{2\pi\sigma^2}\right) - \frac{1}{2\sigma^2}\sum_{k=1}^{K}\sum_{n=0}^{N-1}\left(r_k^2[n] + i_k^2[n] + A_k^2\right). \tag{A.13}$$

Expanding the sine and cosine functions gives

$$\begin{aligned} L(\theta) = L_0 &+ \frac{1}{\sigma^2}\sum_{k=1}^{K}\sum_{n=0}^{N-1} A_k r_k[n]\cos(2\pi f n t_s)\cos(\varphi+\psi_{k1}(\theta)) \\ &- \frac{1}{\sigma^2}\sum_{k=1}^{K}\sum_{n=0}^{N-1} A_k r_k[n]\sin(2\pi f n t_s)\sin(\varphi+\psi_{k1}(\theta)) \\ &+ \frac{1}{\sigma^2}\sum_{k=1}^{K}\sum_{n=0}^{N-1} A_k i_k[n]\sin(2\pi f n t_s)\cos(\varphi+\psi_{k1}(\theta)) \\ &+ \frac{1}{\sigma^2}\sum_{k=1}^{K}\sum_{n=0}^{N-1} A_k i_k[n]\cos(2\pi f n t_s)\sin(\varphi+\psi_{k1}(\theta)). \end{aligned} \tag{A.14}$$

The log-likelihood function can be simplified by recognising that the Fourier coefficient at the signal frequency, f, is defined as

$$X_k(f) = \sum_{n=0}^{N-1} x_k[n]e^{-j2\pi f n t_s} \tag{A.15}$$

$$\begin{aligned} &\equiv \sum_{n=0}^{N-1} r_k[n]\cos(2\pi f n t_s) + i_k[n]\sin(2\pi f n t_s) \\ &\quad + j\sum_{n=0}^{N-1}\{i_k[n]\cos(2\pi f n t_s) - r_k[n]\sin(2\pi f n t_s)\}, \end{aligned} \tag{A.16}$$

and that the magnitude, $|X_k(f)|$, and phase, $\angle X_k(f)$, of the Fourier coefficient at the signal frequency f are given by

$$|X_k(f)| = \sqrt{\Re\{X_k(f)\}^2 + \Im\{X_k(f)\}^2} = A_k N, \tag{A.17}$$

$$\angle X_k(f) = \arctan\left(\frac{\Im\{X_k(f)\}}{\Re\{X_k(f)\}}\right) = \varphi + \psi_{k1}(\theta). \tag{A.18}$$

Using the following trigonometric identity

$$\alpha\cos\gamma + \beta\sin\gamma = \sqrt{\alpha^2+\beta^2}\cos(\gamma - \arctan(\beta/\alpha)), \tag{A.19}$$

the log-likelihood function can be further simplified as follows

$$\begin{aligned} L(\theta) &= L_0 + \frac{1}{\sigma^2}\sum_{k=1}^{K} A_k\Re\{X_k(f)\}\cos(\varphi+\psi_{k1}(\theta)) + A_k\Im\{X_k(f)\}\sin(\varphi+\psi_{k1}(\theta)), \\ &= L_0 + \frac{1}{\sigma^2}\sum_{k=1}^{K} A_k|X_k(f)|\cos\left(\varphi+\psi_{k1}(\theta) - \angle X_k(f)\right), \\ &= L_0 + \frac{N}{\sigma^2}\sum_{k=1}^{K} A_k^2\cos\left(\varphi+\psi(\theta) - \angle X_k(f)\right). \end{aligned} \tag{A.20}$$

In this signal model, the phase delay between the first antenna ($k = 1$) and itself is $\psi_{11}(\theta) = 0°$ by definition. Hence, from (A.18), the angle of the Fourier coefficient of the

first antenna is $\angle X_1(f) = \varphi$. Thus, the log-likelihood function can be written as

$$\begin{aligned} L(\theta) &= L_0 + \frac{N}{\sigma^2}\sum_{k=1}^{K} A_k^2 \cos\left(\psi_{k1}(\theta) - (\angle X_k(f) - \angle X_1(f))\right), && \text{(A.21)} \\ &= L_0 + \frac{N}{\sigma^2}\sum_{k=1}^{K} A_k^2 \cos\left(\psi_{k1}(\theta) - \angle X_k(f)X_1^*(f)\right), && \text{(A.22)} \\ &= L_0 + \frac{N}{\sigma^2}\sum_{k=1}^{K} A_k^2 \cos\left(\angle X_k(f)X_1^*(f) - \psi_{k1}\right), && \text{(A.23)} \\ &= L_0 + \frac{N}{\sigma^2}\sum_{k=1}^{K} A_k^2 \cos\left(\tilde{\psi}_{\text{MLE},k1} - \psi_{k1}(\theta)\right), && \text{(A.24)} \\ & && \text{(A.25)} \end{aligned}$$

where $\tilde{\psi}_{\text{MLE},k1} = \angle X_k(f)X_1^*(f)$ can be considered the maximum likelihood estimate of the phase delay. This derivation is shown in the Appendix A.2.2. The maximum likelihood estimate for the AOA can then be obtained by performing a grid search to find the value of θ_s that maximises the log-likelihood function. By ignoring the components and scalar values that are not AOA-dependent, the maximum likelihood estimator can be described as follows,

$$\hat{\theta} = \overset{\arg\max}{\theta_s} \sum_{k=1}^{K} \cos\left(\tilde{\psi}_{\text{MLE},k1} - \psi_{k1}(\theta_s)\right), \qquad \text{(A.26)}$$

where $\tilde{\psi}_{\text{MLE},k1} = \angle X_k(f)X_1^*(f)$ is the maximum likelihood estimate of the phase delay and $\psi_{k1}(\theta_s)$ is the true phase delay that is expected at θ_s. This expression shows that, in general, the maximum likelihood estimator for the AOA is a grid search algorithm.

A.2.2 Maximum Likelihood Estimator for Two Antennas

The maximum of the log-likelihood function can be explicitly calculated by setting the first derivative of $L(\theta)$ with respect to θ to zero, i.e.

$$\frac{\partial L(\theta)}{\partial \theta} = -\frac{N}{\sigma^2}\sum_{k=1}^{K} A_k^2 \sin\left(\angle X_k(f)X_1^*(f) - \psi_{k1}(\theta)\right)\frac{\partial \psi_{k1}(\theta)}{\partial \theta} = 0. \qquad \text{(A.27)}$$

For the special case of two antennas, i.e. $K = 2$, and recalling that $\psi_{11}(\theta) = 0$ by definition, it can be shown that

$$\begin{aligned} A_2^2 \sin\left(\angle X_2(f)X_1^*(f) - \psi_{21}(\theta)\right)\frac{\partial \psi_{k1}(\theta)}{\partial \theta} &= 0, && \text{(A.28)} \\ A_2^2 \sin\left(\angle X_2(f)X_1^*(f) - \psi_{21}(\theta)\right)\frac{2\pi f d}{c}\cos\theta &= 0, && \text{(A.29)} \\ A_2^2 \sin\left(\angle X_2(f)X_1^*(f) - \psi_{21}(\theta)\right)\cos\theta &= 0, && \text{(A.30)} \\ \psi_{21}(\theta) &= \angle X_2(f)X_1^*(f) \text{ for } \theta \neq \frac{\pi}{2}. && \text{(A.31)} \end{aligned}$$

Thus, the maximum likelihood estimate for the phase delay between the two antennas is given by

$$\hat{\psi}_{\text{MLE},21}(\theta) = \angle X_2(f)X_1^*(f). \qquad \text{(A.32)}$$

From invariance property of maximum likelihood estimators [56], the maximum likelihood estimate of the AOA using two antennas can be obtained by re-arranging (A.2) to give

$$\hat{\theta}_{\text{MLE}} = \arcsin\left(\frac{c\hat{\psi}_{\text{MLE},21}}{2\pi f d_{21}}\right). \tag{A.33}$$

A.3 Cramér-Rao Lower Bounds

A.3.1 Cramér-Rao Lower Bounds for a Non-Uniform Linear Array

The Cramér-Rao Lower Bound (CRLB) specifies the minimum variance that can be obtained for any unbiased estimator and is often used as a benchmark for optimal performance [56]. The derivation of the CRLB for AOA estimation using a non-uniform linear array has been considered many times in the literature [2, 45, 56, 93, 113, 114]. The derivation presented below applies the methodology used by Rife and Boorstyn [17, 115] in their derivation of the CRLB for frequency estimation to the AOA estimation case.

The CRLB for a set of parameters $\boldsymbol{\alpha}$ are the diagonal elements of the inverse of the Fisher Information Matrix, $\boldsymbol{J}$, where $\boldsymbol{\alpha} = [\alpha_1, \alpha_2, \ldots, \alpha_Q]$ is a vector of Q parameters characterising the random process. Given a random process with a probability density function, $p(\boldsymbol{x}_1, \ldots, \boldsymbol{x}_K|\boldsymbol{\alpha})$, and log-likelihood function, $L(\boldsymbol{\alpha})$, the elements of the Fisher Information Matrix are given by

$$J_{ij}(\boldsymbol{\alpha}) = -E\left\{\frac{\partial L(\boldsymbol{\alpha})}{\partial\alpha_i \partial\alpha_j}\right\}, \tag{A.34}$$

where $E\{\cdot\}$ is the expectation operator, $i, j = 1, 2, \ldots, Q$, and α_i and α_j are the i-th and j-th parameter of $\boldsymbol{\alpha}$ respectively. The Fisher Information Matrix is a $Q \times Q$ matrix.

Given the signal model specified in Section A.1, the elements of the Fisher Information Matrix can be written as

$$J_{ij} = \frac{1}{\sigma^2}\sum_{n=0}^{N-1}\sum_{k=1}^{K}\left[\frac{\partial\mu_k[n]}{\partial\alpha_i}\cdot\frac{\partial\mu_k[n]}{\partial\alpha_j} + \frac{\partial\nu_k[n]}{\partial\alpha_i}\cdot\frac{\partial\nu_k[n]}{\partial\alpha_j}\right], \tag{A.35}$$

where $i, j = 1, 2, \ldots, K+3$.

The partial derivatives for $\mu_k[n]$ are given by

$$\frac{\partial\mu_k[n]}{\partial\omega} = -A_k\left(nt_s + \frac{d_{k1}}{c}\sin\theta\right)\sin\left(\omega\left(nt_s + \frac{d_{k1}}{c}\sin\theta\right) + \varphi\right), \tag{A.36}$$

$$\frac{\partial\mu_k[n]}{\partial\varphi} = -A_k\sin\left(\omega\left(nt_s + \frac{d_{k1}}{c}\sin\theta\right) + \varphi\right), \tag{A.37}$$

$$\frac{\partial\mu_k[n]}{\partial\theta} = -A_k\frac{d_{k1}}{c}\omega\cos\theta\sin\left(\omega\left(nt_s + \frac{d_{k1}}{c}\sin\theta\right) + \varphi\right), \tag{A.38}$$

$$\frac{\partial\mu_k[n]}{\partial A_\gamma} = \begin{cases} \cos\left(\omega\left(nt_s + \frac{d_{k1}}{c}\sin\theta\right) + \varphi\right) & \text{if } k = \gamma \\ 0 & \text{if } k \neq \gamma \end{cases}, \tag{A.39}$$

where $\gamma = 1, 2, \ldots, K$. Similarly, the partial derivatives for $\nu_k[n]$ are given by

$$\frac{\partial \nu_k[n]}{\partial \omega} = A_k \left(nt_s + \frac{d_{k1}}{c} \sin\theta \right) \cos\left(\omega \left(nt_s + \frac{d_{k1}}{c} \sin\theta \right) + \varphi \right), \tag{A.40}$$

$$\frac{\partial \nu_k[n]}{\partial \varphi} = A_k \cos\left(\omega \left(nt_s + \frac{d_{k1}}{c} \sin\theta \right) + \varphi \right), \tag{A.41}$$

$$\frac{\partial \nu_k[n]}{\partial \theta} = A_k \frac{d_{k1}}{c} \omega \cos\theta \cos\left(\omega \left(nt_s + \frac{d_{k1}}{c} \sin\theta \right) + \varphi \right), \tag{A.42}$$

$$\frac{\partial \nu_k[n]}{\partial A_\gamma} = \begin{cases} \sin\left(\omega \left(nt_s + \frac{d_{k1}}{c} \sin\theta \right) + \varphi \right) & \text{if } k = \gamma \\ 0 & \text{if } k \neq \gamma \end{cases}. \tag{A.43}$$

The elements of the Fisher Information Matrix are therefore

$$J_{11} = \frac{N}{\sigma^2} \sum_{k=1}^{K} A_k^2 \left\{ \frac{(N-1)(2N-1)t_s^2}{6}, \right. \\ \left. + \quad \frac{d_{k1}}{c} \sin\theta (N-1) t_s + \frac{d_{k1}^2}{c^2} \sin^2\theta \right\} \tag{A.44}$$

$$J_{12} = \frac{N}{\sigma^2} \sum_{k=1}^{K} A_k^2 \left\{ \frac{(N-1)t_s}{2} + \frac{d_{k1}}{c} \sin\theta \right\}, \tag{A.45}$$

$$J_{13} = \frac{N}{\sigma^2} \sum_{k=1}^{K} A_k^2 \frac{d_{k1}}{c} \omega \cos\theta \left\{ \frac{(N-1)t_s}{2} + \frac{d_{k1}}{c} \sin\theta \right\}, \tag{A.46}$$

$$J_{22} = \frac{N}{\sigma^2} \sum_{k=1}^{K} A_k^2, \tag{A.47}$$

$$J_{23} = \frac{N}{\sigma^2} \sum_{k=1}^{K} A_k^2 \left\{ \frac{d_{k1}}{c} \omega \cos\theta \right\}, \tag{A.48}$$

$$J_{33} = \frac{N}{\sigma^2} \sum_{k=1}^{K} A_k^2 \left\{ \frac{d_{k1}^2}{c^2} \omega^2 \cos^2\theta \right\}, \tag{A.49}$$

$$J_{\gamma_1+3, \gamma_2+3} = \begin{cases} \frac{N}{\sigma^2} & \gamma_1 = \gamma_2 \\ 0 & \gamma_1 \neq \gamma_2 \end{cases}, \tag{A.50}$$

where $\gamma_1, \gamma_2 = 1, 2, \ldots, K$.

Using the above elements, the Fisher Information Matrix has the following form

$$\boldsymbol{J} = \begin{bmatrix} J_{11} & J_{12} & J_{13} & 0 & 0 & \cdots & 0 \\ J_{12} & J_{22} & J_{23} & 0 & 0 & \cdots & 0 \\ J_{13} & J_{23} & J_{33} & 0 & 0 & \cdots & 0 \\ 0 & 0 & 0 & \frac{N}{\sigma^2} & 0 & \cdots & 0 \\ 0 & 0 & 0 & 0 & \frac{N}{\sigma^2} & \cdots & 0 \\ \vdots & \vdots & \vdots & \vdots & \vdots & \ddots & \vdots \\ 0 & 0 & 0 & 0 & 0 & \cdots & \frac{N}{\sigma^2} \end{bmatrix}. \tag{A.51}$$

The determinant of $\boldsymbol{J}$ will be required to calculate the inverse of the Fisher Information

Matrix, i.e. $\boldsymbol{J}^{-1}$. The determinant of $\boldsymbol{J}$ is given by

$$\det(\boldsymbol{J}) = \left(\frac{N}{\sigma^2}\right)^K \begin{vmatrix} J_{11} & J_{12} & J_{13} \\ J_{12} & J_{22} & J_{23} \\ J_{13} & J_{23} & J_{33} \end{vmatrix}. \tag{A.52}$$

With some algebra, it can be shown that

$$\det(\boldsymbol{J}) = \left(\frac{N}{\sigma^2}\right)^{K+3} \frac{\omega^2(N^2-1)t_s^2}{12c^2}\cos^2\theta \left(\sum_{k=1}^{K} A_k^2\right)\left(\sum_{k=1}^{K}\sum_{m=1}^{K} A_k^2 A_m^2 d_{m1}(d_{m1}-d_{k1})\right). \tag{A.53}$$

The CRLB for the AOA estimation is given by the third diagonal element of the inverse of the Fisher Information Matrix, i.e.

$$\text{CRLB}(\theta) = J_{33}^{-1} = \frac{1}{\det(\boldsymbol{J})} \begin{vmatrix} J_{11} & J_{12} \\ J_{12} & J_{22} \end{vmatrix} \left(\frac{N}{\sigma^2}\right)^K \tag{A.54}$$

With some algebra, it can be shown that

$$\text{CRLB}(\theta) = \left(\frac{\sigma^2}{\sum_{k=1}^{K} A_k^2}\right) \frac{1}{K\bar{d}^2} \sum_{k=1}^{K}\sum_{m=1}^{K} \frac{c^2}{N\omega^2\cos^2\theta} + \frac{d_{m1}(d_{m1}-d_{k1})12\sin^2\theta}{N(N^2-1)t_s^2\omega^2\cos^2\theta}, \tag{A.55}$$

where

$$\bar{d}^2 = \sum_{k=1}^{K} d_{k1}^2 + \frac{1}{K}\left(\sum_{k=1}^{K} d_{k1}\right)^2 = \frac{1}{K}\sum_{k=1}^{K}\sum_{m=1}^{K} d_{m1}(d_{m1}-d_{k1}). \tag{A.56}$$

Inspection of (A.55) shows that the first term inside the double summation is inversely proportional to N while the second term is inversely proportional to N^3. For large N, the second term is negligible, and so the CRLB can be approximated by

$$\begin{aligned}
\text{CRLB}(\theta) &\approx \left(\frac{\sigma^2}{\sum_{k=1}^{K} A_k^2}\right) \frac{1}{K\bar{d}^2} \sum_{k=1}^{K}\sum_{m=1}^{K} \frac{c^2}{N\omega^2\cos^2\theta}, && \text{(A.57)}\\
&\approx \left(\frac{\sigma^2}{\sum_{k=1}^{K} A_k^2}\right) \frac{1}{K\bar{d}^2} \sum_{k=1}^{K}\sum_{m=1}^{K} \frac{1}{N}\left(\frac{c}{2\pi f\cos\theta}\right)^2, && \text{(A.58)}\\
&\approx K\left(\frac{\sigma^2}{\sum_{k=1}^{K} A_k^2}\right) \frac{1}{\bar{d}^2}\frac{1}{N}\left(\frac{c}{2\pi f\cos\theta}\right)^2, && \text{(A.59)}\\
&\approx K\left(\frac{2\sigma^2}{\sum_{k=1}^{K} A_k^2}\right) \frac{1}{N}\left(\frac{c}{2\pi f\cos\theta}\right)^2 \cdot \frac{1}{2\bar{d}^2}, && \text{(A.60)}\\
&\approx K\frac{1}{\sum_{k=1}^{K}\eta_k N} \cdot \left(\frac{c}{2\pi f\cos\theta}\right)^2 \cdot \frac{1}{2\bar{d}^2}, && \text{(A.61)}
\end{aligned}$$

where $\eta_k = A_k^2/2\sigma^2$ is the signal-to-noise ratio (SNR) of the signal in the k-th channel.

Under the assumption that the SNR of the signal is the same for each channel, i.e. $\eta = \eta_1 = \eta_2 = \cdots, \eta_K$, the CRLB can be further simplified to give

$$\text{CRLB}(\theta) \approx \frac{1}{\eta N} \cdot \left(\frac{c}{2\pi f\cos\theta}\right)^2 \cdot \frac{1}{2\bar{d}^2}. \tag{A.62}$$

A.3.2 Cramér-Rao Lower Bounds for Two Antennas

For the special case of two antennas, i.e. $K = 2$, it can be shown that

$$\bar{d}^2 = \frac{1}{2} d_{21}^2, \tag{A.63}$$

and so the CRLB for two antennas is given by

$$\mathrm{CRLB}(\theta) \approx \frac{1}{\eta N} \cdot \left(\frac{c}{2\pi f d_{21} \cos\theta} \right)^2. \tag{A.64}$$

Bibliography

[1] M. I. Skolnik, *Radar Handbook*. McGraw-Hill, Inc., 2nd ed., 1990.

[2] H. L. Van Trees, *Optimal Array Processing*. Detection, Estimation and Modulation Theory IV, John Wiley & Sons, Inc., 2002.

[3] J. Jones, A. R. Webster, and W. K. Hocking, "An improved interferometer design for use with meteor radars," *Radio Science*, vol. 33, pp. 55–65, February 1998.

[4] H. H. Jenkins, *Small-Aperture Radio Direction-Finding*. Artech, 1991.

[5] R. G. Wiley, *ELINT: The Interception and Analysis of Radar Signals*. Artech House Radar Library, Artech House, Inc., 2006.

[6] D. Adamy, *EW101: A First Course in Electronic Warfare*. Artech House Radar Library, Artech House, Inc., 2001.

[7] A. E. Spezio, "Electronic warfare systems," *Microwave Theory and Techniques, IEEE Transactions on*, vol. 50, pp. 633–644, March 2002.

[8] J. B. Tsui, *Digital Techniques for Wideband Receivers*. SciTech Publishing, Inc., 2nd ed., 2004.

[9] S. E. Lipsky, *Microwave Passive Direction Finding*. SciTech Publishing, Inc., October 2004.

[10] D. Adamy, *EW102: A Second Course in Electronic Warfare*. Artech House Radar Library, Artech House, Inc., 2004.

[11] A. R. Baron, K. P. Davis, and C. D. Hofmann, "Passive direction finding and signal location," *Microwave Journal*, vol. 25, pp. 59–76, September 1982.

[12] P. E. Pace, *Detecting and Classifying Low Probability of Intercept Radar*. Artech House Radar Library, Artech House, Inc., 2004.

[13] P. S. T. Steen, G. F. Stott, and F. Fallside, "The application of feed-forward connectionist models to ESM bearing estimation using signal amplitude," in *Signal Processing Techniques for Electronic Warfare, IEE Colloquium on*, pp. 4/1–4/6, 1992.

[14] G. F. Stott, "DF algorithms for ESM," in *Military Microwaves, Proceedings of the 6th Conference on*, pp. 463–468, July 1988.

[15] S. M. Kay, "A fast and accurate single frequency estimator," *Acoustics, Speech, and Signal Processing, IEEE Transactions on*, vol. 37, pp. 1987–1990, December 1989.

[16] J. P. Y. Lee, "A multi-channel digital receiver for intrapulse analysis and direction-finding," in *Communications, Computers and Signal Processing, Proceedings of the IEEE Pacific Rim Conference on*, pp. 589–592, 1999.

[17] D. C. Rife and R. R. Boorstyn, "Single-tone parameter estimation from discrete-time observations," *Information Theory, IEEE Transactions on*, vol. 20, pp. 591–598, September 1974.

[18] M. A. Richards, *Fundamentals of Radar Signal Processing.* McGraw-Hill, Inc., 2005.

[19] K. L. Fuller, "To see and not be seen," *IEE Proceedings*, vol. 137, Pt F., pp. 1–9, February 1990.

[20] G. Schrick and R. G. Wiley, "Interception of LPI radar signals," in *Radar Conference, Proceedings of the IEEE*, pp. 108–111, May 1990.

[21] J. Edwards, "Focus on compressive sensing [special reports]," *Signal Processing Magazine, IEEE*, vol. 28, no. 2, pp. 11–13, 2011.

[22] R. Baraniuk, "Compressive sensing [lecture notes]," *Signal Processing Magazine, IEEE*, vol. 24, no. 4, pp. 118–121, 2007.

[23] E. Candes and M. Wakin, "An introduction to compressive sampling," *Signal Processing Magazine, IEEE*, vol. 25, no. 2, pp. 21–30, 2008.

[24] W. Du Plessis, P. Potgieter, M. Gouws, and E. Malan, "Initial results for compressive sensing in electronic support receiver systems," in *Electronics, Communications and Photonics Conference (SIECPC), 2011 Saudi International*, pp. 1–6, 2011.

[25] S. A. Tretter, "Estimating the frequency of a noisy sinusoid by linear regression," *Information Theory, IEEE Transactions on*, vol. 31, pp. 832–835, November 1985.

[26] V. Clarkson, "Efficient single frequency estimators," in *Signal Processing and its Applications, Proceedings of the IEEE International Symposium on (ISSPA)*, pp. 1–4, 1992.

[27] G. W. Lank, I. S. Reed, and G. E. Pollon, "A semicoherent detection and doppler estimation statistic," *Aerospace and Electronic Systems, IEEE Transactions on*, vol. AES-9, pp. 151–165, 1973.

[28] S. M. Kay, *Modern Spectral Estimation.* Englewood Cliffs, NJ, 1988.

[29] S. N. Crozier, "Performance and complexity comparison of discrete-time frequency estimation algorithms," in *17th Biennial Symposium on Communications*, pp. 271–275, 1994.

[30] S. N. Crozier, "Theoretical and simulated performance for a novel frequency estimation technique," in *Third International Mobile Satellite Conference, Proceedings of the*, pp. 423–428, 1993.

[31] L. P. Lafrance, M. A. Cantin, Y. Savaria, S. H. Sung, and P. Lavoie, "Architecture and performance characterization of hardware and software implementation of the crozier frequency estimation algorithm," in *Circuits and Systems, Proceedings of the IEEE International Symposium on (ISCAS)*, vol. 4, pp. 823–826, May 2002.

[32] P. J. D. Gething, *Radio Direction Finding and Superresolution.* IET Electromagnetic Waves Series 33, The Instituition of Engineering and Technology, 2006.

[33] R. S. Andrews, "Antenna and other systematic effects on amplitude comparison monopulse systems," *Electronic Circuits and Systems, IEE Journal on*, vol. 3, pp. 103–108, May 1979.

[34] P. Hajiani, H. Habibi, M. Hakkak, and F. Mazlumi, "Accuracy in wideband direction of arrival system," in *Electromagnetic Compatibility, 2007. EMC 2007. International Symposium on*, pp. 394–397, 2007.

[35] J. S. Lim, C. G. Jung, and G. S. Chae, "A design of precision RF direction finding device using circular interferometer," in *Intelligent Signal Processing and Communication Systems, Proceedings of the International Symposium on*, pp. 713–716, November 2004.

[36] S. Germishuizen and D. Baker, "Practical accuracy limitations in airborne microwave interferometric direction finding," in *AFRICON, IEEE 4th AFRICON*, vol. 1, pp. 266–271, September 1996.

[37] G. E. James, "The practical implementation of DF systems using time-to-digital converters," in *Electro Magnetic Remote Sensing Defence Technology Centre Technical Conference, Proceedings of the 2nd*, June 2005.

[38] "TDC-GPX datasheet: Ultra-high performance 8 channel time-to-digital converter." ACAM-Messelectronic GMBH, http://www.acam.de, May 2007.

[39] G. M. Huang, L. X. Yang, and Z. Y. He, "Time-delay direction finding based on canonical correlation analysis," in *Circuits and Systems, Proceedings of the IEEE International Symposium on (ISCAS)*, vol. 6, pp. 5409–5412, May 2005.

[40] "TADC-1000 data sheet: 12.5GS/s digitizer module." Tektronix Component Solutions, http://component-solutions.tek.com, 2011.

[41] C. Brinegar, "Passive direction finding: Combining amplitude and phase based methods," in *National Aerospace and Electronics Conference, Proceedings of the IEEE (NAECON)*, pp. 78–84, 2000.

[42] E. J. Baghdady, "Hybrid interferometry for high-resolution DOA measurement," in *National Aerospace and Electronics Conference, Proceedings of the IEEE (NAECON)*, vol. 4, pp. 2092–2097, May 1989.

[43] S. Chandran, *Advances in Dirrection-of-Arrival Estimation.* Artech House Radar Library, Artech House, Inc., 2006.

[44] Y.-S. Yoon, *Direction-of-Arrival Estimation of Wideband Sources Using Sensor Arrays*. PhD thesis, School of Electrical and Computer Engineering, Georgia Institute of Technology, 2004.

[45] E. Tuncer and B. Friedlander, *Classical and Modern Direction-of-Arrival Estimation*. Academic Press Inc., September 2009.

[46] W. Liu and S. Weiss, *Wideband Beamforming: Concepts and Techniques*. Wiley Series on Wireless Communications and Mobile Computing, John Wiley & Sons, Ltd, 2010.

[47] H. So, "Time-delay estimation for sinusoidal signals," *Radar, Sonar and Navigation, IEE Proceedings* -, vol. 148, no. 6, pp. 318–324, 2001.

[48] R. G. Lyons, *Understanding Digital Signal Processing*. Prentice-Hall, 2nd ed., 2004.

[49] R. G. Lyons, *Understanding Digital Signal Processing*. Prentice-Hall, third edition ed., 2011.

[50] F. Harris, "On the use of windows for harmonic analysis with the discrete fourier transform," *Proceedings of the IEEE*, vol. 66, pp. 51 – 83, jan. 1978.

[51] B. G. Quinn, "Estimating frequency by interpolation using fourier coefficients," *Signal Processing, IEEE Transactions on*, vol. 42, no. 5, pp. 1264–1268, 1994.

[52] T. Grandke, "Interpolation algorithms for discrete fourier transforms of weighted signals," *Instrumentation and Measurement, IEEE Transactions on*, vol. 32, no. 2, pp. 350–355, 1983.

[53] V. Jain, W. L. Collins, and D. C. Davis, "High-accuracy analog measurements via interpolated fft," *Instrumentation and Measurement, IEEE Transactions on*, vol. 28, no. 2, pp. 113–122, 1979.

[54] C. A. Shaffer, *A Practical Introduction to Data Structures and Algorithm Analysis: Java Edition*. Prentice Hall, Inc., 1998.

[55] M. T. Goodrich and R. Tamassia, *Data Structures and Algorithms in Java*. John Wiley & Sons, Inc., second ed., 2001.

[56] S. M. Kay, *Fundamentals of Statistical Signal Processing, Volume I: Estimation Theory*, vol. 1 of *Prentice Hall Signal Processing Series*. Prentice Hall, 18 ed., April 1993.

[57] E. Stansfield, "Accuracy of an interferometer in noise," *Radar, Sonar and Navigation, IEE Proceedings* -, vol. 143, pp. 217–226, August 1996.

[58] S. C. Wang, R. Inkol, S. Rajan, and F. Patenaude, "An exact formula for the probability density of the phase error of a digital interferometer," in *Communications (QBSC), 2010 25th Biennial Symposium on*, pp. 201–204, May 2010.

[59] S. Wang, R. Inkol, S. Rajan, and F. Patenaude, "Probability density of the phase error of a digital interferometer with overlapped fft processing," in *Circuits and Systems (MWSCAS), 2010 53rd IEEE International Midwest Symposium on*, pp. 849–852, August 2010.

[60] D. G. Gregoire and G. B. Singletary, "Advanced ESM AOA and location techniques," in *National Aerospace and Electronics Conference, Proceedings of the IEEE (NAECON)*, vol. 2, (Owego, New York 13827), pp. 917–924, May 1989.

[61] E. Jacobs and E. W. Ralston, "Ambiguity resolution in interferometry," *Aerospace and Electronic Systems, IEEE Transactions on*, vol. 17, pp. 766–780, November 1981.

[62] W. Zheng, X. Zuo, Y. Ma, and Z. Hou, "Algorithm of multi-baseline interferometer phase difference in fuzzy circumstance," in *Consumer Electronics, Communications and Networks (CECNet), 2011 International Conference on*, pp. 3902 –3905, april 2011.

[63] X.-G. Xia and G. Wang, "Phase unwrapping and a robust chinese remainder theorem," *Signal Processing Letters, IEEE*, vol. 14, pp. 247 –250, april 2007.

[64] X. Li and X.-G. Xia, "A fast robust chinese remainder theorem based phase unwrapping algorithm," *Signal Processing Letters, IEEE*, vol. 15, pp. 665 –668, 2008.

[65] X.-G. Xia and K. Liu, "A generalized chinese remainder theorem for residue sets with errors and its application in frequency determination from multiple sensors with low sampling rates," *Signal Processing Letters, IEEE*, vol. 12, pp. 768 – 771, nov. 2005.

[66] W. Wang and X.-G. Xia, "A closed-form robust chinese remainder theorem and its performance analysis," *Signal Processing, IEEE Transactions on*, vol. 58, pp. 5655 –5666, nov. 2010.

[67] X. Li, X.-G. Xia, and H. Liang, "A robust chinese remainder theorem with its applications in moving target doppler estimation," pp. 1289 –1294, may 2010.

[68] X. Li, H. Liang, and X.-G. Xia, "A robust chinese remainder theorem with its applications in frequency estimation from undersampled waveforms," *Signal Processing, IEEE Transactions on*, vol. 57, pp. 4314 –4322, nov. 2009.

[69] G. Li, J. Xu, Y.-N. Peng, and X.-G. Xia, "An efficient implementation of a robust phase-unwrapping algorithm," *Signal Processing Letters, IEEE*, vol. 14, pp. 393 –396, june 2007.

[70] Y. W. Wu, S. Rhodes, and E. H. Satorius, "Direction of arrival estimation via extended phase interferometry," *Aerospace and Electronic Systems, IEEE Transactions on*, vol. 31, pp. 375–381, January 1995.

[71] J.-H. Lee, S.-W. Cho, and H. S. Kim, "Newton-type method in spectrum estimation-based AOA estimation," *IEICE Electronics Express*, vol. 9, pp. 1036–1043, June 2012.

[72] H.-W. Wei and Y.-G. Shi, "Performance analysis and comparison of correlative interferometers for direction finding," in *Signal Processing (ICSP), 2010 IEEE 10th International Conference on*, pp. 393–396, October 2010.

[73] L. Qin, K.-X. Jia, and Z.-S. He, "Performance analysis of correlative interferometer direction finder using cosine function," in *Intelligent Signal Processing and Communication Systems (ISPACS), 2010 International Symposium on*, pp. 1–4, December 2010.

[74] C.-S. Park and D.-Y. Kim, "The fast correlative interferometer direction finder using i/q demodulator," pp. 1–5, Aug. 2006.

[75] X.-B. An, Z.-H. Feng, W.-D. Wang, and T. Li, "A single channel correlative interferometer direction finder using XVI receiver," in *Microwave and Millimeter Wave Technology, 2002. Proceedings. ICMMT 2002. 2002 3rd International Conference on*, pp. 1158–1161, August 2002.

[76] Oxley Consultants, *DF Decoding Software User Guide (Version 8.11)*.

[77] J. Zhong and M. Wang, "Phase unwrapping by a lookup table method: Application to phase maps with singular points," *Optical Engineering*, vol. 38, no. 12, pp. 2075–2080, 1999.

[78] R. L. Goodwin, "Ambiguity resistant three and four antenna interferometers," Tech. Rep. ADB014135, Naval Research Laboratory, September 1976.

[79] S. Holm, A. Austeng, K. Iranpour, and J.-F. Hopperstad, *Nonuniform Sampling: Theory and Practice*, ch. 19, p. 912. Springer, 1 ed., June 2001.

[80] F. Ares-Pena, J. Rodriguez-Gonzalez, E. Villanueva-Lopez, and S. Rengarajan, "Genetic algorithms in the design and optimization of antenna array patterns," *Antennas and Propagation, IEEE Transactions on*, vol. 47, no. 3, pp. 506–510, 1999.

[81] E. Rajo-Iglesias and O. Quevedo-Teruel, "Linear array synthesis using an ant-colony-optimization-based algorithm," *Antennas and Propagation Magazine, IEEE*, vol. 49, pp. 70–79, April 2007.

[82] V. Murino, A. Trucco, and C. Regazzoni, "Synthesis of unequally spaced arrays by simulated annealing," *Signal Processing, IEEE Transactions on*, vol. 44, no. 1, pp. 119–122, 1996.

[83] F. J. Villegas, "Parallel genetic-algorithm optimization of shaped beam coverage areas using planar 2-d phased arrays," *Antennas and Propagation, IEEE Transactions on*, vol. 55, pp. 1745–1753, June 2007.

[84] T. Ballal and C. Bleakley, "Phase-difference ambiguity resolution for a single-frequency signal," *Signal Processing Letters, IEEE*, vol. 15, pp. 853 –856, 2008.

[85] T. Ballal and C. Bleakley, "3d location and orientation estimation using angle of arrival," in *Intelligent Signal Processing, 2009. WISP 2009. IEEE International Symposium on*, pp. 21 –26, aug. 2009.

[86] T. Ballal and C. Bleakley, "Phase-difference ambiguity resolution for a single-frequency signal in the near-field using a receiver triplet," *Signal Processing, IEEE Transactions on*, vol. 58, pp. 5920 –5926, nov. 2010.

[87] B. Friedlander, "Direction finding using an interpolated array," in *Acoustics, Speech and Signal Processing, Proceedings of the IEEE International Conference on (ICASSP)*, vol. 5, pp. 2951–2954, April 1990.

[88] A. J. Weiss and M. Gavish, "Direction finding using ESPRIT with interpolated arrays," *Signal Processing, IEEE Transactions on*, vol. 39, pp. 1473–1478, June 1991.

[89] M. Bühren, M. Pesavento, and J. F. Böhme, "Virtual array design for array interpolation using differential geometry," in *Acoustics, Speech and Signal Processing, Proceedings of the IEEE International Conference on (ICASSP)*, no. 2, pp. 229–232, May 2004.

[90] R. S. Kenett and S. Zacks, *Modern Industrial Statistics: The Design and Control of Quality and Reliability.* Cengage Learning, Inc., February 1998.

[91] L. C. Godara, "Applications of antenna arrays to mobile communications, part ii: Beam-forming and direction-of-arrival considerations," *Proceedings of the IEEE*, vol. 85, pp. 1195–1245, August 1997.

[92] R. A. Monzingo and T. W. Miller, *Introduction to Adaptive Arrays.* SciTech Publishing, Inc., 2004.

[93] P. Stoica and A. Nehorai, "MUSIC, maximum likelihood and cramer-rao bound," *Acoustics, Speech, and Signal Processing, IEEE Transactions on*, vol. 37, pp. 720–741, May 1989.

[94] B. D. Van Veen and K. M. Buckley, "Beamforming: A versatile approach to spatial filtering," *IEEE ASSP Magazine*, vol. 5, pp. 4–24, April 1988.

[95] I. O. L. Frost, "An algorithm for linearly constrained adaptive array processing," *Proceedings of the IEEE*, vol. 60, pp. 926–935, August 1972.

[96] K. M. Buckley, "Spatial/spectral filtering with linearly constrained minimum variance beamformers," *Acoustics, Speech, and Signal Processing, IEEE Transactions on*, vol. 35, pp. 249– 266, March 1987.

[97] K. W. Forsythe, "Utilizing waveform features for adaptive beamforming and direction finding with narrowband signals," *Lincoln Laboratory Journal*, vol. 10, no. 2, pp. 99–126, 1997.

[98] A. Gershman, M. Pesavento, and M. Amin, "Estimating the parameters of multiple wideband chirp signals in sensor arrays," in *Statistical Signal and Array Processing, 2000. Proceedings of the Tenth IEEE Workshop on*, pp. 467–471, 2000.

[99] B. Volcker and B. Ottersten, "Linear chirp parameter estimation from multichannel data," in *Signals, Systems, and Computers, 1999. Conference Record of the Thirty-Third Asilomar Conference on*, vol. 1, pp. 238–242 vol.1, 1999.

[100] A. Zeira and B. Friedlander, "Direction of arrival estimation using parametric signal models," *Signal Processing, IEEE Transactions on*, vol. 44, no. 2, pp. 339–350, 1996.

[101] S. Chen, S. Tan, and L. Hanzo, "Adaptive beamforming for binary phase shift keying communication systems," *Signal Processing*, vol. 87, pp. 68–78, January 2007.

[102] S. Chen, S. Tan, and L. Hanzo, "Linear beamforming assisted receiver for binary phase shift keying modulation systems," in *Wireless Communications and Networking Conference, 2006. WCNC 2006. IEEE*, vol. 3, pp. 1741–1746, 2006.

[103] M. A. de Souza and J. M. P. Fortes, "Maximum likelihood direction-of-arrival estimation of BPSK modulated carriers," in *Information, Communications and Signal Processing, 2003 and the Fourth Pacific Rim Conference on Multimedia. Proceedings of the 2003 Joint Conference of the Fourth International Conference on*, vol. 2, pp. 1043–1047, December 2003.

[104] R. O. Schmidt, "Multiple emitter location and signal parameter estimation," *Antennas and Propagation, IEEE Transactions on*, vol. 34, pp. 276–280, March 1986.

[105] A. Paulraj, R. Roy, and T. Kailath, "A subspace rotation approach to signal parameter estimation," *Proceedings of the IEEE*, vol. 74, pp. 1044–1046, July 1986.

[106] R. Kumaresan and D. W. Tufts, "Estimating the angles of arrival of multiple plane waves," *Aerospace and Electronic Systems, IEEE Transactions on*, vol. 19, pp. 134–139, January 1983.

[107] R. L. Mitchell, "Creating complex signal samples from a band-limited real signal," *Aerospace and Electronic Systems, IEEE Transactions on*, vol. 25, pp. 425–427, May 1989.

[108] J. G. Proakis and D. G. Manolakis, *Digital Signal Processing.* Prentice Hall, 4 ed., 1996.

[109] "Cobham TU-6401 microwave VME tuner datasheet." Cobham, http://www.macom.com/sigint, February 2009.

[110] "Cobham TU-6402 microwave VME RF converter datasheet." Cobham, http://www.macom.com/sigint, February 2009.

[111] "Tekmicro quixilica neptune 2 VXS datasheet." Tekmicro, http://www.tekmicro.com, 2005.

[112] W. B. Kendall, "Unambiguous accuracy of an interferometer angle measuring system," *Space Electronics and Telemetry, IEEE Transactions on*, vol. SET-11, pp. 62–70, June 1965.

[113] P. Stoica and A. Nehorai, "MUSIC, maximum likelihood and cramer-rao bound: Further results and comparisons," *Acoustics, Speech, and Signal Processing, IEEE Transactions on*, vol. 38, pp. 2140–2150, December 1990.

[114] P. Stoica, E. Larsson, and A. Gershman, "The stochastic CRB for array processing: A textbook derivation," *Signal Processing Letters, IEEE*, vol. 8, pp. 148–150, may 2001.

[115] D. C. Rife and R. R. Boorstyn, "Multiple-tone parameter estimation from discete-time observations," *The Bell System Technical Journal*, vol. 55, pp. 1389–1410, November 1976.